Laser-Induced Carbonisation for Biosensing

Zur Erlangung des akademischen Grades eines

DOKTORS DER INGENIEURWISSENSCHAFTEN
(Dr.-Ing.)

von der KIT-Fakultät für Elektrotechnik und Informationstechnik des

Karlsruher Instituts für Technologie (KIT)
angenommene

DISSERTATION

von

M.Sc. Emil R. Mamleyev

Tag der mündlichen Prüfung:	07.03.2023
Hauptreferent:	Prof. Dr. Ulrich Lemmer
Korreferent:	Prof. Dr. Jan G. Korvink

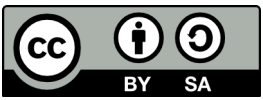

Abstract

The Internet of Things has the goal to build up a global network of devices to monitor a multitude of parameters e.g. to prevent hazards in multiple fields, reducing risks for human life, infrastructure, and the environment. Biomedical point of care devices providing timely assistance for people under personal and external danger are among the fastest growing topics in this developing field. It takes form in arrays of sensors, developed mainly utilising flexible electronics capable of specialised analyte detection. These new devices should meet the following criteria: be easy in manufacturing, economically feasible, and have the reduced carbon footprint. From the diverse number of developed sensors, the carbon-based devices are distinguished by their robustness, high bio-compatibility, excellent response efficiency, and chemical inertness.

The novel manufacturing method provided by the laser-induced carbonization from polymer precursors allows rapid fabrication of carbon-rich porous films directly built in the flexible substrates compared to standard pyrolytic methods and addresses all set goals. This novel material prepared by means of semi-industrial laser systems remains relatively unstudied. This investigation is performed on two widely available polymer precursors used in industrial applications, Kapton and Nomex. The thermal model for the precursor carbonization and evolution was modified and applied to a broad range of the tested laser input parameters. The key findings on the development of laser carbon film match the simulated results. The model provides good approximation of the carbonisation but still requires improvement on the rendering of volumetric parameters influenced by the increase of porosity.

The laser carbon films were studied for their crystalline and surface chemical properties, showing potential for utilisation in the analysis of interfaces, and can be tuned via comprehensible methods for selective detection of the specific analytes. Using this, the biomedical sensors were developed for passive urea detection via intermediate chitosan host layer for the Urease enzyme, and active non-enzymatic sensors anchored via Cu/CuO composite for specific glucose detection. This paves the way for the fabrication of tuned biosensors and chemical sensors on a semi-industrial scale compatible with roll-to-roll methods.

Zusammenfassung

Das Internet of Things hat das Ziel, ein globales Netz von Geräten zur Überwachung einer Vielzahl von Parametern aufzubauen, um z.B. Gefahren in verschiedenen Bereichen vorzubeugen und Risiken für Menschenleben, Infrastrukturen und die Umwelt zu verringern. Zu den am schnellsten wachsenden Themen in diesem sich entwickelnden Bereich gehören biomedizinische Point-of-Care-Geräte, die rechtzeitig Hilfe für Menschen leisten, die sich in einer persönlichen oder externen Gefahr befinden. Sie werden in Form von Sensorfeldern entwickelt, die hauptsächlich aus flexibler Elektronik bestehen und in der Lage sind, spezielle Analyten zu erkennen. Diese neuen Geräte sollten die folgenden Kriterien erfüllen: Sie sollten einfach herzustellen und wirtschaftlich umsetztbar sein und einen geringen ökologischen Fußabdruck aufweisen. Von der Vielzahl der entwickelten Sensoren zeichnen sich die kohlenstoffbasierten Geräte durch ihre Robustheit, hohe Biokompatibilität, hervorragende Reaktionseffizienz und chemische Inertheit aus. Die neuartige Herstellungsmethode, die durch die laserinduzierte Karbonisierung von Polymervorläufern ermöglicht wird, erlaubt im Vergleich zu pyrolytischen Standardmethoden eine schnelle Herstellung von kohlenstoffreichen porösen Filmen, die direkt in flexible Substrate eingebaut werden, und erfüllt alle gesetzten Ziele. Dieses neuartige Material, das mit halbindustriellen Lasersystemen hergestellt wird, ist noch relativ unerforscht. Diese hier durchgeführte Untersuchung wird an zwei weit verbreiteten Polymervorläufern umgesetzt, die in industriellen Anwendungen verwendet werden, nämlich Kapton und Nomex. Das thermische Modell für die Karbonisierung und Entwicklung des Vorläufers wurde modifiziert und auf einen breiten Bereich der getesteten Lasereingangsparameter angewendet. Die wichtigsten Erkenntnisse über die Entwicklung des Laserkohlen-

stofffilms stimmen mit den simulierten Ergebnissen überein. Das Modell liefert eine gute Annäherung an die Karbonisierung, erfordert aber noch Verbesserungen bei der Darstellung der volumetrischen Parameter, die durch den Anstieg der Porosität beeinflusst werden.
Die Laser-Kohlenstoff-Filme wurden auf ihre kristallinen und oberflächenchemischen Eigenschaften hin untersucht, die sich für die Analyse von Grenzflächen eignen und mit nachvollziehbaren Methoden für den selektiven Nachweis der spezifischen Analyten eingestellt werden können. Auf diese Weise wurden biomedizinische Sensoren für den passiven Nachweis von Harnstoff über eine Chitosan-Zwischenschicht für das Enzym Urease und aktive nicht-enzymatische Sensoren, die über ein Cu/CuO-Komposit für den spezifischen Nachweis von Glukose verankert sind, entwickelt. Dies ebnet den Weg für die Herstellung abgestimmter Biosensoren und chemischer Sensoren in einem halbindustriellen Maßstab, der mit Rolle-zu-Rolle-Verfahren kompatibel ist.

Contents

1 Introduction

1.1 Motivation

Internet of Things (IoT) became a groundbreaking new technology concept addressed to the optimisation, simplification, betterment in our everyday life, playing an impactful role in the reduction of carbon emission to the environment [1, 2]. Since the coining of this term in the early 1980s, IoT has evolved into an independent field and undergone a significant shift in the character of data acquisition [3, 4]. The pivotal change was observed in 2009 when ratio between autonomously to manually generated data rose to 1.84 from 0.08 less than a decade prior [2]. Thus, in modern terms, IoT presents as a complex communication web in a short range between people and devices ('things'), and things themselves to remote integration, monitoring, evaluation and manipulation of trends for these devices [5].

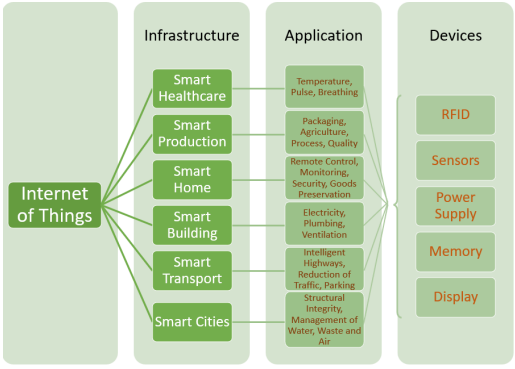

Figure 1.1: IoT infrastructure (adopted from Ref. [4]).

Figure 1.1 shows multiple focal fields in IoT, concentrated either on personal use or the infrastructural maintenance and prevention of hazardous accidents. All of those realised only through several types of devices, such as sensors for environmental monitoring and hazard detection, memory for storage of the collected data, RFID and antennas for broadcasting of those data to computational hubs, power supply for maintaining the operation of the active devices and display for interaction with a user. All of those devices can be implemented through a single or in a combination of several user interfacing apparatuses [4].

Figure 1.2 shows focal points in the current research and industry in IoT, where the top three attributed to electrical engineering, telecommunications and information systems, emphasising data collection, optimisation and immediate evaluation. Moreover, the most important fields include instrumentation, analytical chemistry and applied physics to focus on the environmental sensing for hazards. It is estimated that the global requirement for devices connected to IoT can rise to several trillions [4]. Thus, the device materials and fabrication methods should

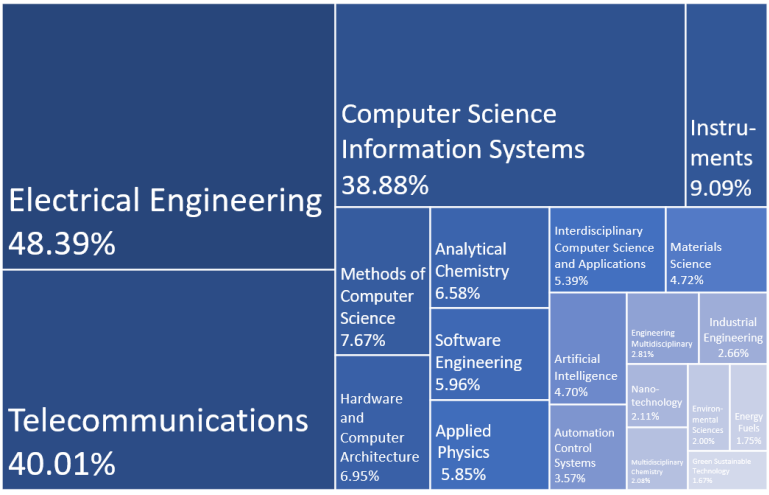

Figure 1.2: Current state in focus of the research fields in IoT. Data provided from Web of Science engine.

be low-cost and addressed for specialised operating conditions in the selected environment to fulfil such needs. Standard fabrication methods for microelectromechanical systems (MEMS) include multistep preparation and processing with a strict requirement of the cleanroom facilities, thus raising the price of a final item and show mechanical stability inherited from the employment of the silicon technology [6]. This creates a need for alternative fabrication techniques and active material variety to meet a performance niche. Lately, due to these requirements, a number of new apparatus and rapid prototyping technologies have emerged, such as printing techniques via screen, inkjet, or spray, 3D printing, hot-embossing, as well as selective sintering *etc.* [7].

Notably, personal care is the most important amongst all IoT fields, showing massive potential in monitoring and preventing health risks. Fabrication of the devices realised through means of flexible and stretchable sensors and electronics, for natural fitting to human with direct connection to the body for the measurement of the property of interest [1, 8]. These devices should meet criteria on robustness, detection below and within risk values, complementary to adequate operation at bent condition, or relate to deviation from the degree of bending [9]. Typically, the devices built-in flexible or stretchable substrates, which can be of polymer, paper or textile, and in order to meet environmental criteria, these substrates and devices should be manufactured from biocompatible and degradable materials [4], dependent on requirements in the operation lifetime.

Figure 1.3 shows contemporary research within flexible and stretchable devices, which indicate a strong emphasis on material science and nanotechnology due to permanent requirements in the new materials with improved electrical, magnetic, optical and chemical properties. Other significant branches include applications, which primarily relates to utilisation in various types of sensors and engineering new types of electronics meeting requirement in the flexible devices.

In raw numbers, the interest of the scientific community in both IoT and flexible/stretchable devices is continuously rising, as seen in Figure 1.4, with a vast number of overlapping multidisciplinary fields. A new type of wearable smart devices (watches, bands, rings) have secured their position in the non-invasive,

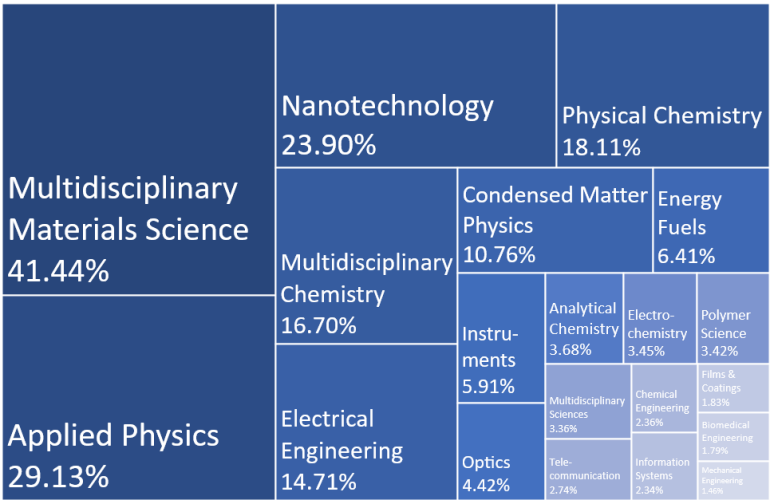

Figure 1.3: Current focal fields in the research of flexible and stretchable devices. Data provided from Web of Science engine.

permanent monitoring of the user condition with reliable output, nearly comparable to professional medicinal devices. Currently, industry is expanding to cover direct real-time health risk monitoring of sweat, saliva, and blood [10]. Notably, it will spur a commercial demand in IoT and flexible electronics, promoting further research and immediate application in the final smart device.

An inclusion of biomedical sensors in the final device rely on their performance durability, selectivity of the detection, combined with mechanical flexibility and ease of manufacturing. However, the sensing area is currently constrained due to design requirements, and the number of sensors limited to the output voltage of the device for practical use throughout the day [10, 11]. New sensors can be included within movable parts, which in part require flexibility and bendability and are compatible with low power consumption as low as ($\sim$100 mW) [11]. Thus, the selection of the material and engineering of the sensor must meet multiple parameters for successful commercial utilisation.

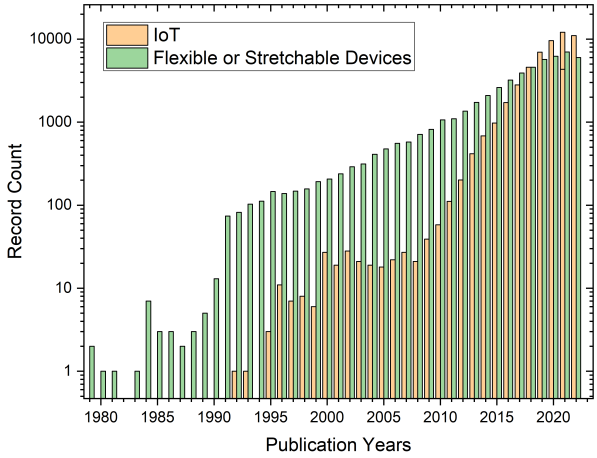

Figure 1.4: The number of papers published on IoT (orage bars) flexible and stretchable electronics (green bars). The data provided from Web of Science engine.

Among the most promising state-of-art substrate materials that are broadly utilised in industry and research are polyethylene terephthalate (PET), polydimethylsiloxane (PDMS) and polyimide (PI), polycarbonate (PC), and polyethylene naphthalate (PEN) [12]. However, a device functionalisation is attained in conjuncture with active materials, providing functionality through electrodes, transducers and actuators [13]. Among those functional materials, one of the most promising classes is carbon-based micro and nanomaterials, such as graphene [14], fullerenes [15], nanotubes [16, 17] and polymer derived carbons ('glassy' carbon) [18, 19], due to their outstanding biocompatibility electrical and electrochemical performance [13]. The graphene technology is envisioned to provide many benefits for the industry in terms of applications, promising new type of lasers [20, 21], environmental sensors [22, 23], desktop quantum experiment setups [24–26], electrical devices capable of operating at THz frequencies [27]. However, the modern approaches in graphene synthesis rely on a highly controlled environment via cleanroom facilities, vacuum technology, CVD, and epitaxy, which are significantly adding cost on the production [28–31]. An alternative approach is proposed utilising

chemical methods for mass production of graphene oxide from graphite and further reduction via chemical or physical methods [32, 33]. However, this reduced graphene oxide suffers from defects, therefore showed the highest suitability for chemical and biological sensing, but does not meet the electrical performance quality of the graphene fabricated with other methods [34].
Alternatively, the glassy carbon (glass-like carbon by IUPAC convention [35]) provided significant advancements in controlled carbon film and 2.5D manufacturing of the low-cost devices [36, 37]. Generally, their fabrication process through pyrolysis can be described as thermal degradation of the natural organic or synthetic polymers in the inert gas environments (N_2, N_2/H_2, Ar) at temperatures above 450 °C [18, 19, 38, 39]. The carbonisation occurs at temperature starting from 800 °C at which molecular oxygen and nitrogen are released and hydrocarbons beginning a dissociation to hydrogen and carbon, with latter retaining as designed microstructure [18, 19, 38, 39]. The yielded material has multiple applications due to its chemical inertness and unique mechanical properties, and have already found industrial niches such as MEMS devices (C-MEMS) substituting Si [40–42], including designs with high aspect ratios [43], an inert electrode material for electrochemistry [42], a construction reinforcing composites through a carbon fibre [44, 45]. Notably, the microfabrication techniques employs electrospinning [18, 46], UV [43, 47], electron beam [48] and nanoimprint lithography [49], from the photoresists containing epoxy and phenolic resins [19, 50, 51]. The following pyrolysis induces a structure shrinkage of up to ∼75 %, thus promoting device size reduction from micro to nano scale [36]. C-MEMS technology meets multiple requirements for flexible electronics showing great potential in environmental sensing and integration with biological systems [52]. However, it remains a multistep process, partially relying on cleanroom facility (UV, e-beam lithography) and the pyrolysis step requiring several hours before finalisation.
Lately, the different methods offered a pivotal change for the film fabrication by the implementation of the one-step process of the laser-induced carbonisation, which can be carried out with any pre-determined shape directly on the desired substrates, with a majority of reports focusing on polyimide (commercially known

as Kapton) [53]. The process promotes rapid phase transformation into carbon-rich film with graphitic content of medium-range order, directly incorporated within the precursor substrate [54–56]. This material showed properties comparable to glassy carbon; nevertheless, it provides superior surface activity advantageous in environmental, chemical and biological detection [57] by virtue its nanostructurally rendered morphology, controllable wetting properties, and presence of oxygen and nitrogen functional groups [56, 58]. The selection of laser type (wavelength), operation parameters such as output power, pulse duration and frequency plays an essential role in the formation and quality of fabricated laser carbon films [53, 59–61]. At the moment, the smallest achieved track width was reported at $\sim$4.3 µm prepared in the laser systems with 405 nm wavelength,in vacuum [62]. The laser carbon films can be fabricated on multiple different precursor materials, most commonly on cheap, abundant, flexible films such as Kapton [54–56], phenolic papers [63, 64], textiles, and cellulose-filled composites with Nomex and Kevlar [65–68].

1.2 Outline

This thesis is structured in seven chapters followed by a conclusion and future outlook. Chapters two and three give an overview of methods used for the fabrication and brief descriptions of the analytical tools required for characterisation. The fourth chapter discusses a selection of the materials, their properties and important characterisation features and compares them to standard reference materials, such as graphite, graphene and pyrolytically derived carbon from the same precursors. Further chapters focus on the laser-induced carbonisation phenomena, its initiation, simulation of the process, followed by detailed characterisation and analysis of the laser carbon films derived from polymer precursors. Chapter six is focussed on Kapton films as a mainly utilised precursor, with a detailed analysis of the application of various preparation regimes. The results provide an indication of surface activity, which was further used in the fabrication of the passive urea biosensor via the intermediate chitosan layer. Chapter seven is focused on Nomex

infused paper insulation sheet, and the analysis performed in a similar manner. However, the chemical composition and the rigidity of the precursor plays a significant role in variation in the fabrication. Nomex films after laser-induced carbonisation were utilised for copper electroplating and, after specific treatment, used as composite flexible antibacterial coating and as rigid glucose biosensors. This thesis is concluded in chapter eight with a summary and the outlook for future research.

1.3 Main Results

This research resulted in the publication of five manuscripts (four published and one under review) with me as the first author or main contributor.

- **Laser-induced hierarchical carbon patterns on polyimide substrates for flexible urea sensors** [69]
  Published in npj Flexible Electronics, 2019
  Contributions: Involvement in conceiving of the idea and analysis strategy. Initial preparation of the laser carbon films, acquisition and data analysis. Lead in writing and figures preparation.
  Content: Structural and chemical analysis of the intermediate transformation steps in polyimide prior to laser-induced carbonisation. After reaching phase transformation, a set of physiochemical properties were analysed dependent on the input parameters of the laser. The best samples were determined and selected for preparation of the composite flexible Urease/chitosan/laser carbon biosensor.

- **Polyaramid-Based Flexible Antibacterial Coatings Fabricated Using Laser-Induced Carbonization and Copper Electroplating** [66]
  Published in ACS Applied Materials & Interfaces, 2020
  Contributions: Initial concept design and the analysis scheme. Composite film preparation, testing and data analysis. Lead manuscript writing with complete figure preparation.

Content: An investigation was conducted of the laser-induced carbonisation of the polyaramid Nomex films. The fabrication parameters were optimised for the laser carbon tailored to the copper electroplating of rigid and flexible composite films. One of the recipes, particularly for flexible films, was utilised for the fabrication antibacterial coatings.

- **Nano- and Microstructured Copper/Copper Oxide Composites on Laser-Induced Carbon for Enzyme-Free Glucose Sensors** [70]
  Published in ACS Applied Nano Materials, 2021
  Contributions: Initial concept design and the analysis scheme. Composite film preparation, electrochemical testing and data analysis. Lead manuscript writing with complete figure preparation.
  Content: The copper composite fabrication process, optimised for the rigid film preparation was further utilised for annealing at the specific recipe to achieve partial melting and agglomeration into copper micro-spheorids and copper oxide micro-urchins. The best composites treatment were selected by electrochemical testing and optimisation for the glucose sensing. The prepared films showed great response at low overpotential, comparable to analogues response, repeatability after multiple testing, and exhibit great signal during flexing with radius at half of the size of the sample.

- **A Technological Approach for Miniaturization of Three-Dimensional Inductive Levitation Microsuspensions** [71]
  Published in IEEE Magnetics Letters, 2022
  Contributions: Microfabrication of the complete device, wirebonding of the separate micro-coils and characterisation of the levitating actuation.
  Content: The reduction of the micro-coil size results in increase of the magnetic field and decrease in operation current. The new device design involves separate fabrication of the micro-posts starting from internal of 900 µm for levitation coil by forming the solenoid coil, followed by separate microfabrication of external post of 1900 µm for stabilization micro-coil.

The fabricated device induced magnetic field for levitation of the disc with 1100 µm, showing the smallest to date levitation for solenoid micro-coils.

- **Calculation of Mutual Inductance between Circular and Arbitrarily Shaped Filaments via Segmentation Method** [72]
  Under review in Elsevier Journal of Magnetism and Magnetic Materials
  Contributions: Establishment of new method for calculation of mutual inductance between a circular filament and a line segment via Kalantarov-Zeitlin method.
  Content: Two analytical formulas are developed by using Mutual Inductance Method (MIM) and Babic's Method (BM), respectively, for the calculation of mutual inductance between a circular filament and line segment arbitrarily positioning in the space. Any curve can be interpolated by a set of line segments, therefore the mutual inductance between a circular filament and arbitrary shaped filament in the space can be determined. The method was numerically validated by using FastHenry software and reference examples from the literature. In particular, the proposed method was successfully applied to the calculation of mutual inductance between the circular filament and the following special curves such as circular arc, elliptic arc, ellipse, spiral, helices and conical helices.

Additionally, I was involved in research and contributed as the second author resulting in the publication of two manuscripts (one accepted and one under review).

- **Surface Characterisation Reveals Substrate Suitability for Cyanobacterial Phototaxis** [73]
  Accepted in AMI: Acta Biomaterialia
  Contributions: The interpretation of the adhesion models via deconvolution of XPS peaks and asserting of their properties to specific tested specimens.
  Content: Cyanobacteria respond to light stimulation, activating localized assembly of type IV pili for motility. The resulting phototactic response

is highly dependent on the nature of the incoming light stimulus, and the final motility parameters depend on the substrate surface properties. This study considers five substrates, widely utilized in microfluidic technology, to identify the most suitable alternative for performing reliable and repeatable phototaxis assays. To prove that motility can be enhanced, polydimethylsiloxane (PDMS) surfaces were plasma treated to alter their surface wettability. The motility on the plasma-treated PDMS showed similar performance as for glass surfaces. In contrast, untreated PDMS surfaces displayed close to zero motility. We also describe the force interctions of cells with the test surfaces using DLVO (Derjaguin-Landau-Verwey-Overbeek) and XDLVO (extended DLVO) theories. Our findings show that twitching motility on tested surfaces can be described mainly from adhesive forces and hydrophobicity/hydrophilicity surface properties.

- **Distributed Feedback Lasers by Thermal Nanoimprint of Perovskites Using Gelatin Gratings**
  Under review in ACS Applied Materials & Interfaces
  Contributions: SEM investigation.
  Content: Thermal nanoimprint lithography (NIL) for patterning hybrid perovskites has always involved an intricate etching step of a hard stamp material or its master. The research demonstrates for the first time the successful nano-patterning of a perovskite film by NIL with a low-cost polymeric stamp, manufactured with a dichromated gelatin grating structured by holographic lithography. The one-dimensional grating is imprinted into a perovskite film, resulting in a high quality second-order distributed feedback (DFB) laser, which exhibits an excellent performance with a threshold of $81\,\mu J/cm^2$, a linewidth of 0.32 nm and a pronounced linear polarization.

The preliminary results were presented in the international conferences and following papers were published in the proceedings:

- **Flexible Carbon-based Urea Sensor by Laser Induced Carbonisation of Polyimide** [74]
  Published in IEEE 2018 International Flexible Electronics Technology Conference (IFETC).
  Contributions: Fabrication and characterisation of Laser Induced Carbon.
  Content: Pyrolysis of patterned polymers is a well-known technique for obtaining carbon microstructures and devices. Alternatively, the carbon structures can be patterned and embedded on commercially available polyimide films by a controlled laser writing, which induces a pyrolysis-like effect. These flexible laser carbon structures are characterised using microscopic and spectroscopic techniques, and are used as electrodes for the chitosan electrodeposition. Subsequently, urease enzyme is immobilised on the chitosan film, and this composite electrode assembly is used for pH-based urea detection.

- **Reduction of the Nested Solenoid Micro-Coil Size as a Path to Transporter Micro-Actuator Array** [75]
  Published in VDE, ACTUATOR 2022; International Conference and Exhibition on New Actuator Systems and Applications.
  Contributions: Conceptualisation of the experiment. Complete fabrication, its optimisation and characterisation of the levitating actuation.
  Content: The novel technological approach for the miniaturization of 3D inductive levitation microactuators (3D-ILMA) was realized via the nested solenoid micro-coils. The developed technological approach allows the solenoid micro-coil fabrication separately from each other, beginning with the smallest innermost coil of the nested microstructure. The nested two micro-coil structure was fabricated, the inner coils having a diameter of 1000 µmr and 14 windings, the outer coil with a diameter of 1900 µm and 8 windings, and demonstrate its application as the inductive levitating micro-suspension. In particular, a fabricated 3D inductive levitating micro-suspension was able to levitate a 1100 µm diameter disc-shaped proof mass

to a height up to 45 µm. Such miniaturisation is further utilised and extended for arrays of micro-coils.

- **Characterisation of Static Pull-In Effect of Hybrid Levitation Micro-Actuators for Square-Shaped Proof Masses** [76]
  Published in VDE, ACTUATOR 2022; International Conference and Exhibition on New Actuator Systems and Applications.
  Contributions: Conceptualisation of the experiment and results analysis.
  Content: The static pull-in phenomenon was studied on a square-shaped proof mass in the hybrid levitation micro-actuators (HLMA), combining inductive suspension and electrostatic actuation. The reported quasi-finite element method (quasi-FEM) modelling is developed describing the pull-in actuation with a calculation of the localised eddy current and magnetic field with the capability of arbitrary modelling shapes. This modification removes the restriction of the blank disc-shaped proof mass only simulation and creates a more extensive application for the HLMA modelling. The obtained result from this model is verified with coherent experimental data.

- **Calculation of Mutual Inductance Between Circular and Arbitrary Shaped Filaments: Segmentation Method** [77]
  Published in VDE, ACTUATOR 2022; International Conference and Exhibition on New Actuator Systems and Applications.
  Contributions: Conceptualisation of the experiment and results analysis.
  Content: A new semi-analytical formulation for calculating the mutual inductance between a primary circular filament and a secondary filament positioned arbitrarily in space is developed. The method flexibility allows the secondary filament to take any random shape. The accuracy of the presented method has been successfully validated against results from similar models, and also against FastHenry software. Furthermore, the formula can be used to model complex electromagnetic systems and predict their performance.

2 Fabrication Methods

In this chapter, fabrication methods are discussed, including the laser radiation source with 10.6 µm wavelength, and reference method of the polymer pyrolysis in the furnace. The electrochemical deposition methods were used for further functionalisation of the fabricated films, and the fundamental basis of these processes are discussed.

2.1 Mid-IR Laser Source

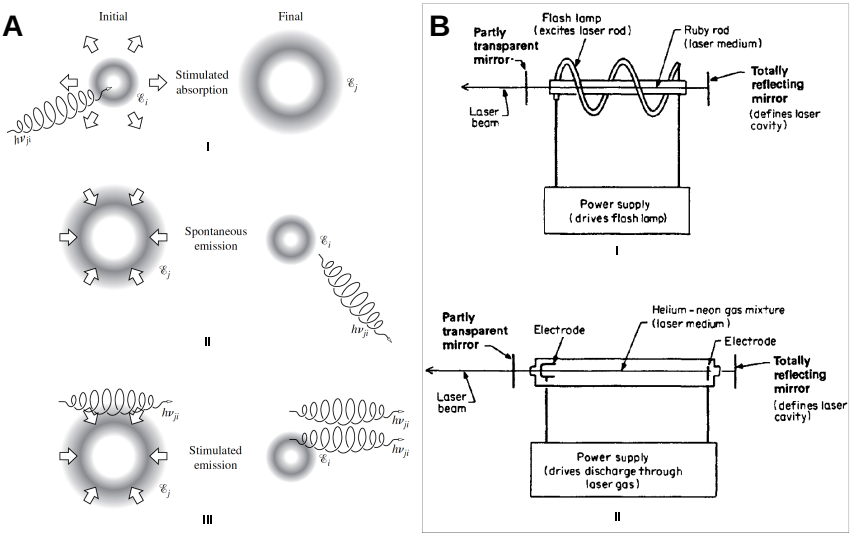

Figure 2.1: (A) Photon transition in the atom (Adopted from [78]). (B) Principle of laser operation (adopted from Ref. [79]).

Light Amplification by Stimulated Emission of Radiation or simply *laser* is an artificial light source, delivering high-intensity radiation with a monochromatic, coherent beam with a divergence bellow 10 mrad [79, 80]. The foundation was created from dynamic equilibrium for a material, which absorbs and re-emits under external electromagnetic radiation. Following Figure 2.1A, the atom, residing at the lowest energy state or the ground-state, is interacted with a photon of adequate energy, thus *absorbs* the energy package. This energy promotes the electron cloud to take a new configuration; where the atom attains state with a higher-energy level. The energy can be transferred to neighbouring atoms via collisions in the medium. Typically, the excess-energy state has $\sim$10 ns lifetime, and causes a *spontaneous emission*, where the atom emits an overload as a photon. However, there is another possible configuration of the *stimulated emission*, where the medium is overflown with electromagnetic radiation, the photon interacts with an excited atom at a high energy state and the atom releases this energy excess with incoming photon [78, 80]. These photons flood the medium and are realised in the form of laser radiation.

Typically, the lasers contain three main components: a medium, where the radiation is generated; a power supply, which allows excitation of the medium to the required energy state; and an optical cavity or a resonator, which concentrates the radiation to stimulated emission. These key components are implemented in different designs dependent on the selected working medium [79].

CO_2 lasers are shown as one of the most versatile lasers and broadly used in industry, research and military, due to power output ranging from under 1 Watt to several kilowatts [79]. The carbon dioxide molecules are a light emitter, but firstly, they require excitation of the vibrational mode to the asymmetrical stretching, with the transition to symmetrical stretching for 10.6 µm radiation generation, or to a bending mode for 9.6 µm, as depicted in Figure 2.2A. The gas tubes are realised in mixture with N_2 for an increase of absorbed energy and further transfer to carbon dioxide molecules; and He gas, which is used as a buffer gas for the heat transfer to higher energy states during excitation and lower stated after emission [79, 81]. The most common type of CO_2 lasers is a sealed-tube gas laser, in the modern setups

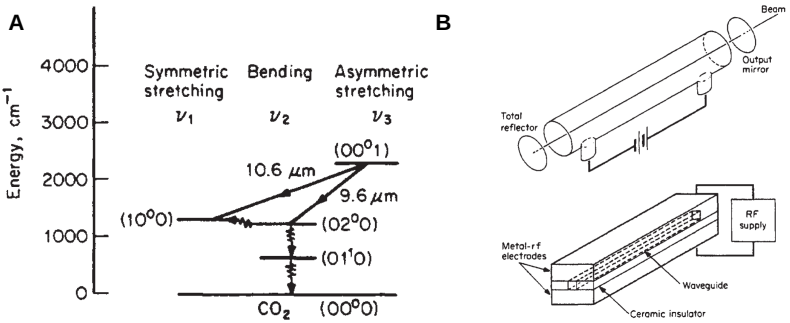

Figure 2.2: (A)Energy level structure in the CO_2 laser with excitation levels of the vibrational modes. (B) The schematics of waveguide laser with RF excitation. Figures adopted from Ref. [79].

complimented with RF excited waveguide. Figure 2.2B shows a typical design, where the gas tube is filled with the aforementioned mixture of gasses with mirrors forming a resonant cavity, with applied high voltage to the electrodes to initiate a discharge through the gas. An applied additional waveguide, perpendicular to the tube axis, provides a reduction in the operating voltage and allows electronic control over output rates in power (up to 100 W) and frequency (up to 10 kHz) [79]. The experiments were carried out on a CO_2-laser ULS Versa Laser 3.50, producing a radiation with 10.6 µm wavelength. The laser radiation is produced in the source unit, collimated and reflected the focus carriage, equipped with sets of lenses and mirrors, which is further controlled by motors along x and y-direction. The focus carriage is equipped with a 2.0' lens, which allows focusing the beam with 120 µm diameter. In the selected laser system, the determination of the pulse duration depends on set power, speed and pulses distance to deliver the equivalent number of irradiation over the length.

Typically fabrication is maintained in ambient conditions. However, the environment is reported to be influencing the surface chemistry of the specimens [56]. To further investigate affect of the environment, the home-made chamber was fabricated from PMMA of total volume $\sim$30 cm^3, depicted in Figure 2.3. The radiation delivery is provided with BaF_2 window with a 22 mm diameter (supplier:

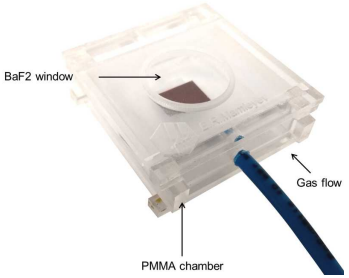

Figure 2.3: The PMMA chamber for N_2 assisted experiments.

MarkIndent), attaining 90 % transparency at 10.6 µm. The nitrogen was supplied at constant rate at 1.0 L/min.

2.2 Thermal Pyrolysis

The pyrolysis is performed in a Carbolite Gero FHA 13 furnace, which consists of a tube made of alumina (Al_2O_3), surrounded by heating coils and sealed in the insulation matrix. This setup is connected to the control unit, where the specific recipe is programmed. The thermal pyrolysis was used for the fabrication of reference glassy carbon (IUPAC: glass-like carbon) films, derived from the same precursors as for the laser-induced carbonisation. For the fabrication, the standard recipe was utilised for a carbon - microelectromechanical systems by heating the polymer in the nitrogen flow (∼0.8 L/min) to 900 °C (unless stated otherwise), at 5 °C min^{-1} ramp rate and holding at this temperature for 1 h [36, 82].

2.3 Electrodeposition of Chitosan

Chitosan is a polysaccharide derived by deacetylation of chitin, which is a structural material of crustaceans and insects shells, making it the second abundant biomaterial. Its solubility strongly depends on the solution pH, and it forms polymer films in neutral and basic conditions.

The process of deacetylation is depicted in Figure 2.4, where acetyl groups are removed from chitin by Chitin-Deacetylase enzyme. The prepared chitosan is highly soluble below aquoues acidic solution with pH $\sim$ 6.5. With an increase of pH, the chitosan forms insoluble hydrogel film by protonation of the -NH_2 functional group on the C-2 position of the D-glucosamine repeat unit [84], which can be obtained with three main methods, including solution casting, printing and electrodeposition. The latter delivery method was found attractive for targeted deposition of the hydrogels on conductive substrates and broadly used for the lab-on-a-chip devices [85, 86]. Figure 2.4B illustrates schematic of chitosan delivery to the electrode, where the potential is applied between a target cathode and an anode immersed in the chitosan solution. In adjacency to the cathode, the amino groups protonate, promoting locally increased pH and forming insoluble film.
As well, chitosan can be modified by other substances. Due to the presence of amine groups, a covalent attachment is promoted of the various biomolecules, antibodies, DNA and enzymes [83]. This property was utilised for immobilisation of the urease enzyme on a composite chitosan/laser carbon carrier film to sense the urea in a solution and discussed in detail Section 6.2.

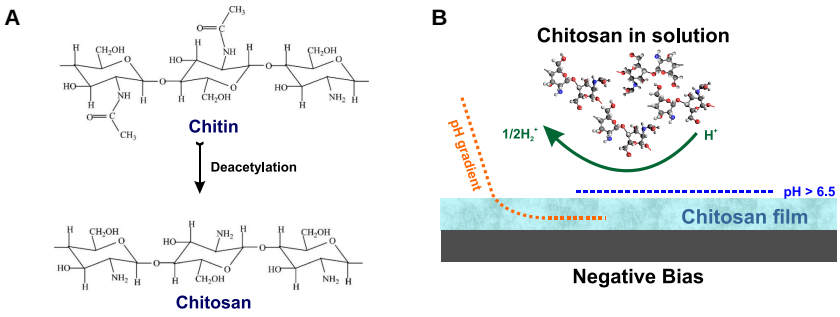

Figure 2.4: (A) Chitosan deacetilation from chitin. (B) The electrodeposition of chitosan on negatively biased substrate. Adopted from Ref. [83].

2.4 Copper Electroplating

A mass transfer on conductive surfaces is implemented via an *electrochemical deposition* or *electroplating*, by adsorption of the charged ions on the target electrode by the applied current in an electrolytic cell. In the cell, the exchange of metal ions occurs between the bulk electrode and the electrolyte and governed by the Nernst equation:

$$E_{cell} = E^0 - \frac{RT}{zF} \ln a(M^{z+}) = E^0 - \frac{0.0592}{z} \lg a(M^{z+}), \tag{2.1}$$

where E the cell potential electrical (electromotive force); E^0 the standard reduction potential; R the gas constant; T the absolute temperature; z a number of electrons involved in the process; F Faraday's constant ($F = 96\,485\,\mathrm{s\,A\,mol^{-1}}$); $a(M^{z+})$ the activity of the ion, dependent on the activity coefficient and molar concentration. The right side of the formula represents a simplified form after implementing all constants in the formula.

The current density behaviour during plating is described by relation to the overpotential, with latter determined through $\eta = E(I) - E$ [87, 88], and has form:

$$i = -i_0 \exp \frac{\alpha z F \eta}{RT} \tag{2.2}$$

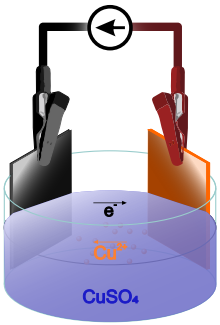

Figure 2.5: (A) Schematic represinatation of the deposition cell. (B) Current-potential scheme of the electrochemical deposition and dissolution.

In order to estimate the quantity of electroplated metal, the Faraday equation is used, which can be modified for the determination of the film thickness t on an electrode with known surface area S:

$$t = \frac{I\tau A}{nF\rho S}, \tag{2.3}$$

where t is the plated thickness, I the applied current, τ the plating time (typically used for 300 s in all cases, unless stated otherwise), A the atomic weight of the material ($A_{Cu} = 63.55\,\mathrm{g\,mol^{-1}}$), n the number of electrons transferred by the ion into the solution (n = 2), ρ the material density ($\rho_{Cu} = 8.96\,\mathrm{g/cm^3}$), and S the electrode surface area.

Copper plating plays an important role in the semiconductor industry in plating parts on plastics, printing circuit boards, electrorefining and electroforming. It is typically performed in copper sulfate - sulphuric acid, oxalate, nitrate, acetate, copper chloride solutions [87, 88]. For the experiments, it was used a self-built electrolyte bath (Cuprostar LP-1, Enthone-OMIGmbH) with 2 M concentration of Cu_2SO_4, 0.7 mM of H_2SO_4. For this system, the standard hydrogen electrode overvoltage for graphite and copper is 0.60 and 0.48 [88] at a current density of $10\,\mathrm{mA/cm^2}$ in 2 M H_2SO_4. The sulfuric baths undergo an anode polarisation and striated deposition at high current density, which is resolved with chlorine ion present in the electrolyte. Due to this 9 µM of HCl was added. Some additional additives were introduced to the bath for promotion of smooth deposition, level and prevent void formation [87, 89]. To provide equivalent ion distribution in the bath, it was constantly stirred by an electric pump. A direct current was applied during plating using a home-built power source [90]. After electroplating, the copper-plated samples were washed with de-ionised water and kept on a hotplate at 90 °C for 300 s for evaporation of the residual moisture and prevention of copper oxidation.

3 Analytical Methods

The fabricated samples were studied with multiple analytical techniques to determine physical and chemical properties. Here, the theoretical background is discussed on the applied techniques determining a surface and bulk morphology, a chemical composition, crystallographic properties, and conductivity.

3.1 Vibrational Spectroscopy

Photons of the specific energy can be absorbed or emitted by a molecule, which results in a rising of the total energy of the molecule from a ground state to a specific excited state. This change in total energy is expressed via relation:

$$\Delta E = h\nu = \hbar c\tilde{\nu}, \tag{3.1}$$

where $h, \hbar$ are a Plank constant, ν is a electromagnetic wave frequency, c is speed of light, $\tilde{\nu}$ is a wavenumber. The total energy of the molecule is composed of electronic (E_{el}), vibrational (E_{vib}) and rotational (E_{rot}) energies, which are additive:

$$E_{total} = E_{el} + E_{vib} + E_{rot}. \tag{3.2}$$

The molecule features rotational transitions observed at $1 - 1 \times 10^2\,\mathrm{cm}^{-1}$ (microwave), and electronic in the $1 \times 10^4 - 1 \times 10^6\,\mathrm{cm}^{-1}$ region (UV-visual-near IR). Both Raman and IR spectra show vibrational transitions in the molecule in the condensed state, which occur at $1 \times 10^2 - 1 \times 10^4\,\mathrm{cm}^{-1}$ range [91].
As a result of Heisenberg's Uncertainty principle there exist a "zero-point energy" level for each electronic state : $E_0 = \frac{1}{2}h\nu$. The intervals between vibrational energy

states decrease with v vibrational quantum number. Following the symmetry of the molecule, there are "allowed and forbidden" transitions, which are emphasised by relevant selection rules. The selection rule allows any transition of $\Delta v = \pm 1$ considering a molecule as a harmonic oscillator. Under ordinary conditions only fundamental transitions occur from $v = 0$ to $v = 1$, following Maxwell - Boltzmann distribution law with population:

$$R = \frac{P(v = 1)}{P(v = 0)} = e^{E_v/kT}, \tag{3.3}$$

where ΔE_v is a vibrational frequency and $kT = 208\,\mathrm{cm}^{-1}$ at room temperature. Following the harmonic oscillator selection rule: the number of allowed transitions greatly reduced, due to symmetry of the molecule; overtones and combinations bands are forbidden. However, later is present due to anharmonicity of the vibration. The main methods for observation of these vabrational transitions realised through infrared and Raman spectroscopy.

3.1.1 Infrared Spectroscopy

Infrared (absorption) spectra originate from vibrational transitions between two levels in an electronic ground state. The IR absorption process contains two essential components: radiation frequency and molecular dipole moment [91]. When the radiation frequency matches with the natural frequency of a particular normal vibration mode, then the resonance condition is met. In order to be absorbed, the IR photon must cause a change in the dipole moment of the molecule, which is a function of the atomic charges (e_i) and the positions (r_i):

$$\mu = \sum e_i r_i \tag{3.4}$$

The IR absorption is estimated from the change in the dipole moment by variation of the partial charge of the molecule and can be evaluated from electronegativities of the constituent atoms. Therefore, the IR active modes are not observed for the homonuclear molecules (covalent polar: H_2, O_2, N_2), due to the absence of the

dipole moment. Nevertheless, non-polar and heteronuclear species make it an excellent tool for the determination of the present species [91]. From the quantum mechanical considerations the IR absorption is an electric dipole operator mediated transition with respect to change in the vibrational amplitude q and must be greater than zero:

$$\left(\frac{\delta\mu}{\delta q}\right)_0 \neq 0 \tag{3.5}$$

Practically, infrared spectroscopy is implemented through Fourier-transform infrared spectroscopy (FTIR), where the signal is collected considering specific geometrical configuration, including absorbance, transmittance, reflectance and attenuated total reflectance (ATR) modes [92]. All measurements were conducted in Bruker Vertex 70 ATR-FTIR spectrometer in the range from $4000\,\mathrm{cm}^{-1}$ to $400\,\mathrm{cm}^{-1}$, with $2\,\mathrm{cm}^{-1}$ resolution.

3.1.2 Raman Spectroscopy

Raman spectrum originates from electronic polarisation caused by UV, visible or near-IR radiation. When the molecule is irradiated by the light of frequency ν, it causes polarisation induced in an electromagnetic field and has the same frequency ν ("Rayleigh scattering") and $\nu \pm \nu_i$ is scattered, with ν_i corresponding to a vibrational frequency of the molecule. This is a shift from the incident frequency. Therefore, due to the weakness of the scattering, the lasers were employed, providing a strong, monochromatic, coherent source of the radiation.
The origins of the spectra can be explained by classical and refined with quantum mechanical theory. Let us consider a light wave with frequency ν with and electric field E, where the fluctuation of E follows:

$$E = E_0 \cos 2\pi\nu t, \tag{3.6}$$

where E_0 is an amplitude of the incoming electric field and t is a time. The dipole moment P in diatomic molecule molecule then is:

$$P = \alpha E = \alpha E_0 \cos 2\pi \nu t, \tag{3.7}$$

where α is a polarizability. In case of vibrating molecule at frequency ν_i, the nuclear displacement q has a form:

$$q = q_0 \cos 2\pi \nu_i t, \tag{3.8}$$

where q_0 is a vibrational amplitude. At small amplitudes α is a linear to q, thus

$$\alpha = \alpha_0 + \left(\frac{\delta\alpha}{\delta q}\right)_0 q, \tag{3.9}$$

where α_0 is a polarizability at equilibrium position and $\left(\frac{\delta\alpha}{\delta q}\right)_0$ is a rate of change of change, evaluated at equilibrium position. By combining Equations 3.8 and 3.9 into Equation 3.7, the dipole polarization takes form:

$$P = \alpha_0 E_o \cos 2\pi \nu t + \frac{1}{2}\left(\frac{\delta\alpha}{\delta q}\right)_0 q_0 E_0 \left[\cos 2\pi(\nu + \nu_i)t + \cos 2\pi(\nu - \nu_i)t\right]; \tag{3.10}$$

The first term represents Rayleigh scattering of the oscillating dipole emitting at frequency ν. The second term corresponds to the Raman scattering. The term vanishes of $\left(\frac{\delta\alpha}{\delta q}\right)_0 = 0$, therefore the vibration is not Raman active unless the polarizability changes during the vibrations. Moreover, the term consist of $\nu + \nu_i$ and $\nu - \nu_i$ corresponding to anti-Stokes and Stokes lines respectively determines Raman frequency. Due to larger population in $\nu = 0$ than $\nu = 1$, the Stokes lines contribute to the spectra more strongly.

The classical theory does not consider the overtone and combinational spectra. However, in the quantum mechanical theory, the solution of the Schrödinger equation of the actual potential in the harmonic oscillator for the diatomic molecule introduces the overtones. The actual potential is formed with the introduction of the cubic correction term:

$$V = \frac{1}{2}Kq^2 - Gq^3, \tag{3.11}$$

where V is a potential energy, K and G are force constants of the vibration. The eigenvalues become:

$$E_v = hc\omega_e\left(v + \frac{1}{2}\right) - hcx_e\omega_e\left(v + \frac{1}{2}\right)^2 + ..., \tag{3.12}$$

where ω_e is the wavenumber corrected for the anharmonicity and $x_e\omega_e$ is a magnitude of such anharmonicity. These values can be observed by series of the overtone bands in Raman (and IR). The equation (3.12) can be revised in a form:

$$(E_v - E_0)/hc = v\omega_e - x_e\omega_e(v^2 + v) + ..., \tag{3.13}$$

with wavenumbers corresponding to:

$$\begin{aligned} &\text{Fundamental :} && \tilde{\nu}_1 = \omega_e - 2x_e\omega_e; \\ &\text{First overtone :} && \tilde{\nu}_2 = 2\omega_e - 6x_e\omega_e; \\ &\text{Second overtone :} && \tilde{\nu}_3 = 3\omega_e - 12x_e\omega_e. \end{aligned}$$

All Raman spectra were collected from a Bruker Senterra equipped with a confocal microscope, and the signal was collected in bandwidth of from 70 cm^{-1} to 3500 cm^{-1} with 0.5 cm^{-1} resolution using a diode-pumped solid-state laser with 532 nm wavelength at 2 mW power.

3.2 X-ray Diffractometery

The development of the Crookes tubes [93] led to the discovery of the x-ray radiation [94], which became a pivotal moment for material science research. The condensed matter consists of crystals of variable sizes and orientations. The diffractometry methods created a foundation for understanding their structure and allowed resolving the features at the atomic scale with high accuracy and reliability.

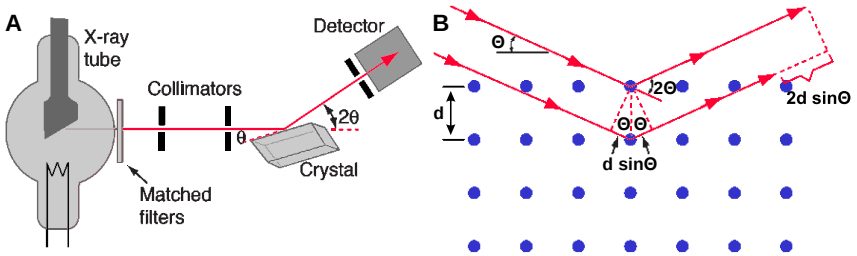

Figure 3.1: (A) The XRD experiment scheme. (B) Path difference geometry in the Braggs'law.

The most prominent method is x-ray diffractometry (XRD) measuring the special arrangements of the atoms in the range from 1×10^{-10} to 1×10^{-6} m [95].
In the typical XRD experiment, the incident wave from the x-ray tube is directed on the specimen, where the beam reflected from the atom electron shell attributing the characteristic of the lattice, as depicted in Figure 3.1A. The incident beam goes through an array of monochromators and collimators for filtering of the incident bremsstrahlung and compression of the beam divergence. This setup improves signal-to-background ratio. The detector is typically rotated around the sample to measure the directions and intensities of the diffracted waves [95].
The diffraction experiment in all presented cases is performed using the Bregg-Brentano geometry; thus, diffraction angles are presented in the θ-2θ angle. For performed experiments, the XRD was performed on a Bruker D8 Advance diffractometer using Cu-$K_{\alpha_{1,2}}$ radiation.
When the photon is scattered between atom planes, it sets the difference in the path length, creating the constructive wave at a selected angle the difference path matches with the wavelength, as shown in Figure 3.1B. This is expressed via Braggs' law [96, 97]:

$$2d_{hkl} \sin(\theta) = n\lambda, \tag{3.14}$$

where the d_{hkl} is an interplanar distance, θ is an angle of incidence of the x-ray beam, λ is an x-ray wavelength, the integer factor n is an order of the reflection.

The interplanar spacing is indexed with *{h k l}* notation, known as Miller indices, representing the family of planes for the orthogonal to the basis of the reciprocal lattice vector and can take integer values [98]. A diffraction pattern of the material typically contains multiple distinct peaks, each representing a specific reflection assigned to a different interplanar spacing. Therefore, the crystal geometry is considered for the calculation of the Miller indices from d.

For simplification, the specific derivation for the three lattice systems applied in the course of this research are presented here. For simple cubic system with lattice constant a_0, the interplanar spacing is implemented using angles of XRD reflections and expressed in the form:

$$\frac{1}{d_{hkl}} = \frac{h^2+k^2+l^2}{a_0^2}; \tag{3.15}$$

$$2\theta_{hkl} = 2\arcsin\left(\frac{\lambda\sqrt{h^2+k^2+l^2}}{2a_0}\right) \tag{3.16}$$

Analogously the hexagonal close packed lattice is treated with additional c_0 lattice constant parameter and the equation takes form:

$$2\theta_{hkl} = 2\arcsin\left[\frac{\lambda}{2a_0}\sqrt{\frac{4}{3}\left(\frac{h^2+hk+k^2}{a_0^2}\right)+\frac{l^2}{c^2}}\right] \tag{3.17}$$

And in the rhombohedral lattice the angle α is considered:

$$2\theta_{hkl} = 2\arcsin\left[\frac{\lambda}{2a_0}\frac{\left(h^2+k^2+l^2\right)\sin^2\alpha+2\left(hk+kl+hl\right)\left(\cos^2\alpha-\cos\alpha\right)}{a_0^2\left(1-3\cos^2\alpha+2\cos^3\alpha\right)}\right] \tag{3.18}$$

However, not all Miller indices can be observed on the diffractogram, and the absent reflections occur due to the identical plane of atoms halfway between two other planes [95]. For specific lattice types, forbidden reflection to feature this condition: as for hexagonal closed packed $(-h+k+l=3n\pm1)$, whereas in the

simple cubic and in the rhombohedral lattice, all reflections are allowed.

Crystalline Size and Internal Strain

The number of the crystallographic planes involved in the diffraction at the selected plane affect the width of the peak. Therefore, the width of the peak β can be attributed to the size of the crystallite, which is expressed in form [99]:

$$L = \frac{K\lambda}{\beta \cos\theta}, \tag{3.19}$$

where L is a crystallite size, K is a structure factor. The structure factor K is dependent on the reciprocal lattice of the specific crystal structure. Mostly, the spherical particles are considered, where the structure factor equilibrated to 0.89. However, for hexagonal lattices, other factors should be considered, and for $h\,k$ Miller's indices, it was estimated at 1.84 [100].

Additionally, the Rietveld refinement was employed for the determination of the crystalline sizes and stresses as a more advanced method. There the determined features match with the standard diffraction pattern for the specific material.

3.3 Electron Microscopy

Resolving of the material features with optical microscopy is limited to Abbe resolution limit, where the feature size is constrained around 1 µm. Additionally, optical microscopy in high resolution suffers from significant defocus dependent on the roughness of the substrate. As it was shown by de Broglie via particle-wave dualism, the image resolution is dependent on the acceleration voltage of the electrons (momentum), and from 1 kV to 100 kV the image can be resolved to 38.7 pm to 3.7 pm. Such resolution lays significantly lower the Abbe limit for photons and below the atom size. Further development in technology brought electron microscopy, and the aforementioned limits were resolved. This technique allows characterisation of the surface morphology with the high depth of field volumetric and crystal features of the substrates.

3.3.1 Scanning Electron Microscopy

Scanning electron microscopy is a powerful imaging technique allowing microstructural identification of the material surfaces. The principle beam path is illustrated in Figure 3.2, where the electron beam goes through a set of the condenser and objective lenses, currently achieved with magnetic lenses [101]. The chamber is evacuated to improve detection without ionisation of atoms in the surrounding. The beam suffers from multiple aberrations, including chromatic, spherical and astigmatism. There the correction is achieved by controlling the electron beam diameter with aperture and the magnetic lenses [101].
After interaction with the specimen surface, the majority of the primary elections penetrate and inelastically scatter within a micrometre range, where the depth is dependent on the atomic weight of the material [102]. This interaction causes the ejection of weakly bounded electrons from valence band for ionically and covalently bonded materials or from conduction band for metals, with binding energy laying in range 1-15 eV. These ejected electrons are referred to as secondary (SE).

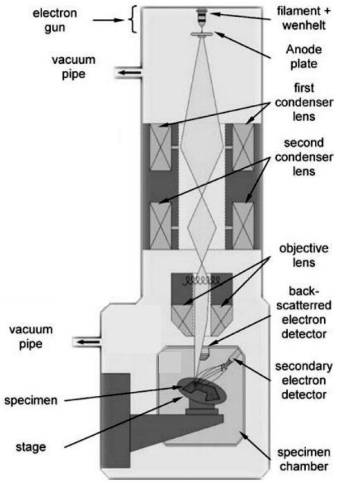

Figure 3.2: Schematic of a typical scanning electron microscope and a beam path. Parts are adopted from Ref. [101].

Transfer of the kinetic energy is small between primary and secondary electrons; thus, an ejection occurs with reduced kinetic energy. Due to inelastic scattering during propagation in the specimen, SE further undergoes loss of kinetic energy, and only a fraction overcomes the surface energy barrier and contributes to the signal [102]. These SE are collected with Everhart - Thornley detector, which consists of scintillator made of thin metal coating, to which applied potential of $\sim$10 kV for SE acceleration and scintillation with optically active material. The detector is surrounded by Faraday's cage to prevent interference with a primary beam. Some of the secondary electrons cause ejection from the chamber walls, which contribute to interference in the received signal.
The part of primary electrons is reflected on a solid angle consisting of high energy electrons and referred to as back-scattered electrons (BSE). The electrons reflect more effectively on heavy elements and can be used for contrast differentiation of the chemical composition. Moreover, BSE exhibit high sensitivity to the surface topology. The BSEs collected with an in-lens semiconductor or a scintillator detector, positioned around the primary electron slit to maximise detection signal and accuracy.
Due to the nature of the beam interaction with surface, the charge is accumulated only on the interface without further dissipation, which causes overcharging for insulating surfaces. It can be compensated by sputtering thin metal layer atop investigated surface. In case of the conducted here study, silver was sputtered with a thickness of 10 - 20 nm or by adjusting the electron beam exit voltage to the electron working function of the studied material, which typically does not exceed 2 keV. All studies were performed on Carl Zeiss AG —SUPRA 60VP SEM. The cathode is.

3.3.2 Energy Dispersive X-ray Spectroscopy

Energy Dispersive X-ray Spectroscopy (EDX) is realised via photoelectric absorption of an X-ray on a semiconductor detector. The energy is transferred to a bound inner shell atomic electron, ejected from the orbital with a kinetic energy equal to

the photon energy with the subtracted binding energy. The ejected photoelectron inelastically scattered in the silicon lattice with ionisation energy at Si K-shell and an L-shell are 1.838 keV and 0.098 keV respectively. The ionisation in the intrinsic semiconductor induces generation of an electron-hole pair in the valence band, both moving towards an applied terminal potential, between the entrance surface of an electrode and the back surface across Si detector. The total energy of electron-hole pair is 3.6 eV, and the number of charge carriers is proportional to the X-ray photoelectron energy: $n = E_p/3.6$. The threshold limit in the EDX systems typically lies between 50 eV and 30 keV.

The EDX is collected using a Bruker X-FLASH 5010, which is realised via a standard silicon drift detector (SDD-EDX). This detector realised via smooth Si front surface electrode and the rear surface patterned with nested ring electrodes, to which applied pattern of potentials, and a small central anode, serving as a collection channel [103].

3.3.3 Transmission Electron Microscopy

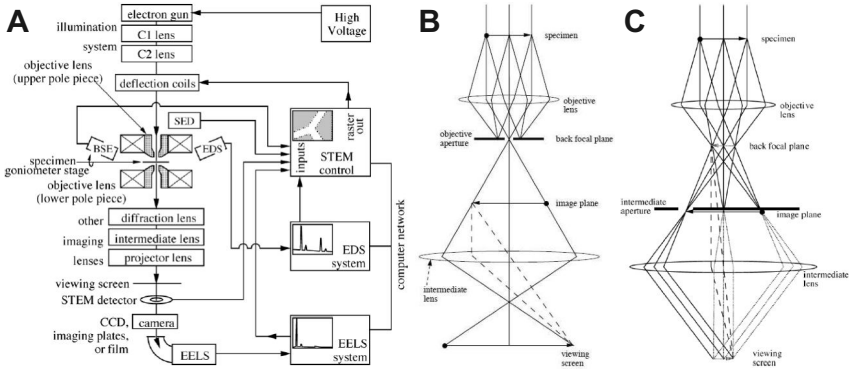

Figure 3.3: (A) Block diagram of TEM/STEM setup. (B) Ray image in the bright-field mode. (C) Selected area electron diffraction mode with an intermediate aperture. Parts adopted from Ref. [95].

Transmission electron microscopy (TEM) has recommended as a versatile technique for the determination of the inner crystalline structure of the materials,

complemented with a number of imaging modes and techniques, capable of resolution within an atomic scale, and providing information on chemical content. Figure 3.3A shows a diagram of a TEM with a capability of multiple instrumentation techniques with the specific location of the instruments in a column. Namely, these techniques are: bright and dark-field imaging, phase-contrast imaging, Z-contrast imaging, selected area electron diffraction, convergent-beam electron diffraction, energy-dispersive x-ray spectroscopy, and electron energy-loss spectroscopy [95]. Further, some relevant for this study techniques are elucidated in detail.

The primary technique used for the observation of materials is a bright field imaging mode. The conventional TEM beam ray path is presented in Figure 3.3B. The collimated electron beam is falling on the specimen, which is located in close proximity to the objective lens ring, realised via magnetic lens [95]. The transmitted beams from the object are focused via the lens and intersected at the back focal plane, where a diffraction pattern of sample is created. The difference in modern TEM systems is achieved via the installed aperture at the back focal plane, allowing only selected diffraction order of rays to pass through. For the bright field, the zeroth diffraction order is transient, and for the dark field in higher orders. The aperture also serves as attenuation of the beam intensity, increasing the final image contrast. The set of intermediate lenses is used for the increase of magnification power and control over the compensation of aberration effects.

TEM was carried out on several machines, including an FEI Titan® 80-–300 at 80 kV using a lacey carbon coated Cu grid with additional 2 nm amorphous carbon coating; on a ThermoFisher Scientific Themis300 operated at 300 kV, with SAED patterns collected at a camera length of 600 mm on a bottom mounted Ceta 16M camera from studied specimens. Diffraction pattern were evaluated using the "PASAD"-plugin [104] of the Gatan Digital Micrograph® software. Laser carbon and CuO-U films were dispersed in the ethanol and ultrasonicated for 1 h, and then deposited on Quantifoil® Holey Carbon Film supports with circular holes, type R1.2/1.3 + 2nm additional continuous C layer on Au grid with 200 mesh.

3.3.4 Selected Area Electron Diffraction

The selected area electron diffraction allows collection of the diffraction patterns from the objects of ∼1 µm in diameter, which is limited by spherical aberration. To implement it in TEM, the beam path is closed with an intermediate aperture located close to the image plane, where only diffracted beams are transient and then collected on the viewing screen (Figure 3.3C). From the collected pattern, the separation between the lattice planes can be deducted through the 'camera equation'. The diffraction is described via Bragg's law (Equation 3.14). Considering TEM, the diffraction angle is $<1°$ and through de Broglie equation the electron wavelength is ∼0.04 Å. For such small angles, $\sin\theta \sim \tan\theta \sim 1/2\tan(2\theta)$, with TEM geometry can be rewritten as $\tan(2\theta) = r/L$, where r is a distance from a separation between diffraction spots and L is the 'camera-length'. The final substitution into Bragg's equation gives:

$$d = \frac{\lambda L}{r} \tag{3.20}$$

This equation allows to determine of the interplane distances and can be used as for x-ray diffraction patterns.

3.4 Stylus Profilometry

The stylus profilometry was used for the evaluation of the surface roughness and texture in a sub-micron regime up to several millimetres. The measurements are typically conducted by moving in a single direction sample beneath a stylus with the diamond tip. The tip is mechanically coupled to the linear variable differential transformer, which converts the analogue signal driven by the stylus position change to the digital signal. The stylus profilometry was performed on DEKTAK V220-Si (Veeco Instruments Ltd., Cambridge, UK) equipped with 12.5 µm diamond stylus. The sample table is attached to the quartz table, the motion along the x-axis promoted by the remotely mounted motor.

3.5 Electrical Conductivity

The four-probe van der Pauw is one of the most effective and widely used methods for the determination of the electrical resistance of thin films. Using the geometrical estimations the sheet resistance R_s is derived to [105, 106]:

$$R_s = \frac{\pi}{2\ln 2}\frac{R' + R''}{2} f(R'/R''), \tag{3.21}$$

where R' and R'' are resistances measured in perpendicular orientation. The term $f(R'/R'')$ is a geometrical factor dependent on the probe position, which should be estimated from table values [106]. This factor can be reduced to 1 for all tested here cases, due to square geometry of the electrode setup. The conductivity σ was further determined considering the thickness t determined with profilometry for each sample following the formula $\sigma = 1/R_s \cdot t$.

The measurement of the resistance of the fabricated laser carbon samples with van der Pauw geometry was performed on the physical properties measurement system with installed nanovoltemeter and nanoamperometer Keithley 2182A and Keithley 2460, respectively. Independently, all measurements were performed in Chapter 7 on a four-probe station Hioki 3540 mΩ HiTester.

3.6 Combustion Analysis

The elemental (combustion) analysis measurements were performed on an ELEMENTAR Vario Micro and determined the average value throughout the thickness of the film. As an analytical scale, the model SARTORIUS M2P was used. The machine was calibrated to determine the mass per cent for hydrogen, carbon and nitrogen. The mass per cent of oxygen was estimated by subtraction of determined elements due to the insignificant contribution of other elements in the precursor preparation and processing.

3.7 X-ray Photoelectron Spectroscopy

X-ray photoelectron spectroscopy (XPS) is a widespread technique for the analysis of material composition electronic properties, oxidation, wear and friction based on interfacial microchemistry. The effect is induced by x-ray photons interaction with the core electrons of the sample atom, where the ionised states are created, promoting emission of a photoelectron with specific kinetic energy E_{kin} approximated by the difference between the photon energy $h\nu$ and the binding energy E_b. Considering this relation, and the analyser work function Φ_S and the electron kinetic energy in vacuum Φ_A, the binding energy can be derived:

$$E_{kin} = h\nu - E_b - \Phi_S \tag{3.22}$$

$$E_{kin} = h\nu - E_b - \Phi_S - (\Phi_A - \Phi_S) \tag{3.23}$$

$$E_b = h\nu - E_{kit} - \Phi_A \tag{3.24}$$

Typically the analyser work function is experimentally determined by setting the energy scale to zero at the Fermi edge of the reference sample and typically takes values about 4–5 eV. Thus, Φ_A set to 0 eV and binding energy determined using the formula:

$$E_b = h\nu - E_{kin} \tag{3.25}$$

However, the Fermi energy edge is set to 0 eV only for conductive samples and equal for the sample and the analyser. In the case of insulators, the energy scale might shift due to sample charging but can be compensated by ion gun coupling. XPS is based on the element-specific binding energies of elements in the atomic shell. Thus, the notation is spectroscopic, and it is given in principal quantum numbers 1, 2, 3 etc., and the angular momentum denoted *s, p, d, f*. The spectra collected in a wide range (survey) feature corresponding peaks on the composition of the material, as well as the x-ray-induced Auger electron spectra. As mentioned above, the spectra are resolved for each specific element; most significantly, there,

the change in a core binding energy is influenced by chemical bonding in the compound and referred to as the *chemical shift*. This is explained by the atom effective charge potential variation. There, the ionised atom in a shell is replaced by a vacancy in the valence shell, causing a shift in the binding energy of atom [107]. XPS was conducted using Al K_α radiation ($E = 1486.6\,\text{eV}$), and the spectra were collected with the hemispherical energy analyser RG Scienta 4000. Survey spectra were collected with the resolution of 1 eV; the high-resolution spectra with a 0.05 eV step on specific elements. The spectra were analysed using the *CasaXPS* software. The Shirley background was extracted from the measured spectra, excluding Cu 2p spectra which were fit using the spline Tougaard background, and peaks were fitted to the Gaussian-Lorentzian function (GL30).

3.8 Cyclic Voltammetry

Cyclic voltammetry is one of the most useful analytical electrochemical techniques for the observation of redox reaction electrochemical kinetics. It allows studying the interfacial phenomena of an electrode surface with electrolyte, reactions involved in the diffusion of species, and specific bulk properties of the electrode material [108, 109]. This is achieved through the determination of the following: the formal reduction potential, the number of transferred electrons in the redox reaction, the diffusion coefficient, electrochemical reversibility, and influence of the scan rate and concentration [110]. Due to such a broad variety of reactions, it can be applied in fields of electrochemistry, biochemistry, organic and inorganic chemistry [111]. The main apparatus is provided via potentiostat, which controls voltage in a three-electrode system immersed in an electrolyte within the electrolytic cell [112]. The three-electrode system consists of a counter electrode, typically a platinum electrode; a reference electrode, currently used Ag/AgCl electrode immersed in 1 M HCl with a salt bridge, to avoid contact with an investigating electrolyte; and a working electrode, requiring investigation of the interaction with an electrolyte.

The voltage sweeps between negative and positive potential, causing a respective reduction or oxidation of the working electrode, where rapidly induced cathodic (i_{pc}) and anodic (i_{pa}) currents result in peaks formation. These peaks give useful information on specific electrode processes, and implementing them in the Nernst equation gives significant insight into the reacting species [111]. For the reversible reactions, the ratio should be $i_{pa}/i_{pc} = 1$. The increase of scan rates shows a higher measured current due to species diffusion variation on the electrode surface. For the reversible reaction, the slope from scanning rate ($v^{1/2}$) vs. peak currents provided can be used for the determination of the diffusion coefficient and calibrate the electrolyte concentration in the unknown solutions, as described by Randles-Sevcik equation [110]

During the course of the performed experiments, Autolab PGSTAT128N potentiostat/galvanostat system was utilised. The applied potential was ranged, depending on the performed experiment, but did not exceed 10 V. The working electrodes were selected to have an area of 1 cm^2 for uniformity of the experiment. All experiments were conducted under constant stirring at 500 rpm to facilitate equivalent ion concentration within the electrolytic cell. The collected data were processed with smoothing using the Savitzky–Golay filter at the indicated selected cases. The scanning rates were adjusted for specific to the experiment.

4 Materials

In this chapter, the discussion contemplates the fundamental properties of selected carbon allotropes, focusing on the crystalline structure of hexagonal and rhombohedral graphite and how they can be translated to the crystal structure of the selected polymer precursors after pyrolysis in order to set comparison to laser-induced carbonisation.

4.1 Carbon Allotropes

The carbon exists in a wide variety of different polymorphs (allotropes), attaining properties from semi-metals to insulators. Theoretically hypothesised the existence of over 500 different carbon allotropes, with some of them confirmed to be stable and synthesised in the lab [113, 114]. According to some systematisation, all these allotropes can be distributed in six classes [114]: (I) diamonds, (II) graphites, (III) lonsdaleite [115], (IV) fullerenes [15], (V) amorphous carbon, (VI) carbon nanotubes [17] and various composites between these classes.
The graphites and graphite-like allotropes drive significant attention due to their conductive properties and variation of the bandgap from semi-metals (0 eV band gap) to semiconductors, which is demanding in the industry. The most notable of them is a graphene [14], which was theoretically predicted in 1947 [116], with some initial observation in the oxidised form [117]. As its states from the IUPAC nomenclature, the graphene is a single sheet of carbon, where each atom is covalently bound to three neighbouring atoms in a honeycomb-like lattice, and attaining sp^2 hybridisation [118]. It is model material, due to its 2D arrangement, and gives multiple possible topological conjugations, namely: the fullerenes as 0D structure by folding into a sphere of the single sheet, the carbon nanotube as 1D structure

by folding along one of the edges of the sheet, and the graphite as 3D allotrope, by stacking in the regular way of the number of coplanar graphene layers. As a single sheet, the graphene exists in multiple chemical modifications, such as graphene oxide as a sheet abundant with hydroxyl and carboxyl functionalities [119], graphane as a hydrogenated sp^3-hybridised graphene sheet [120], flurographene with partial film fluorination attached to the sheet [121], and graphyne with asymmetric lattice connecting hexagons with a sp bond [122].
All of the aforementioned allotropes attain unique physical and chemical properties. However, the current methods of production are still restricted to the laboratory scale due to the low yield of the manufactured product. In addition, the machining of naturally available resources is restricted by the cost of preparation, mechanical properties and their low abundance. As an alternative method for large scale manufacturing, pyrolysis allows direct conversion of the polymer precursors into carbon-rich material, with yield in the chemical composition and mechanical properties from the selected precursor. The development in microfabrication allowed the preparation of the films patterned within microscale with possible 2.5D structure, which can be further scaled down into nanostructures [40, 42, 43, 123].

4.1.1 Graphene and Graphite

As previously stated, graphene is a building block for multiple carbon allotropes. As a result, the properties are inherited from it and expanded with variation depending on the topological confirmation and its chemical modification. The most common naturally occurring form is the graphite, arranged by stacking of the graphene sheets, and it exists in two possible crystallographic forms: hexagonal and rhombohedral. In naturally occurring graphites, the macroscopic single crystals are not present, and the best 'single' crystalline *kish* graphite consists of randomly oriented crystallites with maximal sizes of $100\text{x}100\,\mu m^2$ [124]. The best crystallographic orientation was achieved in the highly oriented pyrolytic graphite (HOPG), which is artificially grown at 3200 °C under pressure and used as the standard for the research [124].

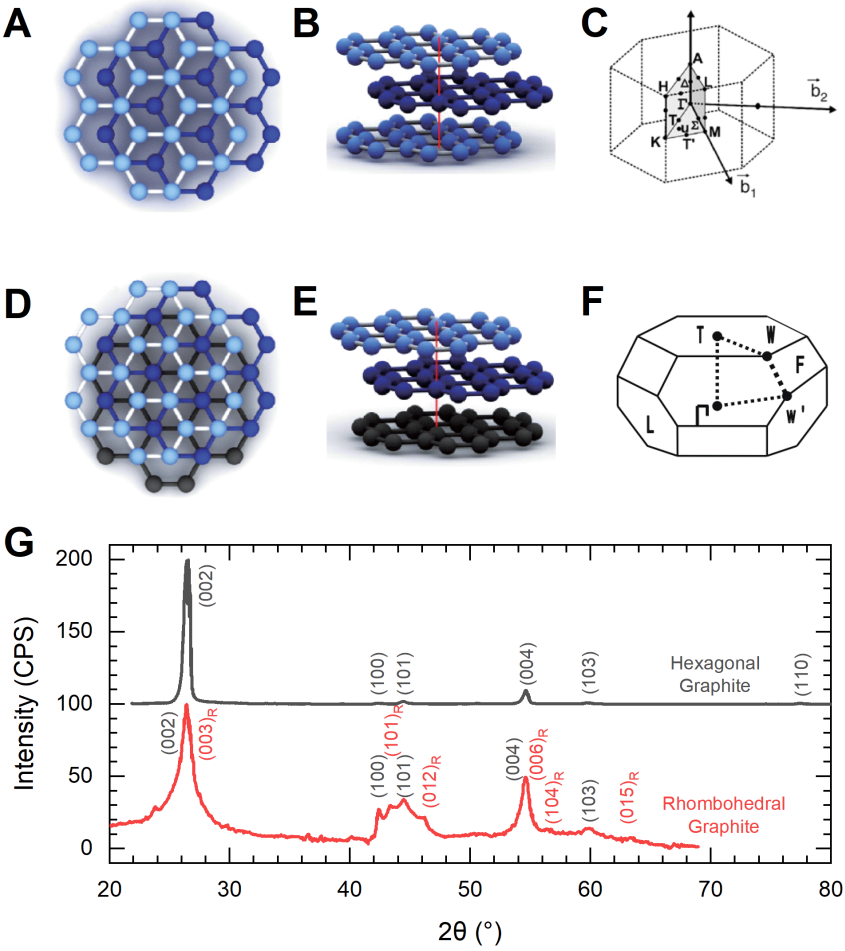

Figure 4.1: A three-layer graphene in a hexagonal (Bernal) structure (ABA) in (A) 2D projection, (B) 3D multilayer and (C) its first Brillouin zone. The rhombohedral modification of graphite in (D) 2D projection, (E) 3D multilayer and (F) its first Brillouin zone. (G) X-ray diffractograms of the hexagonal (top) and rhombohedral (bottom) modifications graphite. Parts of figures are adopted from Ref. [125–129].

The initial investigation of the crystallographic structure of graphite powders suggested representation with a rhombohedral unit cell [130]. However, the vigorous investigation with XRD provided evidence for a better fitting of with the hexagonal modification [131]. Such hexagonal (Bernal) structure in the graphites is the most abundant, with some minor incorporations of the additional rhombohedral phase [132].

There, the hexagonal networks of individual graphene layers stacked in the perpendicular direction (c-axis), where the positions of carbon atoms in the second layer aligned to the centres of hexagonal corners in the first layer and presented in the alternating ABA layer structure, as it is depicted in Figure 4.1(A & B) [127, 133]. Considering the hexagonal lattice structure, the reciprocal for the 2D graphene sheet as well attributes a hexagonal structure. The first Brillouin zone is shown in Figure 4.1C with high symmetry points, namely: Γ point at the zone centre, M points at the middle of the hexagonal edges, K and K' at corners of the hexagon [116, 124, 133]. New planes at $k_z = 0$ and $k_z = \pi/c$ constructed after extending the reciprocal cell in the third dimension, corresponding to the lower and upper plane of the first Brillouin zone [133].

The position of each graphene sheet in a rhombohedral crystallographic modification of graphite is different from hexagonal, where atoms of hexagon edges of the third stacked layer are located at centres of the first layer and the crystal composed of these alternating ABC stacks, as it is shown in Figure 4.1(D & E) [127, 134]. This configuration is promoted by shear stress in the crystallite, and therefore it is metastable, transforming to ABA configuration after annealing at 1300 °C for 4 h [134]. Nevertheless, multiple reports indicate the content of 5% - 15% in a rhombohedral modification in the natural graphite [127, 134] and thin films, the ratio can rise to 40% [129].

Due to such structural variation, the reciprocal lattice shows a significant difference from the hexagonal modification. The first Brillouin zone is formed by perpendicular bisection of reciprocal planes organised into fourteen faces polyhedron, as it is depicted in Figure 4.1F [135].

These reciprocal lattices were utilised for reconstruction of the real-space lattice from the XRD reflections for both modifications, due to diffraction of the x-ray photons on the atoms. Figure 4.1G shows characteristic reflections for both modifications, with top graph attributed to hexagonal graphite and the bottom with inclusions of the rhombohedral modification. For Bernal graphite, the prominent peaks were observed at 26.7°, 42.2°, 44.4°, 54.6°, 59.8°, 77.4°, 83.5° and 87.0° responsible for (002), (100), (101), (004), (103), (110), (112) and (006) reflections [128, 136–138], additional peaks in the rhombohedral modification were observed at 43.4° and 46.1° corresponding to (101) $_{\mathrm{R}}$ and (012) $_{\mathrm{R}}$ reflections [129, 139, 140]. The unit cell of hexagonal graphite contains four atoms, which belongs to the space group $P6_3/mmc$ (D^4_{6h} point group). From these reflections, the lattice constants are calculated at $a = 0.246\,\mathrm{nm}$ in-plane and at $c = 0.670\,\mathrm{nm}$ perpendicular to basal plane [132, 133], whereas the single graphene sheet consist of two atoms per unit cell and belongs to the space group $P\bar{6}m2$ (D^1_{3h} point group). The structure of the unit cell for rhombohedral modification slightly changes, consisting of six atoms per unit cell, which is classified into $R\bar{3}m$ space group (D^5_{3d} point group). There, the lattice constant along basal plane remain as for the hexagonal modification at $a = 0.246\,\mathrm{nm}$ and at $c = 1.070\,\mathrm{nm}$ [132, 134]. Notably, the natural graphites feature angular misalignment between the planes, which is called turbostratic graphite, featuring interplane distance over 0.342 nm higher than estimated from the lattice structure $c/2 = 0.335\,\mathrm{nm}$. The crystallite sizes can be effectively determined from the diffractograms along both crystallographic directions using following equations $L_c = \frac{0.89\lambda}{B\cos\theta}$ and $L_a = \frac{1.84\lambda}{B\cos\theta}$, where λ is a wavelength of the incoming x-ray, B is a FWHM of the reflection, θ is a position of the reflection and structural factors are determined from the geometry of the unit cell [100]. These equations were utilised to analyse samples presented in further chapters but not applied for the aforementioned specimens.

For studying the physical properties of graphites, it is sufficient to estimate the properties of single layer graphene due to weak interaction between the layers with van der Waals force. However, even such weak interaction plays an important role in the crystal selection rules in the normal vibrational modes and affects

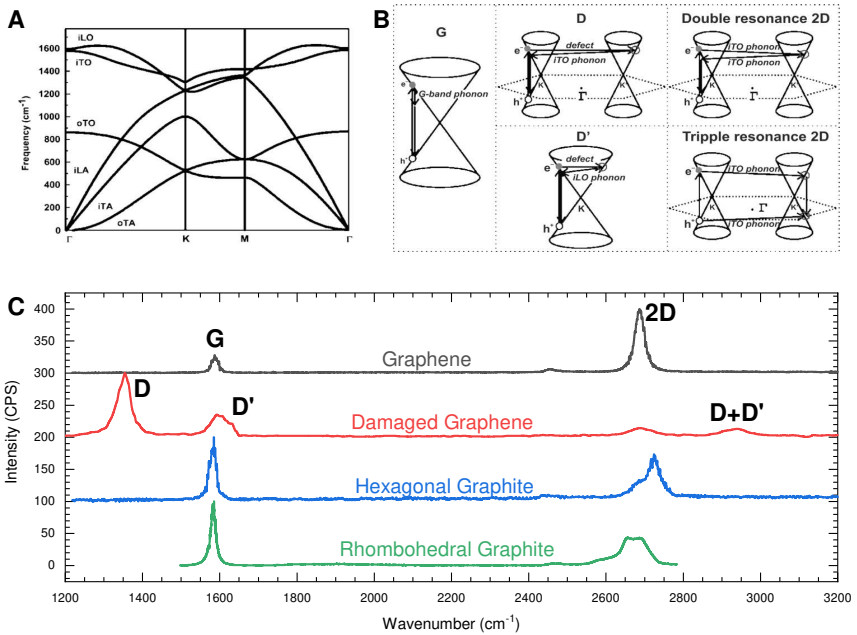

Figure 4.2: (A) Band diagram of the graphite. (B) Electron-hole interaction with an incoming phonon at the band centres at Γ and K included in the formation of G, D, D' and 2D bands. (C) Raman spectra of a single sheet of exfoliated graphene and a damaged graphene, hexagonal and rhombohedral graphite. Parts of figures are adopted from Ref. [141–143].

the spectroscopic analysis of the material. The dispersion of phonons plays an important role is directly related to the Raman scattering in the graphene. The phonon dispersion plays an important role in determining the graphene quality and number of the stacked sheets. The unit cell contains two carbon atoms in a single graphene sheet, presenting by six phonon dispersion bands, three for optic (O) and three acoustic (A) branches. In each of the branches, the one out-of-plane (o) atomic vibration is present perpendicular to the graphene plane. The other two phonon branches are in-plane (i) vibrations, traditionally referred to as longitudinal (L) and transverse (T), following parallel and perpendicular carbon-carbon vibrations, respectively. Therefore, the vibrations propagate along ΓM and

ΓK directions within the first Brillouin zone and are assigned as iLO, iTO, oTO, iLA, iTA and oTA phonon modes [124, 133], as it is shown in Figure 4.2A.
Here, near the Γ point zone centre iTO and iLO modes correspond to the vibration of the sublattice, which belongs to E_{2g} symmetry with a double degenerate optical vibration and thus Raman active [124, 133]. This vibration gives rise to the *G*-band in the Raman spectrum, which is a normal first-order Raman scattering. The position of this G-band is centred around $1580\,\mathrm{cm}^{-1}$ for films with the highest sp^2-hybridised carbon [144, 145]. The other prominent modes arise around the K point, where iLO and iLA branch produce double degenerate phonon with A_{1g} symmetry. These phonon modes contribute to D and 2D bands in the spectrum, which are second-order Raman scattering. All aforementioned modes play an important role in the renormalisation of the phonon energy by generation of an electron-hole pair and can be described with the band diagram, which is depicted in Figure 4.2B. The bands are represented by Dirac cones with an intersection at K (Dirac) point. At the frequencies of D and 2D, the double-resonance Raman process occurs. There, the initiated phonon wave-vector $\boldsymbol{q}$ preferentially couples to the wave-vector $\boldsymbol{k}$ of electronic states in relation $\boldsymbol{q} \simeq 2\boldsymbol{k}$. This double-resonance process is initiated by absorption of a photon with E_{photon} energy by an electron with a $\boldsymbol{k}$ wave-vector. It promotes inelastic scattering by a defect or a phonon with $\boldsymbol{q}$ wave-vector at Dirac cone from K to K' point with total wave-vector of $\boldsymbol{k}+\boldsymbol{q}$. Then, this electron is scattered back to the K point, where it recombines with a previously generated hole. Such a double-resonance process in D-band is promoted by one elastic scattering event on the defect within the crystal and one inelastic scattering by emission or absorption of phonon. In the case of 2D-band, the double-resonance initiated by two inelastic scattering events with two phonons for electron, or the triple-resonance by promoting simultaneous inelastic scattering of both electron and photon with recombination at K' point [124, 133, 141, 146]. The variation in the energy of incoming photon causes a shift in the $\boldsymbol{k}$ wave-vector and thus the position of all Raman bands, and it was observed experimentally [141, 144]. Moreover, a contribution from sp^3-hybridised bonds, due to contamination or a

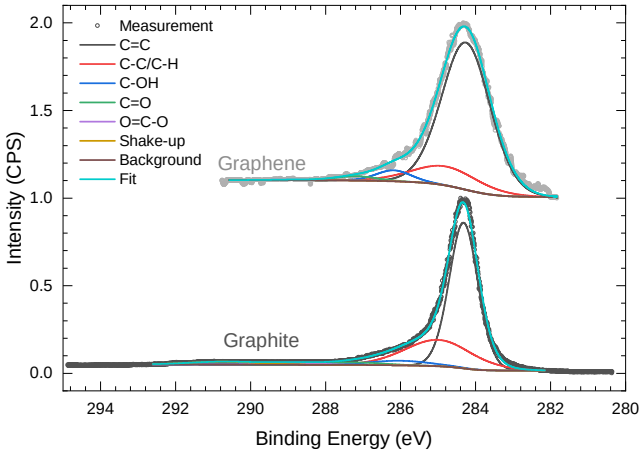

Figure 4.3: X-ray photoelectron spectra of C 1s peak for an annealed graphene and a graphite peak. The data adopted from Refs. [150, 151].

film amorphisation, results in the position shift to significantly higher and lower frequencies [141, 144].

Figure 4.2C shows collected Raman spectra from the sample with different crystallographic structures, namely hexagonal and rhombohedral graphite, exfoliated and damaged graphene. These collected spectra provide critical information about each allotrope, primary hybridisation and amorphisation; after derivation of the band ratios, they further support a defect contribution, and a stacking thickens. The defect contribution and the crystalline sizes are derived from an integral ratio between D and G-bands, supporting the observations with diffractometry [147, 148], and it follows the relation $L_a = (2.4 \cdot 10^{-10})\lambda_l^4 \frac{I_G}{I_D}$ with λ is a wavelength of the laser. The number of graphene sheets can also be estimated from Raman spectrum from the G-band position [146], and the width of 2D-band and by an intensity ratio of 2D over G-band, at >2 for a single sheet, $\simeq 2$ a double layer, $\simeq 1$ multilayer (up to 10 layers) and with higher ratio thicker graphite-like structures [133, 149]. The surface chemical composition of graphene-based allotropes retains relatively close due to the crystal structure's variation and does not exhibit any significant

chemical modification. However, an investigation, conducted with XPS, feature some difference in the composition for graphite and a single sheet graphene. Several methods in the graphene preparation lead to a significant difference in its quality and presence of multiple functional groups, which can be improved and standardised by sample annealing [150].
Figure 4.3 depicts the XPS spectra collected from a single graphene sheet and graphite, and both exhibit high resemblance. The major significance in XPS spectra for graphene/graphitic materials plays a position of C 1s spectral line and its deconvolution by fitting multiple conjugated species. The carbon-carbon bonds are separated into two species: sp^2-hybridised C=C bond with a binding energy at $<$284.5 eV, and sp^3 carbon for C–C and C–H bonds at $<$285.0 eV originated from an adventitious carbon or the boundary conjugated species [150, 151]. As a general trend, the graphene films exhibit significantly lower contribution from C–C/C–H species, which is specified by narrowing of the C 1s peak and its shifts towards $\sim$284.5 eV. The defects at the edge of crystallite promote an asymmetric tail in the C 1s peak, due to some contribution from oxygen conjugated species such as C–OH, C=O and O=C–OH centred at 286.2 eV, 287.6 eV and 288.8 eV respectively [151–153]. Another prominent feature is a π - π^* shake-up satellite originated from electron transition in aromatic rings and located at 290.7 eV [151].

4.1.2 Pyrolytic Carbons and Chars

According to IUPAC pyrolysis is "a chemical degradation reaction that is caused by thermal energy in the controlled inert environment" [155]. During such procedure, the polymers undergo significant structural and chemical changes, resulting in one of three possibilities depending on the precursor selection [18]:
(i) the polymer degrades into small molecules and leave no or unsubstantial carbon residue.
(ii) the chains coalescence into an aromatic membrane followed by their stacking forming 'mesophase', these precursors typically form graphitising carbon upon

heating to 2700 °C [18] (Figure 4.4A). A typical example of such precursor is polyvinylchloride, petroleum coke, pitch coke [38].
(iii) the chains chemically degrade, keeping space orientation, show no merging with neighbouring chains, and show no transformation to the plastic state. These polymers typically preserve the orientation and anisotropic/isotropic properties of the polymer, and yielding carbon is non-graphitising above 2700 °C [38] (Figure 4.4B). These type of material is called *vitreous* or *glassy carbon*, and it exhibit presence of both sp^2 and sp^3 hybridised atoms folded into fullerene-like shells and domains [82, 154] (Figure 4.4C-D). Glassy carbon attributes a unique chemical inertness, broadly used in crucibles, prosthetics, an electrode material for electrochemistry, and shows resistance towards a mixture of sulphuric and nitric acid, which causes severe damage and pulverisation in the graphite [154]. Most known

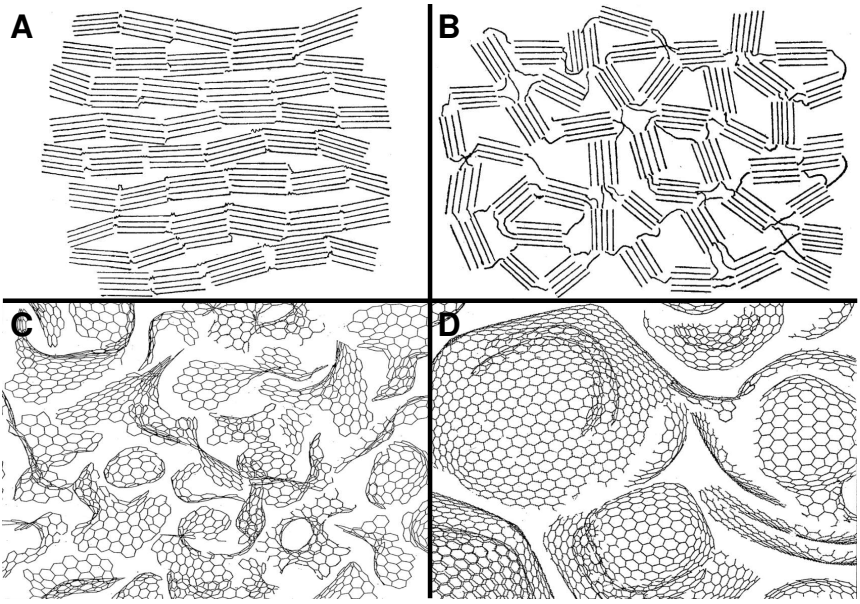

Figure 4.4: Schematic representation of (A) a graphitizing and (B) non-graphitizing carbons. Models of glassy carbon prepared at (C) low and (D) high temperature. All figures are adopted from Ref. [38, 154].

polymers yielding this material are polyvinylidene chloride, coal, sucrose, lignin, cellulose, epoxy resins [38, 156].
The polymers of type (ii) and (iii) undergo multiple stages in structural and chemical composition: (i) the *precarbonisation* stage, at which excess monomers and solvents are evaporated; (ii) the *carbonisation* stage, laying in range 300 °C to 500 °C, where the polymer losses weight rapidly with decomposition of oxygen and nitrogen conjugated species; (iii) *dehydragenation* stage, which observed between 500 °C to 1200 °C, promoting a loss of hydrogen, cross-linking between chains and an improvement of conductivity; (iv) the *annealing* stage occurs above 1200 °C, providing further crystallographic improvement and graphitisation [18]. Therefore, different precursors are selected dependent on the final application. For mechanically robust, electrically conductive required glassy carbons with high graphitisation. Therefore, the standard procedure with heating to 800 and 900 °C employed in manufacturing focused from SU-8, an epoxy-based negative photoresist for fabrication microstructures [43]; polyacrylonitrile, an organic semicrystalline thermoplastic for manufacturing carbon fibre [18] and others.

4.2 Polymer Precursors

However, not all precursors were found suitable despite high graphitisation during thermal pyrolysis and followed several requirements in the laser-induced carbonisation. The fabrication of laser carbons requires strong bonding within and between the polymer monomers to cause bond cutting without ablation of the majority of dissociated species. Typically, these types of polymers attain a thermal conductivity in the range between $0.04\,\mathrm{W\,m^{-1}\,K^{-1}}$ to $0.36\,\mathrm{W\,m^{-1}\,K^{-1}}$ to and a specific heat $0.9\,\mathrm{J\,g^{-1}\,K^{-1}}$ to $1.42\,\mathrm{J\,g^{-1}\,K^{-1}}$. Typical industrial thermosets as polyimide (Kapton) [157], polyaramid (Nomex and Kevlar) [65], polysulfone, polyphenylsulfone [158], polyetherimide (Ulse) [55] and from naturally occurring polymers lignin and cellulose [65], with some more precursors listed in Ref. [65]. Out of this selection, two commercial polymers were selected for detailed study of the laser carbon formation regimes, namely Kapton and Nomex. These poly-

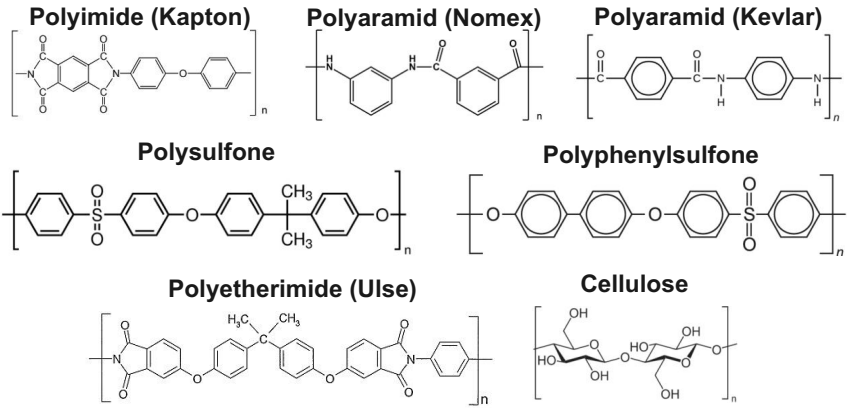

Figure 4.5: The chemical structure of widely used precursors for the laser-induced carbonisation.

mers are widely available in commercial use due to their remarkable properties in particle shielding, thermal and electrical insulation, and both attain a price below 5€/m^2.

4.2.1 Polyimide Kapton-HN

Polyimides are broadly used polymers, exhibiting good chemical resistance against many organic solvents, mechanical tearing and stretching, high tensile strength, lows creep, keeping these properties in a wide temperature range from −269 °C to 400 °C [159]. Aromatic polyimides are prepared by reaction between tetracarboxylic dianhydride and diamine, through dehydration to poly(amic acid) via thermal or chemical processing [160]. The most common and commercially available polyimide is Kapton, prepared by condensation of pyromellitic dianhydride and 4,4'-oxydiphenylamine (PMDA/ODA) as repeating units.

The pyrolysis to 900 °C was used for fabrication of a reference pyrolytic carbon derived from Kapton. Kapton was found forming glassy carbon due to a rigid polymer backbone structure. During carbonisation, several volatile species evolve including CO, CO_2, CH_4 at range from 500 °C to 900 °C, phenol, aniline and

cyanobenzene [161]. Multiple pathways are discussed in the literature for decomposition of Kapton and polycondensation into glassy carbon lattice [161–163].

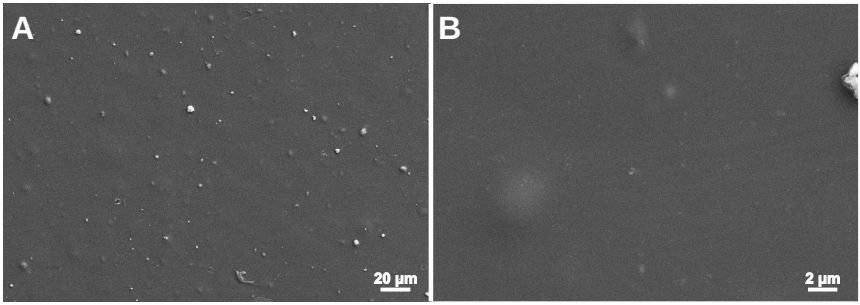

Figure 4.6: Surface morphology of Kapton film after pyrolysis in (A) low and (B) high magnification.

The Kapton film shrunk losing ∼55 % from the initial size and mass, retaining its original shape. The surface microstructure remained smooth, with a minor inflammation caused by volume shrinkage and gas expulsion from the bulk, as it is seen in Figure 4.6.

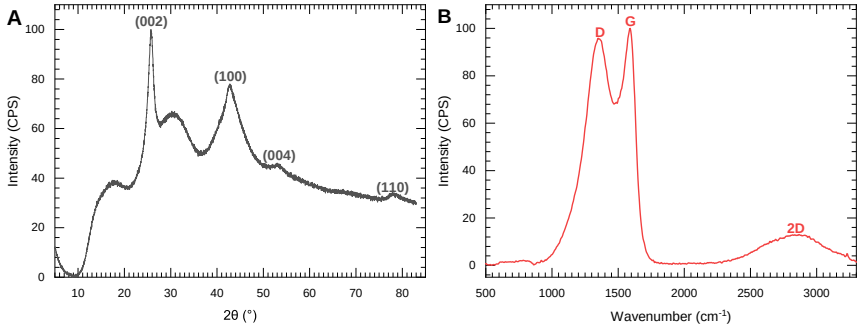

Figure 4.7: (A) X-ray diffractogram and (B) Raman spectrum of Kapton sheet after the thermal pyrolysis. Parts adopted from Ref. [56].

The crystallographic properties were determined with XRD and depicted in Figure 4.7, exhibiting characteristic to the hexagonal graphite peaks at 25.7° and 42.9° corresponding to (002) basal plane and (100) reflections. The interlayer distance was calculated at 3.47 Å using Bragg's law, which is lower than due to

the difference in the valence angles between graphene sheets in polymer derived carbons. The crystallite sizes L_a and L_c were calculated at 3.6 nm and 5.1 nm using equation derived by Warren [100]. Other reflections correspond to the space-group $P6_3/mmc$ and were identified at 53.2° and 78.3° and marked to (004) and (110) planes, respectively. Raman spectroscopy indicated presence of characteristic D and G-bands at 1349 cm^{-1} and 1591 cm^{-1}, and secondary resonance 2D peak centred at 2835 cm^{-1}. The graphitisation ratio, determined from the intensity ratio (I_G/I_D), was estimated at 0.33, showing a ratio comparable to the standard pyrolytic photoresists [164].

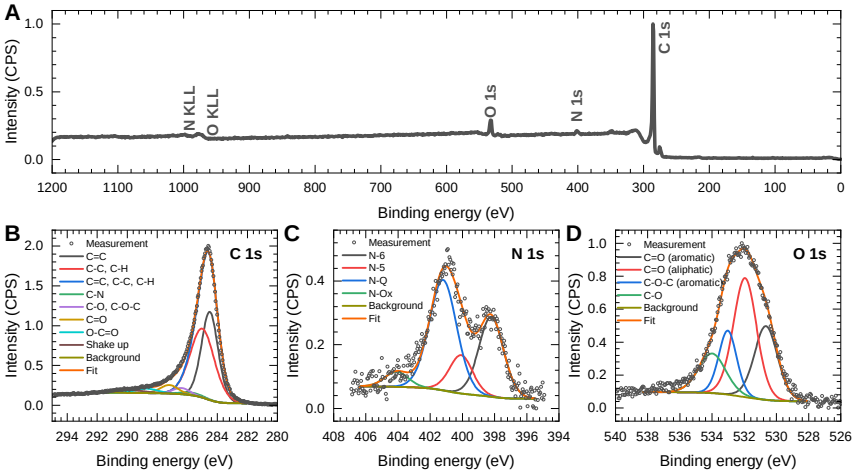

Figure 4.8: (A) XPS survey spectrum collected from Kapton sheet with detailed analysis on (B) C 1s peak, (C) N 1s peak and (D) O 1s peak.

The surface chemical composition was estimated with the combustion analysis and XPS, which evaluated each species's total elemental contribution and detailed spectrum. Figure 4.8A shows the survey spectra, indicating the presence of C 1s, N 1s and O 1s peaks with determined respective elemental percentage of 93.5 %, 1.6 % and 4.9 %, respectively. In all cases, the observed spectral lines were corrected using the position of adventitious carbon in C 1s peak centred at 284.5 eV.

Figure 4.8B presents C 1s peak is deconvoluted into seven carbon-based species and fit to the measured spectrum at the following binding energies: C=C at 284.2 eV, C–C/C–H at 284.9 eV, C–N at 285.7 eV, C–O/C–O–C at 286.4 eV, C=O at 287.2 eV, O–C=O at 288.7 eV and a shake-up arising from aromatic rings at 290.0[165, 166]. Figure 4.8C shows deconvoluted N 1s peak in four nitrogen-based species, namely: pyridinic (N-6) at 398.5 eV; pyrrolic (N-5) at 400.1 eV; quaternary (N-Q) at 401.7 eV; and oxidic ($N–O_x$) at 404.2 eV [167–170]. Figure 4.8D shows a fit of O 1s spectra with four oxygen containing species, namely: the aliphatic and aromatic carbonyl species C=O at 530.7 eV and 532.1 eV respectively, aromatic ether group C–O–C at 533.0 eV and hydroxyl C–OH at 533.9 eV. All spectra featured widening of the hydroxyl peak due to the undefined contamination from the environment. The detailed percentage from all deconvolutied species is presented in Appendix. The specimen attributed equivalent contribution from sp^3 and sp^2 hybridised carbon supporting low graphitisation ratio. Additionally, the elemental composition indicates presence of predominant oxygen confined heteroatoms. The elemental spectra shows preference for carbonyl species distributed along the chain due to its higher dissociation energy from other species. The nitrogen species are distributed withing the lattice by predominant contribution from quaternary nitrogen or along the edge of the graphene sheets.

4.2.2 Nomex Polyaramid Fibres

Polyaramids are wholly aromatic polyaramides exhibiting non-withstanding mechanical and thermal properties for other man-made fibres. The fibre is prepared from poly-p-bezamide, forming a liquid crystalline solution due to the repetitiveness of the molecular backbone. The liquid crystalline solution is processed through a spinneret, allowing alignment of the randomly orientated domains in the shear direction with the full extension of the chains. Such process results in the attainment of high mechanical strength, high elastic modulus and toughness, with high-temperature stability above 300 °C. Commercially available

two types of fibre with para- and meta- orientation at a benzene ring as it is shown in Figure 4.5, namely Kevlar poly(para-phenylene terephthalamide) and Nomex poly(1,3-phenylene isophthalamide). Poly(1,3-phenylene isophthalamide) is widely used as shielding material for electrical and thermal insulation and is commercially known under Nomex®Type 410 as an insulation paper (DuPont™; supplied by RS Components), prepared by calendar pressing and results in films of different thickness. In presented work, films were used of (130 ± 13) µm thickness, which were rinsed with isopropanol and dried at least for 10 min naturally prior to processing.

For laser-induced carbonisation, the sheets were fixed on a glass slide with acrylic adhesive films (3M-467MP) to prevent film folding during fabrication.

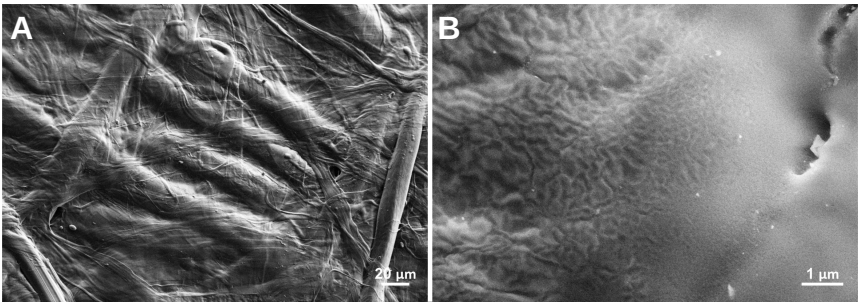

Figure 4.9: Surface morphology of the pyrolysed Nomex in (A) low and (B) high magnification.

The pyrolytic Nomex attribute mass decrease of 65 % and volume decrease of 60 %. Figure 4.9A and B present the morphology of the thermally carbonised Nomex film, exhibiting fibrous microstructure similar to the morphology to the original precursor film.

Thermally pyrolysed Nomex showed strong reflections at 24.3° and 44.4°, which corresponds to a (002) and (100) planes [138]. A d-spacing of the specimen is determined with Braggs´ law at 3.69 Å, featuring the increase in crystalline size (L_a) at 2.0 nm and stacking thickness (L_c) at 1.0 nm. All these observations propose high contribution from the amorphous state in pyrolytic Nomex.

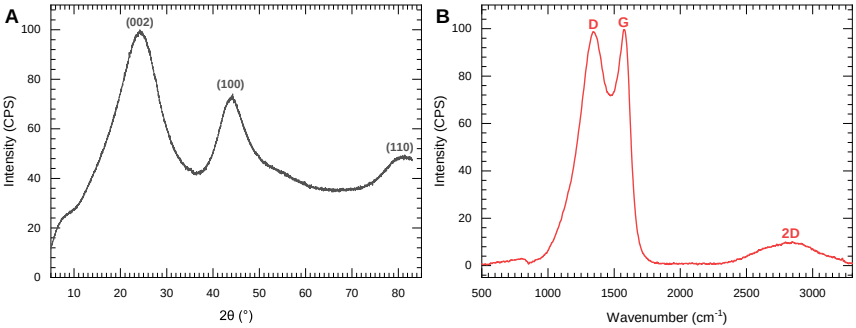

Figure 4.10: (A) X-ray diffractogram and (B) Raman spectrum of Nomex sheet after the thermal pyrolysis. Parts adopted from Ref. [66].

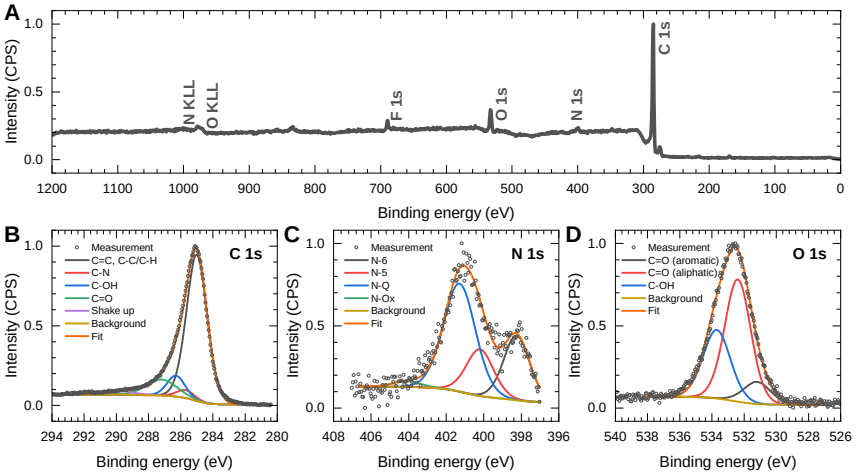

Figure 4.11: (A) XPS survey spectrum collected from Nomex sheet with detailed analysis on (B) C 1s peak, (C) N 1s peak and (D) O 1s peak.

The surface chemical composition was determined from XPS. Figure 4.11A shows a survey scan, from which the contribution was estimated from C 1s, N 1s, O 1s and F 1s of *at. wt.%*, *at. wt.%*, *at. wt.%* and 1.5 *at. wt.%*, respectively. The flourine originates from the manufacturing process and it was considered as an

undesirable residue. The exact contribution from functional groups was further studied in the high-resolution and depicted in Figure 4.11B-D.

Figure 4.11B shows the C 1s peak centred at 284.4 eV and features a strong asymmetry, due to the occurrence of a tail originating from an additional species. There, five carbon-based species were assigned with the corresponding binding energies: C=C/C–C/C–C at 284.7 eV, C–N at 285.6 eV, C–OH at 286.2 eV, C=O at 287.3 eV and shake-up from aromatic rings 290.2 eV [165, 166, 171, 172]. The high-resolution spectrum collected from the N 1s peak is depicted in Figure 4.11C, featuring four characteristic species, namely: pyridinic nitrogen (N-6) at 398.9 eV, pyrrolic nitrogen (N-5) at 400.2 eV, quaternary (graphitic) nitrogen (N-Q) at 401.6 eV, as well as a minor contribution from oxidised nitrogen (N-Ox) at 404.5 eV[167, 168]. Figure 4.11D shows O 1s with a non-symmetrical peak, deconvoluted into three species, namely: aromatic carbonyl (C=O) 531.2 eV, aliphatic carbonyl (C=O) at 532.4 eV and hydroxyl (C–OH) at 533.9 eV [173]. In all specimens, the widening of the hydroxyl spectral line and tailing with higher binding energy was caused by contamination from undefined species originating from the environment.

The specimen attributed similar functionalities to the pyrolytic Kapton, featuring preferential positioning of aliphatic carboxyl within the lattice, carbonyl at the edges of the graphene sheet and quaternary nitrogen substituting carbon in the lattice. The most significant difference is attained by increase of FWHM of each band due to the smaller crystalline size, supported by the crystallographic measurements.

5 Laser-Induced Carbonisation

The following Part covers the emergence of the research on laser-induced carbonisation and ablative photochemical etching, and the processes involved in their evolution.
The numerical model has been used to approximate the surface temperature, including corrections after pyrolytic phase transformations. These models were applied to estimate the phase transformation temperatures and the quality for tested Kapton and Nomex films. The sets of the simulation were experimentally verified, followed by testing with multiple analytical techniques, including Raman spectroscopy, conductivity test with van der Pauw geometry and stylus profilometry. The number of reference samples was selected for each tested precursor, and the properties were investigated in detail using XRD, TEM and XPS.
The films were functionalised and tailored to fabricate the composite biosensors and active surfaces using those acquired characterisation data.

5.1 Process Initiation

The research on laser-induced carbonisation (LIC) arose from experiments on an ablative photochemical etching (APE) performed on various polymers purposed for a polymer coating and packaging of the electrical circuits [174, 175]. Primarily, these studies were conducted using excimer UV laser radiation between 193 nm to 308 nm with a pulse duration $\sim$10 ns, due to the high dissociation energy of the used thermoset monomers such as Kapton, PET and PC [157].
In this case, the light absorption promotes specific atoms sensitive at the selected wavelengths (chromophores). The delivered phonon energy transfers electrons from the lowest ground state to an excited upper electronic level. At this state,

the electron may exceed energy higher the bonding between two atoms, and the system becomes metastable [53]. The energy relaxation occurs by bond dissociation with an incoming phonon. It is accepted that this pathway results in a purely photochemical reaction. However, this process competes in multiple pathways: the excited state can also promote fluorescence, an internal conversion for further dissociation at the ground state, a vibrational deactivation, a collisional quenching, and intersystem crossing into another electronic state. All processes mentioned above are equivalent to the thermal process and result in a photothermal dissociation mechanism. Thus, the exact relaxation mechanism is complex, and each of the processes cannot be exactly numerically estimated [53]. The complexity of this dissociation mechanism increases with a decrease in the wavelength within the UV region, where the specificity of transitions is no longer assigned to particular chromophores.

The pulse duration affects selection for the mechanism of ablation. Thus, if the ablation time is in the order of laser pulse duration, the thermal diffusion length is minimal, and the substrate does not undergo any thermal damage [176]. However, the relation holds only for the UV wavelengths of nanosecond and subnanosecond duration, and with the wavelength increase, the separated photochemical APE requires a reduction to femto and picosecond pulses due to change in the material-specific absorption coefficient [60, 177].

Kapton (PMDA-ODA) is the most attractive among studied materials due to its high absorption coefficient and high chemical and physical stability. Moreover, it exhibits one of the highest monomer dissociation energy $\sim$37 eV for polymers, which requires at least seven UV photons at the wavelength of 193 nm [178]. Such an absorption mechanism supports the hypothesis about the multiphoton process. The laser irradiation with substrate induces cutting on the weakest bonds in the PMDA-ODA molecule, namely on the imide ring [60, 178–180], which is supported by the observation in the mass spectra from CN, CNH dissociated compounds, with the characteristic rise of this content with an increase in the fluence and the photon energy [181]. The initial scission causes fragmentation on the site and reduces the dissociation energy in the remaining

polymer backbone due to partial charge redistribution and the monomers ionisation. Further ablation accompanied by a fragmentation and an expulsion of $C_2, CO, CO_2, H_2O, C_6H_6$ molecules [176], in addition with various aromatic compounds ($C_6H_5OH, C_6H_5NH_2, C_6H_4(CN)_2$ etc.) and bigger carbon clusters (>C_{38}) observed with *in situ* FTIR [182]. These expulsed gaseous by-products attain high velocity and temperature in the generated plume and discharged region resembling plasma.

Multiple models very applied to estimate the temperature in this region. The investigation conducted with high induced fluorescence spectroscopy near the bandhead of CN radicals by rotational state occupation estimates the temperature after ablation starting from 1400 K for the first-order dissociation at the surface and over 2800 K from carbonaceous C_2 spectra corresponding to the second phase-order [183].

Notably, the polymer films are affected by laser radiation within several microns causing attenuation of the incoming intensity of the pulse within film volume. The main criteria in the delivered energy depend on the area covered with the laser beam, so-called fluence ($\Phi = E/A$). Thus, this fluence attenuation ($\Phi(z)$) in the depth of material (z) governed with the Beer's law and dependent on the applied fluence ($\Phi(z)$), and the material specific properties on the threshold fluence (Φ_0) and the absorption coefficient (α) [53, 157]:

$$\Phi(z) = \Phi_0 \exp^{-\alpha z} \tag{5.1}$$

The etching regimes can be separated into multiple regions as is depicted in Figure 5.1 [177]. At low fluence, the threshold is reached, and the ablation is incubated but resides at a low etching rate. Further fluence increase into the intermediate range leads to efficient polymer decomposition and involves exothermic reactions promoted by photothermal mechanisms. In the high fluence regime, the generation of characteristic plasma/plume is observed, and the ablation rate retains within linear range for many polymers [177, 184].

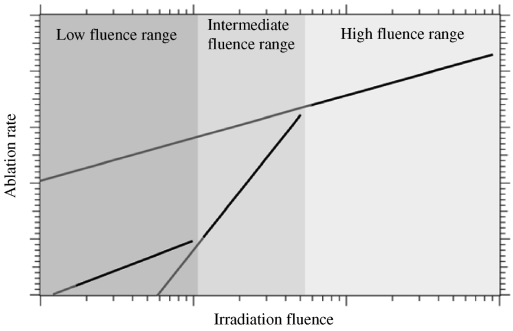

Figure 5.1: Schematic of the three fluence ranges for polymer etching. Adopted from Ref. [177]

Specifically, the high fluence regime is extensively governed by the photothermal electron relaxation mechanism, which involves a considerable heat accumulation within the radiation affected region. This heat affected zone undergoes phase transformations, depending on the polymer backbone, where they directly reach an etching temperature (i.e. PMMA, PET) or, in the case of the stronger bonding in the backbone, undergoes a pyrolytic transformation as for the Kapton [53]. The latter causes formation of a thin carbon-rich layer in laser-induced carbonisation (LIC). Depending on the selected wavelength and the precursor, this laser carbon (LC) tightly reside on the film or can be easily released from it due to low adhesion with precursor [60, 66]. The most common features of the laser carbon are high graphitisation, conductive properties comparable to materials obtained with conventional pyrolytic methods, high porosity inherited from the fabrication process in nano and microscale due to interference with released by-product and shrinkage of the precursor. Despite the pyrolysis-like conditions at the laser interface with polymer, this material rendered significantly different from graphite, various glassy and activated carbons, with physical and chemical properties residing between those allotropes.

It was shown that only a number of thermosets and naturally occurring polymers are suitable for LIC [55, 65]. The general trend for selecting these polymers lies in the high enthalpy for complete dissociation of a single monomer, which

results in high mechanical toughness and high degradation temperature. The known precursors with their physicochemical properties are listed in Table **??**. The majority of these precursors attain a thermal conductivity in range $0.1\,\mathrm{W\,m^{-1}\,K^{-1}}$ to $0.3\,\mathrm{W\,m^{-1}\,K^{-1}}$ and a specific heat between $0.9\,\mathrm{J\,g^{-1}\,K^{-1}}$ to $2\,\mathrm{J\,g^{-1}\,K^{-1}}$.

5.2 Thermal Models for Laser Carbon Formation

The photochemical surface models do not apply for the pulses with duration over nanosecond [185, 186]. Thus, the thermal models considering the dominance of the photothermal dissociation mechanism, which only considers the heat accumulation required and the models developed for the laser ablation of metals in the surface and bulk thermal propagation [186, 187].

As it is broadly discussed in the CMEMS field, the processing temperature, pressure and working environment play an essential role in the degree of graphitisation after pyrolysis of epoxides, photoresists, phenolic resins and natural polymers lignin chitosan [82, 164, 188, 189]. Thus, the precursor temperature during the process must be considered to estimate the quality of yielded carbon-rich film after the laser-induced carbonisation. Its evaluation was performed using multiple thermal models with the estimation of a gradient at the laser beam spot.

One of the direct approaches involves solving a heat equation with a finite element method with direct computation at each node [180]. Such methods require high computational power and can be further rationalised.

The most effective and most straightforward model to simulate the surface temperature was showed by Dyer [187], without accounting for the chemical decomposition presented in the wavefront and accessing the velocity of the released by-product. The model considers the increase of the absorption driven through the photothermal mechanism and thus restricted to the wavelengths above UV [190]. The model considers only radial dissipation from the heat source within the material without any external cooling from convection. This approximation is valid only for the cases with a characteristic absorption depth higher than the diameter of a Gaussian beam a, as this criterion matches a wavelength selection rule.

The temperature increase for the pulsed laser irradiation is derived from the one-dimensional heat equation, following Neumann's integral theorem, and includes the Bessel function of zero-order for solving heat conduction in the cylindrical coordinate system [187, 191]. It is expressed in the form:

$$T(r,t) = T_0 \int_0^{\infty} \exp[-z^2/a^2] \exp[-(z^2+r^2)/4\kappa t] \cdot I_0(rz/2\kappa t) z/2\kappa t dz; \quad (5.2)$$

With z is the depth of probing, t is the time duration in a model, κ is a thermal diffusivity determined from the thermal conductivity over a c_P specific heat and the material density, r is a radial probe position, I_0 is a Bessel function, and T_0 is the peak temperature at $r = 0$. The latter is determined from the equation:

$$T_0 = (1-R)\alpha F_0 / c_P; \quad (5.3)$$

where R is the reflection coefficient, α is the absorption coefficient and F_0 is the peak fluence. In the modelled CO_2 laser system, the peak fluence determined from the equation related to the average power and the focus carriage velocity over selected pulse regime, which typically results in the pulse frequency ν of $\sim$1 kHz. After solving the standard integral in Equation 5.2, the expression takes an analytical form:

$$T(r,t) = T_0\{\exp(-r^2/[4\kappa t + a^2])\}/(4\kappa t/a^2 + 1) \quad (5.4)$$

It can be further improved by including the train of pulses n via equation:

$$T_n(r,t) = \sum_0^{n-1} T(r, t - n/\nu) \quad (5.5)$$

In the experimental system, the pulses are not distributed at the same irradiation spot due to the movement of the focus carriage. In the selected scanning mode, only five irradiation events should be considered with a reduction of overlapping. All these considerations were implemented in the model with a MATLAB code presented in Appendix A-2.

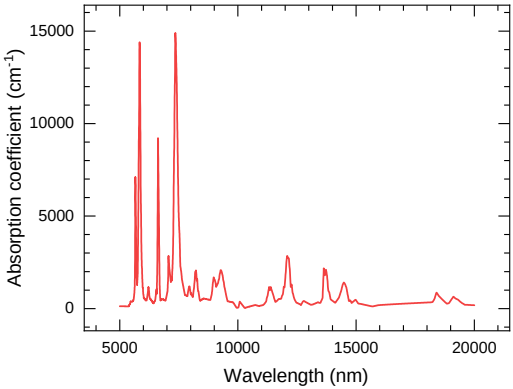

Figure 5.2: The absorption coefficient of Kapton estimated from the extinction coefficient.

The model includes specific physical and chemical properties for several materials collected from table values for the studied laser carbon. However, the absorption coefficient is a wavelength specified parameter, which is collected through the optical transmission and reflection studies to determine an extinction coefficient. The relation is expressed through the equation: $\alpha = 4\pi k/\lambda$ with k is the extinction coefficient, and λ is the wavelength. Due to simplicity and multiple uses in the literature, Kapton values are used as an example. Figure 5.2 shows the absorption coefficient calculated for IR spectrum, which at the selected wavelength is $149\,\mathrm{cm}^{-1}$.

The original model considers the rise of the absorption over a number of pulses due to the formation of the carbon-rich phases through the internal function. However, such approach fails to estimate the heat dissipation within the film, considering the change in the specific heat and the heat conductivity. In the presented model, the switch was introduced for improvement of all those properties after reaching 550 °C for a modification to glassy carbon phase, and over 1500 °C to a graphitic phase, all evaluated from the mass loss. Even such crude approximation already provides significant validation of the phase transformation and evaporation after reaching temperatures above the graphite sublimation.

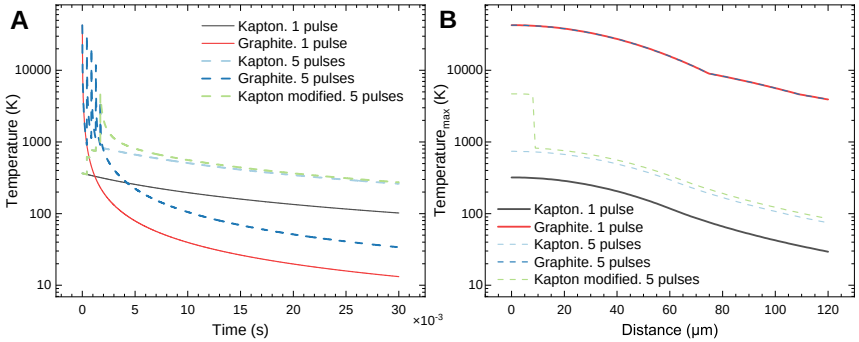

Figure 5.3: Simulated maximal temperature attenuation (A) over time and (B) from centre of the Gaussian beam.

Laser carbon testing formation was performed with laser operation parameters at 4.0 J/cm^2 fluence and 3 W power. The simulation considers parameters solely for Kapton and graphite with a single shot and after five consecutive shots considering a laser overlap during the focus carriage movement. The simulation was further modified with consideration of the Kapton phase transformations to glassy carbon and graphite with five shots. Figure 5.3A shows temperature attenuation with a time, where Kapton modified exhibits near sublimation temperatures at the beam spot. After a single irradiation pulse, Kapton does not reach the temperature required for the phase transformation, but only after the aforementioned set of pulses. Figure 5.3B depicts maximal temperature from the Gaussian beam, which gradually drops in all cases. Kapton modified features drop rapidly in the temperature over 10 µm due to the non-continuous absorption coefficient variation between used phases. Notably, for all studied cases, graphite samples indicate temperature above sublimation.

This simulation provides valuable information considering estimated temperatures, from which it is possible to derive the degree of graphitisation through referencing reached values with correlation to the Raman spectra, and model the etching rate, the velocity of expulsion by implementing the results into the Arrhenius equation [186].

5.3 Further Model Development

The presented thermal model does not consider the threshold fluence due to the initiation of the chemical modification and its influence on carbonisation and ablation. Moreover, the plume nature and its absorption spectrum remain an open issue, requiring further investigation. A significant part of the laser radiation is absorbed in the plume explicitly affecting the produced films quality. Current models, including the molecular dynamics simulation, cannot accurately estimate an interference from the working environment and approximate a change in the chemical composition after fabrication in the reactive and inert atmospheres.
Several molecular dynamics simulations were proposed from these estimated temperatures accounting for the formation of graphitic layers from the initial precursor, which found good correspondence to the experiment.

6 Laser-induced Carbonisation of Kapton

Polyimide (widely known under the trade name Kapton) is the most commonly used synthetic polymer in the laser-induced carbonisation [192]. Kapton possesses exceptional mechanical properties and durability in extreme operation conditions, including preventing damage from high ionic, electronic and photonic radiation fluences [193, 194]. These properties play an essential role for the laser carbon generation in a wide range of wavelengths, from low UV at 193 nm to mid-IR at 10.6 µm.

Lately, the development of cheap and accessible semi-industrial laser systems has brought machines operating in the mid-IR range, which made them a valuable and powerful tools for machining a large number of materials in the dayly work in labs and workshops. The broad utilisation of such laser systems prompted the re-emergence of interest in LIC [55] as a method for the fast and reliable fabrication of the conductive films for sensors. Moreover, the new generation laser systems provide high throughput with semi-industrial production of the low-cost devices embedded directly within the polymer film, matching the needs of the flexible point-of-care sensors. Those laser carbon films showed suitabile for the chemical and biological sensors due to the synergy of the conductive properties, crystal structure, biocompatibility, and surface chemistry.

However, the kinetics of laser carbon generation under 10.6 µm wavelength laser radiation remains unstudied, mainly focusing on the films utilisation and its composites as supercapacitors, reactive electrodes for hydrogen generation, chemical and biological sensors [55, 195–197]. This chapter presents initiation processes of the laser-induced carbonisation and corroborates with the previously discussed

thermal model [187]. This model was further utilised to estimate temperature by variation of fabrication laser input parameters, such as fluence, power, rasterisation speed and pulse sequencing. These results were implemented to fabricate three sample sets with the same fluence in each set but varied laser power and rasterisation speed. The quality of these samples between each set and each other was estimated using benchmark tests with a vigorous investigation of their crystallographic and chemical properties. From acquired data, the best films were determined and studied in detail. The distinguished laser carbon film properties were applied for directed electrodeposition of the natural biopolymer chitosan in the form of a hydrogel, which serves as an excellent media for chemical and biological sensors as well as catalysis. The composite film was assembled into a low-cost passive urea bioelectrode as a proof of concept. A detailed study was performed on the kinetics of hydrogel adhesion to the substrate. For this composite sensor, the enzymatic anchoring was used of urease immobilised within chitosan hydrogel or by direct adhesion to the laser carbon film.

6.1 Laser Carbon Synthesis with Mid-IR Laser

The selected mid-IR laser radiation delivers photon energy of $\sim$0.12 eV, which is insufficient for the direct bond scission at the lowest energy within a single monomer, and over 20 fold smaller for its complete dissociation. However, CO_2 laser systems are designed for delivering high intensities of the radiation at the focal spot. However, the polyimides exhibit very low absorbance at the selected wavelength, contributing only to stretching vibration of the C – H bond [198]. These vibrations further propagate into the polymer backbone, causing electron excitation followed by the photothermal relaxation mechanism. In pair, this results in localised temperature rise cascading within the volume sufficient for the bond scission and promoting the generation of various hydrocarbon, hydroxyl and carboxyl byproducts. The composition of these byproducts is mostly volatile and causes further temperature increase due to the exothermic chemical reaction in ambient conditions. Experimentally it was observed an immediate generation of

a discharged region with plume/plasma above irradiated area in air and nitrogen environment [69]. However, the inlet of argon reduces or completely suppresses the plasma discharging. This observation suggests the reactive nature of the oxygen and nitrogen processing environment, which affects the surface morphology and process propagation. Meanwhile, the remaining ionised phenolic compounds within the polymer film stabilise by re-arranging as graphene-like fragments, and under the effect of a thermal gradient, it is subjected to pyrolysis-like transformation under the discharged region.

To elucidate the evolution of the polymer into the laser carbon under applied radiation, the comparative study was carried out employing microscopy and FTIR spectroscopy, and are depicted in Figure 6.1.

The initial Kapton film morphology and its chemical composition are presented in Figure 6.1(A & B). The initial film surface attributed uniformity with some minor damage caused by handling. FTIR from this film indicated characteristic peaks of C=O bending, C–O–C, C–N–C and C=O out-of-phase stretching at 721 cm^{-1}, 1086 cm^{-1}, 1112 cm^{-1} and 1711 cm^{-1}, respectively [194, 199], with detailed deconvolution listed in Table A2. In order to determine the variation between studied films in the contribution of each chemical species, the absorbance was normalised to a maximal peak at 1711 cm^{-1} contributing to C=O out-of-phase stretching. The selected species were assumed to retain the same chemical state with relative oligomer quantity to other functionalities due to high enthalpy energy required for its dissociation in contrast to other bonds, which is matching to the simulation and spectroscopy results from plume [179, 200, 201].

The first morphological changes were observed after reaching fluence of 2.4 J/cm^2, at which the built-up pressure from the volatile byproducts caused film swelling into characteristic 'bubbles', with some rapture and expulsion of the dissociated material on the surface, as it is observed in Figure 6.1C. These swollen bubbles arose $\sim$5 µm above the average level and stretched longitudinally following the train of pulses during rasterisation. Figure 6.1C shows the FTIR spectrum from this film, indicating the reduction of integral contribution for multiple peaks, suggesting a drop in the number of selected species, or due to the constraining

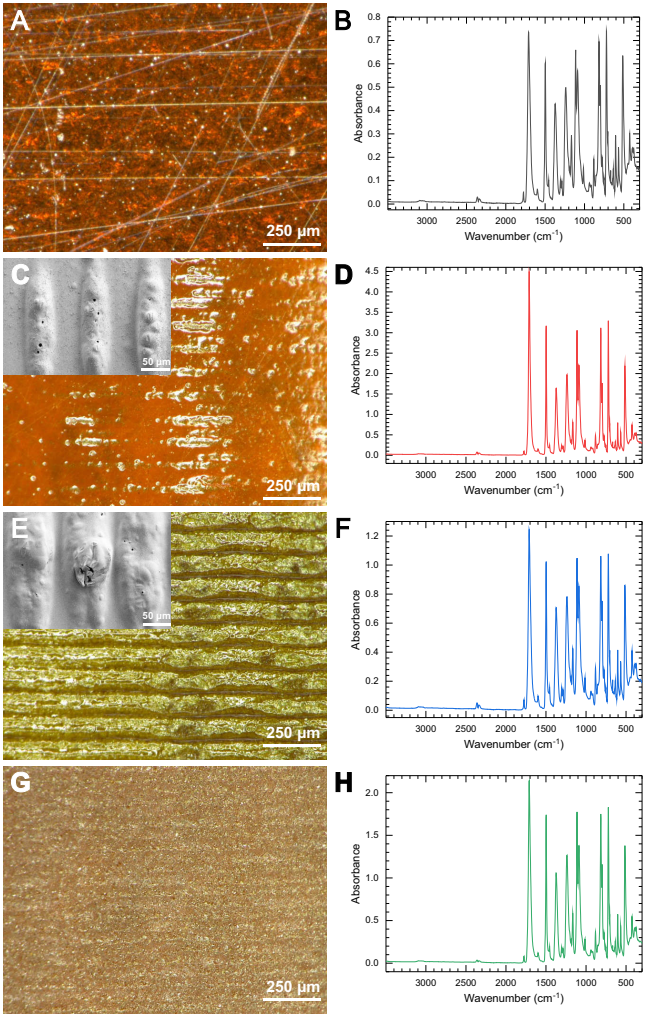

Figure 6.1: (A,C,E,G) Optical micrographs and relevant SEM images in insets on the surface morphology of the Kapton films from initial precursor and after an irradiation with fluences 2.4 J/cm^2, 2.6 J/cm^2 and 3.3 J/cm^2 respectively and the corresponding FTIR spectra (B,D,F,H). In (G,H) the Kapton surface was exposed after removal of the laser carbon layer.

of a particular vibrational mode. Namely, it significantly reduced all bands in the imide ring, confirming preferable dissociation along imide ring and aromatic ring species [163, 201].

Further rise of fluence to $2.6\,J/cm^2$ shows increase in the lateral sizes of these bubbles ranging between $51.4\,\mu m$ and $82.0\,\mu m$, as depicted in Figure 6.1E. Moreover, the number of bubbles also rose with occasional rapture and initiation at the spot of carbon islands. Figure 6.1F shows the FTIR spectrum collected from this film. After aforementioned normalisation, it exhibits similar reduction in integral contribution of same species and additional vibration modes corresponding to out-of-plane bending in C_6H_3, tangential C_6H_5 in the aromatic ring, and $C-O-C$ out-of-phase stretching and CH_2 in-plane bending at 881, 1497, 1239 and $1455\,cm^{-1}$ respectively, due to confined chemical state [194, 199, 202].

The first uniform laser-induced carbonisation events were observed after reaching fluence of $3.3\,J/cm^2$, coupled with a generation of the plume above the surface during fabrication. Notably, at this threshold fluence, the laser carbon film attained some electrical conductivity, but its uniformity between samples exceeded the measurement error, requiring further tailoring the laser operating parameters. Moreover, the presented study consolidates in the determination of Kapton modification, for which purpose the laser carbon film was removed with acetone and the remaining film was rinsed in DI water and ultrasonicated. The retaining Kapton film showed in Figure 6.1G, featuring significant modification in morphology from previous cases, with high roughness covered by characteristic micro and nano indentations, but without the presence of any swelling rising above the film surface. As it was observed in Figure 6.1H, the post-carbonisation residual Kapton exhibited the absorbance of 0.15 in the operating laser wavelength region, which was higher compared to the untreated film. This attributes to chemical modification, increased roughness affecting the film reflectance and possible entrapment of the carbon nanoparticles with higher absorbance on the surface. Notably, the post-carbonization residual film showed improvement in $C-N-C$ out-of-plane bending, transverse stretching and axial stretching, and $C-O-C$ out-of-phase stretching at $721\,cm^{-1}$, $1112\,cm^{-1}$, $1374\,cm^{-1}$ and $1239\,cm^{-1}$, respectively. The

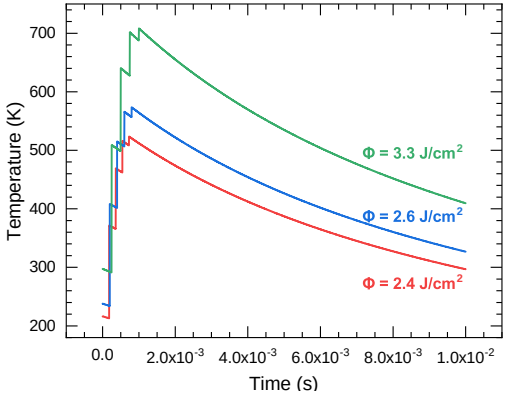

Figure 6.2: Thermal model after irradiation with indicated fluences.

C – N – C bond is the weakest in the monomer, and such improvement suggests the reduction of the dissociation energy at the bottom of laser carbon film interfacing with native Kapton.

The collected FTIR spectra indicated variation in the absorbance for wavelength operation regime in the untreated Kapton and films after irradiation at fluences $2.4\,\mathrm{J/cm^2}$ and $2.6\,\mathrm{J/cm^2}$ were 0.09, 0.19 and 0.12 respectively. The absorbance after laser irradiation was significantly improved between batches attributing increase for all specimens from the untreated film as shown in Figure 6.1(B, D, F & H), which can be caused by the increased roughness via variation of scattered and reflected photons, and additional application of the Kubelka-Munk function modifying the original data.

The tested laser parameters were implemented in the thermal simulation and depicted in Figure 6.2 at each selected fluence. The temperature regime retains within Kapton heating range without transformation to glassy carbon regime. This indicates a fit with the observed changes but hints for additional exothermic chemical reactions involved during carbonisation and plume generation.

These thermal models have proved the appropriate fitting for the estimation of working regimes and can be used to simulate a wide range of pulse regimes.

6.1.1 Working Parameters Selection and Process Evolution

The temperature evaluation during fabrication plays an essential role in guiding the laser carbon formation and its quality. Thus, the aforementioned thermal model is implemented for the wide range of laser input parameters.

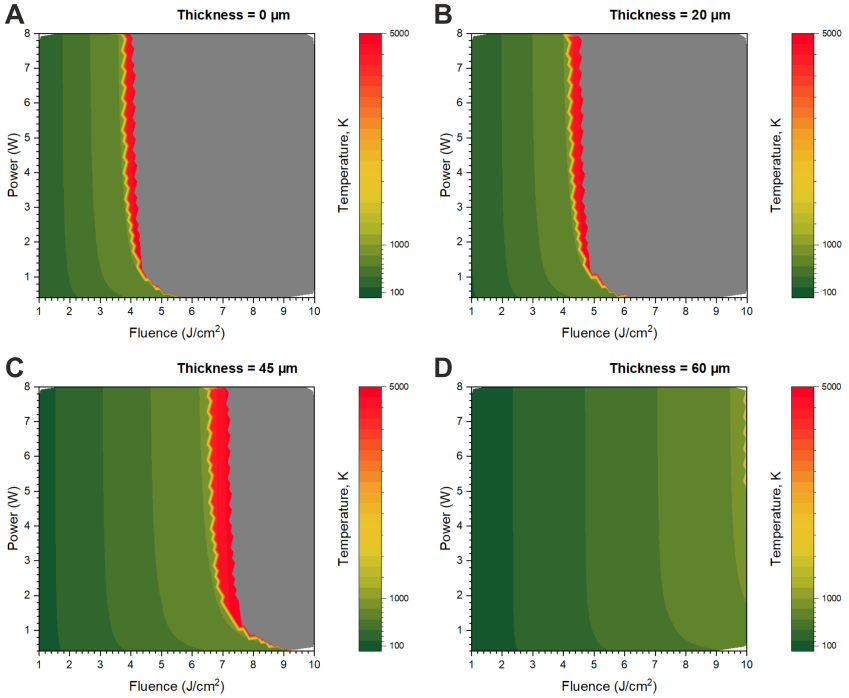

Figure 6.3: Diagrams of the simulated maximal temperature on the fluence and the applied power with penetration depth at the beam spot at (A) 0 µm, (B) 20 µm, (C) 45 µm and (D) 60 µm.

The simulation was modified to achieve phase transformations to glassy carbon and graphite. The heating under laser radiation for these materials was independently studied, and the results are presented in Appendix A-4. Figure A1 depicts diagrams after simulation on purely glassy carbon and graphite, where it indicates excessive heating and reaching temperatures ∼200 000 K corresponding to the immediate ablation and material sublimation at the focal spot. However, the cool-

ing appears significantly faster due to the higher thermal conductivity of these materials. Figure A2 shows a diagram of Kapton with the phase transformations at full temperature range, where it reaches maximum ∼100 000 K at the focal spot suggesting rapid ablation. Thus, considering graphite sublimation temperature, the limit was set at 5000 K to reduce the dispensable contribution to the simulation. Considering these factors, Figure 6.3 depicts a diagram of Kapton heating during LIC by variation of fluence and power inputs at different depths of the film at the focal spot. The non-uniform temperature distribution originates from a variation of the pulse input and is dependent on the focus carriage speed and PPI, from which fluence is determined, causing a higher irradiation frequency.

Figure 6.3A depicts temperature at the surface of the Kapton film, where the carbonisation is possible even at fluences above 2 J cm^{-2} with high power input, where the temperature exceeds minimal 600 K for initiation of the pyrolysis. Indeed, some tests indicated that carbonisation is possible at low fluence and high power but lacks repeatability and shows poor carbon quality, therefore not been widely investigated. The temperature above 800 K observed over 2.5 J cm^{-2} fluence and 3 W power, at which the threshold laser parameter for LIC was determined. The maximal temperature with the carbon sublimation occurs over 4 J cm^{-2} fluence in the power range from ∼3.5 to 8 W. In the depth of the film, the temperature gradually drops Particularly, Figure 6.3B shows temperature distribution at the 20 µm film thickness. The phase transformation to carbon occurs in the region above 3 J cm^{-2} in the power range from ∼3 to 8 W. The maximal limiting temperature with the carbon sublimation occurs over 4.5 J cm^{-2} fluence in the power range from ∼4 to 8 W. In further Kapton film depth at 45 µm, the carbon phase transformation computed starting over 4.6 J cm^{-2}, as depicted in Figure 6.3C. Figure 6.3D shows the temperature distribution at 60 µm, which is a half-thickness for the tested Kapton films. There, the carbon phase transformation region is further shifted above 7 J cm^{-2}, and the maximal temperature at 10 J cm^{-2} fluence is estimated at ∼2500 K. Notably, in all cases, the isotherm region significantly expands in the film depth providing a wider window for the production of laser carbon of the same quality.

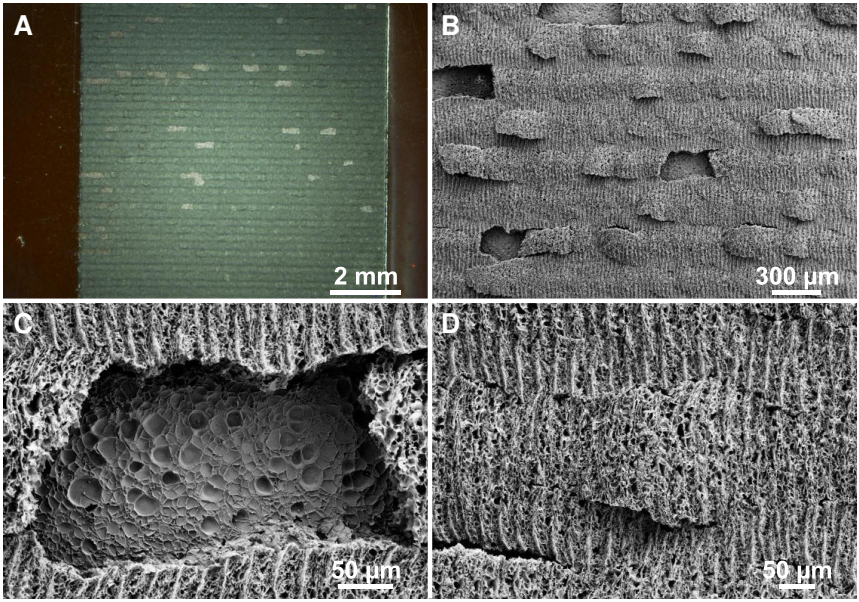

Figure 6.4: The surface morphology after rastering with interline distance at ∼25 µm. (A) The optical micrograph, (B-D) the SEM imaging.

There, the simulation results were further empirically tested after the fabrication of three sample sets with fluences variation and power input and then investigated with a number of standard techniques to determine of graphitisation, crystal structure and chemical composition.

6.1.2 Laser Carbon Films Procedure Selection and Morphology

After reaching the threshold laser fluence of $3.3\,\mathrm{J/cm^2}$, the Kapton undergoes the laser-induced carbonisation at the selected wavelength. Three batches of carbon patterns were fabricated employing various fluences at $4.0\,\mathrm{J/cm^2}$, $5.2\,\mathrm{J/cm^2}$ and $7.8\,\mathrm{J/cm^2}$. The starting fluence was selected above the threshold value due to improvement in the selected fluence in the electrical stability along the measurement direction, morphological and formation uniformity of the laser carbon film.

Independent from the fluence values, the fabrication procedures were carried out with the interline distance between raster passing of $\sim$100 µm and broader. The narrowing of interline distance causes significant structural deterioration, where the laser carbon films start to self-exfoliate from the substrate film, as depicted in Figure 6.4. These films were selected out as not useable for any application. On the contrary, widening the interline distance promoted the reduction of the electrical conductivity perpendicular to the rastering direction, which was also unyielding.

Table 6.1: Selected parameters for fabrication of the laser carbon.

Φ, J/cm^2	P, W	v, cm s^{-1}	Designation
4.0	2.0	4.1	–
	2.8	5.8	–
	3.8	7.8	–
	4.8	9.9	A1 & N1
	5.6	11.6	–
5.2	2.0	3.8	–
	2.8	4.5	A2 & N2
	3.8	6.0	–
	4.8	7.6	A3 & N3
	5.6	8.9	–
7.8	2.0	2.1	–
	2.8	2.9	A4 & N4
	3.8	3.9	–
	4.8	5.1	A5 & N5
	5.6	5.9	–

Two distinct working environments were selected. Primarily, the ambient environment was tested and secondly, the samples were prepared under the permanent

nitrogen flow in a sealed home-made PMMA box with BaF_2 window transparent in the selected wavelength (design in Section 2.1) for each specified parameter set. The general assessment is performed for all batches in both fabrication environments. The applied laser parameters during fabrication are listed in Table 6.1, highlighting five selected samples, on which the detailed studies were conducted and each prepared in air and nitrogen, denoted A# and N#, respectively.

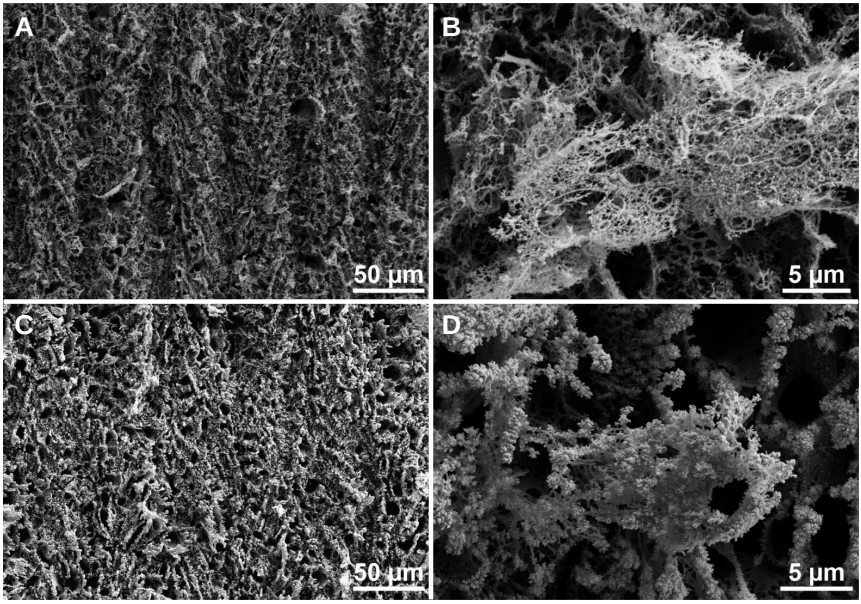

Figure 6.5: The surface morphology of the selected laser carbon sample fabricated in (A-B) air and (C-D) udner nitrogen flow.

Both working environments resulted in the formation of characteristic surface morphology. Figure 6.5 depicts a structure for both types of films. The laser carbon prepared in air exhibits the formation of a porous carbon film resembling randomised lamella structure with variable roughness, promoted by excessive expulsion of the dissociated byproduct. The detailed morphology from each selected specimen is presented in Figures B1. Notably, specimens fabricated at $7.8\,\mathrm{J/cm^2}$ fluence exhibit the aligned protrusions following the raster patterning

direction, originating from the interface with a laser beam. After the introduction of nitrogen during fabrication, it exhibits rougher morphology with the pronounced formation of the dendrite-like structures across the surface layer. As well, the raster direction patterns were more pronounced for samples above 5.2 J/cm^2. The detailed imaging for a comprehensive sample set is presented in Figure B2.

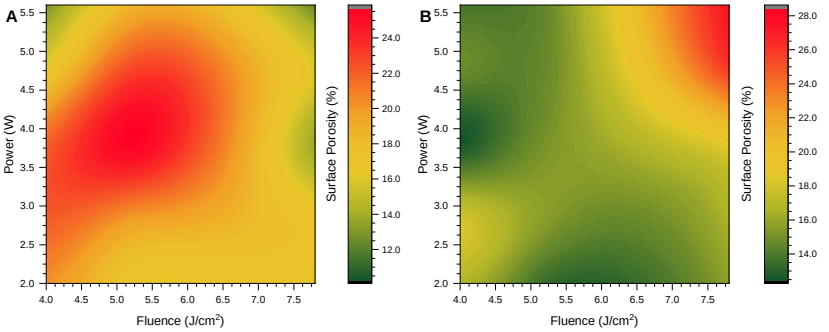

Figure 6.6: The thin-plate spline interpolation curve on the surface porosity of the laser carbon fabricated in (A) air and (B) nitrogen.

From the obtained SEM images, the surface porosity was determined from the difference between the overall material coverage to the void area and presented in Figure 6.6 as a thin-plate spline through interpolation from measured samples. Figure 6.6A shows such TPS from films fabricated in air, which exhibited the peak porosity at $\sim$5 J/cm^2 fluence in the power range between 3 and 5 W. Contrarily to the estimated temperature rise, the porosity dropped with higher fluence and delivered laser power. However, considering the reaching of carbon sublimation threshold temperature at this regime, the exposure of deeper laser carbon layers supports this drop, containing film fabricated at a lower temperature and thus reduced porosity.

Nevertheless, the more controllable temperature rise and the promoted porosity distribution were observed in the nitrogen assisted sample set, as depicted in Figure 6.6B. This effect was promoted by the reduction of the operating temperature due to a combination of the pulse attenuation after passing through BaF_2 window,

change of the reaction kinetics in the inert environment, and interference with supplied N_2.

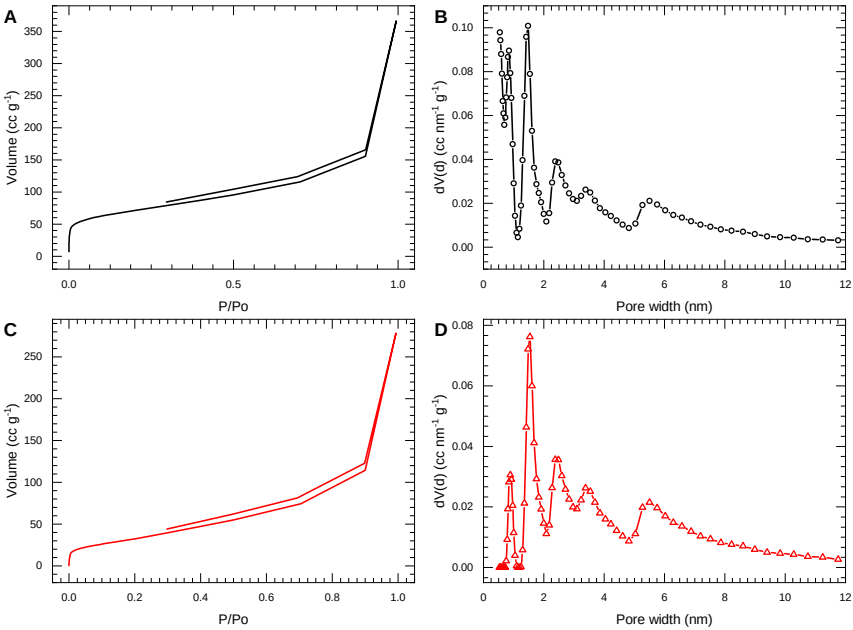

Figure 6.7: The BET isotherm and the derived pore sizes for the powder extracted from (A-B) A1 and (C-D) N1.

The selected A1 and N1 samples underwent vigorous investigation on the distribution of nanopores with Brunauer-Emmett-Teller method (BET) from argon isotherms, which is depicted in Figure 6.7. Evidently, laser carbons prepared in each working environment display different porosity, which indicated a specific surface area of 255 and 106 m^2/g for A1 and N1, respectively. The ratio agrees with the previously observed values from the surface porosity between the samples. The pore size was approximated with the DFT model using a combination of cylindrical and spherical shaped pores. The detailed distribution of the pore sizes is depicted in Figure 6.7(B, D) for A1 and N1, respectively. Here, a maximum pore fraction lays in the range between 0.8 and 1.5 nm for A1, and at 1.6 nm for N1.

However, this model provides the best fit to the isotherm with the majority of pores assigned to width below 100 nm, but material exhibits larger meso-pores observed from SEM and TEM not computed in this model. BET confirms densely packed laser carbon prepared under nitrogen flow in nanoscale and higher specificity to the pore size.

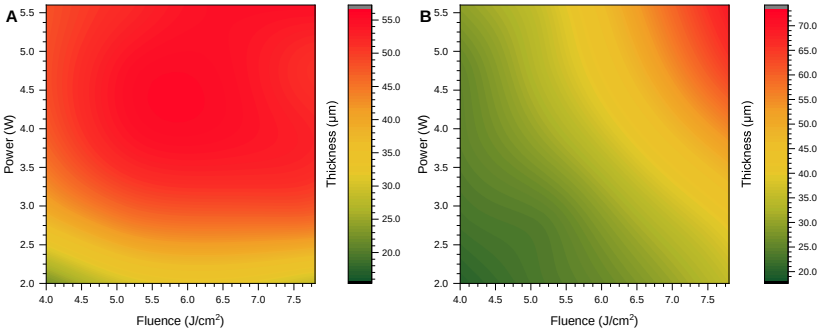

Figure 6.8: The thin-plate spline interpolation curve on the thickness of the laser carbon fabricated in (A) air and (B) nitrogen.

The films thickness analysis was performed with the stylus profilometry (details in Section 3.4) across all batches and presented via TPS in Figure 6.8 with the variation of the thickness to the fluence and power for both working environments. The similar trend was observed in both samples, where the thickness steadily increases with both fluence and power. The trend follows Beer-Lambert law previously observed in the formation of laser carbons [176, 203] and supported by temperature rise within the volume after reaching threshold temperature for pyrolitic transformation. Notably, the topology of the films differ from the applied fluence, where carbon film rises above the median Kapton surface, but after reaching 6.0 J cm^{-1} laser carbon majorly ablating leaving characteristic valleys, which was previously observed with SEM. The minimal thickness in both environments is determined at ∼20 µm, but in air, the thickness significantly rises with the power after 3 W for all fluences. On the contrary, no rapid rise is observed under nitrogen flow in the similar regime at the same fabrication conditions. Overall, the laser carbon in the

nitrogen set indicates wider variation from the thinnest films at minimal delivered power, and fluence to maximal with ∼70 µm at the highest input parameters.
This suggests improvement in fabrication stability after the introduction of nitrogen in both terms of porosity and thickness. Presence of nitrogen prevents conjugated exothermic reactions and follows more directly the temperature related phase transformations leading to the laser carbon formation.

6.1.3 Crystalline Properties

Raman spectroscopy is a widespread technique for the determination of crystalline properties and quality control of semiconductor materials, which additionally found numerous applications in the research of carbon-based material and accepted a common technique in the quantification of intrinsic properties. All prepared samples were extensively studied with Raman spectroscopy and show presence of the two distinctive first-order peaks at ∼1340 and ∼1580 cm^{-1} corresponding to D and G-band, characteristic to graphitic materials. In addition, the secondary disorder D'-band is present at ∼1620 cm^{-1} and the second-order overtone, 2D-band, at ∼2690 cm^{-1} was observed for all cases. The combination bands were presented at ∼2460, ∼2930 and ∼3230 cm^{-1} designated as (T+D), (D+G) and 2D' respectively [69].
However, only the first and the second-order peaks provide quantitative information about the determination of the graphitisation and the predominant lattice hybridisation state. D, G, 2D bands and their ratio (I_G/I_D, I_{2D}/I_G) are studied and presented in Figures 6.9 & 6.10 in TPS for the set fabricated in air and nitrogen assisted environments respectively.
It is accepted that the position of G-band, in combination with graphitisation ratio between the bands: I_G/I_D are critical parameters in the ratio estimation in hybridised carbon between sp^2 and sp^3 states [144, 204].
In all cases the I_G/I_D ratio determined above 0.50, which corresponds to nanocrystalline carbon [144]. The electronic transport properties are governed by the presence of sp^2 hybridised state, which is typically manifested by the presence

Table 6.2: Crystalline properties of laser carbon.

	Air	Nitrogen
Derived from Raman spectroscopy		
Graphitisation		
Crystallite size, nm		
Derived from XRD		
Interlayer distance, Å	3.48	3.44
Crystallite size L_a, nm	4.0	3.6
Crystallite size L_c, nm	7.1	8.6
Conductivity, $S\,cm^{-1}$	10.2 ± 2.4	23.4 ± 2.3

of the 2D-overtone. The intensity ratio between 2D and G-bands presents a level of hybridisation and can estimate the number of layers in the graphene stack. In the observed cases depicted in Fig. 6.9D, the ratio does not exceed 0.65, which is characteristic for systems about 10 graphene layers.

Figures 6.9A & B show TPSs for D and G-bands, which exhibit similar behaviour. There, the band position minimum is observed at the lowest tested fluence and proportionally decreases with the power increase. The further increase in the fluence and power results in peaks shift towards higher wavenumbers, reaching $1352\,cm^{-1}$ and $1588\,cm^{-1}$ in case of D and G-bands, corresponding to a gradual shift towards surface layer rich with amorphous carbon. The difference in the state can be induced by precipitation of unreacted species from laser-induced plasma or exposure after ablation of the interface layer by a deeper structure fabricated at a lower temperature. Such change further agrees with the graphitisation degree estimated by the areal ratio of the G over D-band, and the electronic properties by the peak ratio of 2D over G, depicted in Figure 6.9C & D. There, TPSs feature inverted relation, the maximum observed at minimal fluence and minimal power

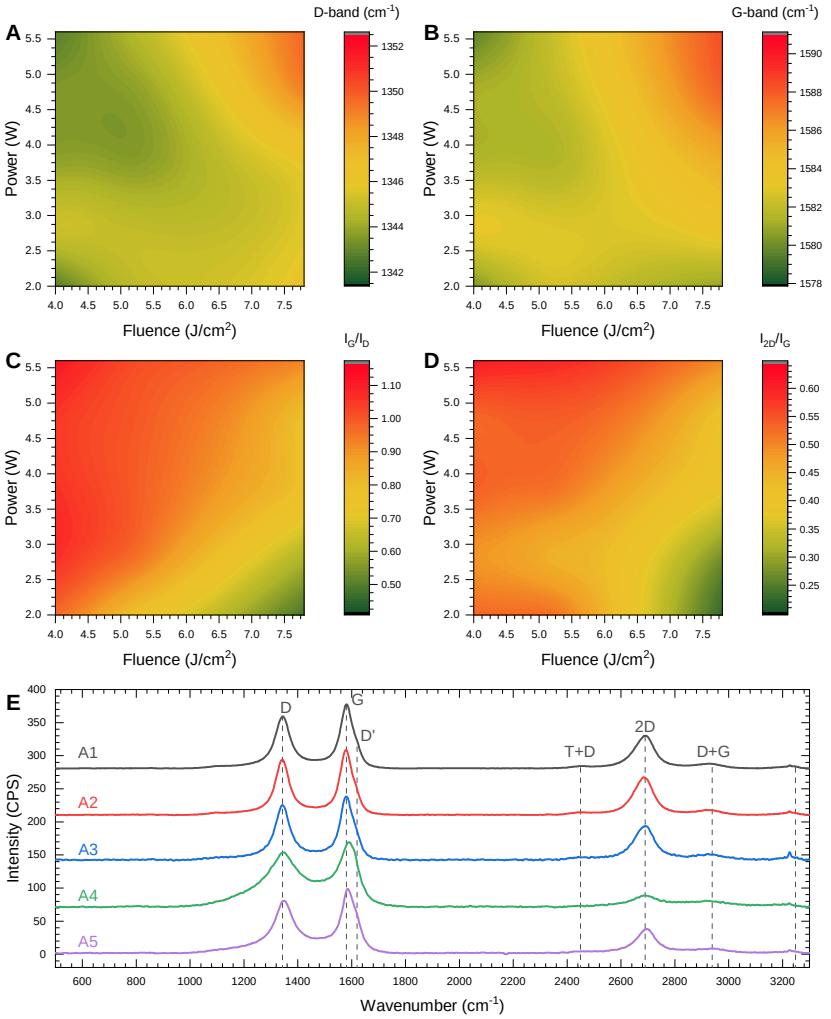

Figure 6.9: The thin-plate spline interpolation on the laser carbon fabricated in air derived from the Raman spectroscopy: (A) the G-band peak position, (B) the G-band FWHM, (C) the graphitisation via I_G/ I_D ratio, (D) the graphene layer stacking via I_{2D}/ I_G ratio,(E) the Raman spectra of the selected samples.

and further decreased with the rise of these both parameters. Indeed, such change can be observed in the detailed analysis of each individual Raman spectra from Figure 6.9E, where the ratio between these bands drops, and the FWHM significantly rises, suggesting an increase of amorphisation, and thus more significant contribution from sp_3 hybridised carbon rending the lattice more amorphous. There, D and G-bands are sharp, with the best separation in the case of the lowest fluence, namely A1. FWHM for both bands follows the general trend: they widen with an increase in the fluence, and the higher laser power improves the narrowing and the band separation. The best example was observed between samples A4 and A5, which were prepared at the same fluence but A5 with the higher power and thus exhibited the higher graphitisation. The film A1 also featured the highest intensity in the 2D-band among other air-fabricated samples, which signifies that the specimen has the highest graphitic content with the higher quantity of sp^2 fragments.

The graphitisation can be recalculated to the crystallite size with Tuinstra-Köning relation, which is typically corroborated with XRD methods [147]. However, in the studied case, the variation of crystalline sizes between XRD and Raman spectroscopy determined at 7.1 and 28.9 nm respectively. This strong difference is speculated to originate from internal stress in the film and substantial variation in crystallinity between the surface and the bulk.

Similar analysis is performed for the samples fabricated in the nitrogen assisted environment and presented in Figure 6.10. Figure 6.10A depicts D -band position located maximum at $\sim$1353 cm^{-1} , fabricated at the lowest fluence of 4.0 $J\,cm^{-2}$ at power $\sim$4 W. The position shifts to lower wavenumbers by the increase in the fluence independent from power variation and does not follow any particular trend. On the other hand, G-band centring exhibits a gradual rise towards high wavenumbers with the increase in both fluence and power, which is shown in Figure 6.10B. There, the position peaks at $\sim$1592 cm^{-1} with fluence of 7.7 $J\,cm^{-2}$ and power of $\sim$3.6 W. Figure 6.10C presents TPS on the degree of graphitisation from I_G/I_D bands ratio, where the local maximums are reached at 4.0 $J\,cm^{-2}$ fluence with powers of 2.0 W and 5.5 W, and similarly at 5.5 $J\,cm^{-2}$ with 2.0 W. Overall, the

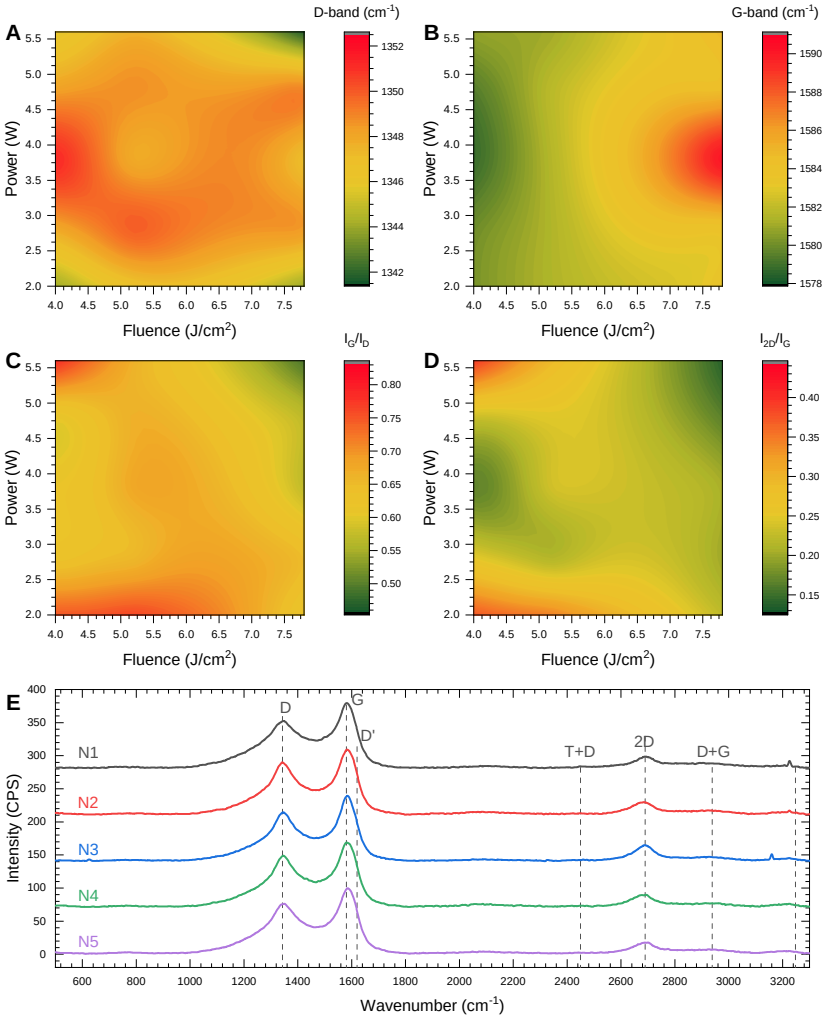

Figure 6.10: The thin-plate spline interpolation on the laser carbon fabricated under nitrogen flow derived from the Raman spectroscopy: (A) the G-band peak position, (B) the G-band FWHM, (C) the graphitisation via I_G/ I_D ratio, (D) the graphene layer stacking via I_{2D}/ I_G ratio,(E) the Raman spectra of the selected samples.

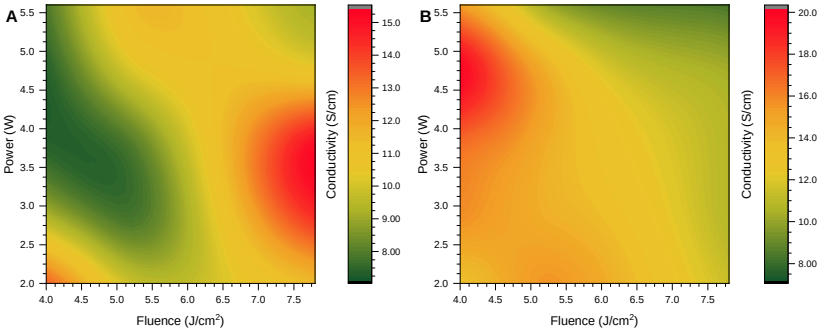

Figure 6.11: The thin-plate spline interpolation on the conductivity of the laser carbon fabricated in (A) air and (B) nitrogen.

graphitisation degree is dropped to ~ 0.8 from the air prepared samples. Matching trend is observed in I_{2D}/I_G band ratio, which is depicted in Figure 6.10D. Figure 6.10E shows five selected Raman spectra featuring significant changes from air prepared specimens. Namely, all Raman bands are widened significantly, presence of D'-band can only be estimated by the asymmetry in the G-band caused by overlapping. The intensity of combinational and the second-order 2D-band decreased significantly, and their peaks are widened.

Such radical changes are promoted by the increase of disorder and presence of higher amorphous carbon fraction on the surface within measurement beam penetration depth of $\sim$1 µm, which is uncharacteristic for specimens prepared in the inert environments. However, these changes can be promoted by inference of plume with nitrogen flow or direct removal under it.

Notably, A3 and N3 feature the narrowest bands, the highest graphitisation degrees, and the most intense 2D-bands, suggesting the best selection in the fabrication parameters independent from the working environment.

The conductivity served as principal merit in qualitative determination between fabricated specimens and their further possible utilisation. The sheet resistance was determined using the four-probe method with van der Pauw geometry (vdP) and discussed in detail in Section3.5. TPS interpolation is applied for both sets of

the working environment and depicted in Figure 6.11. Despite the same laser operation parameters, the electrical conductivity exhibit significant variation between presented TPS sets. Figure 6.11A shows the electrical conductivity improvement with fluence increase, but with the operation power rise over $\sim$3.5 W, it tends to deteriorate throughout the spline. The maximum was indicated in the set prepared using a fluence of 7.8 J cm^{-1} with electrical conductivity reaching $\sim$15 S cm^{-1}. Figure 6.11B depicts TPS for the set prepared under nitrogen flow, where on the contrary, the electrical conductivity features the gradient at lowest tested fluence at 4.0 J cm^{-1} in the operating power range between 3.5 W to 5.5 W, where it measured at $\sim$20 S cm^{-1}. However, the further fluence increase resulted in electrical conductivity deterioration, featuring the minimum of $\sim$7 S cm^{-1} at the power of 5.5 W.

From the TPSs overview, the electrical conductivity is directly proportional to surface porosity and inversely proportional to the film thickness. Therefore, the better electrical conductivity is reinforced by less porous thinner films produced at temperature range bordering to sublimation region. Despite higher generated temperature at the surface in thicker films, they undergo more rapid gas expulsion, supporting more porous morphology. Additionally, there the featured decrease in graphitisation, and sp^2 hybridised carbon ratio, induced by ablation over graphite sublimation point. Notably, the preparation under nitrogen shows a more gradual decrease in conductivity TPS, partially matching with the derived graphitisation degree from Raman spectra. Additionally, it is also influenced by the determined parameter variation from the thickness and porosity. On the other hand, the air prepared counterpart features the more abrupt variation in the electrical conductivity, supported by the involved exothermic chemical reactions assisted by the native oxygen during ablation and governed mainly by the film porosity. The observed features show a suitable correlation to the presented temperature model and provide the good guidance for optimising the fabrication parameters.

The film porosity features the variable diameters distributed across the volume, depending on the process temperature, the material expansion rate and pyrolytic transformation kinetics. Due to technical constraints, it is not straightforward to

determine features of the pores, and further studies with 3D x-ray and electron tomography can elucidate the exact volumetric morphology and help estimate the conductivity of laser carbon films. Meanwhile, the quality variation in-depth and the pore diameter distribution can be evaluated with the combination of SEM and Raman through the film cross-section.

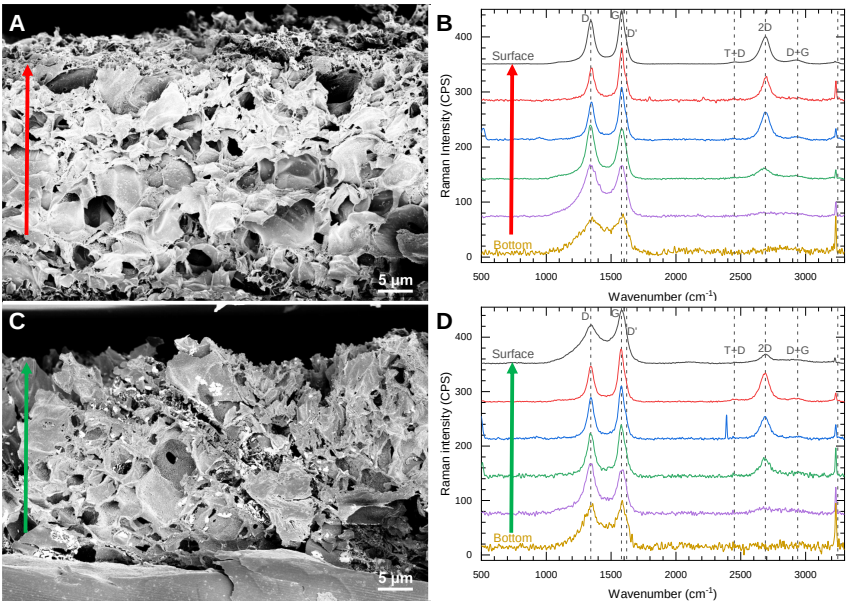

Figure 6.12: The cross-section from specimens fabricated in (A-B) air and (C-D) under nitrogen flow. (A,C) The SEM imaging; (B,D) the Raman spectra of the cross-section.

For this procedure, the samples A1 and N1 were selected, and their cross-section is presented in Figure 6.12(A & C), respectively. The micrograph from A1 shows the porosity variation from the surface-level towards the middle, featuring the biggest pore diameter, with the further decrease closer to the bottom at the Kapton interface. From these observations, one can visualise the hierarchical porosity distribution in the air-fabricated sample. On the other hand, Figure 6.12C shows the nitrogen assisted specimen, featuring a relatively uniform porosity throughout the thickness. Figure 6.12(B & D) show the Raman spectra, exhibiting the proportional increase

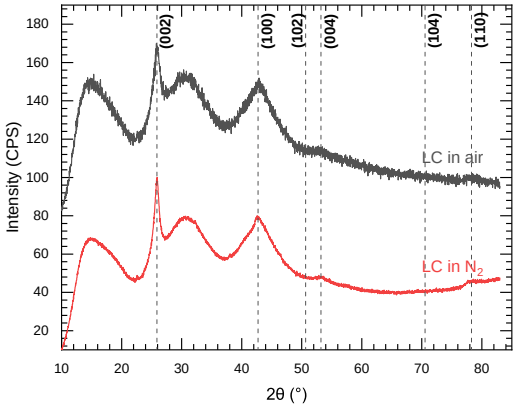

Figure 6.13: XRD reflections of the laser carbon prepared in air (black) and under nitrogen flow (red). The characteristic reflection from the F6/mmc symmetry group marked with dashed line.

of the D-band intensity, decrease in 2D-band contribution, and widening of all characteristic bands from the surface interface to bottom layer for both films. Notably, the 2D-band in N1 features stronger intensity than the counterpart along with the whole depth with the similar distance increment. The 2D-band is not detectable in the bottom $\sim$10 µm. Additionally, for both specimens, the sharp peak at $\sim$3230 cm^{-1} appeared, which can be attributed to amine stretching [198], due to the entrapped residual precursor. Generally, the Raman spectra indicate an increase in graphitic content from the laser carbon base to the top, which is drastically different for the top $<$1 µm in the nitrogen-fabricated sample. Here, the interference with nitrogen flow rendered top $<$1 µm more amorphous, with broad D and G-bands, and suppressed 2D overtone.

Considering the variation in the graphitic properties between the surface and the bulk, the XRD was performed as one of the reliable methods for averaging the crystallite sizes and measured after extracting carbon-rich material as a powder. Figure 6.13 depicts these XRD diffractograms for A1 and N1, featuring characteristic to graphitic carbon peaks discussed previously in Section 4.1.1, namely: (002) peak at 25.6° and 25.9°; (100) peak at 42.6° for both powders. The secondary

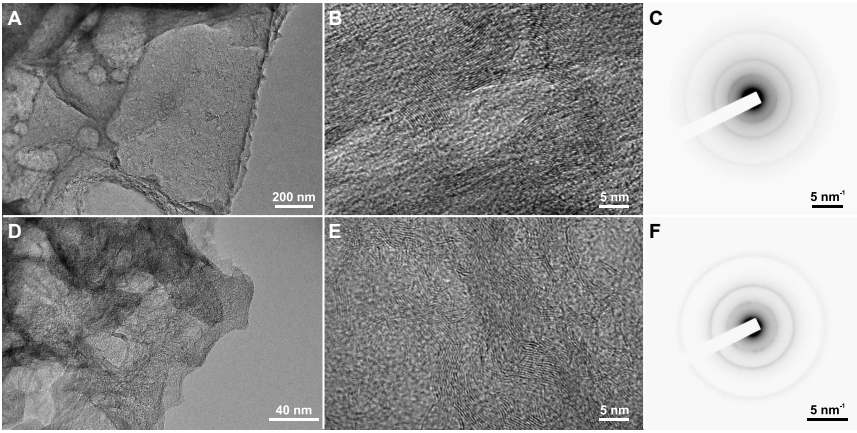

Figure 6.14: TEM micrographs and the SAED pattern of the laser carbons fabricated in (A-C) air and (D-F) nitrogen.

peaks were indicated for planes (102), (004), (104) and (110) at 50.6°, 53.2°, 70.5° and 78.3° respectively. All these reflections correspond to $P6_3/mmc$ spacegroup, characteristic for graphitic carbons [125, 126] and suggest a high degree of graphitisation with the medium-range order. Moreover, the peaks were observed in the 2θ range 10-20° and ∼30°, arising potentially from the residual Kapton impurities comparable to the diffractogram of the virgin Kapton (Section 4.2.1).

Only (002) and (004) reflections were fit with the Gaussian function for determination of crystallite sizes following the Scherer equation modified by Warren [100], and are listed in Table 6.2. The interlayer distance (d-spacing), calculated using Bragg's diffraction law, was estimated the biggest for A1 at 3.48 Å and 3.44 Å for N1. Therefore, N1 featured the lowest interlayer distance but reduced stacking size (L_c) and improvement in crystallite size (L_a) comparatively to A1. These properties suggest improvement in graphitisation in N1, going in accordance with the cross-sectional Raman analysis.

The imaging of crystallographic structure was performed via TEM for the selected A1 and N1 samples presented in Figure 6.14. Both samples feature the presence of long crumbled stacks of the graphene sheets characteristic for the polymer-

derived carbons [82]. The additional phase is present with characteristic short and randomised fragments corresponding to the amorphous carbon. Such complex phase and morphology originate from the precipitation of the carbon-rich deposits from plasma, fast pyrolysis kinetics, already rendering crystal in graphetic phase, but with some retention of poorly pyrolysed original polymer fragments. The SAED patterns indicate absence of a long-range order due to the presence of the diffusion rings corresponding to {002}, {100} and {110}, which is typical of polymer-derived carbons and is also substantiated by the XRD analysis. The SAEDs indicate the minor shape variations, particularly in N1, where {002} and {100} feature multiple shoulders, suggesting the relatively higher graphitic rendering. In the case of A1, no thick stacks of graphene layers L_c were detected despite the extensive search. On the other hand, a slightly higher stacking in occasional crystallites is observed in N1, which agrees with calculations derived from XRD.

6.1.4 Chemical Composition

During the laser-induced carbonisation, the pyrolytic transformation of polyimide rapidly raptures bonds and restructures into the griphite-like crystal structure, leaving a significant amount of residual heteroatoms within lattice volume and specifically implant new heteroatoms from the working environment due to interference at the plasma boundary. This imparts variation of the chemical properties performed by means of the combustion elemental analysis and the surface chemical composition with the x-ray photoelectron spectroscopy (XPS).
Figure 6.15 depicts the concentration variation after the elemental analysis between the selected samples in three test batches with the increase in the fluence prepared at the same power output. The carbon content of the laser carbon was higher than from the precursor after thermal pyrolysis. In both types of samples, the increase in the fluence promoted the plummeting of the carbon content, and rising of the oxygen and hydrogen contribution. As a general trend, Figure 6.15B shows the nitrogen content steadily increases with fluence. However, it attains some drop

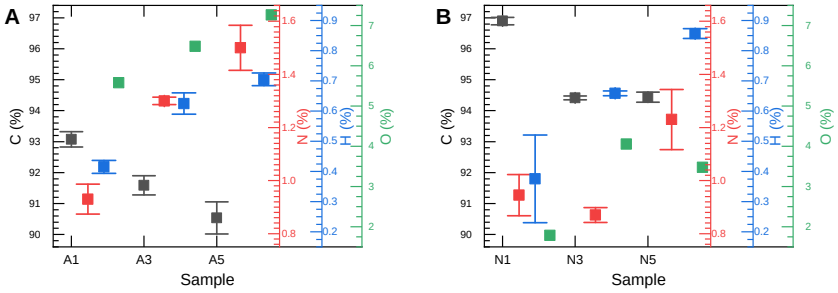

Figure 6.15: The combustion analysis from the selected specimens fabricated in (A) air and (B) nitrogen.

in nitrogen environment at 5.2 J cm^{-2}, which can be attributed to the measurement error. Notably, the total carbon content is higher than in the air-fabricated counterpart, suggesting favourable carbonisation in the inert environments.

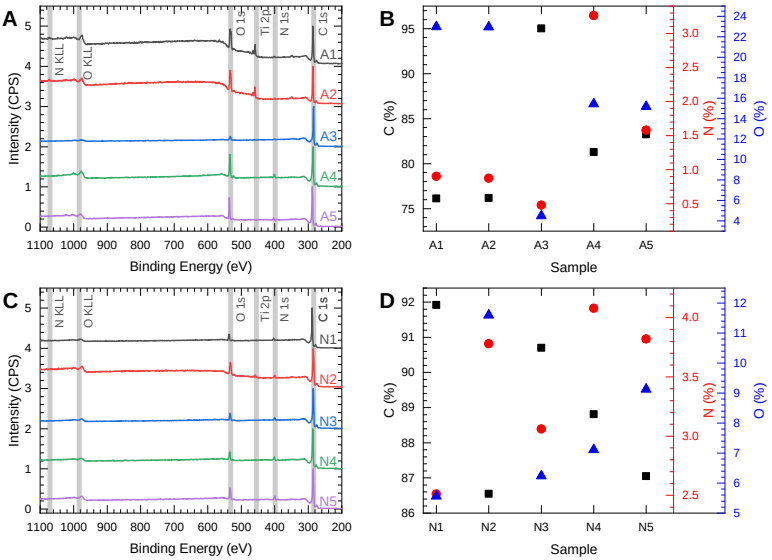

Figure 6.16: XPS survey spectra from the selected specimens fabricated in (A) air and (B) nitrogen. The derived concentration from those spectra from the samples fabricated in (C) air and (D) nitrogen.

The surface chemistry plays a significant role in determination of properties and possible conjugation for the specific utilisation. The surface composition is determined with XPS and compared between the five selected fabrication parameters, repeated in the air and nitrogen environment. The surveys are presented in Figure 6.16(A & C) with derived atomic concentration shown in Figure 6.16(B & D). Samples A1, A2 and N2 suffered some contamination from Ti 2p spectrum, originating from interference of holder, which caused some variation in C 1s and O 1s spectra. Its contribution was determined, subtracted from the total spectrum, and readjusted for the remaining elemental survey.

In air-fabricated samples depicted in Figure 6.16B, the carbon content rises with the increased fluence and the applied power within each batch. Similarly to the carbon content rise, the oxygen contribution drops for all cases, and the nitrogen significantly fluctuated due to its low contribution bordering with the machine measurement limit. Figure 6.16D shows the variation in nitrogen sample composition, where the general trends between components remain similar. Moreover, the total nitrogen yield remained fluctuating, but the contribution rose almost twofold, supporting interference with the environment and incorporation of some heteroatoms from the initiated plasma. Notably, the fabrication parameters used in A3 featured the highest carbon content, and in N3, it is detected a measurable increase in the C 1s and N 1s peaks, and a decrease in the O 1s, suggesting the favourable temperature for the best carbon yield. This result for A3 confirms with the Raman spectroscopy, where it also shows the highest graphitisation among the tested specimens.

Figure 6.17 presents the detailed XPS spectra for C 1s, N 1s and O 1s for samples fabricated in air. In all cases, all observed spectral lines were corrected using the position of adventitious carbon in C 1s peak centred at 284.5 eV. C 1s peak is deconvoluted into seven carbon-based species and fit to the measured spectrum at the following binding energies: C=C at 284.2 eV, C–C/C–H at 284.9 eV, C–N at 285.7 eV, C–O at 286.4 eV, C=O at 287.2 eV, O–C=O at 288.7 eV and a shake-up arising from aromatic rings at 290.0 eV. In previously specified cases with contribution from Ti 2p peak, the C 1s peak featured a shoulder assigned to

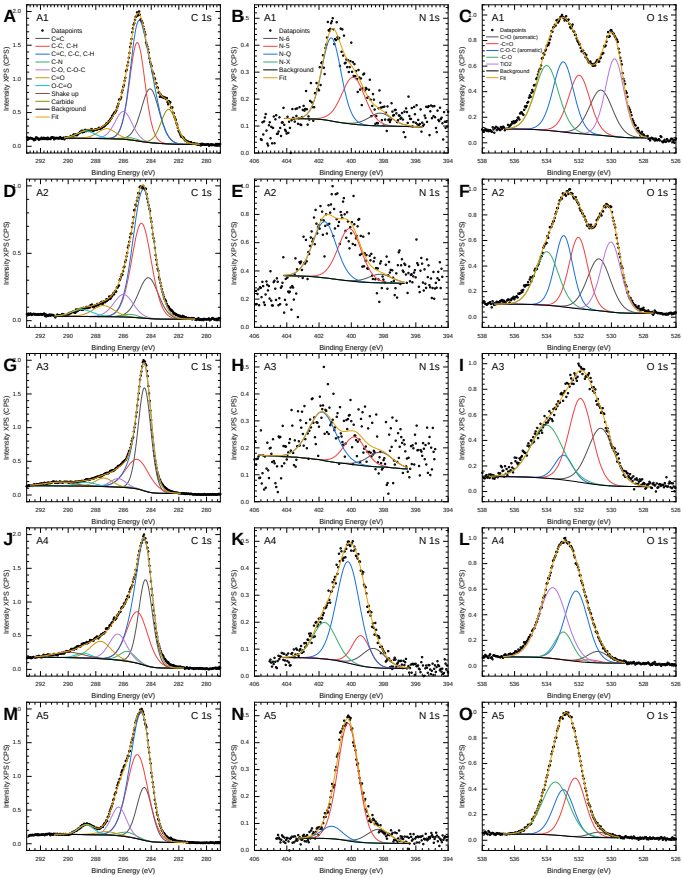

Figure 6.17: The detailed XPS spectra of five selected samples fabricated in air for (A,D,G,J,M) C 1s peak, (B,E,H,K,N) N 1s peak and (C,F,I,L,O) O 1s peak.

the carbide specie at 283 eV. N 1s peak is deconvoluted in five nitrogen-based species, namely: pyridinic (N-6) at 398.5 eV; amide at 399.6 eV; pyrrolic (N-5) at 400.1 eV; quaternary (N-Q) at 401.7 eV; and oxidic ($N-O_x$) at 404.2 eV [167–170]. O 1s spectra is fit with the five oxygen containing species, namely: the aliphatic and aromatic carbonyl species C=O at 530.7 eV and 532.1 eV respectively, amide at 531.4 eV, aromatic ether group C–O–C at 533.0 eV and hydroxyl

C−OH at 533.9 eV. All spectra featured the widening of the hydroxyl peak due to the undefined contamination from the environment. Contribution from TiO_2 at 529.8 eV was assigned in the samples influenced by Ti contamination. The results on the detailed spectra for each specie are presented in Table B1.

C 1s spectra feature narrow C=C peaks and C−C/C−H with the increased width. Additional species are presented in the abundant nitrogen and oxygen confinement. The oxygen species attained nearly equal contribution from the aliphatic and aromatic bonds and were confirmed after the deconvolution of O 1s peak. N 1s peak features asymmetry, due to the most prominent peaks attributed to N-5 and, occasionally, for N-Q, indicating the mild restructuring of the precursor imide bond by partial retention of the monomer PMDA side, promoting to occupy the edge in the graphene lattice. Notably, the specimen A3 shows narrowing of the FWHM for C=C, C−N, C−O and C=O peaks in the C 1s.

Figure 6.18 shows the detailed spectra of nitrogen-fabricated samples for same elemental peaks. The deconvolution followed under the previously established guidelines. Notably, all specimens prepared in nitrogen featured the FWHM widening, suggesting the increased amorphisation or the crystallite size reduction at the surface. C 1s peaks featured a nearly equivalent contribution from both hybridised carbon states at lower fluence (sp^2 in C=C vs sp^3 in C−C/C−H) and showed a further rise of C−C/C−H species after the increase in the fluence and the applied laser power. In pair, the oxygen confined species rose similarly. In particular, the N3 specimen showed uncharacteristic high sp^2 contribution, supporting that the selected for the preparation laser parameters favour a higher carbonisation yield on the surface, regardless of the selected working environment. There, the N 1s peak features improvement in the symmetry and centred along the single binding energy at ∼401 eV. The significant contribution was observed from the quaternary nitrogen, suggesting interference of the plume with the environment and inclusion of the ionised species into the lattice. However, only the N1 specimen showed the dominant contribution from N-5 species with a significant quantity from N-Q. The O 1s peak appears symmetrical for the majority of samples, excluding N2 suffered from TiO_2 contamination. Here, the increase in power and

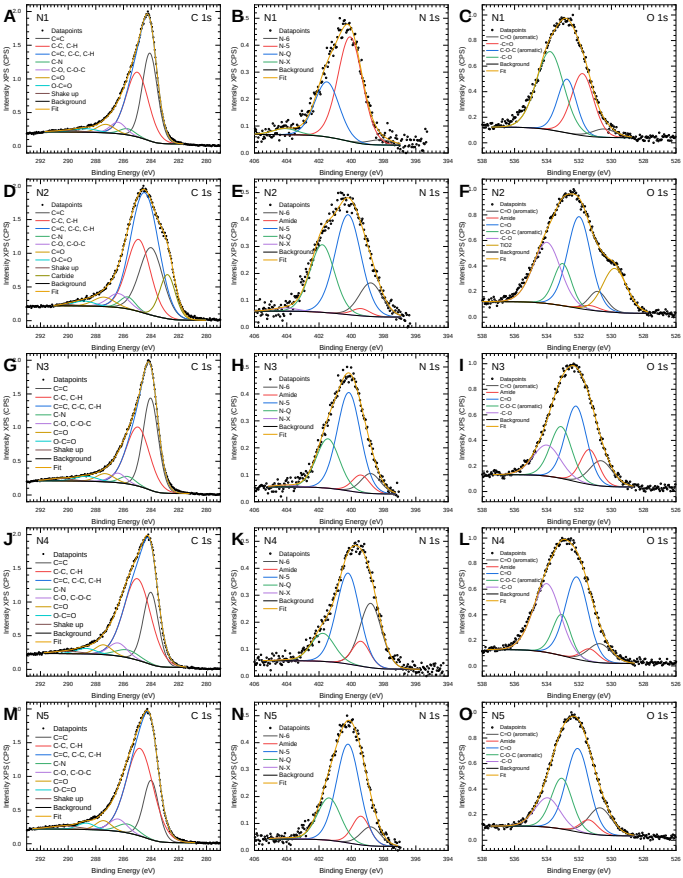

Figure 6.18: The detailed XPS spectra of 5 selected samples fabricated in nitrogen for (A,D,G,J,M) C 1s peak, (B,E,H,K,N) N 1s peak and (C,F,I,L,O) O 1s peak.

fluence promoted the redistribution of the species from the dominant hydroxyl functionality to aromatic confinement with carbonyl and ether species, having higher enthalpy. The results on the detailed spectra for each specie are presented in Table B2.

All these results suggest a strong influence of pulse on the chemical composition driven by heteroatoms entrapment from the fast kinetics of laser pyrolysis of the

beam interface with already carbonised polymer and virgin film. Additionally, the plasma discharged along the laser beam interacts with the ambient environment, providing the constant oxygen supply and promoting the exothermic reactions. Overall, the nitrogen flow reinforces a better quality carbonisation, supported by the higher carbon contribution with a decreased amount in all other heteroatoms confirmed in both combustion analysis and XPS [55].

During the initial experiments, it was observed that the laser carbon fabricated under nitrogen was rendered hydrophobic with a contact angle of $\sim$120°, while the air-fabricated carbon was hydrophilic with a the contact angle of $\sim$70°. This goes in accordance with the kinetics of the reaction, where the carbons prepared in the presence of air often carry the oxygen-rich surface functional groups. On the other hand, the introduction of nitrogen facilitates inert surroundings and limits the formation of such groups. According to the surface functionality analysis based on XPS, the nitrogen-prepared sample exhibits a higher carbon fraction on the surface compared to that prepared in the air. Among the detected functional groups, the polar ones such as hydroxyl (C–OH), aliphatic and aromatic carbonyl (C=O) and with nitrogen heteroatom (C–N) are associated with hydrophilicity, while non-polar C=C/C–C/C–H species render the material hydrophobic [205, 206]. The deconvoluted high-resolution spectra indicate that they dominate in all air-prepared samples, and the fraction of these polar groups is higher than in the samples prepared under nitrogen flow, where the non-polar groups are more abundant.

6.2 Composite Urea Biosensor

The laser carbon exhibits multiplicity and richness in the surface chemical species in addition to high graphitisation. These properties allowed the utilisation of the material in multiple thermal, environmental, chemical and biological sensors [207–209]. Here is reported the fabrication of the composite biosensor for the determination of the urea concentration. The urea plays a vital role in the metabolism in animal biology due to its function in the utilisation of excess blood

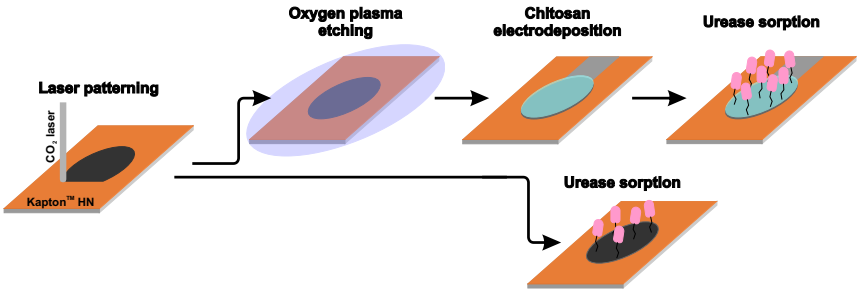

Figure 6.19: The scheme of electrodepostion direclty on LC electrode and via chitosan bed.

nitrogen. The excess of urea can cause severe damage to the body, including chronic renal failure [210], cardiovascular diseases [211], extreme fatigue [212] and cognitive dysfunction [213]. Moreover, urea is a standard fertiliser, which can lead to the reduction of crop yield in case of oversaturation and should be accurately monitored [214].

The urea concentration can be accurately determined via reaction supported by urease, namely hydrolysis into ammonia and water [215]. However, the urease retains active in the aqueous environment, thus requires a specific storage conditions. This can be achieved by chitosan electrodeposition from the solution, which forms a hydrogel film on the conductive surfaces through electrodeposition promoted by the chemical gradient at the electrode surface (Section 2.3). These films exhibit high biocompatibility and biodegradability required for such sensors. In turn, the laser carbon provides the sufficient electrical conductivity to maintain the electrodeposition, features a sufficient surface affinity for the bonding with chitosan, and also high biocompatibility. This way, the laser carbon proves to be a model substrate for such a biosensor.

The selected sample, A1, was employed in the urea biosensor fabrication. This biosensor was fabricated with the use of two possible pathways. Under the first one, the Kapton film after LIP underwent the oxygen plasma treatment for the wetting improvement, the chitosan-based hydrogel was electrodeposited from the solution, and finally, the urease enzyme was immobilised on the composite

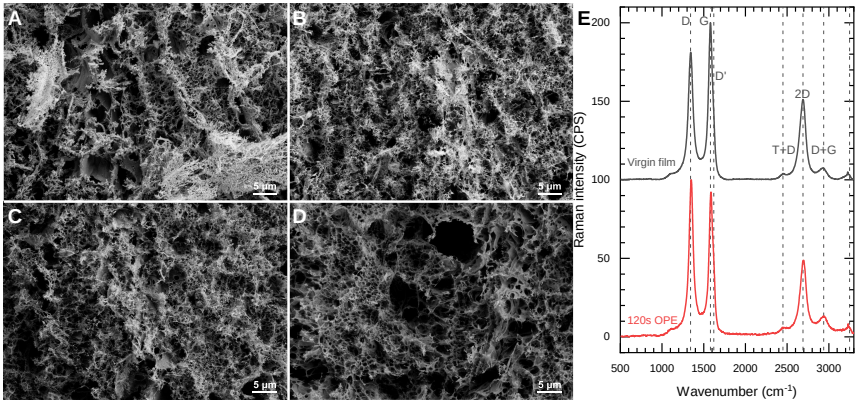

Figure 6.20: SEM micrographs of the laser carbon (A) as-prepared, and oxygen plasma treatment for: (B) 30 s, (C) 60 s and (D) 120 s. (E) Raman spectra measured from untreated film (black) and after 120 s OPT (red).

electrode surface via the linker. The contact with laser carbon was realised via silver sputtering. The second pathway included only the direct immobilisation of urease on the laser carbon due to the surface affinity. The second pathway involved the urease immobilisation directly on the laser carbon surface. In all cases, the diameter of the laser carbon electrode was kept at 8 mm.

6.2.1 Chitosan Electrodeposition on Laser Carbon

The chitosan affinity to laser carbon can be significantly improved by introducing higher quantity polar groups, including hydroxyl, carbonyl and carboxyl functionalities on the surface. This is further promoted with the oxygen plasma treatment (OPT), showing improvement in the deposition after the course consequent treatments for 30 s, 60 s and 120 s. There the surface attributed a significant change by the precipitate removal and revealing the lamella-like fragments with an increase in the OPT duration, depicted in Figure 6.20(A-D). In addition, the OPT induced the crystalline changes in the carbon, estimated with the Raman spectroscopy, presented in Figure 6.20E. There, the significant rise of the D-band and widening of the G-band was indicative of the graphitisation reduction, and

an additional improvement in the D'-band is observed, promoted by defects and C–OH/C=O vibrational modes [216]. Notably, the 2D-band suffered from the intensity reduction, which follows the reduction in graphitisation and ratio of sp^2 hybridised carbon [144]. Moreover, the treatment for 120 s retained the surface activity and extreme hydrophilicity even after a week of storage and showed the similar absorption of chitosan as for the freshly performed OPT.

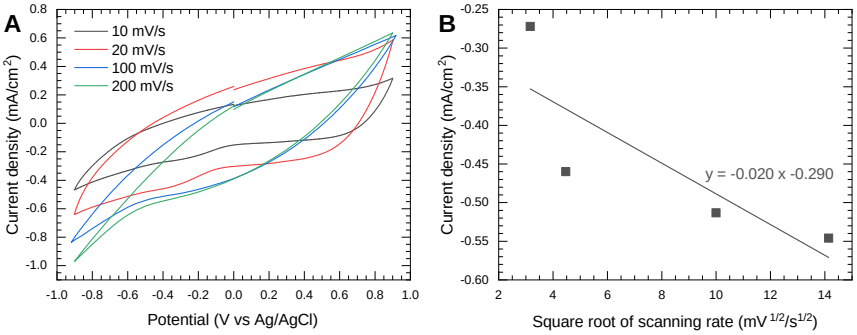

Figure 6.21: (A) Cyclic voltammograms performed in 200 mM HCl with variation of the scanning rate. (B) The reduction current density at −0.4 V on the speed of scanning rate.

The electrochemical mechanism of electrodeposition was elucidated with the cyclic voltammetry, depicted in Figure 6.21A preformed in the standard solution and by the scanning rates variation between 10 mV s^{-1} to 200 mV s^{-1}. The sweeps in reduction and oxidation regions were studied. However, chitosan electrodeposition occurs by deprotonation in the hydroxyl and the amine reactive functional groups in the pyranose ring [83, 217]. The cyclic voltammograms feature a characteristic reduction peak in the potential range −0.5 V to −0.3 V, induced by electron transfer with the formation of amine and hydrogen generation [217]. The reduction peak current decreased with the increase in the scanning rate due to uncompensated solution ohmic drop [218]. Figure 6.21B shows an increase of the reduction current proportional to the square root of the scanning rate, indicating the diffusive behaviour.

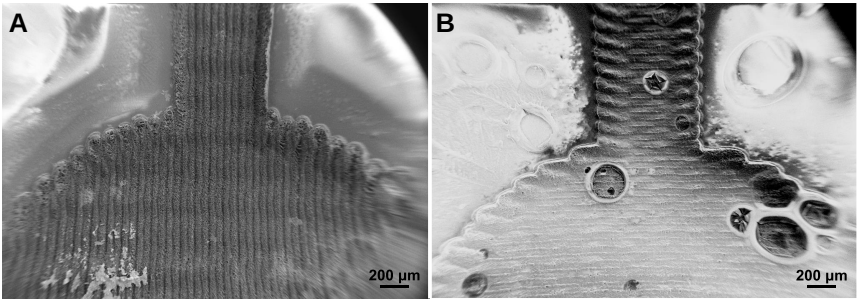

Figure 6.22: The electrodeposited chitosan on a circular carbon electrode with current applied (A) along and (B) perpendicular to the rasterization lines.

Notably, the direction of the applied electrical current along specific rasterisation lines directions played an essential role in the deposition quantity due to anisotropic resistance in the laser carbon with the lowest following the longitudinal pulse propagation. This variation can be easily observed optically and presented in Figure 6.22. There, the tracks fabricated along the rasterisation direction exhibited lower resistance to one measured in the perpendicular direction due to the lower overlapping between the pulses. However, the chitosan electrodeposition had the preferable orientation along with higher resistance for the applied current, suggesting accumulation of the higher potential on the electrodes and, therefore, the higher induced chemical potential. This was further utilised for the standard protocol.

The duration of performed electrodeposition plays the essential role in the quantity of deposited chitosan. Thus, multiple regimes were tested at 5 min, 10 min and 15 min and evaluated with the fluorescence microscopy, as depicted in Figure 6.23A. Some tests with the longer duration were performed, but the no-significant difference was observed to 15 min; thus, the latter was chosen as a standard. The SEM studies were performed after the drying overnight, and depicted in Figure 6.23(B-D) reflecting the biopolymer distribution improvement, and the surface roughness reduction, both with an the deposition time increase. Figure 6.23E displays the reference test performed using the untreated laser carbon

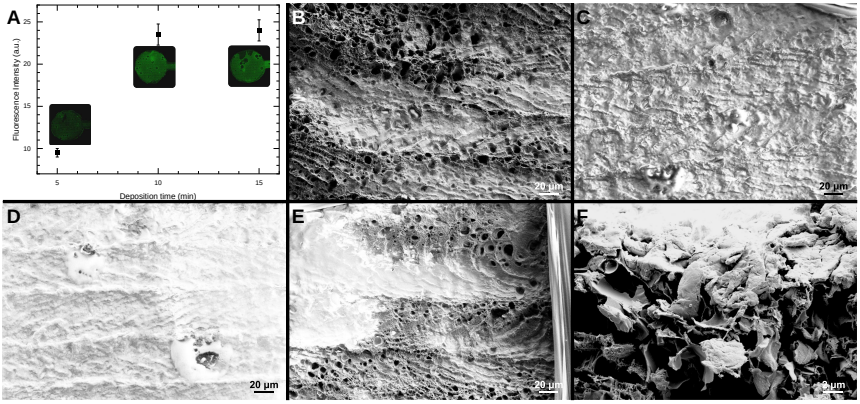

Figure 6.23: (A) The fluorescence microscopy after chitosan deposition for the selected time duration. SEM micrographs after electrodeposition performed on the electrode after OPT for (B) 5 min, (C) 10 min and (D) 15 min. (E) The electrodeposition on the untreated electrode performed for 15 min.

electrode after 15 min of the electrodeposition, which exhibited the non-uniform distribution with the reduced quantity comparable to 5 min of the deposition. The dried film thickness was determined at 2 µm, as in Figure 6.23F, thus the thickness of the hydrogel is estimated to be over 20 µm, due to its water content over 90 %. It was observed that the chitosan deposition was limited only to the carbon surface without any deposition in volume, which goes in accordance with the process kinetics.

Figure 6.24 depicts the FTIR spectrum collected after the chitosan electrodeposition on laser carbon. The spectrum features the multiple characteristic peaks and attributed to the vibrations in OH at 3415 cm^{-1}, NH at 3370 cm^{-1}, $-CH_2$ in the pyranose ring at 2920 cm^{-1}, 2880 cm^{-1}, 1480 cm^{-1}, 1320 cm^{-1}, 1270 cm^{-1} and 1250 cm^{-1}, C=O in the amide at 1650 cm^{-1}, NH_2 at 1585 cm^{-1}, OH and CH in the pyranose ring at 1420 cm^{-1} and 1320 cm^{-1} respectively, CH_3 at 1375 cm^{-1}, C=O at 1255 cm^{-1}, C–O–C in glucosidic bond in the range between 1150 and 1040 cm^{-1}, and CH_3COH at 890 cm^{-1}. All correspond to the reported values of chitosan [217, 219, 220], which proves the successful deposition onto the laser carbon surface.

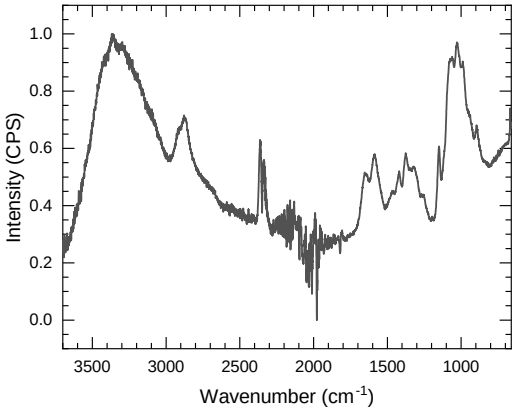

Figure 6.24: FTIR spectra collected from the chitosan deposited the laser carbon.

6.2.2 Passive Urea Biosensor

The passive urea biosensor was prepared by the Urease enzyme immobilisation on the active surface.

Two types of enzyme immobilisation schemes were tested: via the intermediate electrodeposited chitosan layer; and directly on the laser carbon surface. As the merit of the urea hydrolysis, the pH test was employed, and the activity was compared with an absolute value to a stock solution. A circular electrode, connected to a sputtered silver contact pad, was used as the electrode for chitosan electrodeposition, as depicted in Figure 6.25A. For all cases, the initial urease concentration in the solution was $1\,\mathrm{mg\,mL^{-1}}$. The adequately detect the risk limits, the device sensitivity should be at the risk limits for blood urea in humans at 1×10^{-2} M [221]; therefore the prepared devices were tested witin this limit or below. The Urease immobilisation to chitosan is performed via glutaraldehyde coupling, following standard preparation recipe [222], and the sensitivity tests with urea using this assembly is depicted in Figure 6.25B. The response for all cases shows saturation after $\sim$140 s, and the limit of detection is estimated at 1×10^{-4} M. As can be observed, within the 1×10^{-4} M to 1×10^{-1} M concentration range,

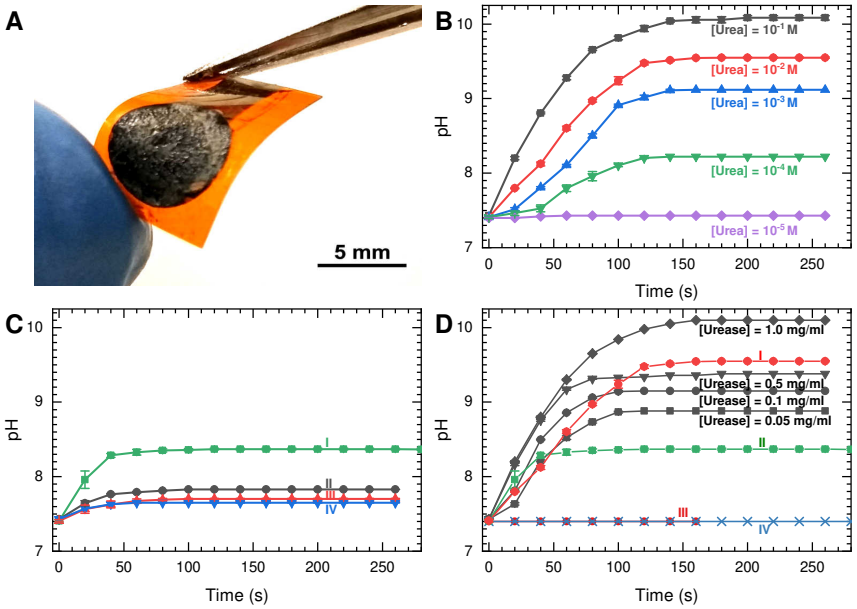

Figure 6.25: (A) The micrograph of the fabricated composite biosensor. (B) Urea detection using chitosan-urease sensors. The film was exposed to a 1 mg mL^{-1} urease solution for immobilisation and thoroughly washed before exposure to the urea solutions. (C) Urease activity on (I) the untreated carbon film, (II) coupled to glutaraldehyde; (III) after oxygen plasma treatment and (IV) coupled to glutaraldehyde; [urea] = 1×10^{-2} M in all cases. (D) Urease activity in a solution (black curves), and (I) the sensor with electrodeposited chitosan and (II) in the presence of the untreated film; (III, IV) control film, untreated with and without electrodeposited chitosan, respectively. Urea concentration is 1×10^{-2} M in all cases. All measurements were performed in triplicate, and data points report the mean $\pm$ standard deviation.[56]

the rate of urease catalysis increases with the increase in the urea concentration. Alternatively, the urease immobilisation was conducted on the laser carbon in four different ways: (I) as-fabricated film, (II) as-fabricated film with glutaraldehyde linker, (III) OPT film, and (IV) OPT film with glutaraldehyde linker. Figure 6.25C shows determined pH values in 1×10^{-2} M concentration of urea for these four cases, where the response is saturated after $\sim$40 s, and as-fabricated laser carbon film indicates the highest response.

The two best samples from each representative immobilisation schemes were tested along with the control experiments in the stock solution. Figure 6.25D depicts a comparison to the enzyme activity in the stock solution with its concentration varied to estimate the fraction of active Urease on different tested sensors. There, the urease activity showed the best for the stock solution, but the composite chitosan/laser carbon biosensor showed the best among fabricated sensors, with some reduction in the activity. This can be explained by the deactivation of the enzyme reactive sites by glutaraldehyde during electrodeposition and confinement of the reactive sites within the substrate. Nevertheless, the bare laser carbon electrode without any treatment exhibits activity but significantly reduces pH magnitude. Laser carbon obtained in both air and nitrogen can potentially facilitate enzyme absorption. From XPS, the functional groups can be recognised, but their activity towards various chemical species cannot be confirmed yet, and the mechanism of enzyme immobilisation on the untreated carbon is not clear at this point. The employment of glutaraldehyde indeed reduced the yield of catalytically active enzyme, which can be explained by: (a) glutaraldehyde undergoes self-polymerisation or facilitates protein polymerisation and thus reduces the bound active urease fraction; (b) glutaraldehyde reacts only with substrate active groups, removing both itself and potential substrate reactive sites from urease attachment; (c) the non-specific glutaraldehyde reaction with urease renders some fraction of the enzyme catalytically inactive.

The flexible Kapton substrate allowed rolling up the fabricated sensors in the catheter tube of 6 mm diameter, as depicted in Figure 6.26A. Figure 6.26B shows a comparison of the urea sensing ability of a rolled-up to a flat biosensor with the same surface area. There, the rolled-up sensor performance shows identical activity within a standard deviation. A similar structure was rolled up and fixed inside a tube, and a pH indicator paper was inserted in the forward flow direction. A 1×10^{-2} M urea solution was passed through this assembly, which turned the yellow/ green pH paper into a pink/purple colour (residence time: 50 s), confirming a basic pH caused by the hydrolysis of urea. A video of this process can be found in the online Supplementary Information (Video SI V1).

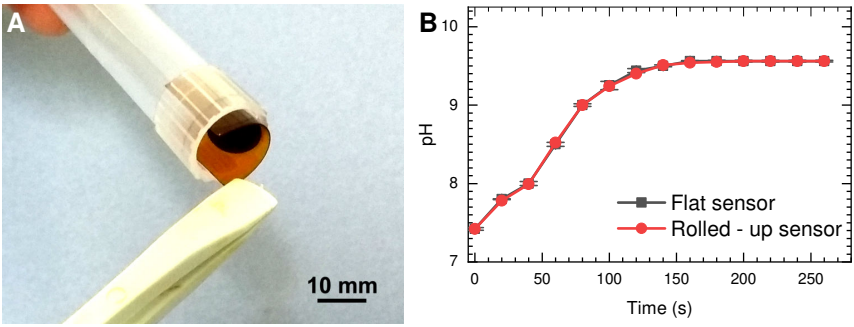

Figure 6.26: (A) The rolled biosensor in the catheter tube. (B) The activity of the flat sensor vs. rolled-up.

6.3 Summary

The implementation of extended thermal model showed correspondence with attributed combination of properties for the laser carbon film. However, the model requires further development in terms of evaluation of the film porosity and built up pressure from the precursor ablation, to further match with the experimental data. The highest matching was achieved for the nitrogen-prepared samples, promoted by inert environment. Nevertheless, the Raman spectroscopy results suggest that the nitrogen prepared samples feature a higher surface disorder, which is in line with the XPS data. However, it contradicts with the results obtained from the electrical conductivity, TEM and XRD. This can be explained by the differences in surface and bulk properties of the material. Both XPS and Raman are measured on the sample surface (10 nm nm and <1 µm deep, respectively), while other measurements are performed on bulk of the film. The alteration in the preparation environment reinforces the process kinetics difference, rendering the higher scaffold density and the carbonisation in the nitrogen prepared samples, promoting the better electrical conductivity. However, they attain hydrophobicity and smaller variety in surface chemical functionality, restraining use in the chemical sensing.

The surface properties of the laser carbon films attain number of non-polar functional groups, favourable for the physi- and chemisorption of number of functional groups specific for the chemical and biological sensors. This is utilised for the electrodeposition of the chitosan, a biocompatible, biodegradable, and non-toxic biopolymer, which provides a hydrogel matrix that mimics the cellular microenvironment. This was used as the Urease enzyme carrier for activity preservation and directed utilisation. This technology opens a pathway for the patternable bioelectrode preparation with desired properties, combining chitosan ability in hosting a number of enzymes broadly utilised in medical application and industry.

7 Laser-Induced Carbonisation of Nomex

Another low-cost precursor compatible with the laser-induced carbonisation is polyaramid utilised in the form of fibres and sheets [65, 66]. They exist in two commercial forms: known as Nomex (poly(1,3-phenylene isophthalamide)) and Kevlar (poly(para-phenylene terephthalamide)). Their chemical structure is depicted in Figure 4.5, where the backbone chain contains aromatic rings interconnected via amide and carboxyl bonds, resulting in a high tensile strength (2900–3600 MPa), a high elastic modulus (70.5–112.4 GPa), good chemical inertness (degradation only in formic acid), and a high thermal resistance (0.04–0.25 $\mathrm{W\,m^{-1}\,K^{-1}}$) [223]. All those properties facilitated widespread use in the industry and damped the price of these materials, with applications mostly focusing on personal protection against mechanical tear, high-temperature operations, and shielding in electrical circuits.

This chapter elucidates characteristic features of LIC for polyaramide Nomex, which provide a specific rendering of the laser carbon, providing flexible and bulk films. In the chapter, further exploited features to fabricate composite films with electroplated copper. The kinetics of the electroplating were analysed, and the films were studied for bulk and surface properties. These copper/laser carbon composites showed film flexibility and antibacterial properties. A variation in fabrication parameters yielded more rigid laser carbon films, which underwent electroplating and annealing, and was used as selective enzyme-free glucose sensors.

7.1 Laser Carbon Synthesis

As previously stated, the operational wavelength for LIC was selected at 10.6 µm from a semi-industrial CO_2 laser source. In order to investigate the optical absorption of Nomex, FTIR was conducted, from which the absorption coefficient was approximated by referencing a collected signal to table values of a known material (Kapton) and then using the correction coefficient for adjusting a signal for the film under investigation. Thus, the absorption coefficient at 942 cm^{-1} wavenumber is estimated of 135 cm^{-1}. There, the possible deviations can originate from such crude estimation, scattering effects on the film and during measurement, the roughness of the studied film, and more detailed study require determination of the extinction coefficient following the procedure used in Ref. [193].

Figure 7.1 shows ATR-FTIR spectrum, elucidating the characteristic bands of the Nomex sheet. Namely, the peaks assigned at 3300 cm^{-1} to N–H stretching vibrations in secondary amide, 1645 cm^{-1} to amide C=O stretching in amide, 1603 cm^{-1} to C=C stretching in aromatic ring, 1522 cm^{-1} and 1254 cm^{-1} to C–N stretching mode, 1304 cm^{-1} to aromatic C–N stretching, 775 cm^{-1} and 681 cm^{-1} to out-of plane C–H vibrations [224]. Several additional species were determined at plateau between 2970 cm^{-1} and 2840 cm^{-1} assigned to O–H stretching, at 1470 cm^{-1} to C=C aromatic stretching, at 1380 cm^{-1} to C–H rock-

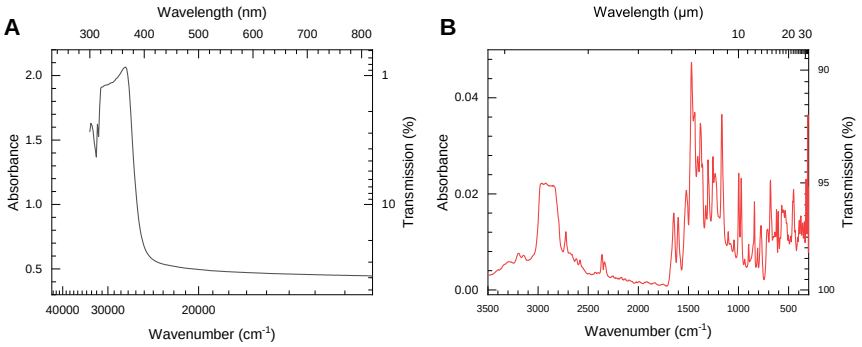

Figure 7.1: Spectral characteristics of the Nomex sheet in IR region.

ing, and 973 cm^{-1} to C–H out-of-plane bending [198]. The peaks observed at 1167 cm^{-1} and 1000 cm^{-1}, were unidentified for Nomex and originated from filler (cellulose) during manufacturing process or contamination.

7.2 Laser Carbon Synthesis with Mid-IR Laser

As for Kapton, Nomex exhibits high dissociation energy of the single monomers at ∼20 eV [65, 225], which is exceeds the delivered energy by a single mid-IR photon of ∼0.12 eV. The selected laser wavelength and the pulse duration hint at a predominant photothermal electron relaxation mechanism. During this, the temperature accumulation follows the same kinetics as in Kapton, at out-of-plane bending of C–H bonds at the aromatic ring due to their optical absorbance in the selected wavelength. The phonon vibrations further translate along the monomer backbone and initiate dissociation of the weakest bonds in the chain, C–N and C=O, located between phenolic rings [176, 226]. This initiates laser-induced carbonisation, which occurs over a threshold laser intensity of 2×10^4 W/cm^2. It is complemented with an extensive ionised plume formed above the surface, where the molecules ejected at high pressure of ∼3 GPa after dissociation and further interfered with the laser radiation [180]. This plume causes partial shielding and further absorbs the laser radiation, which can substantially contribute to the temperature accumulation above the film, and above the precursor surface it is estimated over 2000 °C [227]. Under the plume, the temperature gradient causes an immediate pyrolysis-like process, abundant of recombined graphene sheets with nitrogen and oxygen heteroatoms, inherited from process rapidness.
Due to the dominance of the photothermal mechanism during LIC, the thermal simulation was utilised and updated for the Nomex case. There, the new properties were implemented with a specific heat of 1.42 $mJ\,kg^{-1}\,K^{-1}$ and a heat conductivity of 123 $mW\,m^{-1}\,K^{-1}$, density of 880 kg/m^3 and previously estimated absorption coefficient [65, 225]. The script is presented in Appendix A-2. The transition temperature for Nomex to glassy carbon was set to 400 °C, as the mass reduction

was observed via a thermogravimetric analysis corresponding to the initiation of pyrolysis [228]. Other properties retained previously stated values.

The polyaramid fibres exhibit ablation of a significant part of the graphitised fragments under the focused laser beam [65, 66]. To counteract such effect, beam defocusing was introduced, resulting in an improvement of the electrical conductivity, mechanical stability, and adhesion of the laser carbon film to the precursor substrate [61, 65, 66]. The defocusing at 1.5 mm leads to a broadening of the minimal feature size within a single track to ∼250 µm. Molecular dynamic simulations support these observations, stating that an excessive temperature gradient causes the ablation and built-up pressure, leading to the induction of high internal stresses within the formed laser carbon, causing its cleavage [60].

Figure 7.2 shows the yielded temperatures after simulation for different beam diameters. Notably, the temperature significantly drops with an increase in the spot size radius. However, all modelled cases do not correspond to phase transition temperature to glassy carbon. This implies the limitation of a model for the phase transition, without consideration of continuous carbonisation, but approximate on the immediate process.

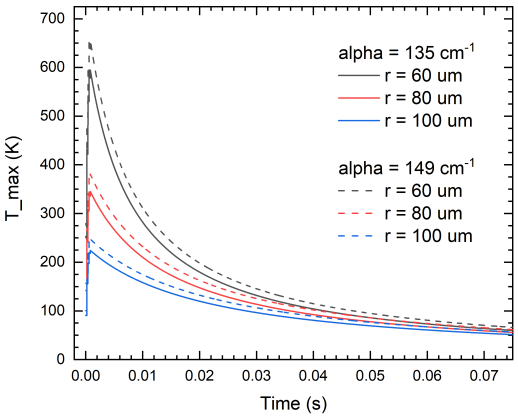

Figure 7.2: Thermal model for LIC of Nomex.

7.2.1 Operation Parameter Selection

To investigate LIC kinetics, the number of experiments were conducted by varying the laser output power and the velocity of focus carriage, thus changing the delivered fluence and pulse duration. However, only at a single fluence of $3\,\mathrm{J\,cm^{-1}}$, the laser-induced carbonisation yielded functional film. The electrical conductivity was used as a merit of quality to select the best parameter set.

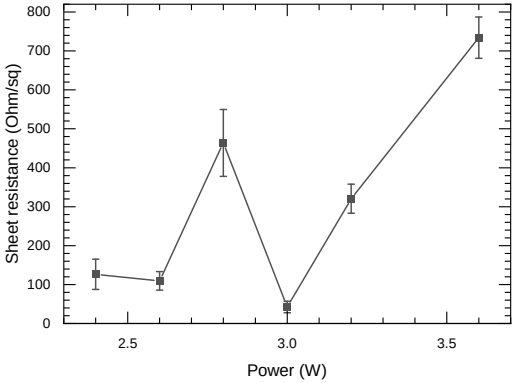

Figure 7.3: Sheet resistance after a single laser irradiation.

Figure 7.3 shows sheet resistance with a variation of the operation power. There, the lowest value was observed for a specimen fabricated at 3 W. Below 3 W the heating is not sufficient for the formation of a stable track, and above the deterioration was suggested by oxidation and a material ablation [55]. The selected power and the focus carriage speed used for patterning of this sample were the most effective. However, the film thickness is $(20.0 \pm 10.9)\,\mu\mathrm{m}$, such variation indicates a metastable laser carbon.

These considerations were taken into account for further design of the experiment with an additional laser passing was reported for an improvement in quality and a more uniform carbonisation [65, 66]. Figure 7.4 shows three selected procedures. The first procedure (LC1) utilised an initial of single irradiation of the film with 1000 pulses per inch ($\sim$25 µm a pulse distance) within rasterisation line and

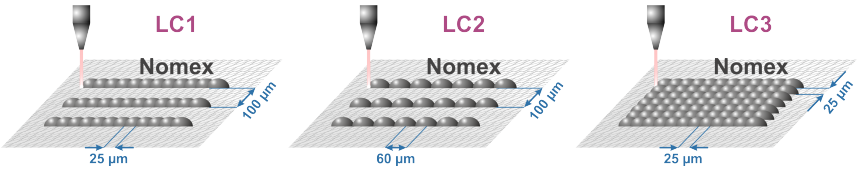

Figure 7.4: The selected fabrication procedures (dimensions not to scale).

750 PPI (∼100 µm) between the lines, for which the speed of focus carriage was kept constant at ∼13 cm s^{-1}.

The second type of laser carbon was fabricated with double irradiation (LC2). The procedure was modified by variation of PPI to 400 (∼60 µm), keeping a rasterisation distance at ∼100 µm, and during a second scan, the scanning speed was increased to 32 cm s^{-1} and PPI at 1000 (∼25 µm). Such a recipe provided initiation of the seed layer and an increase in the optical absorbance of the film at a selected laser wavelength. According to the laser manufacturer, a decreased pulse throughput (increased pulse distance) delivers higher intensity pulses and keeps the average distributed power across the line at a selected value, which results in a larger heat affected zone and improves the quality of the laser carbon. Afterwards, the second irradiation was performed with a standard pulse throughput and with an increased transition speed at 32 cm s^{-1}, inducing annealing of the film to higher graphitisation. The film thickness was determined at (28.9 ± 4.9) µm and indicates a reduction in surface roughness compared to LC1. It was reported that the double irradiation procedure could be performed at the same laser parameters [65]. However, it was found that the procedure described here is better suited for LIC of Nomex, allows faster processing and is designed for better electroplating of copper retaining flexibility of the film (Section 7.3).

The third type was performed with triple irradiation (LC3), where an interline pitch was modified to ∼25 µm during first passing, and PPI at 1000 with the distance between pulses in a line set at ∼25 µm, which provided pulse overlap around 90%. The following laser passings over the same area were repeated as for LC2, but the pulse distance was kept at ∼25 µm for remaining repetitions. The widening

of the laser heat-affected zone with a reduced temperature gradient caused the formation of carbon of higher quality. The second and third irradiation provided further annealing of the fabricated film. Notably, during the final laser pass, the expulsion of a plume had been significantly reduced compared to previous steps, which was caused by the reduction of released heteroatom confined functional groups from the polymer, and affected only by interface with oxygen from the ambient environment.

Further detailed studies were performed only on LC2 and LC3. Additionally, the films with the same fabrication parameters were replicated under the inert nitrogen flow, and their properties were studied. The details on fabrication under nitrogen flow are given in Section 2.1.

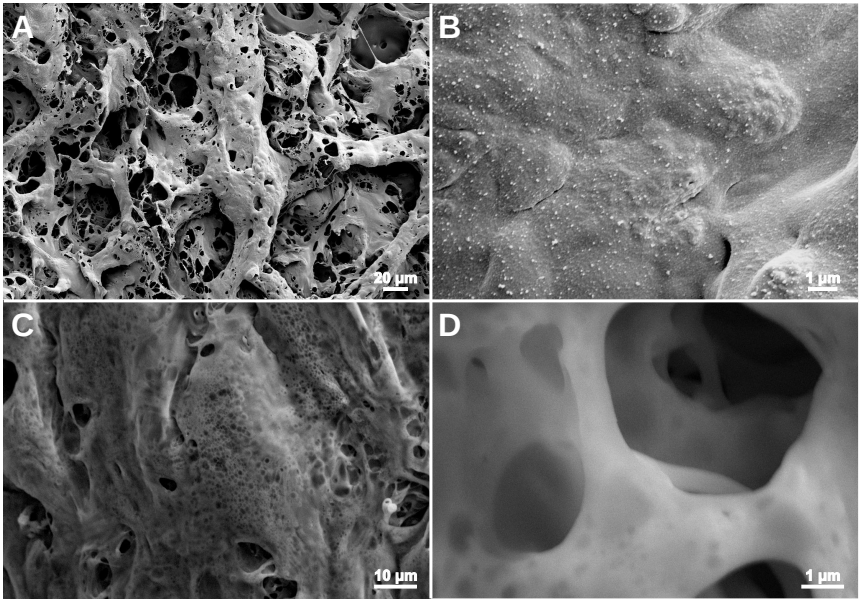

Figure 7.5: Morphology of the laser carbons using the fabrication procedures for (A-B) LC2 and (C-D) LC3.

The surface morphology shows a significant difference from the fabrication procedure. The surface of LC2 is shown in Figure 7.5(A-B) and displays a significant

porosity, ranging from hundreds of nanometer voids and wrinkles to pores of over 10 µm. The carbon surface is smooth with some charged precipitate. Figure 7.5(C-D) shows the morphology of sample LC3, which features a reduced quantity of pores larger than ∼1 µm, and an increase in the number of smaller pores ∼100 nm. The reduced interline distance between tracks induces higher localised temperature, which promotes better graphitisation and improves absorbance coefficient over precursor. This causes an increase in temperature accumulation during the repetition of the laser passing, which results in partial ablation of the interface carbon layers, exposing deeper microstructure with characteristic lower pore distribution [56].

Notably, the specific surface area, examined with gas sorption, confirms the reduction of the pore distribution in bulk LC3, from 117 m^2/g for LC2 to 71 m^2/g. As it was previously observed and discussed in Section 6.1.3, such reduction of the porosity affects the bulk properties of the film and results in an increase of the electrical conductivity, determined at $(5.4 \pm 0.9)\,S\,cm^{-1}$ and $(45.2 \pm 10.7)\,S\,cm^{-1}$ for LC2 and LC3 respectively.

The surface morphology features significant change after fabrication under nitrogen flow. Due to the expulsion of decomposed volatile material, the applied nitrogen flow additionally erodes the laser carbon in both recipes. LC2 film is depicted in Figure 7.6(A-B) and attributes the reduction in the surface smoothness with an increase of the reabsorbed volatile precipitate. The film features less uniform coverage with characteristic protrusions along the laser pulse irradiations, with a majority of the laser carbon formed along the edges of the heat-affected zone. On the other hand, LC3 attributes a high resemblance to the air fabricated counterpart, as it is seen in Figure 7.6(C-D). However, the alignment along the rasterisation lines is slightly corrupted, thus rendering the film rougher. The mesoporous structure below 100 nm is no longer observable, suggesting an effect promoted by a change of the working environment.

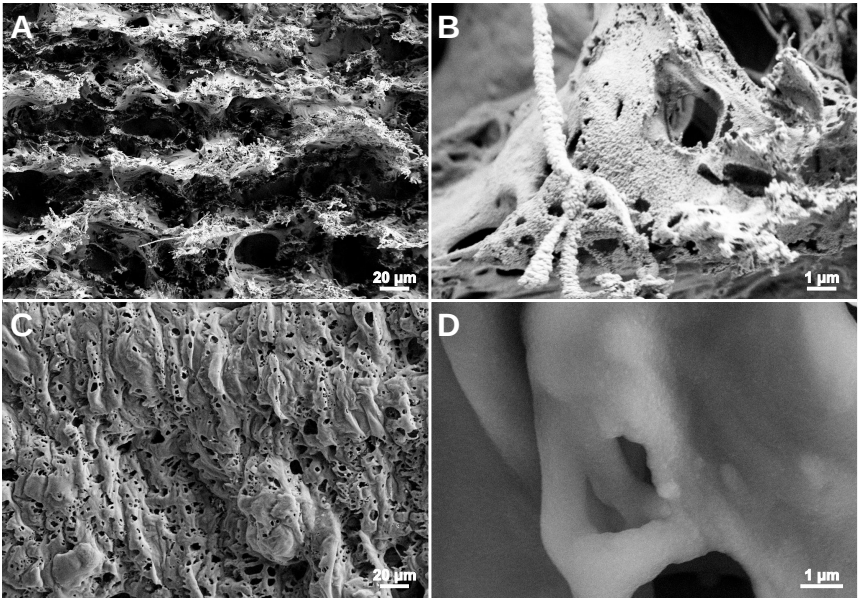

Figure 7.6: Morphology of the laser carbon after introduction of the nitrogen flow on (A-B) LC2 and (C-D) LC3.

7.2.2 Chemical Composition

LIC significantly differs from standard C-MEMS pyrolysis in their surface and bulk properties. Notably, the interference with an ambient environment influences variation in the chemical composition [55, 56]. It was studied with the combustion analysis for the determination of the bulk content and with XPS to observe the surface functionality.

The combustion analysis was performed after extraction of the powders, and the results are presented in Table 7.1. Both types of laser carbon feature significantly higher contribution from carbon than pyrolytic Nomex, confirming a significantly higher fabrication temperature with the removal of other heteroatoms from the lattice. However, despite a higher laser throughput during fabrication of LC3, it exhibits a lower carbon quantity with increased contribution from oxygen and

Table 7.1: Chemical properties of laser carbons LC2 and LC3.

		LC2	LC3
Elemental analysis, wt.%	C	97.25 ± 0.40	90.24 ± 0.06
	H	0.30 ± 0.03	0.39 ± 0.04
	N	0.94 ± 0.06	1.77 ± 0.06
	O	1.52	7.60
Contact angle, degree		60.5 ± 3.6	156.2 ± 4.0

Table 7.2: Determined surface elemental composition from an XPS survey.

		LC3 in air	LC3 in N_2
XPS, at. %	C 1s	89.46	96.75
	N 1s	4.56	0.29
	O 1s	5.98	2.96

nitrogen heteroatoms in the lattice comparatively to LC2. Such discrepancy can be attributed to the reduced interline distance by increased quality throughput determined in the machine settings during the fabrication of LC3. There, a single pulse delivers smaller intensity with the same average power along with the unit distance. Notably, the fabrication of LC2 was performed with a longer distance between pulses. Thus a higher single pulse intensity is delivered, converting a significant part to carbon. LIC renders LC3 more uniformly, whereas LC2 features islands with higher graphitic content but lacking integrity throughout the film.
Due to these factors, the LC2 was observed to be protruded through the film, partially exposing the opposite side of the film, constraining the determination of surface chemistry with contaminants originating from the acrylic adhesive. Therefore, a variation of the surface functional groups was further investigated with XPS for LC3 films prepared in air and nitrogen working environments.

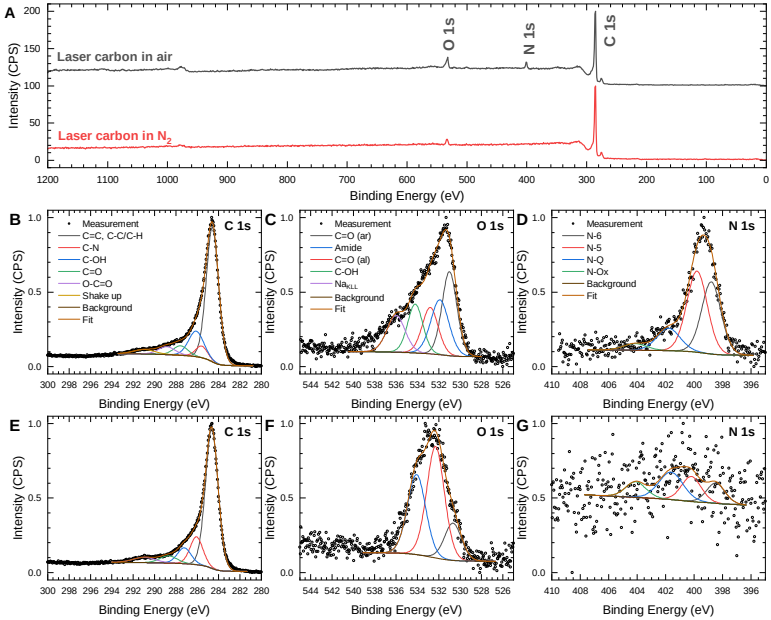

Figure 7.7: XPS survey of LC3 fabricated in air and N_2 (top to bottom). The high-resolution spectra collected from (B,E) C 1s, (C,F) O 1s and (D,G) N 1s peaks.

The survey spectra from LC3 is shown in Figure 7.7A, and the derived elemental composition is presented in Table 7.2. Both spectra contain observable peaks of C 1s, N 1s and O 1s, with a minor contribution of Na 1s and Auger Na_{KLL} in air, origination from residual components used in Nomex manufacturing. An introduction of the nitrogen flow during fabrication notably improves the laser carbon quality, observed with an increase in C 1s content and a reduction of both remaining elements. Despite saturation with nitrogen in the processing chamber, interference and incorporation in the lattice of ionised radicals did not occur, promoting a film erosion to deeper, more graphitic layers.

The detailed spectra for C 1s, O 1s and N 1s, are shown in Figure 7.7B-G, deconvoluted into several species and presented in Table C1. Figure 7.7(B,E) depicts the C 1s peak, which is centred at 284.4 eV and features a strong asym-

metry, due to the occurrence of a tail originating from the additional functional species. There, five carbon-based species were assigned with corresponding binding energies: C=C/C–C/C–C at 284.6 eV, nitrile (C–N) at 285.6 eV, hydroxyl (C–OH) at 286.1 eV, carbonyl (C=O) at 287.4 eV and shake up from aromatic rings 291.0 eV [165, 166, 171, 172]. Particularly, the LC3 in nitrogen exhibit the slight increase in contribution of C=C/C–C/C–C specie and shake up, corresponding to higher the graphitisation. Other species attribute reduction as confirms from the survey data. Figure 7.7(C,F) shows O 1s from LC3 fabricated in the air and N_2, where both feature the non-symmetrical peaks. Each spectrum was deconvoluted into three major species, namely: aromatic carbonyl (C=O) at 530.9 eV, aliphatic carbonyl at 532.3 eV and hydroxyl (C–OH) at 534.1 eV [173]. Notably, the O 1s peak for LC3 in the air suffers from widening and asymmetry. It required additional fit with amide species at 531.0 eV supported from deconvolution of N 1s. The widening contributed from additional interference with Auger Na_{KLL}. Additionally, for all specimens, the widening of the hydroxyl spectral line and tailing with higher binding energy was caused by contamination of the undefined species originating from the environment and sample handling. The high-resolution spectra collected from the N 1s peak depict on Figure 7.7(D,G) feature four species in each specimen, namely: pyridinic nitrogen (N-6) at 398.6 eV, pyrrolic nitrogen (N-5) at 400.0 eV, quaternary (graphitic) nitrogen (N-Q) at 401.7 eV, as well as a minor contribution from oxidised nitrogen ($N\text{-}O_x$) at 404.1 eV. The detailed spectrum cannot be precisely deconvoluted in the nitrogen prepared LC3 due to the minor total contribution from the N 1s peak and a low signal-to-noise ratio.
As it is previously estimated, the bulk and surface chemical composition exhibit relatively close values for carbon content, with a significant rise in nitrogen on the surface and some increase of oxygen in bulk. The nitrogen rise is speculated by exothermic reaction with oxygen from the environment during fabrication and confirmed by the presence of amide specie. Furthermore, the selectivity of this reaction is underpinned by the introduction of the inert environment, improving the carbon content and reducing contribution from other species.

7.2.3 Crystalline Properties

LIC features localised heating with a short pulse duration, which drives the crystallisation considerably different from the thermal pyrolysis. At the focal spot, as the simulations show, the temperature gradient sufficient for the sublimation of the graphitic carbon and the adjacent heat-affected zone reaches graphitising regime [18]. However, the short duration of such heating affects the crystallisation kinetics, rendering the crystallites with variable size and orientation. Thus, a detailed investigation on the crystalline structure is conducted by means of the Raman spectroscopy, the x-ray diffractometry, and the transmission electron microscopy on the selected LC2 and LC3 samples.

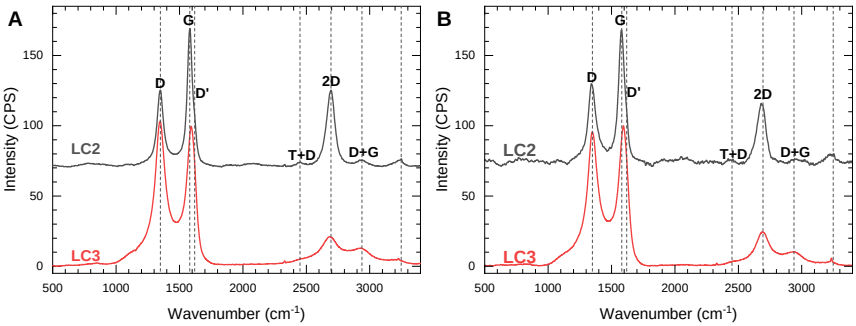

Figure 7.8: The Raman spectra (A) at the various irradiation; (B) under nitrogen flow.

Table 7.3: Peak position, FWHM of Raman bands and calculated areal band ratio (I_G/I_D) and hybridisation ratio (I_{2D}/I_G).

	D-band		G-band		2D-band		I_G/I_D	I_{2D}/I_G
	Position, cm^{-1}	FWHM, cm^{-1}	Position, cm^{-1}	FWHM, cm^{-1}	Position, cm^{-1}	FWHM, cm^{-1}		
Fabricated in air								
LC2	1348	57.5	1582	48.4	2695	69.6	1.55	0.55
LC3	1348	111.5	1593	74.7	2685	162.6	0.67	0.21
Fabricated in N_2								
LC2	1342	67.7	1578	54.0	2680	68.9	1.37	0.46
LC3	1349	116.4	1595	77.8	2690	130.8	0.73	0.24

Raman spectra were collected from the laser carbons and shown in Figure 7.8, featuring characteristic carbon peaks observed at $\sim$1345 cm^{-1}, $\sim$1580 cm^{-1} and $\sim$2690 cm^{-1}, assigned to the D, G and 2D bands, confirming polymer conversion to carbon, as discussed in detail in Section 4.1.1. Moreover, the 2D-band arise from a second-order overtone originating from sp^2 hybridisation in the carbon-lattice [145], ergo indicates significantly higher graphitisation comparatively to the standard pyrolysed reference. This 2D-band prominently contributed to the spectrum of LC2 and, to a less extent, on LC3, independent of the working environments. Moreover, the laser carbon were indexed with some additional observable peaks at $\sim$1620 cm^{-1}, $\sim$2450 cm^{-1}, $\sim$2935 cm^{-1} and $\sim$3250 cm^{-1} corresponding to the D', T+D, D+G and 2D' bands [69]. The band position, FWHM were extracted from the spectrum, with these results is shown in Table 7.3. The bands are not centred at a specific wavenumber but show some variance, corresponding to a variation in sp^3 to sp^3 ratio in the samples and the crystallite size, dependent on the selected preparation procedure. Raman shift towards $\sim$1600 cm^{-1} attributes fragmentation of the lattice to nanocrystalline graphite [144, 147, 204]. This features for both LC3 samples, as well as a widening of the FWHM comparatively to LC2. There, LC2 was fabricated with higher delivered power of a single irradiation event with a wider distance between the pulses, which promoted rapid annealing by discontinuously separating highly graphitised islands from each other. This was further confirmed by the derived I_G/I_D areal ratios, which indicated higher values in LC2. Moreover, the I_{2D}/I_G intensity ratio was used to estimate the ratio between hybridised states for both samples, where LC2 indicated the highest values typically discussed as a multilayer graphene lattice [133].
In the fabrication of LC3, the pulse distance was reduced to $\sim$25 µm, which decreased the delivered power for a single pulse, but featured continuity between the heat affected regions. After transformation of the precursor into the carbon-rich film, the thermal conductivity increases to $\sim$0.7 W m^{-1} K^{-1} [229], which provides a faster heat distribution with an incoming pulse and thus more uniform annealing during further laser passings. This supports complete material transformation from the precursor and features a higher conductivity. However, Raman spectra featured

a D-band intensity increase, a shift of 2D overtone, which can be attributed to disorder in the hexagonal lattice by heteroatoms or to a formation of the rhombohedral lattice confirming in pair rise of D+G combinational peak [126, 127].
Notably, the change of the working environment to nitrogen caused a slight widening of D and G bands. In both samples, FWHM of 2D-band indicated narrowing, facilitated by improvement in sp^2-hybridised crystallites [144, 204]. However, a decrease in the band ratios is exhibited for LC2, suggesting interference with N_2 flow resulting in a decrease of the crystallite sizes. On the other hand, LC3 features improvement in both band ratios, suggesting interference of the oxygen from the air in the laser carbon formation and erosion to the deeper layers with slightly higher graphitisation unaffected by surface chemical reactions.

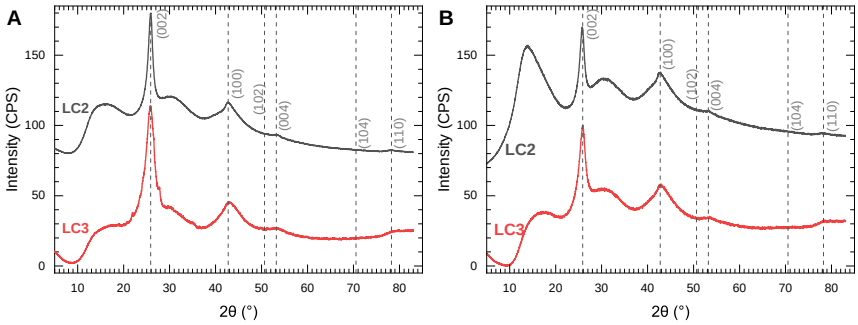

Figure 7.9: XRD reflections at the various irradiation procedures fabricated in (A) air and (B) under nitrogen flow.

Table 7.4: Crystallographic values derived from XRD on the laser carbons.

	Crystallite size (L_A), nm	Stacking thickness (L_C), nm	Interlayer distance, Å	Conductivity, S/cm^2
Fabricated in air				
LC2	3.8	7.0	3.45	5.4 ± 1.1
LC3	4.3	5.6	3.45	45.2 ± 10.7
Fabricated in Nitrogen				
LC2	3.7	7.8	3.46	5.4 ± 0.9
LC3	3.5	5.8	3.45	25.4 ± 2.1

In order to support previous observations and create a complete model including the bulk crystalline structure, the x-ray diffractometry from the powder was performed, and it is shown in Figure 7.9. The diffractograms feature several prominent peaks for all specimens at 25.8°, 43.0°, ∼53° and ∼78° corresponding to (002), (100), (004) and (110) reflections, characteristic for carbon-based materials according to the space-group #173 $P6_3$ [128, 136–138]. The collected reflections were derived to determine the crystallite sizes and the interlayer distances using Scherrer's equation [99] and Bragg's law [96] respectively, which were listed in Table 7.4. The diffractograms additionally feature reflections at ∼16° and ∼30° with a characteristic wide FWHM, originating from the untransformed polymer residue incorporated within the lattice. These peaks have shifted from the original indexing in Nomex, suggesting an expansion between fibres and shrinkage along the backbone chains due to polymer degradation and the preliminary stages of the carbonisation. LC2 was observed to be less graphitised in bulk, contradicting derived ratios from Raman spectroscopy due to its limitation solely to the interface layers. LC3 specimens feature a reduction of the stacking thickness (L_C) and the elongation of the crystallite size (L_A), providing extension of the graphene sheets with a lower number of stacked layers, confirmed by an improvement in the bulk electrical conductivity. Particularly, the samples fabricated under nitrogen attain improvement in the stacking thickness but narrow the crystallite size. Such an effect suggests the interference with the nitrogen flow and reduction of the delivered laser intensity due to attenuation of the radiation after passing through the BaF_2 window.

Nonetheless, the bulk properties of LC3 show the higher conductivity, not significantly different from LC2 in the observed x-ray diffractometry and the chemical composition. LC3 samples were released from the polymer film, and XRD was performed on a free-standing film, showing significantly different diffractogram as it is shown in Figure 7.10A. There, it exhibited a narrower (002) plane reflection with the highest peak and reduced intensity in the (100) reflection. After magnification on this region, the diffractogram shows splitting into two peaks at 42.9° and 46.4°, which can be indexed for two graphitic phases, corresponding

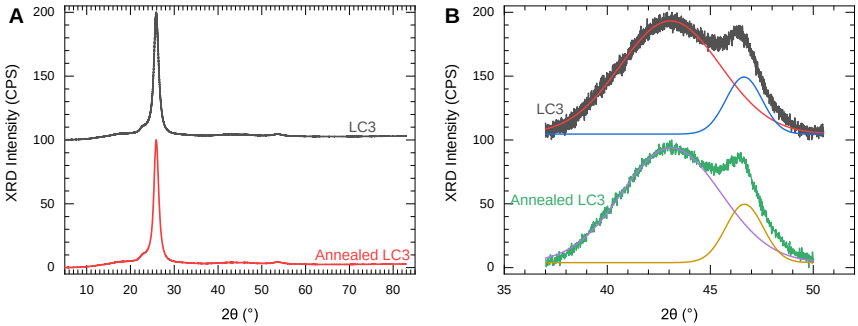

Figure 7.10: XRD reflections from (A) LC3 film and (B) magnification at (10) plane region.

Table 7.5: Deconvolution of the XRD reflections and conductivity measurement from LC3 before and after annealing at 1300 °C in argon.

		Before annealing	After annealing
$(100)_H$	Peak position, °	43.06	43.11
	Interlayer distance, Å	2.10	2.10
	Crystalline size, nm	3.6	3.62
$(110)_R$	Peak position, °	46.64	46.66
	Interlayer distance, Å	1.95	1.95
	Crystalline size, nm	10.09	9.76
Conductivity, $S\,cm^{-1}$		45.22 ± 10.68	20.34 ± 4.92

to the hexagonal $(100)_H$ and to the rhombohedral graphite phase at $(110)_R$ plane according to a space-group $R\bar{3}m$ [140, 230] with crystallite size along the plane calculated at 10 nm. The rhombohedral phase is metastable, and it was observed a phase transition to hexagonal after annealing over 1300 °C for 4 h [134]. The heat treatment was replicated at 1300 °C under argon flow ($\sim$0.8 L/min) for 1 h with a heating rate of 5 °C min^{-1}. The collected XRD diffractogram after annealing is presented in Figure 7.10B. The changes before and after annealing are presented in

Table 7.5, which indicated a slight decrease in crystallite size along $(110)_R$ plane and an increase in $(100)_H$ plane, with a significant reduction of the conductivity to $(20.34 \pm 4.92)\,S\,cm^{-1}$, suggesting initiation of a phase transition to the hexagonal lattice, but hindered by a short duration of the process and annealing only at the phase transition boundary temperature.

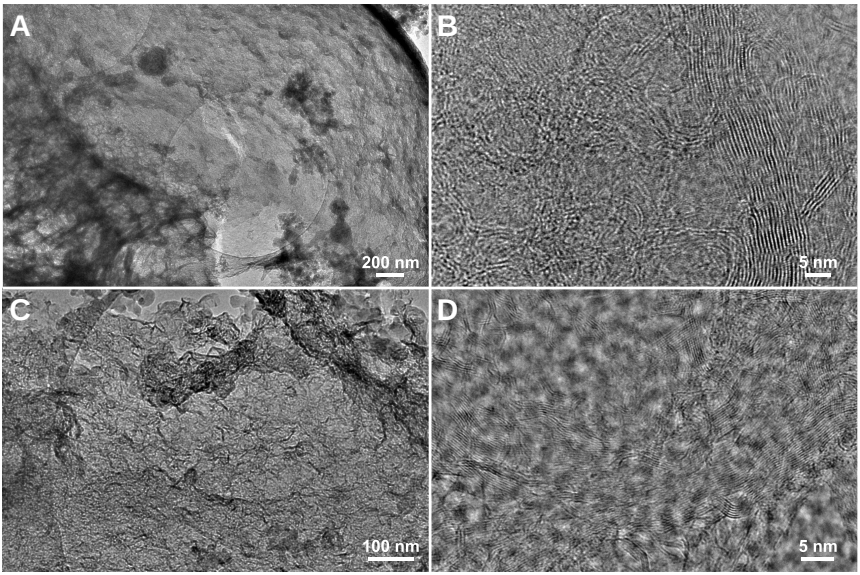

Figure 7.11: TEM imaging of LC2 from Nomex fabricated in (A-B) air and (C-D) under nitrogen flow.

The further crystallographic properties were elucidated with transmission electron microscopy and allowed direct imaging of the lattice planes with the selected area electron diffraction in areas of interest. Figure 7.11 depicts LC2 prepared in the air and the nitrogen. Both laser carbon samples attain a significant number of pores and voids throughout the volume ranging from tens of nanometers to microns, matching the surface morphology, as it is seen in Figure 7.11(A & C). The high magnification images are presented in Figure 7.11(B & D), indicating a mixture of the crumbled long graphene sheets and the short randomly oriented crystallites.

These observations suggest the presence of glassy carbon and amorphous carbon states, agreeing with the previous observations on laser carbon derived from Kapton. Notably, the samples fabricated under nitrogen flow indicate an increase in the crystallite length and the reduction of the stacking thickness, which agrees with XRD data.

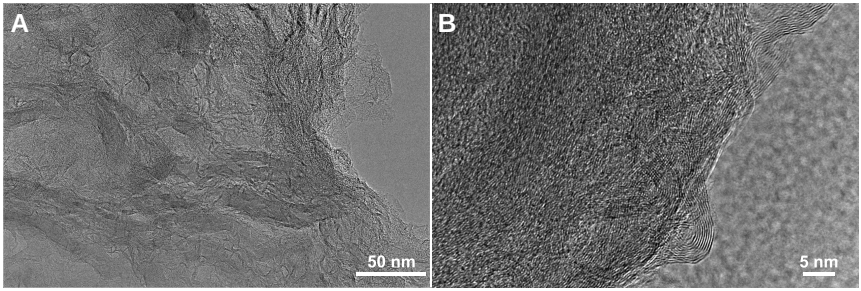

Figure 7.12: TEM imaging of LC3 from Nomex fabricated in (A) high and (B) low magnification.

Figure 7.12 shows TEM imaging from LC3 fabricated in air. A low magnification imaging suggests a reduction of the internal porosity limited to the pore size <100 nm, which matches with surface observations. Moreover, this sample exhibits a significant shift in the fraction of the oriented long crystallites, corresponding to the improved graphitic phase and lower contribution from the amorphous state, as it is seen with high resolution in Figure 7.12B.

The aforementioned samples were analysed with SAED, which is shown in Figure 7.13, indicating the presence of the diffused concentric rings due to the medium-range order without any specified crystal orientation. Notably, Figure 7.13C shows LC3 film, indicating the lower dispersion in the rings and the presence of the high-order reflections, further supporting the better crystallinity than LC2. All SAED are deconvoluted, normalised along {100} the family of planes and presented as the intensity profiles in Figure 7.13D with indexing to the respective family of planes. There, both LC2 samples exhibit the strong reflections along {002}, {100}, {004} and {110} family of planes. The laser carbons have sharper intensity than the pyrolytic reference for {002} peak and the better

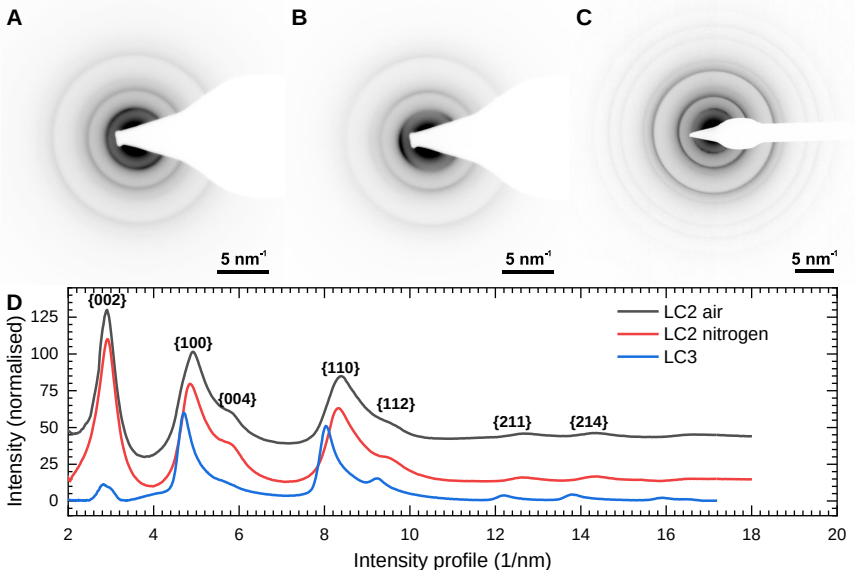

Figure 7.13: SAED collected from LC2 fabricated in (A) air and (B) under nitrogen flow. (C) SAED of LC3. (D) The intensity profile derived from all SEADs.

visibility of the {004} peak, suggesting the thicker packing of graphitic sheets and slightly sharper {100} and {110} peaks indicating more extended graphene sheets. The nitrogen assisted LC exhibited a slightly better graphitic order in all directions, which was corroborated with Raman spectra and XRD. Such improvements may be attributed to the inertness and different thermal conductivity of the nitrogen environment (26.0 $mW\,m^{-1}\,K^{-1}$) vs air (26.4 $mW\,m^{-1}\,K^{-1}$), causing a reduction of heat dissipation which allows reaching higher temperatures on the surface than when compared to an air environment [56]. In part, LC3 additionally features reflections in {112}, {211} and {214} with some suppression in {002} and {004} due to observed further elongation of the crystallites and presence of a higher quantity of graphite-like carbon.

7.3 Copper Electroplating

The electrochemical deposition (electroplating) of metals is a widely employed method for the directed delivery from metal ion electrolytes on the conductive substrates. Electroplating allows the well-defined distribution of the material quantity, matching with modern environmental preservation goals and reducing the carbon input. However, the substrate materials should meet requirements in good electrical conductivity and adhesion to the delivered material, for which the carbon films were fabricated with LIC attribute favourable properties. Copper was selected for electroplating as one of the broadly used materials, which found multiple applications in the industry, microelectronics, radio transmission, sensor material and antibacterial coatings. The fabricated laser carbon attains favourable specifications for the adhesion of the copper ions from the electrolyte.
Such electroplated composite material opens the new possibilities in a direct fabrication on the customised polymer surfaces for smart textiles and flexible sensors. The section discusses mechanisms involved in the electroplating by means of CV and XPS; the quality of the films was assessed with the XRD and the four-probe van der Pauw conductivity tests, the retention of this property was analysed after a number of bending tests.

7.3.1 Electrochemical Characterisation of Deposition

Cu electroplating is a redox reaction where the oxidation takes place at the anode with simultaneous reduction of the cathode, which leads to the deposition of a Cu layer on the precursor material. To overcome the potential difference of the reaction, an external current is provided. The presence of heteroatoms in the graphene sheets bolster charge accumulation at their site, in the case of both oxygen and nitrogen conjugated species [231]. The site provides a higher negative potential following the Allen electronegativity scale comparatively to carbon, thus inducing preferable oxidation of Cu ions during electroplating and passivating the heteroatom charge. Therefore, the experiments were conducted on LC2 and

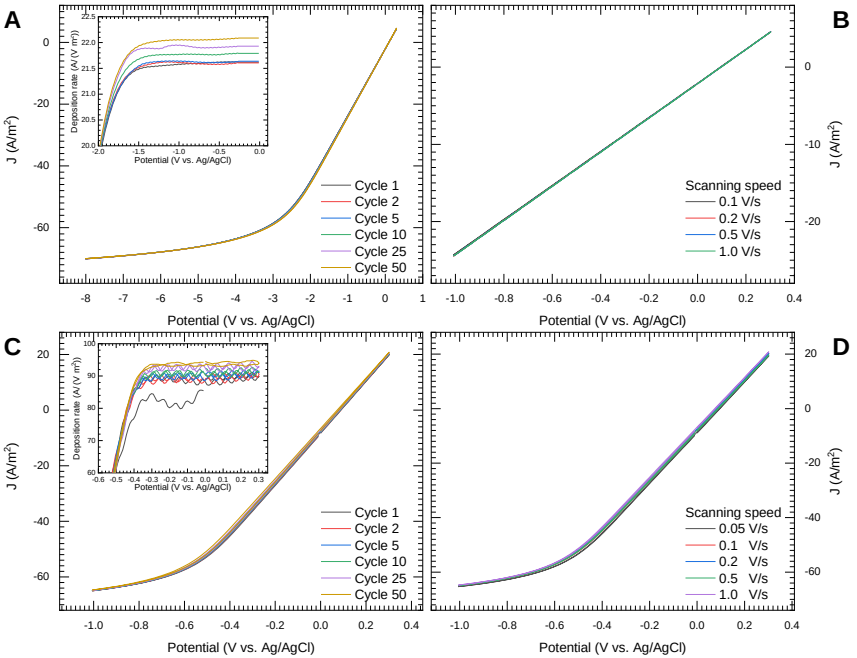

Figure 7.14: The cyclic voltammetry on (A-B) LC2 and (C-D) LC3. The experiment conducted in standard solution.

LC3 fabricated in the air due to its increased concentration of oxygen and nitrogen heteroatoms.

To elucidate the behaviour during electroplating, the cyclic voltammetry is performed and conducted in the potential ranges between −8 V and −1 V to 0 V and 0.2 V for LC2 and LC3 respectively. The results are depicted in Figure 7.14. The initial tests were performed at the equivalent voltage ranges and exhibited the symmetrical behaviour. However, the electroplating occurs only after oxidation of Cu^{2+} ions from the solution, thus by the substrate reduction. Therefore, the relevant investigation of voltammograms is performed in the reduction voltage range. The CV exhibited hysteresis, and the area was reduced with an increase in scanning speed, which suggests depletion of the electron transfer equilibrium on the sur-

face [232]. All samples displayed two plating regimes: a steady-state deposition, without any significant peaks attributed to reduction/oxidation at the heteroatom species, and the saturation current regime. In all samples, the steady-state regime switched at $\sim -60\,\mathrm{mA/cm^2}$. Indeed, during electroplating, the deposition was limited and showed current overflow after an increase above the saturation current, which corresponds to limitation of Cu^{2+} ion flow due to a hydrogen evolution reaction on the electrode surface [232]. The threshold voltage was dependent on the resistance of the selected specimen and observed at $\sim -1.7\,\mathrm{V}$ and $\sim -0.4\,\mathrm{V}$ for LC2 and LC3, respectively. As observed in Figure 7.14(A & C), the cycle repetition did not have any significant contribution to the plating behaviour. However, the saturation current slightly increased with the number of cycles, suggesting an improvement in conductivity by plating. The derivative of the current was taken to determine the highest electroplating rate, and they are depicted in the insets of Figure 7.14(A & C). Notably, the electroplating rate rises after each cycle, which in pair confirms the increase of conductivity by adhered Cu in the reduced state, promoting further crystal growth. Due to the slow crystal growth in such system, this rate, characteristic to plating on the selected specimen, retained within a slight deviation, thus the mean deposition rate was estimated after the averaging and listed in Table 7.6. This indicated that LC3 exhibits the highest deposition rate, which can be attributed to the lower sample resistance, the smaller specific surface area and equivalent charge distribution on the sample surface. A significantly lower deposition rate was observed for LC2, which corresponds to the largest specific surface area.

In order to estimate the degree of reduction, the film surface chemistry required investigation, which was provided with XPS. Due to the previously discussed reasons of exposure to the film bottom and interference with the acrylic adhesive, the surface chemistry was performed only on LC3 samples after electroplating for 10 min at $30\,\mathrm{mA/cm^2}$. Figure 7.15 shows the XPS spectrum from the survey and detailed spectra for Cu 2p, O 1s and C 1s. The elemental composition of the surface layer is investigated with XPS and shown in Figure 7.15A, which corresponds to a contribution of 59.32 at.%, 2.16 at.%, 30.98 at.%, 7.54 at.%

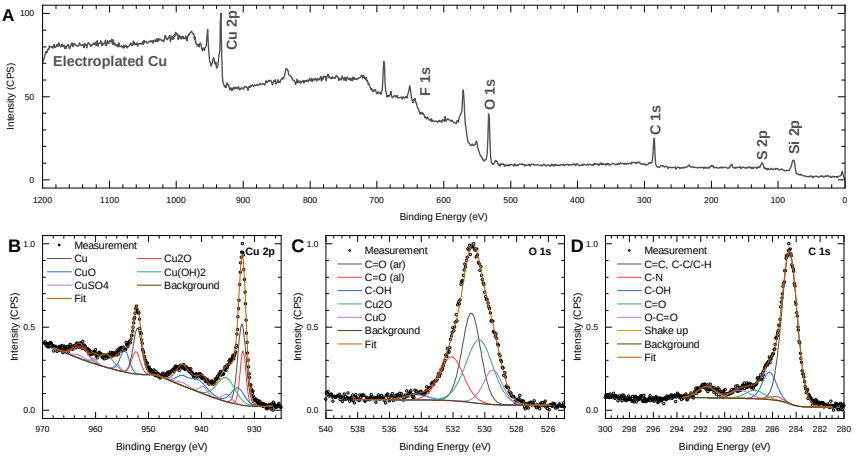

Figure 7.15: XPS collected from the electroplated Cu: (A) survey, and detailed spectra of (B) Cu 2p, (C) O 1s, and (D) C 1s.

and 2.99 at.% from C 1s, N 1s, O 1s, Cu 2p and S 2p. Figure 7.15B shows the Cu 2p spectrum deconvoluted into five species: a copper, a cuprous oxide, a cupric oxide, a copper hydroxide ($Cu(OH)_2$) and a copper sulfate ($CuSO_4$) [233–235]. The major contribution originates from copper and cuprous oxide due to oxidation on the surface immediately after extraction from the electrolytic bath. The presence of other oxidised species as well fell into rapid oxidation prior to post preparation annealing. Figure 7.15C depicts O 1s spectrum, which is fit with three carbon confined species (aromatic C=O, aliphatic C=O and C–OH) previously reported in Section 7.2.2 with the supplementary species of CuO at 529.7 eV and Cu_2O at 530.3 eV. Figure 7.15D shows C 1s spectrum, fit with all previously reported species. The comparison of the global chemical composition after electroplating to virgin LC3 shows a significant reduction in the nitrogen contribution. Further analysis of the detailed spectra in C 1s and O 1s peaks indicates a significant drop in amide, hydroxyl and carboxyl functional groups, additionally supporting preferential Cu adhesion sites at the heteroatom due to their induced higher electronegativity.

7.3.2 Characterisation of Composite Film

After investigation of the electroplating kinetics, the most suitable parameters must be selected in terms of an electroplating duration and the electrical current density, delivering for the LC uniform copper coverage. Thus, the newly fabricated composite films require vigorous investigation of their morphology, crystalline properties and chemical stability over time. These studies were performed by means of SEM, XRD and four-probe van der Pauw electrical resistance test.
All experiments were conducted on a square sample of $1\,\mathrm{cm}^2$ exposed to the electrolyte, and electroplating was performed for 300 s. Figure 7.16A shows a reduction of the sheet resistance with the increase of applied electrical current density during plating in a semi-log plot, recorded after a deposition duration of 300 s. Notably, a film with electroplated copper on LC3 exhibited a significantly lower sheet resistance, following a higher deposition rate as determined from CV slope, and reaching the minimum at $(6.63 \pm 0.86) \times 10^{-2}\ \Omega\ \mathrm{sq}^{-1}$. The limiting current density was observed for LC2 at $40\,\mathrm{mA/cm}^2$ with the overpotential above and plating became constrained. The samples, electroplated at $30\,\mathrm{mA/cm}^2$ were selected for further studies due to their adhesion retention to the substrate, complete coverage with copper by optical change of film tint, flexibility, and resistance properties under bending.

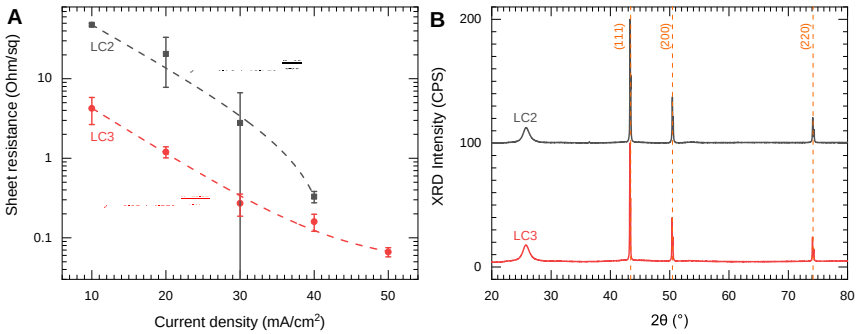

Figure 7.16: (A) Variation of the sheet resistance with current density, Cu was electroplated for 300 s in all cases. (B) X-ray diffraction of electroplated films.

Table 7.6: The electroplating rate and crystallographic properties of plated copper.

		LC2	LC3
Deposition rate, $V/(Am^2)$		21.8 ± 0.2	91.0 ± 1.8
Mass of deposited copper, mg		14 ± 4	42 ± 17
(111)	Peak position, °	43.32	43.28
	d, Å	2.09	2.09
	L, nm	98.10	122.30
(200)	Peak position, °	50.45	50.41
	d, Å	1.81	1.81
	L, nm	58.33	81.90
(220)	Peak position, °	74.12	74.08
	d, Å	1.28	1.28
	L, nm	95.40	116.50

The XRD performed for this composite film (Figure 7.16B) shows the strong reflections at 25.9°, 43.3°, 50.4° and 74.1°; the first peak corresponds to the carbon (002) plane, and the remaining peaks are contributed from the (111), (200) and (220) reflections of copper, respectively. The positions of these peaks correspond to the $Fm\bar{3}m$ space-group of Cu. The splitting of peaks is observed in all copper reflections due to a doublet in the radiation source. The peaks were fit with the Lorentzian function, and the crystallite sizes were determined using the Scherrer formula, with the results listed in Table 7.6. The Rietveld refinement was performed on the diffractogram, not indicating any internal stresses after plating. The copper crystallite size increased with the improvement of graphitisation, featuring the smallest size deposited on LC2 and the largest for LC3. The structure inheritance from carbon film facilitated copper growth in a substantially more

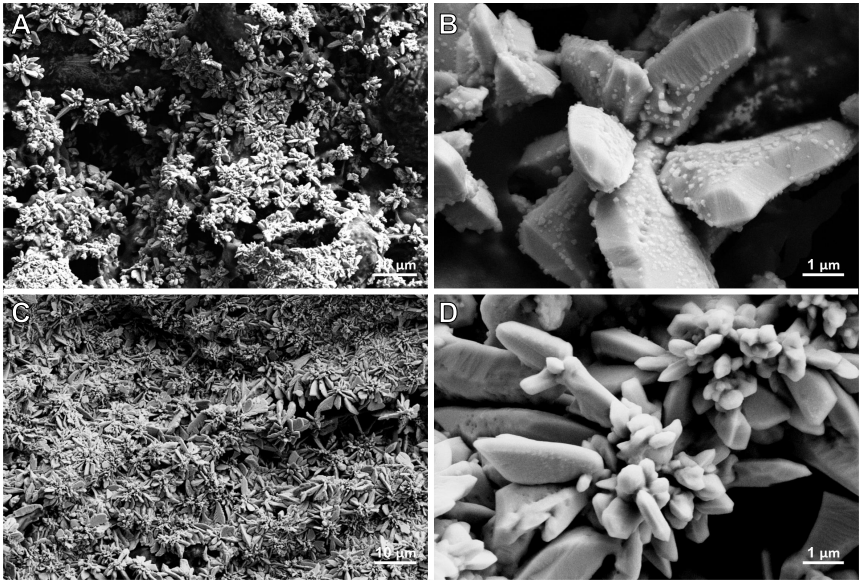

Figure 7.17: Surface morphology after electroplating of (A-B) LC2 and (C-D) LC3.

organised fashion for LC3, resulting in the largest crystallites, and due to a lower ordering present in LC2, the crystallites were grown the smallest [236].
Figure 7.17(A-D) shows the surface morphology of these composite films on LC2 and LC3. In each case, the copper deposited as an elongated crystal with length over (3.2 ± 0.9) µm and (3.0 ± 1.3) µm, and width (1.1 ± 0.3) µm and (1.1 ± 0.5) µm for both respective specimens. In LC3, the distribution in the length of the crystals was observed over a wider range. All crystals were fixed on a central anchor site and continuously interconnected with neighbouring crystals, providing the electrical stability. The electroplated film contained the areal coverage with the copper of 64 % and 79 % for LC2 and LC3 determined from SEM micrographs. The grown film thickness was determined as 3.7 µm using Faraday's equation implementing only the surface area 1 cm^2. However, the average thickness of the electroplated copper exceeded the calculated value due to the preference on the deposition sites and further dispersion between voids inherited from LC.

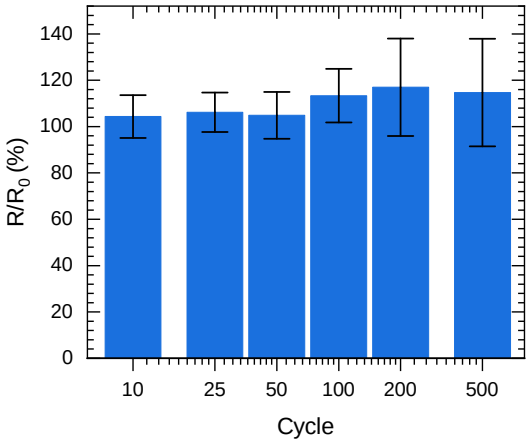

Figure 7.18: Sheet resistance variation after number of bending cycles performed at 90°.

The LC3 exhibited the highest mass increase after plating (Table 7.6), but the film was constrained in bending by exhibiting fracturing and showed the exfoliation of the carbon/copper film from the Nomex substrate during the bending test. Therefore, the test was performed only for the selected LC2, which showed good flexibility at 90° with bending radius of 5 mm without any mechanical deterioration and insignificant degradation of the surface. Figure 7.15 depicts the normalised sheet resistance to the initial measurement after a number of repetitions. The bending was repeated for multiple cycles and showed resistance deterioration after the tenth repetition. After 100 cycles, the resistance dropped to 15 %, and with repetition, to 500 cycles, no further resistance decrease was observed presenting good retention of the sheet resistance.

The copper films exposed to the air tend to oxidise due to retaining humidity in the environment. This influences the properties of electroplated copper effectively by increasing in Cu_xO content and causes the electrical conductivity deterioration. Such deterioration was observed after two weeks for both plated laser carbon films exposed to the air and estimated with EDX (Figure 7.18A, B). The ratio of copper

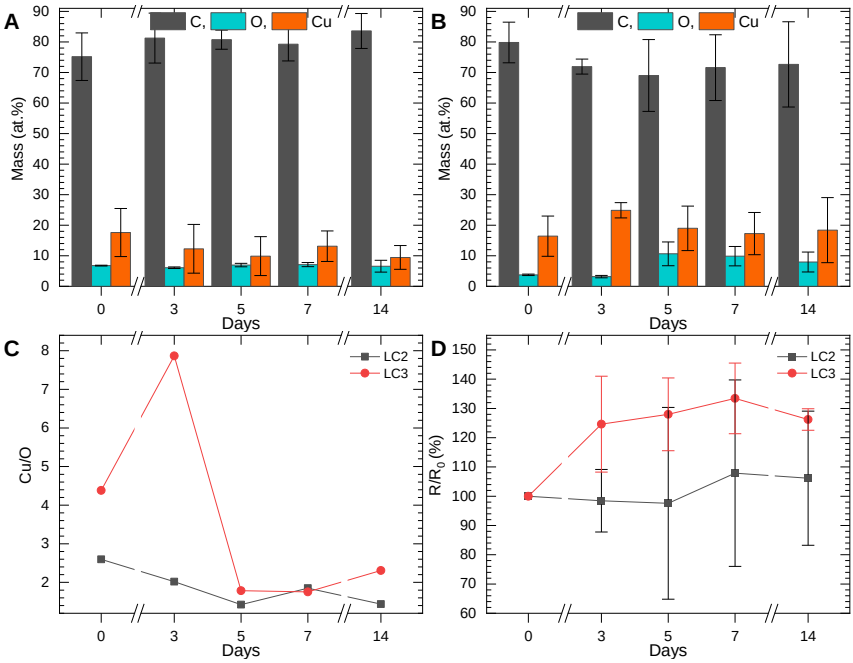

Figure 7.19: Change in the elemental composition over time determined with EDX spectroscopy on plated (A) LC2 and (B) LC3. (C) The variation of copper to oxygen mass percentage over time. (D) Variation of the sheet resistance of plated films over time.

to the oxygen was estimated and depicted in Figure 7.18C showing an increase in the oxygen. After a week of storage, the oxidation saturated showed the resistance increase in 10 % and 30 % for LC2 and LC3, respectively, and afterwards reached saturation. Particularly, in LC3, the ratio significantly rose after the third day and was considered as the measurement error. This observation corresponds to the sheet resistance variation (Figure 7.18D), which shows a drop with the increase of storage time and saturation after a week.

In summary, these studies indicated the best plating parameter at 30 mA cm^{-1} for 300 s, due to uniform copper distribution, a significant improvement in the electrical conductivity. LC2 procedure can be further used for the flexible films

preparation owing to insignificant sheet resistance rise after a series of bending tests showing prospects in the fabrication of the specialised coatings, the highly electrically conductive flexible films and smart textiles operating at high temperatures. Electroplating of LC3 exhibits even higher electrical conductivity and delivered mass of copper. However, the film does not exhibit the same degree of flexibility, and after a number of bending cycles causes the exfoliation and should be supported with additional packaging to retain shape. Nevertheless, the procedure provides excellent means in the rapid fabrication of the electrodes with customised designs and can serve as the valuable types of composites.

7.4 Flexible Antibacterial Copper Coating

Antimicrobial protection of the surfaces plays a significant role in disease prevention, and lately, targeting for the spread reduction of new bacterial and viral infections, particularly lately emerged COVID-19. It was reported mutual support and predisposition to spread of the combinations of bacterial and viral infections [237], with the lately observed increase of severity in COVID-19 patients infected with both [238]. Antibacterial coatings are especially interesting considering that nosocomial infections are becoming a significant threat in the medical environment due to cross-contamination of surfaces and the increase of antimicrobial resistance in pathogens [239]. The reduction of contaminants is usually achieved by frequent cleaning, including the use of surface disinfectants. However, their frequent use can breed microbes with a developed resistance against the antimicrobial substance, which can also be linked to antibiotic resistance, making the microbe less susceptible to both surface disinfectants and antibiotics [240]. Once this resistance has manifested, the microbe can cover the environment since the cleaning procedure no longer eliminates it. In the worst case, this resistance can transfer to other microbes by horizontal gene transfer [241].

Although multiple carbon allotropes feature exceptional biocompatibility due to their compositional relatedness to living cells, they are reported to be used as a substrate for antibacterial composites. Antibacterial coatings based on copper and

silver circumvent antibiotic resistance and therefore are viable options to counteract microbial contamination and nosocomial infections [239, 242]. However, most available coatings use bulk material dispersed in the matrix, which can be significantly reduced by targeted electroplating on the conductive surface.
In this Section, previously studied electroplated flexible copper/laser carbon composites are used as a model for prevention in developing bacterial colonies. The films are compared between several model substrates, and the results are analysed. Such customisation of a polyaramid substrate can also be a step towards developing antibacterial coatings of various areas.

7.4.1 Coating Fabrication

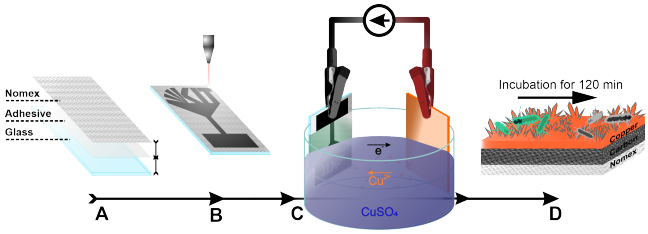

Figure 7.20: Schematic representation of the experiment. Fabricated Nomex film electroplated with copper and tested for antibacterial activity.

To address this problem and investigate the effect of the composite, the study was designed, which is schematically shown in Figure 7.20. Nomex films were prepared with LIC using LC2 recipe, with the further copper electroplating, following the aforementioned best procedure. Those films are used for bacterial testing of *Escherichia coli* and *Bacillus subtilis*.

7.4.2 Characterisation and Testing

Table 7.7 shows a reduction in the quantity of the bacterial colonies upon the initial exposition to the LC2 copper carriers of *E. coli* and *B. subtilis*. The copper ions generating from the copper surface can produce reactive oxygen species in a

Table 7.7: Percentage of bacterial count based on the amount of colony-forming units after the initial exposition (i.E.) in comparison to the initial colony amount counted on steel control carriers and after incubation (a.I.) in comparison to the initial amount counted on the individual carriers

.

Carrier	*E. coli* i.E.	*E. coli* a.I.	*B. subtilis* i.E.	*B. subtilis* a.I.
Stainless steel		677 %		19 %
Nomex paper	3 %	894 %	3 %	219 %
LC2	40 %	133 %	271 %	4 %
LC2 Copper	>0.1 %	N/A	>0.1 %	N/A

Fenton-like reaction, which can cause damage to lipids, protein and DNA [243]. Furthermore, copper destabilises iron-sulphur clusters, which are required in the active centre and as co-factors in many vital enzymes, ultimately leading to the death of the cell [243]. In general gram-positive bacteria are less susceptible to copper exposure, especially so if they are from the class of micrococci [244]. The initial exposure time of the 75 min drying process before the first samples for the Miles and Misra method are extracted. However, it was sufficient to eliminate any measurable trace of the species *E. coli* and *B. subtilis*, which explains why the data after incubation is unavailable for both. In the case of the LC2 carrier, the amount of colony-forming units extracted after first exposure is drastically increased for *B. subtilis* and decreased for *E. coli*. The results for *B. subtilis* suggest that in comparison to steel, it is more difficult for the Bacilli to attach to the carbon surface. *E. coli* bacteria are struggling to increase their biomass on this carrier during incubation time, while the amount of *B. subtilis* is significantly decreased. It is observed that the nanostructures inhibit or even eliminate bacterial growth [245, 246]. In comparison, both LC2 and the copper-plated LC2 carriers have nanocrystalline features, which can hinder bacterial growth. However, the bactericidal effect of the LC2 copper carrier originates from the decisive lethality of copper ions. Nomex paper itself is able to decrease the number of bacteria extracted after initial exposure. However, both bacteria were able to significantly

increase their biomass after an incubation after 120 min, so while it prevents bacterial adhesion, it does not hinder their growth significantly.

The large discrepancy between the colony counts after incubation of the two organisms can be explained by the species' different growth rates and surface adhesion properties. While *E. coli* K12 has a doubling time of approximately 15 -20 min [247] and very poor adhesion characteristics on steel surfaces [248], *B. subtilis* species has a doubling time of approximately 120 min [249], and is a model organism for adhesion and biofilm formation [250]. In comparison to *B. subtilis*, *E. coli* is able to increase its biomass faster, and more of it is flushed from the carrier during sample extraction.

The results show that the copper electroplated on the carbon film antimicrobial activities are similar to other antimicrobial copper surfaces [251]. Combined with the properties ease of fabrication [55, 65] and controllable copper plating thickness as well as the flexibility of the material, this enables access to a reliable and cost-efficient antimicrobial surface.

It was observed that the PBS (0.01 M, pH 7.4) acquired a blue taint during the resuspension steps of the LC2 copper carriers. This taint is characteristic of the copper ions presence in the solution, confined in coordination complexes as $CuCl_2$, $Cu_3(PO_4)_2$, $Cu(HPO_4)_2$ and $CuSO_4$ originating from PBS and the residual electrolyte. However, only a minor contribution of sulphur was detected by EDX analysis after drying the assay on a reference gold-coated silicon chip, with elemental composition predominately originating from Na, Cl, P, characteristic for the content of PBS. Therefore, it was concluded that only copper ions were effectively involved in the antimicrobial properties. However, the quantitative determination of the copper ions with titration did not provide any satisfactory results due to the strong dilution during the procedure, and the near-neutral pH constraining the use of the colour indicators. For the qualitative evaluation, the FTIR was performed for assays before and after incubation, and characteristic vibrational modes of H_2O and some ions from PBS were observed.

7.5 Amperometric Glucose Enzyme-free Sensors Based on Cu and CuO Composites

Biological sensors play an important role in the point-of-care devices due to their ability in addressing an exact detection concentration only for the selected analytes and omit contribution from other possible species from the test analyte [252, 253]. One of the most crucial biosensors operates for glucose detection due to its essential role in microbiome regulation, specifically for people suffering from *diabetes mellitus*. Increased levels of blood sugar directly relate to the risks in the development of cardiac arrests [254], renal failure [255], blindness [256], cerebral, and neuronal damage [257]. Globally, the number of people diagnosed with *diabetes mellitus* is currently estimated at over 500 million by the International Diabetes Federation [258], with numbers steadily rising and laying a huge burden on the healthcare system. Thus, direct monitoring of glucose concentration in blood and sweat is essential for timely assistance and prevention [258, 259].

Traditional glucose sensors are mostly enzymatic sensors, where a glucose oxidase enzyme is immobilised on a sensing material [260]. The sensing mechanism of such sensors relies on the oxidation of glucose to D-gluconolactone, the subsequent generation of hydrogen peroxide, and further on to gluconic acid [261, 262]. However, extraction of the enzymes from fungus, such as industrially accepted *Aspergillus niger* [260, 262], is expensive. Furthermore, long-term stability and storage of the enzymatic sensors are of major concern [261]. Therefore, in recent years, significant attention has been paid to enzyme-free biosensors, where several noble metals [263–265], metal nanoparticles [253, 266–268], and transition metal oxides [261, 269] have been exploited as the electroactive material for glucose sensing.

The use of these materials for biosensing majorly relies on the fabrication of composite electrodes, typically with a carbon-based material such as graphene [270, 271], carbon nanotubes [272, 273], and glassy carbon [274–276], which further reinforces the essential biocompatibility of the sensing material. Among various electroactive materials, copper and copper oxide exhibit a significant electrocat-

alytic activity for glucose oxidation due to its lower overpotential induced by an electron transfer [261, 274, 277]. Moreover, copper oxide nanowires allow an improvement in the sensitivity of detection due to their higher surface to volume ratio [235, 267, 278]. Notably, the growth of the nanowires on spheroids can further increase the surface area, leading to an urchin-like morphology. Because of their superior morphologies, the urchin materials have demonstrated significantly higher sensitivity for glucose detection compared to other copper-based materials [279]. However, the CuO urchin-based glucose sensors reported to date were rigid sensors, used for the detection of H_2O_2 [280] and humidity [281]. Even though the fabrication of flexible biosensors has been reported using bulk copper oxide [282] and its nanowires [235, 261, 271, 274, 283], the urchin-morphologies are still not utilised for flexible sensor devices. Furthermore, the current state of the art for the synthesis of urchin morphologies only includes the hydrothermal method and chemical synthesis [280, 281].

In this Section, the fabrication of copper microspheroids (Cu-MS) and cupric oxide urchin based (CuO-U) glucose sensor is described , where the urchin structures are achieved solely by thermal annealing through variation of the working environment. The composite films were characterised by their crystal and chemical properties. The activity toward the selected analytes was performed with electrochemical techniques, such as cyclic voltammetry and real-time amperometry.

7.5.1 Sensor Fabrication

The fabrication of the glucose sensor is illustrated in Figure 7.21. The flexible Nomex Type 410 insulation sheets were irradiated with the mid-infrared laser radiation, forming a carbon-rich conductive seed layer. The fabrication was performed with the standard procedure for LC3 film.

The laser carbon was used for the subsequent copper electroplating, at which a direct current of 30 mA was applied for the specified duration. The electrode exposed to the electrolyte had a square shape with a 15 mm side length. The consequent annealing was performed in a horizontal tube furnace under the constant

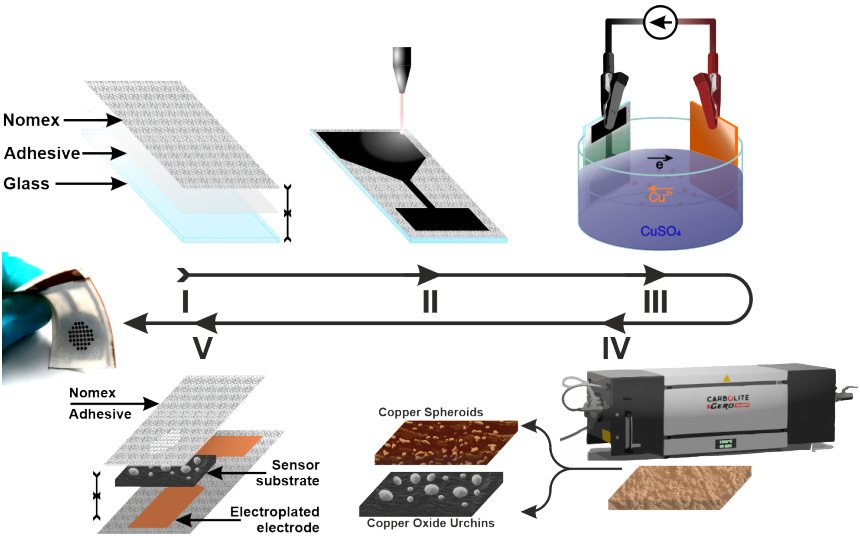

Figure 7.21: Schematic representation of the glucose sensor fabrication: (I) Nomex film attached to a glass slide, (II) the precursor undergo LIC, (III) the laser carbon film electroplated with copper, (IV) the plated film removed from precursor and annealed in N_2 and air, (V) the film encapsulated onto the plated flexible electrode and tested.

nitrogen flow (∼0.8 L/min) with the heating rate of 5 °C min^{-1}, and was held at the specified temperature for 1 h. Investigation of the copper folding into micro-spheroids was conducted by annealing at multiple temperature sets followed by natural cooling under N_2 flow, namely under 800 °C, 900 °C, 1000 °C and 1100 °C. CuO-U were grown after the air influx was introduced at 450 °C during the cooling step, matching with a specific regime promoting the nanowire growth [284, 285]. CuO-U growth mechanism was repeated for all aforementioned temperature sets. Both types of the annealed samples fabricated at 1000 °C were selected for the enzyme-free glucose sensing and used for the amperometric studies.

The separate supporting electrode fabrication from Cu electroplated laser carbon was carried out for the bendable amperometric tests and were fabricated using the LC2 procedure.

The electroplating was performed under 30 mA; however, the plating time was increased to 3000 s due to the reduced plating rate and the increase of the total plated area to 3.5 cm^2, and a higher resistance for laser carbon films prepared with LC2. These bioelectrodes were tested both in a flat and in a bent state for enzyme-free glucose detection.

7.5.2 Materials Characterisation

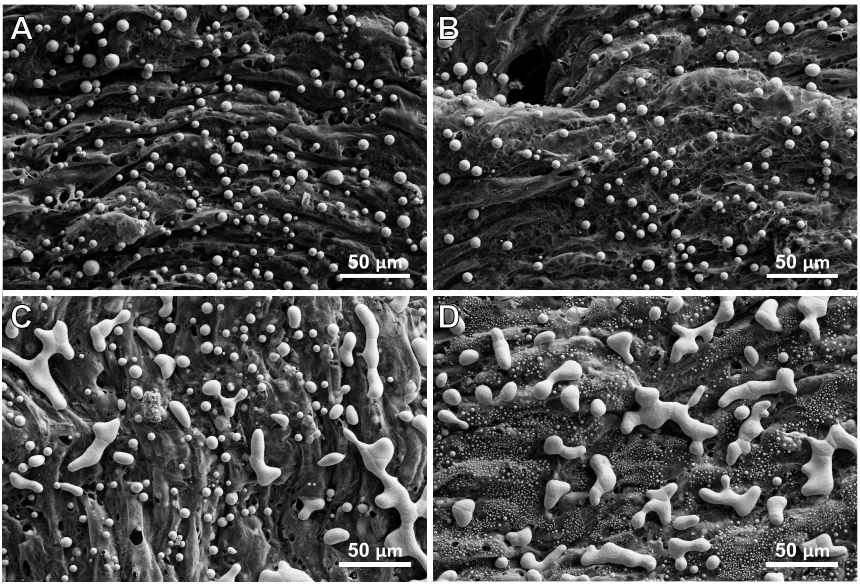

Figure 7.22: The annealed copper films microstructure in N_2 at 1100 °C with plating time: (A) 150 s, (B) 600 s, (C) 1200 s and (D) 2400 s. Parts are taken from Ref. [70]

The annealing and cooling in the nitrogen working environment resulted in aggregation into the bigger copper clusters, folding into microspheres and nanoparticles, as is shown in Figure 7.25(A, B). The copper agglomeration and sphere folding, their diameter and the quantity are directly proportional to the selection of a plating duration, depicted in Figure 7.22. The shape of such agglomerates, the microspheroids' diameters, their quantity and uniformity distribution on the laser carbon

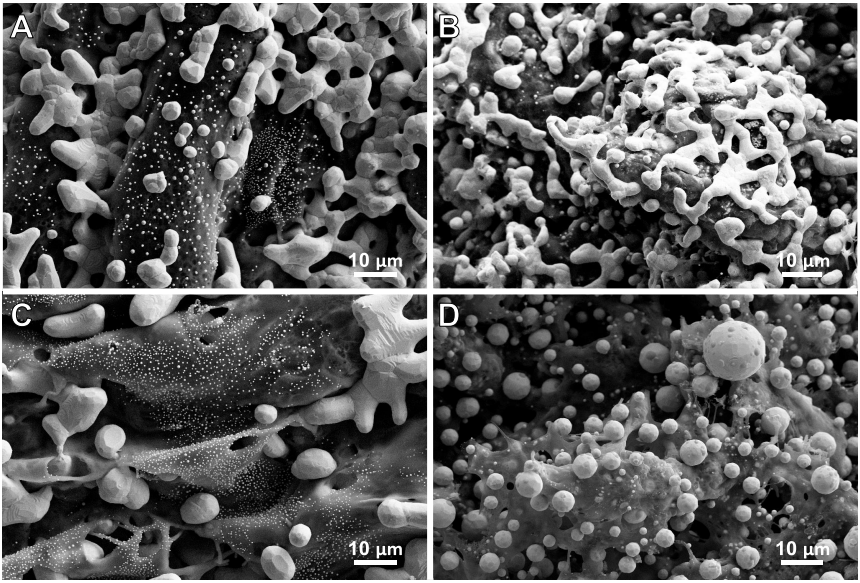

Figure 7.23: Microstructure of the folded copper spheroids on the laser carbon film after annealing in N_2 at: (A) 800 °C, (B) 900 °C, (C) 1000 °C and (D) 1100 °C. Parts are taken from Ref. [70]

were directly proportional to the plating duration, as indicated in Figure 7.22 and Table C2. However, a plating time over 10 min resulted in the agglomeration of asymmetrical crystals with random shapes.

The microspheroids are formed of nearly spherical shape only at the annealing temperature of 1000 °C. At lower temperatures, the plated copper partially melted and agglomerated into bigger crystals, decreasing the film roughness and areal coverage on the underlying laser carbon, as seen in Figure 7.25. Annealing of the copper/carbon composite film showed persistent low diffusion of the carbon into the copper due to its low solubility, as is indicated in the specific phase diagrams [286]. The annealing of thin copper films at 1000 °C promoted melting and led to aggregation as droplets (microspheroids) on laser carbon, induced by heterogeneous melting with reduced Gibbs free energy for the thin films [287, 288]. The surface energies of copper and carbon are 1.79 J cm^{-2} and 0.26 J cm^{-2}

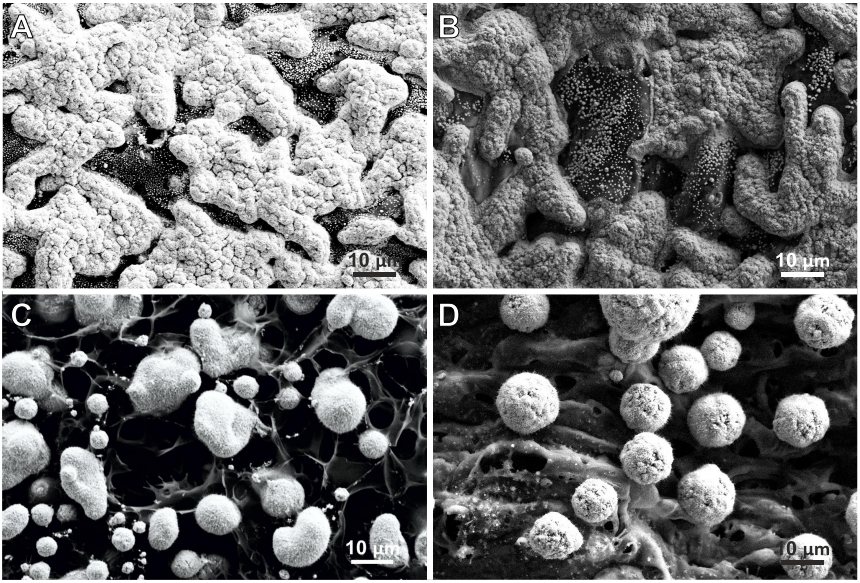

Figure 7.24: Microstructure of the grown copper oxide nanowires after annealing in air at 450 °C for the copper spheroids folded at: (A) 800 °C, (B) 900 °C, (C) 1000 °C and (D) 1100 °C. Parts are taken from Ref. [70]

respectively [289], which also supports the aggregation of the molten copper into microspheroids by a reduction of the contact area, due to significantly higher surface energy, causing non-wetting of the copper on the laser carbon [290]. The surface roughness further promoted the contact area reduction by copper [290]. Figure 7.25(B-D) shows a grown copper oxide nanowires on Cu-MS, resulting in urchin-like microstructure, which was achieved after introduction of air at 450 °C during the cooling step yielded shell oxidation. The introduction of air during cooling at 450 °C induced a copper nanowire growth, which was promoted by a vapour-solid growth mechanism [291]. With an excess of oxygen, a Cu_2O phase formed, fostering hillock aggregation due to relief of compressive stresses. At a temperatures above 400 °C, the Cu_2O phase is not thermodynamically stable.

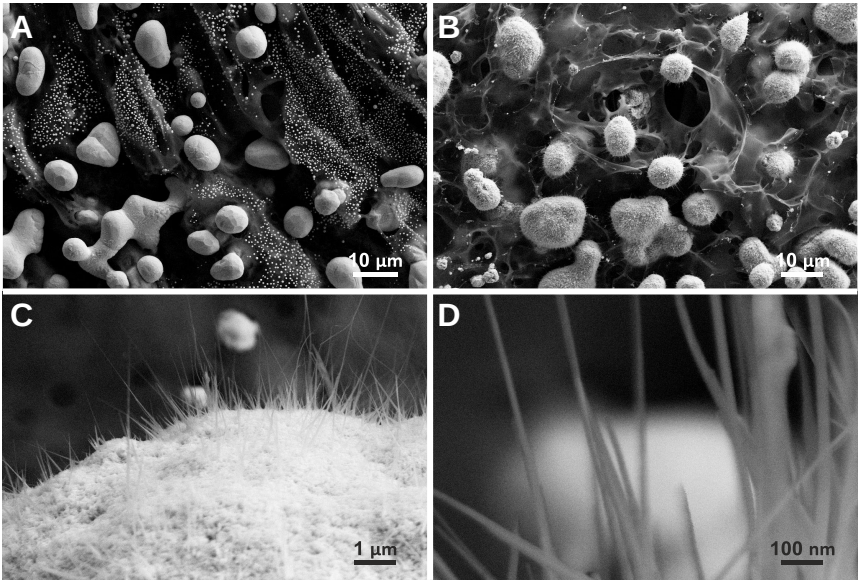

Figure 7.25: Microstructure of: (A) a folded copper into spheroids, and (B) a copper oxide urchins, (C-D) a magnification on the copper nanowires. Parts are taken from Ref. [70]

Therefore, with further oxygen supply, the nanowires of CuO started growing, with the hillocks as the nucleation sites [285, 291, 292].

A small increase in diameter of the microspheroids was indicated and listed in Tables C3 & C4. CuO-U obtained from a precursor sample with a plating time above 10 min resulted in the fracturing of the oxidised shell of the microspheroids as it is seen in Figure 7.23. This was caused by the excessive stress release, resulting in the deterioration of oxidised shell adhesion to the microspheroid and the precipitated material is in loose contact with the laser carbon, which negatively affected the composite electrode sensing capability. Figure 7.25(C-D) shows densely grown nanowires, which featured diameters ranging from 15 nm to 150 nm with lengths up to 5 µm.

The selection of the samples for further detailed characterisation was based on the highest amperometric response without any significant signal deterioration after

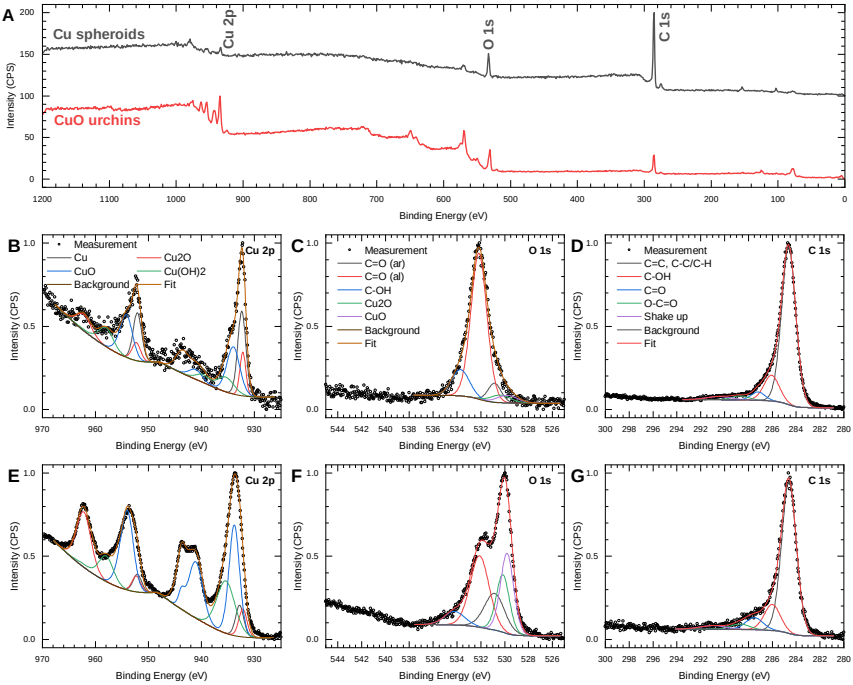

Figure 7.26: X-ray photoelectron spectra: (A) survey, and detailed spectra of Cu 2p, O 1s and C 1s for (B-D) Cu spheroids and (E-G) CuO urchins.

saturation. From these results, the samples obtained after annealing at 1000 °C exhibited the best amperometric signal for both Cu-MS and CuO-U.

The fabricated materials attain features in micro and nanometer scale significantly influencing their properties. The surface chemistry plays the essential role in understanding the effects of the functional groups, and, therefore, it was studied with XPS.

The survey spectra are depicted in Figure 7.26A, which features the presence of C 1s, O 1s and Cu 2p in both films. Annealing significantly reduced the contaminants present in the initial electroplated copper, as seen in Figure 7.15, but featured an insignificant contribution from Al 2p, originating from the sample

handling. Figure 7.26(B & E) shows Cu 2p peaks, which are fit into the four species as previously discussed in Section 7.3.1 omitting a copper sulfate, due to its decomposition over 650 °C [293]. Comparatively to the initial electroplated sample, the total contribution of a collected signal after annealing dropped due to the reduction of the coverage area by copper. In the detailed spectra, Cu-MS film exhibits predominance from metallic copper, with some presence of CuO of few top nanometres of Cu-MS by virtue of the rapid oxidation by exposure to the air; and it is present in such chemical form due to its high stability as an oxidised specie comparatively to others. In part, CuO-U film shows a significant reduction in metallic copper and development of high ratio CuO and $Cu(OH)_2$ species, expected from the air-rich annealing. Figure 7.26(C & F) shows O 1s peak for both annealed films, where the peak features two supplementary species to the laser carbon base spectrum corresponding to the cupric oxide (CuO) at 529.7 eV and the cuprous oxide (Cu_2O) at 530.3 eV. The oxygen contribution in Cu-MS is confined only on the laser carbon substrate, with the majority indexed to aliphatic carboxyl species. In the second annealing recipe with the air introduction, Cu-MS actively oxidise, featuring a strong increase in CuO peak with nanowire growth. Moreover, the laser carbon confinement showed a predominant shift to aromatic carboxyl, suggesting further oxygen evolution and incorporation within graphene lattice. Figure 7.26(D & G) depicts the detailed spectra collected from C 1s peak for Cu-MS and CuO-U respectively, and features the presence of the same functional groups as indicated in Section C-3, excluding C – N bond due to the scarce nitrogen presence. Annealing procedures do not significantly affect the shape, the elemental composition and species in C 1s. However, the deconvoluted peaks from the carbon bonds indicate a slight improvement in contribution, and all oxygen species reduce, indicating further pyrolysis with an improvement of carbonisation during annealing. Notably, after the oxidation step, the relative contribution from C = C · C – C/C – H peak slightly reduced with the increase on all oxygen confined species compared to Cu-MS, suggesting slight oxidation at the dangling bonds of the laser carbon surface even at the selected temperature regime. The detailed results after deconvolutions for all spectra are presented in Table C5.

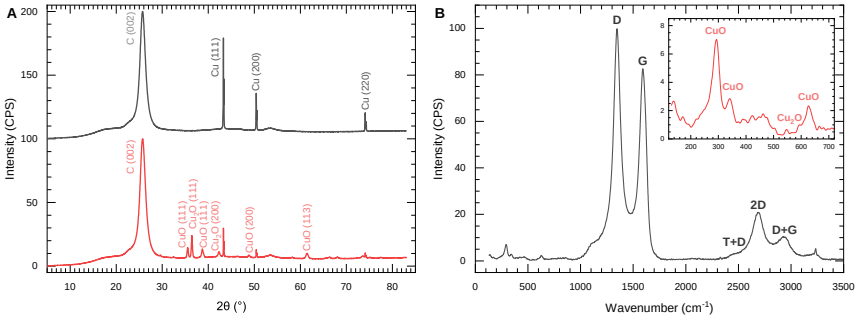

Figure 7.27: (A) Diffractograms collected from Cu spheroids and CuO urchins films. (B) Raman spectrum of CuO urchin film.

Table 7.8: Crystallographic properties of the selected films after Rietveld refinement.

		Interplane distance, Å	Crystallite size, nm	Internal strain
Electroplated Cu	C (002)	3.47	9	0.008
	Cu (111)	2.09	178	0.001
Cu-MS	C (002)	3.46	12	0.008
	Cu (111)	2.09	265	0.013
CuO-U	C (002)	3.46	12	0.008
	Cu (111)	2.09	265	0.013
	Cu_2O (111)	2.53	75	0.343
	CuO ($11\bar{1}$)	2.47	75	0.580

Figure 7.27A depicts XRD reflections collected from Cu-MS and CuO-U composites. After the formation of Cu-MS, the peak composition was not modified, but the intensity of all peaks slightly dropped, indicating a reduction in the total acquired signal. CuO-U film exhibits a significant reduction in Cu reflections, but some new peaks arose corresponding to Cu_2O and CuO, matching to JCPDS #05-0667 and #48-1548 [294], both confirming phase transition of copper to an oxidised phase. The interplane distances were calculated using Bragg's law, the crystallite sizes and the internal stresses for each component were derived after using Rietveld refinement [295], and the results are listed in Table 7.8. It indicates

an increase in the internal stress in both oxidised states compared to the remaining Cu. Notably, Cu_2O shells exhibited lower internal stress due to stress-induced growth of CuO nanowires [285, 291], which can be further reduced by an increase in the annealing time.

Figure 7.27B shows collected Raman spectrum from CuO urchins on the laser carbon film. The laser spectrum from LC3 is observed by characteristic D, G, 2D and D+G bands at 1347 cm^{-1}, 1589 cm^{-1}, 2681 cm^{-1} and 2932 cm^{-1}. Moreover, the spectrum contains tree additional peaks at 294 cm^{-1}, 341 cm^{-1} and 627 cm^{-1} characteristic to CuO [235, 296, 297]. CuO has a monoclinic lattice, belonging to C_{2h}^6 space group containing two molecules in the primitive cell. Theoretically predicted existence of twelve optical phonon modes with symmetries: $4A_u + 5B_u + A_g + 2B_g$, from which only three $A_g + 2B_g$ modes are Raman active. Those modes correspond to A_g at 294 cm^{-1} and B_g modes at 341 cm^{-1} and 627 cm^{-1}. The band position is in agreement to the crystallite sizes determined with XRD and close to the bulk, due to Raman shift at a lower wavenumbers in nanocrystalline powders [296].

Figure 7.28 shows TEM imaging and collected with SAED of nanowires grown from CuO-U and neighbouring areas. The projections correspond to a long-range order in the crystal and presence of two copper oxide phases: cubic Cu_2O at the Urchin with a unit cell determined at (4.60 ± 0.34) Å, and monoclinic CuO with a lattice distance of 2.53 Å calculated for the $(11\bar{1})$ plane. Within top 5 nm of the Urchin shell, crystallites with layered or random orientation were found, characteristic for a monoclinic CuO lattice or an intermediate amorphous phase. As is seen in Figure 7.28C, above 5 nm within the shell, the structure featured an initial cubic lattice specific to Cu_2O with a matching unit cell size [285, 291]. At the nucleation site and in the grown nanowire, the crystal structure attained stacked-layer formation, and further along the length of crystal featured the moiré fringes due to an overlapping of the different crystal orientations. The core nanowire crystallite was circularly surrounded by a shell in the same phase. The presence of both oxide phases supports XRD and matches with the nanowire growth mechanism.

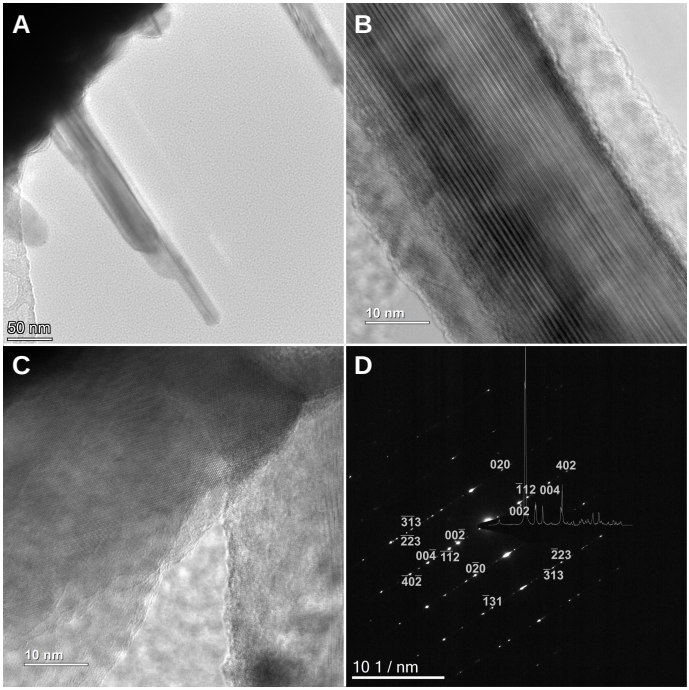

Figure 7.28: TEM imaging of CuO-U with (A) an overview of the urchin, (B) a magnification on CuO nanowire and (C) a shell of the microshperoid exhibiting cubic lattice characteristic to Cu_2O. (D) SAED of the CuO nanowire.

Figure 7.28D shows SAED collected from a single nanowire with the electron beam focused along the $[\bar{1}10]$ orientation with the reflected planes marked accordingly. SAED pattern confirmed reflections from the sole CuO phase and exhibited the presence of two crystallographic orientations of CuO with rotational symmetry.

7.5.3 Sensor Electrochemical Testing

All chemical reactions involved in the transfer chain are presented in Figure 7.29, showing the oxidation of the electrode from Cu and CuO. In part, the D-glucose oxidises to D-gluconolactone and further on to gluconic acid [261, 262].

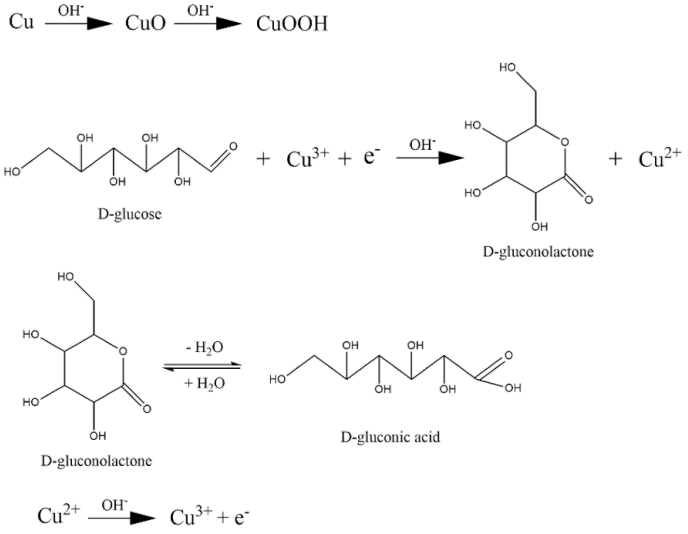

Figure 7.29: Catalytic oxidation of D-glucose on Cu and CuO (parts adopted from Ref. [298]).

Composite films of Cu-MS and CuO-U were further utilised in the enzyme-free glucose biosensors. The highest effectiveness of the sensors is typically achieved by a functional electrical current detection at the lowest potential. Enzyme-free glucose sensors rely on the glucose oxidation at selected overpotential induced by an electron transfer during substrate oxidation [261, 274, 277]. In order to determine optimal operating conditions of the electrode, electrochemical testing is required to determine an oxidation overpotential evolution in the presence of the electrolyte and mixture with the analyte (glucose).

Figure 7.30(A & B) shows cyclic voltammograms from the annealed films (Cu-MS and CuO-U) within the potential range −0.8 V to 0.8 V. The electrochemical measurements were independently performed in the initial alkaline electrolyte, the presence and absence of 1 mM glucose. The selected electrolyte provided a charge transfer during the glucose sensing and showed some influence of the concentration of NaOH in the amperometric signal but without any significant contribution above 100 mM, which was chosen as a standard concentration for the

solution in tests [261]. Figure 7.30A shows the oxidation peaks in Cu-MS, which were observed at −0.32 V and −0.10 V, and can be attributed to the evolution of Cu^0 to Cu^{1+} (Cu_2O) and from Cu^0 and Cu^{1+} to Cu^{2+} (CuO), respectively. The reduction peak was observed at −0.54 V and −0.74 V, corresponding to the transition from Cu^{2+} to Cu^{1+} and then to Cu^0 [298–300]. Mixture of the electrolyte with glucose resulted in a decrease in the intensities of all the peaks, and a shift of the oxidation peak to −0.23 V, which was due to the transition from Cu^0 to Cu^{1+} [70, 298, 299].

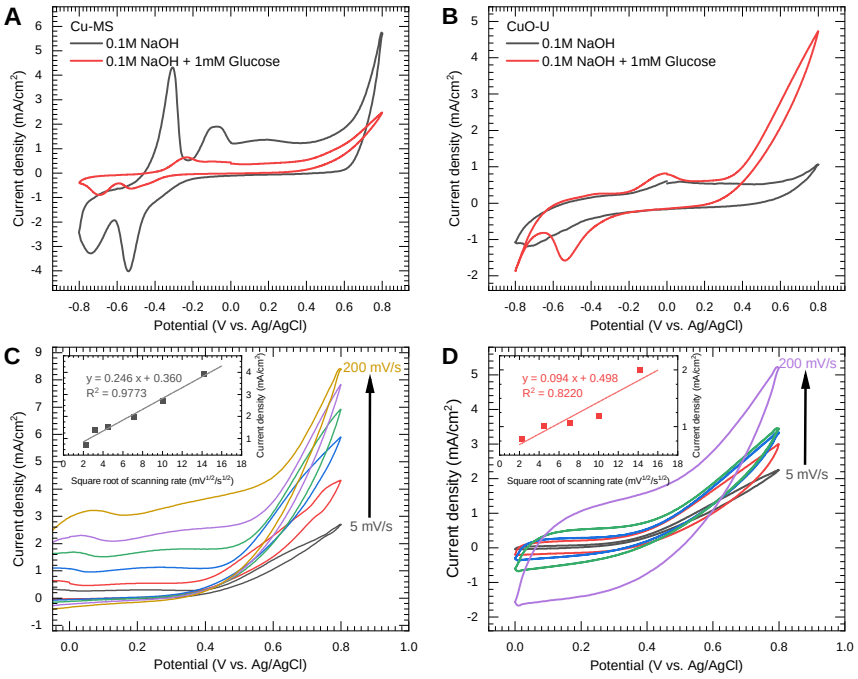

Figure 7.30: The full scan cyclic voltammograms in presence and absence of the glucose on (A) Cu-MS and (B) CuO-U. The oxidation current density at 0.5 V on the speed of scanning rate on (C) Cu-MS and (D) CuO-U. In insets a derived oxidation rate at 0.5 V for each respective film (part adopted from [70]).

Figure 7.30B shows cyclic voltammograms from CuO-U/laser carbon composite. Here, the oxidation peaks were observed at −0.02 V and 0.05 V, attributing to the transition from Cu^{1+} to Cu^{2+} and from Cu^{2+} to Cu^{3+}, respectively. The reduction current featured peaks at 0.35 V and −0.60 V, which promoted by transition to multiple copper groups from Cu^{3+} to Cu^{2+} and from Cu^{3+} to Cu^{1+}, respectively. After mixture with glucose, the signal response is improved over 0.2 V and −0.3 V, corresponding to oxidation and reduction responsible for the transition of Cu^{2+} and Cu^{3+}.

As the glucose molecules yield an oxidative behaviour on the electrodes, the oxidation current is characterised in detail to evaluate a sensing behaviour and presented in Figure 7.30(C & D). The oxidation peak current increased with an increase in the scanning rate for both the electrodes due to fast oxygen transfer to the working electrode, promoting an uncompensated solution ohmic drop [111]. Insets of Figure 7.30(C & D) show an increase of the oxidation current proportional to the square root of the scanning rate, which follows a linear law, corresponding only to diffusive behaviour in the electrocatalytic glucose oxidation, which is advantageous for amperometric sensing [299]. However, Cu-MS film exhibited a steeper slope, supporting the improved oxidation rate from Cu^0 compared to the CuO counterpart.

Due to the importance of the oxidative current in the amperometric sensing, the CV was repeated only at the oxidation voltage, and it is shown in Figure 7.31. There, it is emphasised the significantly superior performance of both Cu-MS and CuO-U films comparatively to laser carbon and the supporting copper tape. With the presence of 1 mM glucose in the electrolyte, the total area of the CV curve and the peak current increased for all the studied films. Notably, after three repetitions, the oxidative current from Cu-MS showed a higher response in the presence of glucose, which corresponds to the development of the oxidised layer and its response to the overpotential. Therefore, the potential at 0.5 V was selected due to a significant improvement of the current response in the CV was observed for the CuO film in the presence of glucose. Among all tested specimens, CuO-U electrode exhibited the highest sensitivity due to superior electron transfer for

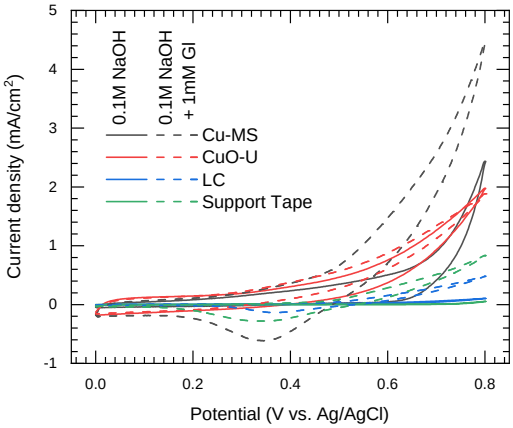

Figure 7.31: CV comparison of the selected composites and the reference films in presence and absence of the glucose in the electrolyte.

the material at the selected overpotential [261], supported by a nanostructured morphology. Both tested films exhibit improved response in the presence of glucose compared to the reference solution with the overpotential above 0.4 V. Thus, the overpotential was selected at 0.5 V for further real-time amperometric tests.

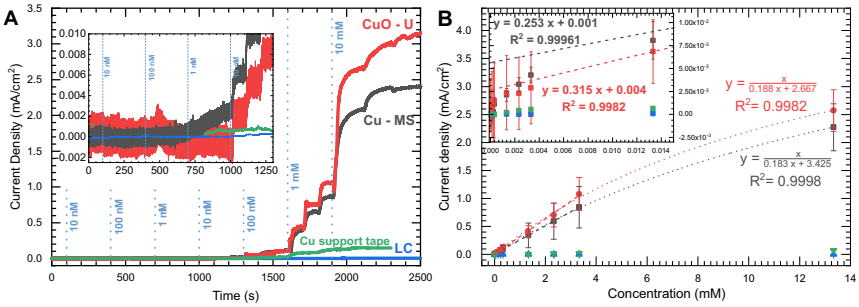

Figure 7.32: (A) Amperometric response by increasing of the glucose concentration in 100 mM NaOH electrolyte and (B) the extracted calibration curves of a current response on the glucose concentration.

Figure 7.32A shows amperometry response of the Cu-MS and CuO-U electrodes, after consequent injection of different glucose molarity starting from 10 nM to 10 mM in the 100 mM NaOH electrolyte. For comparison, the amperometric response of the laser carbon film and the supporting copper tape is also presented, each of which exhibited only a minor contribution to the total signal during the measurement. The calibration curves for both test samples are plotted in Figure 7.32B, and follow a linear dependency on the glucose concentration up to 3 mM. Particularly, the CuO-U electrode exhibited a more uniform step-like signal at low concentration and featured the current density saturation at a glucose concentration over 10 mM. The linear range of the amperometric response for both films was fit from 1 µM to 3 mM, with an R^2 of 0.9996 and 0.9982 for the CuO-U and the Cu-MS, respectively. The non-linear (hyperbolic) function as well can be used for fitting improvement for concentrations starting from minimal at 1 µM and allows the sensitivity range extension to 10 mM. The sensitivity of the CuO-U and the Cu-MS electrodes was 0.25 $mA\,cm^{-2}\,mM^{-1}$ and 0.32 $mA\,cm^{-2}\,mM^{-1}$, respectively, whereas the lower limit of detection (LOD) of these electrodes was 1.74 µM and 7.56 µM, respectively. Some increase in amperometric signal was observed after the glucose injection of 100 nM, but caused by high signal-to-noise ratio cannot reliably be derived. Thus, the fitting was initiated from 1 µM.

Both tested composite electrodes exhibited similar performance in terms of linear range and sensitivity, but suffered from thehigher LOD of glucose when compared to the carbon-based glucose sensors reported by other authors, as shown in Table 7.9. Such discrepancy is promoted by a reduction in the detection potential and reduction of the current and the electrode oxidation rate.

CuO-U film exhibits the presence of the majority Cu^{2+} oxide species and shows their retention after the amperometry tests, with minor chemical modification, as it was priorly observed via CV tests. Moreover, CuO urchins show strong adhesion to LC substrate providing robustness under mechanical strain. During the amperometric test, only the soluble hydroxyl species are adsorbed on CuO-U, thus the film can be reused after rinsing in the DI water [261]. These features facilitated the selection of this film for further multiple repetitions test, with rinsing

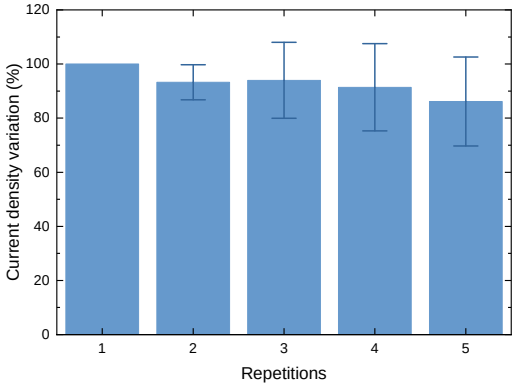

Figure 7.33: Amperometric signal reduction after multiple uses.

in the DI water after each cycle. Figure 7.33D shows the amperometric response retention after multiple repetitions, where the signal shows deviation within 15 % after five cycles.

The surface morphology and chemistry after the last amperometric measurement was studied with SEM depicted in Figure 7.34. The population of the Cu-MS and the CuO-U microparticles decreased ∼7 % and ∼15 %, respectively. In particular,

Table 7.9: Comparison of flexible and carbon based glucose sensors

Electrode	Detection potential, V	Sensitivity, $mA\,cm^{-2}\,mM^{-1}$	Linear range, mM	LOD, μM	Ref.
Cu-MS/LC	0.50	0.25	0.001–3.3	1.75	This work
CuO-U/LC	0.50	0.32	0.001–3.3	7.56	This work
CuO-U/LC (bent)	0.50	0.13	0.01–0.3	5.54	This work
CuO/graphene	0.55	1.36	0.002–4	0.70	[270]
Cu nanowire/graphene	0.60	1.10	0.005–6	1.60	[271]
CuO/MWCNT	0.55	2.19	0.001–3	0.80	[272]
CuO NW/SWCNT	0.60	2.19	0.001–0.034	0.05	[273]
Naflon/CuO/GC	0.60	0.41	0.05–2.55	1.00	[274]
Cu/MnO_2/GC	0.70	0.38	0.25–1.02	0.10	[275]
Pt–NiO/rGO/GC	0.50	0.83	0.008-14.5	2.67	[276]
Ni-SnOx/PANI/CuO	0.65	1.63; 1.33	0.001–1; 1-10	0.13	[282]
GOx/PtNP/LC	0.40	0.07	0.001–2.1	0.30	[253]
Cu NP/LC	0.50	0.50	0.01–6	0.39	[268]

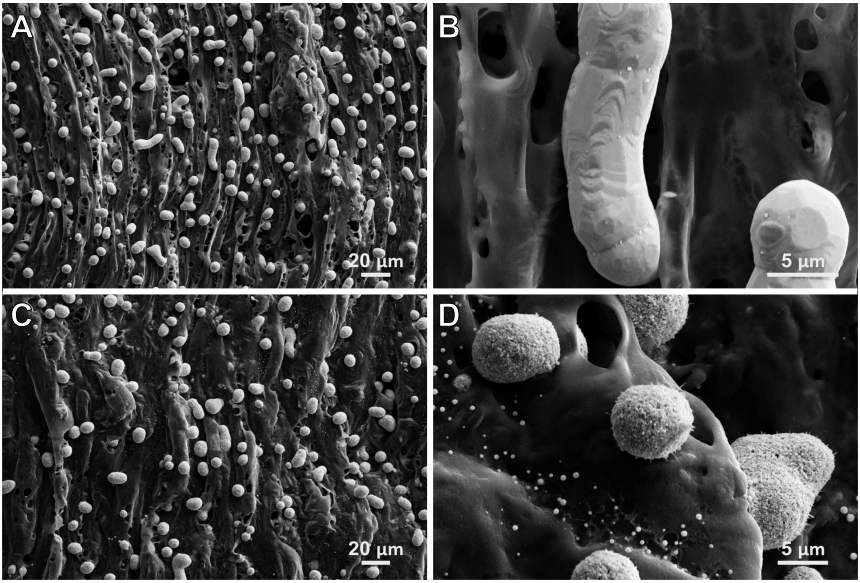

Figure 7.34: SEM imaging the film surfaces after the amperometric tests of (A,B) Cu-MS and (C,D) CuO-MS.

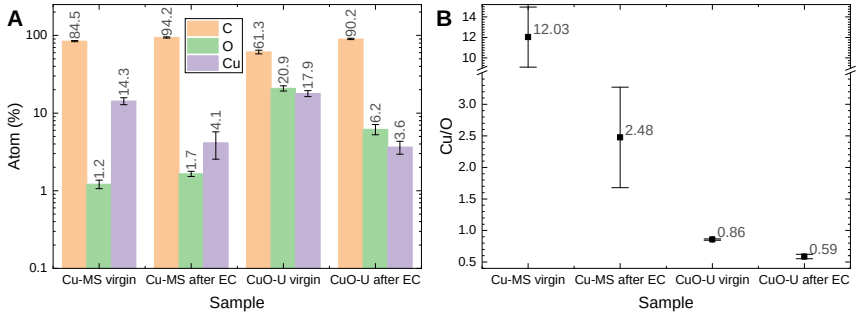

Figure 7.35: (A) Surface chemical composition determined with EDX before and after amperometric test. (B) Derived Cu/O ration from chemical composition.

the nanometric features, nanowires and particles, from both substrates almost completely detached after the amperometric testing. Due to such reduction, the copper chemical composition significantly dropped in both cases, as depicted in

Figure 7.35A. The substrate does not feature significant oxidation, and most of the oxygen is bonded with the microparticles. Figure 7.35B features estimation of the copper to the oxygen ratio showing a significantly faster oxidation rate for Cu-MS rate. The revealing of the rough CuO-U surface with the reduced nanowire presence and underlying microparticles is still sufficient to provide the adequate oxidation rate for amperometric signal within relatively close limits and show signal deterioration $\sim$5 % after each cycle. Despite EDX showing a significant change in the Cu/O ratio, we speculate that the surface remains predominately in CuO phase, due to depth penetration of the electron beam within microns, the contribution from the core Cu_2O. During the amperometric test, only the soluble hydroxyl species were adsorbed on CuO-U, thus the electrode could be reused after their removal by rinsing with DI water [261].

Such a low-cost glucose sensor was additionally tested after flexing at $\pm 90°$, and presented in Figure 7.36. However, it suffered from significant deterioration of the signal at low concentration and exhibited signal response from 10 µM to $\sim$20 mM, which was fit with Michaelis–Menten function, characteristic to the catalytic systems [301]. The linear range was observed between 10 µM to 300 µM, with signal reaching saturation and attributing reduction of the sensitivity to 0.13 mA cm^{-2} mM^{-1}. All these changes can be attributed to the reduction of the

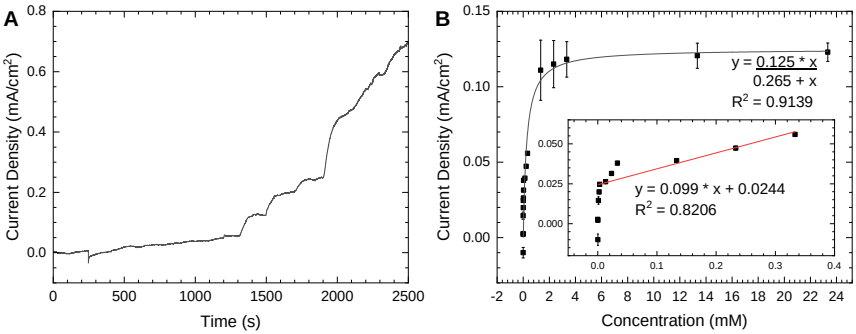

Figure 7.36: (A) Amperometric response performed after film bending $\pm 90°$ with (B) the calibration curves of a current response on the glucose concentration. Parts are taken from Ref. [70]

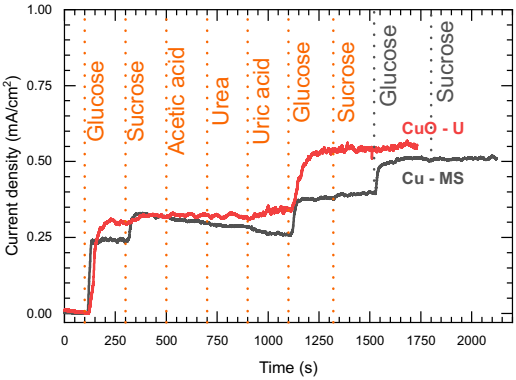

Figure 7.37: Amperometric response of the composite films by consecutive adding 1 mM of each the indicated analytes.

sensing area and poor electrical connection between the electrode and electroplated copper. Although the amperometric response deteriorated in sensitivity and LOD in the bent state, the fabricated material remained in line with other flexible glucose sensors as indicated in Table 7.9.

The glucose detection in the blood and the sweat requires selectivity in sensing due to other interfering endogenous compounds such as urea, uric acid, acetic acid, other sugars (sucrose, fructose), which could constrain the functionality of the enzyme-free sensors [261]. As it is shown in Figure 7.37, no signal was detected in the presence of the other analytes, but Cu-MS responses to sucrose. Such response attenuates to the baseline level after $\sim$1000 s, and further do not show any significant contribution after multiple sucrose additions. The activity to the sucrose occurs due to oxidation of the micro and nanostructured copper [302]. There, the sucrose hydrolyses to fructose and glucose in the presence of an alkaline electrolyte, further promoting the generation of the gluconic acid through a similar reaction chain. The involved reaction with sucrose is shown in Figure C1. The additional electrochemical testing with sucrose on both substrates is depicted in Figure C2. At the selected potential, only Cu-MS indicate an increase in amperometric signal, whereas CuO-U is active only in the presence of glucose.

Thus, Cu-MS was selected for the detailed amperometric study in the presence of sucrose, and it is shown in Figure C3.

7.6 Summary

Polyaramid showed good laser-induced carbonisation as independent fibres and embedded rolled sheets mixed with cellulose, which can be rendered in arbitrary planar shapes. The fabrication demonstrates the tunability of the properties through variations of pulse distances and irradiation sequences. The two best recipes were indicated, yielding a flexible carbon-rich film with low sheet resistance or a robust film with the constrained bendability but significantly lower electrical resistance due to presence of a metastable rhombohedral phase firstly demonstrated through LIC. The further copper electroplating makes this composite a viable option in the multiple fields.

These composite films were successfully used for the antibacterial coatings, in particular against *E. coli* and *B. subtilis*. While the copper film itself showed the elimination of countable colonies after the initial exposition of its carbon precursor significantly decreased the growth rate of *E. coli* and the overall amount of colonies of *B. subtilis*. The porosity and the surface activity of the prepared laser carbon films with this recipe, in conjunction with the delivered thin copper layers, is suitable for the use as disposable antimicrobial surfaces, but also flexible sensing electronics, molecular sieves, catalysis, could potentially serve as a hydrogen storage platform.

The second recipe was utilised as a substrate for the growth of the copper and copper oxide composites filled with micro and nanostructured features, suitable for enzyme-free glucose detection. The kinetics in the formation of such structures on laser carbon was elucidated, and their properties were vigorously analysed. Both electrode types exhibited amperometric activity in the presence of glucose with a superior sensitivity compared to other carbon-based glucose sensor materials. The sensitivity of the Cu-MS and the CuO-U electrodes was $0.25\,\mathrm{mA\,cm^{-2}\,mM^{-1}}$ and $0.32\,\mathrm{mA\,cm^{-2}\,mM^{-1}}$ respectively within a linear range between $1\,\mu\mathrm{M}$ and

$\sim$3.3 mM. The limit of detection was estimated at 1.75 µM and 7.56 µM for the Cu-MS and CuO-U electrode, respectively, which is in line with other carbon-based glucose sensors. Furthermore, the fabricated electrodes exhibited excellent selectivity towards the glucose. However, the Cu-MS electrode also exhibited some sensing activity in the sucrose presence. The composite electrodes were also flexible and retained their sensing capabilities after the multiple bending repetitions. The saturation sensitivity of the electrodes was determined at $\sim$300 µM, which requires further improvement for a viable device. These fabricated substrates are suitable for the personalised, flexible point-of-care glucose monitoring and the determination of sugar concentration in the food industry.

8 Conclusions & Future Outlook

The main questions set in introduction of this thesis is searching the effective technologies and materials suitable for point of care devices to timely medical monitoring addressed by the Internet of Things via flexible electronics. The main criteria are set as follows: ease of production, accessibility, abundance of substrates and materials, and low-cost of complete manufacturing process for the extensive application in technological cycle. Here, those challenges are elaborated, and the potential in future work is discussed.

The laser-induced carbonisation (pyrolysis) has been manifested as a one-step fabrication technology through the direct native polymer processing in controlled or ambient environment. Multiple precursors exhibit a tendency for such phase transformation, among which Kapton, Nomex, Kevlar were the best, and more over established in the abundant manufacturing chains. Due to the large production scale and high customer demand, the average cost for these precursors is estimated to be below at 5 € for a square meter of the film. Moreover, the newly developed mixtures with naturally occurring bio-polymers show potential in LIC with similar properties opening a niche for environmentally friendly manufacturing.

The laser processing duration significantly reduces the production time compared to thermal bulk pyrolysis, additionally sustained by fabrication in the ambient conditions instead of specifically supported inert environment. The rasterisation with different shapes directly incorporated within a flexible precursor matrix provides a significant benefit for the final device fabrication and avoids any additional steps in transferring to the carrier substrate. Driven by these factors, the manufacturing process is shown capable of scaling up into the semi-industrial and the industrial levels within the roll-to-roll machines.

In addition to the advantages mentioned above, the fabricated with LIC films attain the quality comparable to the glassy carbon or even exceeding it due to the extreme high temperatures involved in the process. However, the specific electrical conductivity remains a challenge due to the high film porosity. Additionally, stoichiometry and chemical reactivity are controllable by selecting multiple parameters: the wavelength, due to the absorption capability of each precursor in the selected radiation regions, and the processing parameters, such as power, fluence, and pulse duration, and the working environments. Separate research on these aspects was already laid out, but it requires more systematic analysis to precisely estimate the controllable film characteristics. Additionally, the phase transformation model should expand and approximate all possible contributions for the film properties.

All these factors appeal to confirm the great potential of the LIC produced carbon-rich films for the industrial use and set a route for utilisation in IoT sensors. They have already shown multiple prospective applications in force and stress sensors, humidity detectors, magnetic actuators and supercapacitors. However, the strongest side of the laser carbon films resides in the chemical detection due to the present functional groups and high surface to volume ratio. The specific analytes can be triggered by influencing functional markers on the laser carbon substrate, in some cases native or easily adhered to the substrate. This would allow large scale manufacturing of passive and active sensors for the long-term health monitoring and assessing possible risks.

From this range of tasks, the LIC was selectively tested for Kapton and Nomex, the thermal model was applied for the intrinsic processing parameters estimation at the selected wavelength and the pulse duration. The thermal model allowed the estimation of the temperature range for the wide thickness range. The simulation was modified with the transitional temperatures to the glassy carbon and graphite at selected regimes. This model showed good corroboration with the observed physical and chemical properties of the films and allowed a better understanding of the processes. It requires further modification for estimation of the expulsion

jet flux and built-up pressures for more precise morphological structure, which can further help approximate the intrinsic properties.

Utilising the potential of chemical surface activity of Kapton film, the composite enzymatic chitosan/laser carbon Urea sensor was built. This sensor can be easily and quickly prepared showing the great potential for storage in low-maintaining controlled conditions, and is used for passive Urea sensing. The detection limit is set at $\sim$100 µM, which is twofold below the human risk limit. Further conjugation with other enzymes could allow the active analyte detection. Nevertheless, the composite preparation with chitosan shows a great potential in the wide range of enzymatic sensors and microchannels with the predefined shapes by rasterisation patterns.

Nomex was selected as an alternative precursor and showed a greater specificity in fabrication due to the weaker monomer bonds and less dense packing. Despite these constraints, specific parameters were selected for fabrication of the conductive tracks serving as a seed layer for the plating of copper, which significantly improved the electrical conductivity, and at the specific plating regime at 30 mA cm^{-2} for 300 s allowed balanced preparation of the flexible film, featuring retention after the multiple bending cycles. Such films were utilised for antibacterial coatings and showed properties comparable with the native metals, despite being a few microns thick. More rigid laser carbon films attributed properties significantly closer to the highly graphitised carbon from polymer precursors. They served as the great composite substrate for seeding with copper/copper oxide nano and microstructures after a specific annealing regime. These composites were used for enzyme-free glucose sensing, and both types showed detection limits $<$10 µM, which is twofold below the required detection limit from urine, saliva, sweat and blood for prevention of the health risks for diabetes patients.

The LIC provides a great possibility in the analytes' localised detection, particularly due to the scalable and controllable fabrication of several micron-thick tracks. To date, these approaches can allow the incorporated test systems preparation for analytes like glucose, urea, hydrogen peroxide, thrombin, biogenic amines, specific changes in nucleic acids, acetylcholinesterase inhibitors and excess antibiotic

contaminants like chloramphenicol. Moreover, the preparation techniques allow simultaneous monitoring from a volume of nanoliters within microfluidic cells, multielectrode arrays and directly alert the patients medical risks.

Bibliography

[1] Lee, S., Shi, Q., and Lee, C. From flexible electronics technology in the era of IoT and artificial intelligence toward future implanted body sensor networks, *APL Materials*, **2019**, *7*.

[2] Evans, D. The internet of things: How the next evolution of the internet is changing everything, *CISCO white paper*, **2011**, *1*, 1–11.

[3] Magrassi, P. Why a universal RFID infrastructure would be a good thing, *Technology*, **2002**, *16*, 0038.

[4] Zhan, Y., Mei, Y., and Zheng, L. Materials capability and device performance in flexible electronics for the Internet of Things, *J. Mater. Chem. C*, **2014**, *2*, 1220–1232.

[5] Stallings, W. *Foundations of modern networking: SDN, NFV, QoE, IoT, and Cloud*; Addison-Wesley Professional, **2015**.

[6] Nathan, A. et al. Flexible Electronics: The Next Ubiquitous Platform, *Proceedings of the IEEE*, **2012**, *100*, 1486–1517.

[7] Kumar, A. Methods and Materials for Smart Manufacturing: Additive Manufacturing, Internet of Things, Flexible Sensors and Soft Robotics, *Manufacturing Letters*, **2018**, *15*, 122–125.

[8] Chung, M., Fortunato, G., and Radacsi, N. Wearable flexible sweat sensors for healthcare monitoring: A review, *Journal of the Royal Society Interface*, **2019**, *16*.

[9] Huang, T.-C., Shao, L., Lei, T., Beausoleil, R., Bao, Z., and Cheng, K.-T. Robust design and design automation for flexible hybrid electronics, 2017 IEEE International Symposium on Circuits and Systems (ISCAS), **2017**; pp. 1–4.

[10] Matzeu, G., Florea, L., and Diamond, D. Advances in wearable chemical sensor design for monitoring biological fluids, *Sensors and Actuators B: Chemical*, **2015**, *211*, 403–418.

[11] Maurer, U., Rowe, A., Smailagic, A., and Siewiorek, D. P. eWatch: a wearable sensor and notification platform, International Workshop on Wearable and Implantable Body Sensor Networks (BSN'06), **2006**.

[12] MacDonald, W. A., Looney, M., MacKerron, D., Eveson, R., Adam, R., Hashimoto, K., and Rakos, K. Latest advances in substrates for flexible electronics, *Journal of the Society for Information Display*, **2007**, *15*, 1075–1083.

[13] Ling, H., Liu, S., Zheng, Z., and Yan, F. Organic flexible electronics, *Small Methods*, **2018**, *2*, 1800070.

[14] Novoselov, K. S., Geim, A. K., Morozov, S. V., Jiang, D., Zhang, Y., Dubonos, S. V., Grigorieva, I. V., and Firsov, A. A. Electric field effect in atomically thin carbon films, *science*, **2004**, *306*, 666–669.

[15] Kroto, H. W., Heath, J. R., O'Brien, S. C., Curl, R. F., and Smalley, R. E. C60: Buckminsterfullerene, *nature*, **1985**, *318*, 162–163.

[16] Iijima, S. Helical microtubules of graphitic carbon, *nature*, **1991**, *354*, 56–58.

[17] Iijima, S., and Ichihashi, T. Single-shell carbon nanotubes of 1-nm diameter, *nature*, **1993**, *363*, 603–605.

[18] Jenkins, G. M., Jenkins, A., and Kawamura, K. *Polymeric carbons: carbon fibre, glass and char*; Cambridge University Press, **1976**.

[19] Jiang, S., Shi, T., Zhan, X., Xi, S., Long, H., Gong, B., Li, J., Cheng, S., Huang, Y., and Tang, Z. Scalable fabrication of carbon-based MEMS/NEMS and their applications: a review, *Journal of Micromechanics and Microengineering*, **2015**, *25*, 113001.

[20] Sun, Z., Hasan, T., Torrisi, F., Popa, D., Privitera, G., Wang, F., Bonaccorso, F., Basko, D. M., and Ferrari, A. C. Graphene mode-locked ultrafast laser, *ACS nano*, **2010**, *4*, 803–810.

[21] Popa, D., Sun, Z., Hasan, T., Torrisi, F., Wang, F., and Ferrari, A. Graphene Q-switched, tunable fiber laser, *Applied Physics Letters*, **2011**, *98*, 073106.

[22] Ratinac, K. R., Yang, W., Ringer, S. P., and Braet, F. Toward Ubiquitous Environmental Gas Sensors- Capitalizing on the Promise of Graphene, *Environmental science & technology*, **2010**, *44*, 1167–1176.

[23] He, Q., Wu, S., Yin, Z., and Zhang, H. Graphene-based electronic sensors, *Chemical Science*, **2012**, *3*, 1764–1772.

[24] Recher, P., and Trauzettel, B. Quantum dots and spin qubits in graphene, *Nanotechnology*, **2010**, *21*, 302001.

[25] Wu, G., Lue, N.-Y., and Chang, L. Graphene quantum dots for valley-based quantum computing: A feasibility study, *Physical Review B*, **2011**, *84*, 195463.

[26] Rohling, N., and Burkard, G. Universal quantum computing with spin and valley states, *New Journal of Physics*, **2012**, *14*, 083008.

[27] Otsuji, T., Tombet, S. B., Satou, A., Fukidome, H., Suemitsu, M., Sano, E., Popov, V., Ryzhii, M., and Ryzhii, V. Graphene-based devices in terahertz science and technology, *Journal of Physics D: Applied Physics*, **2012**, *45*, 303001.

[28] de Heer, W. A., Berger, C., Wu, X., First, P. N., Conrad, E. H., Li, X., Li, T., Sprinkle, M., Hass, J., Sadowski, M. L., Potemski, M., and Martinez, G. Epitaxial graphene, *Solid State Communications*, **2007**, *143*, 92–100, Exploring graphene.

[29] Sutter, P. W., Flege, J.-I., and Sutter, E. A. Epitaxial graphene on ruthenium, *Nature materials*, **2008**, *7*, 406–411.

[30] Reina, A., Jia, X., Ho, J., Nezich, D., Son, H., Bulovic, V., Dresselhaus, M. S., and Kong, J. Large area, few-layer graphene films on arbitrary substrates by chemical vapor deposition, *Nano letters*, **2009**, *9*, 30–35.

[31] Gao, L., Guest, J. R., and Guisinger, N. P. Epitaxial graphene on Cu (111), *Nano letters*, **2010**, *10*, 3512–3516.

[32] Stankovich, S., Dikin, D. A., Piner, R. D., Kohlhaas, K. A., Kleinhammes, A., Jia, Y., Wu, Y., Nguyen, S. T., and Ruoff, R. S. Synthesis of graphene-based nanosheets via chemical reduction of exfoliated graphite oxide, *carbon*, **2007**, *45*, 1558–1565.

[33] Marcano, D. C., Kosynkin, D. V., Berlin, J. M., Sinitskii, A., Sun, Z., Slesarev, A., Alemany, L. B., Lu, W., and Tour, J. M. Improved synthesis of graphene oxide, *ACS nano*, **2010**, *4*, 4806–4814.

[34] Zhu, Y., Murali, S., Cai, W., Li, X., Suk, J. W., Potts, J. R., and Ruoff, R. S. Graphene and graphene oxide: synthesis, properties, and applications, *Advanced materials*, **2010**, *22*, 3906–3924.

[35] Fitzer, E., Kochling, K.-H., Boehm, H. P., and Marsh, H. Recommended terminology for the description of carbon as a solid (IUPAC Recommendations 1995), *Pure and Applied Chemistry*, **1995**, *67*, 473–506.

[36] Wang, C., and Madou, M. From MEMS to NEMS with carbon, *Biosensors and bioelectronics*, **2005**, *20*, 2181–2187.

[37] Wang, C., Zaouk, R., Park, B. Y., and Madou, M. J. Carbon as a MEMS material: micro and nanofabrication of pyrolysed photoresist carbon, *International Journal of Manufacturing Technology and Management*, **2008**, *13*, 360.

[38] Franklin, R. E. Crystallite Growth in Graphitizing and Non-Graphitizing Carbons, *Proceedings of the Royal Society A: Mathematical, Physical and Engineering Sciences*, **1951**, *209*, 196–218.

[39] Chakraborty, S., Ed. *Microfluidics and Microfabrication*; Springer US, **2010**.

[40] Schueller, O. J. A., Brittain, S. T., and Whitesides, G. M. Fabrication of glassy carbon microstructures by pyrolysis of microfabricated polymeric precursors, *Advanced Materials*, **1997**, *9*, 477–480.

[41] Schueller, O. J. A., Brittain, S. T., Marzolin, C., and Whitesides, G. M. Fabrication and Characterization of Glassy Carbon MEMS, *Chemistry of Materials*, **1997**, *9*, 1399–1406.

[42] Kim, J., Song, X., Kinoshita, K., Madou, M., and White, R. Electrochemical Studies of Carbon Films from Pyrolyzed Photoresist, *Journal of The Electrochemical Society*, **1998**, *145*, 2314–2319.

[43] Wang, C., Jia, G., Taherabadi, L. H., and Madou, M. J. A novel method for the fabrication of high-aspect ratio C-MEMS structures, *Journal of microelectromechanical systems*, **2005**, *14*, 348–358.

[44] Standage, A., and Prescott, R. High elastic modulus carbon fibre, *Nature*, **1966**, *211*, 169–169.

[45] Chung, D. D., and Chung, D. *Carbon fiber composites*; Elsevier, **2012**.

[46] Yamaguchi, T. Galvanomagnetic properties of glassy carbon, *Carbon*, **1963**, *1*, 47–50.

[47] Lee, J. A., Lee, S. W., Lee, K.-C., Park, S. I., and Lee, S. S. Fabrication and characterization of freestanding 3D carbon microstructures using multi-exposures and resist pyrolysis, *Journal of Micromechanics and Microengineering*, **2008**, *18*, 035012.

[48] Malladi, K., Wang, C., and Madou, M. Fabrication of suspended carbon microstructures by e-beam writer and pyrolysis, *Carbon*, **2006**, *44*, 2602–2607.

[49] Penmatsa, V., Kawarada, H., and Wang, C. Fabrication of carbon nanostructures using photo-nanoimprint lithography and pyrolysis, *Journal of Micromechanics and Microengineering*, **2012**, *22*, 045024.

[50] Du, R., Ssenyange, S., Aktary, M., and McDermott, M. T. Fabrication and characterization of graphitic carbon nanostructures with controllable size, shape, and position, *Small*, **2009**, *5*, 1162–1168.

[51] Wang, C., Zaouk, R., and Madou, M. Local chemical vapor deposition of carbon nanofibers from photoresist, *Carbon*, **2006**, *44*, 3073–3077.

[52] Gueli, C., Vomero, M., Sharma, S., and Stieglitz, T. Integration of Micro-Patterned Carbon Fiber Mats into Polyimide for the Development of Flexible Implantable Neural Devices, 2019 41st Annual International Conference of the IEEE Engineering in Medicine and Biology Society (EMBC), **2019**; pp. 3931–3934.

[53] Srinivasan, R. Ablation of polymers and biological tissue by ultraviolet lasers, *Science*, **1986**, *234*, 559–565.

[54] Srinivasan, R., Hall, R. R., Wilson, W. D., Loehle, W. D., and Allbee, D. C. Formation of a Porous, Patternable, Electrically Conducting Carbon Network by the Ultraviolet Laser Irradiation of the Polyimide PMDA-ODA (Kapton), *Chemistry of Materials*, **1994**, *6*, 888–889.

[55] Lin, J., Peng, Z., Liu, Y., Ruiz-Zepeda, F., Ye, R., Samuel, E. L. G., Yacaman, M. J., Yakobson, B. I., and Tour, J. M. Laser-induced porous graphene films from commercial polymers, *Nature Communications*, **2014**, *5*, 5714.

[56] Mamleyev, E. R., Heissler, S., Nefedov, A., Weidler, P. G., Nordin, N., Kudryashov, V. V., Länge, K., MacKinnon, N., and Sharma, S. Laser-induced hierarchical carbon patterns on polyimide substrates for flexible urea sensors, *npj Flexible Electronics*, **2019**, *3*, 2.

[57] Luong, D. X., Yang, K., Yoon, J., Singh, S. P., Wang, T., Arnusch, C. J., and Tour, J. M. Laser-induced graphene composites as multifunctional surfaces, *ACS nano*, **2019**, *13*, 2579–2586.

[58] Ye, R., James, D. K., and Tour, J. M. Laser-Induced Graphene: From Discovery to Translation, *Advanced Materials*, **2019**, *31*, 1–15.

[59] Li, Y., Luong, D. X., Zhang, J., Tarkunde, Y. R., Kittrell, C., Sargunaraj, F., Ji, Y., Arnusch, C. J., and Tour, J. M. Laser-Induced Graphene in Controlled Atmospheres: From Superhydrophilic to Superhydrophobic Surfaces, *Advanced Materials*, **2017**, *29*, 1–8.

[60] Chen, Y., Long, J., Zhou, S., Shi, D., Huang, Y., Chen, X., Gao, J., Zhao, N., and Wong, C. UV Laser-Induced Polyimide-to-Graphene Conversion: Modeling, Fabrication, and Application, *Small Methods*, **2019**, *3*, 1900208.

[61] Carvalho, A. F., Fernandes, A. J. S., Leitão, C., Deuermeier, J., Marques, A. C., Martins, R., Fortunato, E., and Costa, F. M. Laser-Induced Graphene Strain Sensors Produced by Ultraviolet Irradiation of Polyimide, *Advanced Functional Materials*, **2018**, *28*, 1–8.

[62] Stanford, M. G., Zhang, C., Fowlkes, J. D., Hoffman, A., Ivanov, I. N., Rack, P. D., and Tour, J. M. High-Resolution Laser-Induced Graphene. Flexible Electronics beyond the Visible Limit, *ACS Applied Materials & Interfaces*, **2020**, *12*, 10902–10907.

[63] Zhang, Z., Song, M., Hao, J., Wu, K., Li, C., and Hu, C. Visible light laser-induced graphene from phenolic resin: a new approach for directly writing graphene-based electrochemical devices on various substrates, *Carbon*, **2018**, *127*, 287–296.

[64] Mendes, L. F., de Siervo, A., Reis de Araujo, W., and Longo Cesar Paixão, T. R. Reagentless fabrication of a porous graphene-like electrochemical device from phenolic paper using laser-scribing, *Carbon*, **2020**, *159*, 110–118.

[65] Chyan, Y., Ye, R., Li, Y., Singh, S. P., Arnusch, C. J., and Tour, J. M. Laser-Induced Graphene by Multiple Lasing: Toward Electronics on Cloth, Paper, and Food, *ACS Nano*, **2018**, *12*, 2176–2183.

[66] Mamleyev, E. R., Falk, F., Weidler, P. G., Heissler, S., Wadhwa, S., Nassar, O., Shyam Kumar, C. N., Kübel, C., Wöll, C., Islam, M., Mager, D., and Korvink, J. G. Polyaramid-Based Flexible Antibacterial Coatings Fabricated Using Laser-Induced Carbonization and Copper Electroplating, *ACS Applied Materials & Interfaces*, **2020**, *12*, 53193–53205.

[67] Wang, H., Wang, H., Wang, Y., Su, X., Wang, C., Zhang, M., Jian, M., Xia, K., Liang, X., Lu, H., Li, S., and Zhang, Y. Laser Writing of Janus Graphene/Kevlar Textile for Intelligent Protective Clothing, *ACS Nano*, **2020**, *14*, 3219–3226, PMID: 32083839.

[68] Nasser, J., Lin, J., Zhang, L., and Sodano, H. A. Laser induced graphene printing of spatially controlled super-hydrophobic/hydrophilic surfaces, *Carbon*, **2020**, *162*, 570–578.

[69] Mamleyev, E. R., Heissler, S., Nefedov, A., Weidler, P. G., Nordin, N., Kudryashov, V. V., Länge, K., MacKinnon, N., and Sharma, S. Laser-induced hierarchical carbon patterns on polyimide substrates for flexible urea sensors, *npj Flexible Electronics*, **2019**, *3*, 2.

[70] Mamleyev, E. R., Weidler, P. G., Nefedov, A., Szabó, D. V., Islam, M., Mager, D., and Korvink, J. G. Nano- and Microstructured Copper/Copper Oxide Composites on Laser-Induced Carbon for Enzyme-Free Glucose Sensors, *ACS Applied Nano Materials*, **2021**,

[71] Mamleyev, E. R., Voigt, A., Moazenzadeh, A., Korvink, J. G., Kohl, M., and Poletkin, K. A Technological Approach for Miniaturization of Three-Dimensional Inductive Levitation Microsuspensions, *IEEE Magnetics Letters*, **2022**, *13*, 1–4.

[72] Poletkin, K. V., Babic, S., Kumar, S. S., and Mamleyev, E. R. Calculation of Mutual Inductance between Circular and Arbitrarily Shaped Filaments via Segmentation Method, *arXiv preprint arXiv:2209.00464*, **2022**,

[73] Julius, L. A. N., Matter, L., Schuergers, N., Lützenkirchen, J., Trouillet, V., Gil-Díaz, T., Mamleyev, E. R., Wilde, A., Badilita, V., and Korvink, J. G. Surface characterisation reveals substrate suitability for Cyanobacterial phototaxis, *Acta Biomaterialia*, **2022**,

[74] Mamleyev, E. R., Nordin, N., Heissler, S., Länge, K., MacKinnon, N., and Sharma, S. Flexible Carbon-based Urea Sensor by Laser Induced Carbonisation of Polyimide, 2018 International Flexible Electronics Technology Conference (IFETC), **2018**; pp. 1–6.

[75] Mamleyev, E., and Poletkin, K. Reduction of the Nested Solenoid Micro-Coil Size as a Path to Transporter Micro-Actuator Array, ACTUATOR 2022; International Conference and Exhibition on New Actuator Systems and Applications, **2022**; pp. 1–4.

[76] Lee, C. H., Kumar, S. S., Mamleyev, E., and Poletkin, K. Characterisation of Static Pull-In Effect of Hybrid Levitation Micro-Actuators for Square-Shaped Proof Masses, ACTUATOR 2022; International Conference and Exhibition on New Actuator Systems and Applications, **2022**; pp. 1–4.

[77] Kumar, S. S., Lee, C. H., Mamleyev, E., and Poletkin, K. Calculation of Mutual Inductance Between Circular and Arbitrary Shaped Filaments: Segmentation Method, ACTUATOR 2022; International Conference and Exhibition on New Actuator Systems and Applications, **2022**; pp. 1–4.

[78] Hecht, E. Optics 2nd edition, *opt2*, **1987**,

[79] Hecht, J. *The laser guidebook*; McGraw-Hill, New York, NY, **1986**.

[80] Herd, R. M., MRCP(UK),, Dover, J. S., and Arndt, K. A. BASIC LASER PRINCIPLES, *Dermatologic Clinics*, **1997**, *15*, 355–372.

[81] Pan, Y.-L., Bernhardt, A. F., and Simpson, J. R. Construction and Operation of a Double-Discharge TEA CO2 Laser, *Review of Scientific Instruments*, **1972**, *43*, 662–666.

[82] Sharma, S., Kumar, C. S., Korvink, J. G., and Kübel, C. Evolution of glassy carbon microstructure: in situ transmission electron microscopy of the pyrolysis process, *Scientific reports*, **2018**, *8*, 16282.

[83] Koev, S. T., Dykstra, P. H., Luo, X., Rubloff, G. W., Bentley, W. E., Payne, G. F., and Ghodssi, R. Chitosan: an integrative biomaterial for lab-on-a-chip devices, *Lab on a Chip*, **2010**, *10*, 3026.

[84] Rinaudo, M. Chitin and chitosan: Properties and applications, *Progress in polymer science*, **2006**, *31*, 603–632.

[85] Nordin, N., Bordonali, L., Davoodi, H., Ratnawati, N. D., Gygli, G., Korvink, J. G., Badilita, V., and MacKinnon, N. Real-time NMR monitoring of spatially segregated enzymatic reactions in multilayered hydrogel assemblies, *Angewandte Chemie*, **2021**,

[86] Davoodi, H., Nordin, N., Bordonali, L., Korvink, J. G., MacKinnon, N., and Badilita, V. An NMR-compatible microfluidic platform enabling in situ electrochemistry, *Lab on a Chip*, **2020**, *20*, 3202–3212.

[87] Reid, J. Copper Electrodeposition: Principles and Recent Progress, *Japanese Journal of Applied Physics*, **2001**, *40*, 2650–2657.

[88] Schlesinger, M., and Paunovic, M. *Modern electroplating*; John Wiley & Sons, **2011**; Vol. 55.

[89] Kelly, J. J., Tian, C., and West, A. C. Leveling and Microstructural Effects of Additives for Copper Electrodeposition, *Journal of The Electrochemical Society*, **1999**, *146*, 2540–2545.

[90] Nassar, O., Meissner, M. V., Wadhwa, S., Korvink, J. G., and Mager, D. Load sensitive stable current source for complex precision pulsed electroplating, *Review of Scientific Instruments*, **2019**, *90*, 104704.

[91] Larkin, P. *Infrared and Raman spectroscopy: principles and spectral interpretation*; Elsevier, **2017**.

[92] Griffiths, P. R., and De Haseth, J. A. *Fourier transform infrared spectrometry*; John Wiley & Sons, **2007**; Vol. 171.

[93] Crookes, W. V. The Bakerian Lecture.—On the illumination of lines of molecular pressure, and the trajectory of molecules, *Philosophical Transactions of the Royal Society of London*, **1879**, 135–164.

[94] Röntgen, W. On a New Kind of Rays, *Nature*, **1896**, *53*, 274–276.

[95] Fultz, B., and Howe, J. M. *Transmission electron microscopy and diffractometry of materials*; Graduate Texts in Physics; Springer Science & Business Media: Berlin, Heidelberg, **2012**.

[96] Bragg, W. H., and Bragg, W. L. The reflection of X-rays by crystals, *Proceedings of the Royal Society of London. Series A, Containing Papers of a Mathematical and Physical Character*, **1913**, *88*, 428–438.

[97] Friedrich, W., Knipping, P., and Laue, M. Interferenzerscheinungen bei Röntgenstrahlen, *Annalen der Physik*, **1913**, *346*, 971–988.

[98] Kittel, C., McEuen, P., and McEuen, P. *Introduction to solid state physics*; Wiley New York, **1996**; Vol. 8.

[99] Scherrer, P. *Kolloidchemie Ein Lehrbuch*; Springer, **1912**; pp. 387–409.

[100] Warren, B. E. X-ray diffraction in random layer lattices, *Physical Review*, **1941**, *59*, 693–698.

[101] Sutton, M. A., Li, N., Joy, D. C., Reynolds, A. P., and Li, X. Scanning Electron Microscopy for Quantitative Small and Large Deformation Measurements Part I: SEM Imaging at Magnifications from 200 to 10,000, *Experimental Mechanics*, **2007**, *47*, 775–787.

[102] Goldstein, J. I., Newbury, D. E., Michael, J. R., Ritchie, N. W. M., Scott, J. H. J., and Joy, D. C. *Scanning electron microscopy and X-ray microanalysis*; Springer, **2017**.

[103] Gatti, E., and Rehak, P. Semiconductor drift chamber—An application of a novel charge transport scheme, *Nuclear Instruments and Methods in Physics Research*, **1984**, *225*, 608–614.

[104] Gammer, C., Mangler, C., Rentenberger, C., and Karnthaler, H. Quantitative local profile analysis of nanomaterials by electron diffraction, *Scripta materialia*, **2010**, *63*, 312–315.

[105] Philips'Gloeilampenfabrieken, O. A method of measuring specific resistivity and Hall effect of discs of arbitrary shape, *Philips Res. Rep*, **1958**, *13*, 1–9.

[106] Ramadan, A., Gould, R., and Ashour, A. On the Van der Pauw method of resistivity measurements, *Thin Solid Films*, **1994**, *239*, 272–275.

[107] Hofmann, S. *Auger-and X-ray photoelectron spectroscopy in materials science: a user-oriented guide*; Springer Science & Business Media, **2012**; Vol. 49.

[108] Nicholson, R. S. Theory and Application of Cyclic Voltammetry for Measurement of Electrode Reaction Kinetics, *Analytical Chemistry*, **1965**, *37*, 1351–1355.

[109] Rusling, J. F., and Suib, S. L. Characterizing Materials with Cyclic Voltammetry, *Advanced Materials*, **1994**, *6*, 922–930.

[110] Van Benschoten, J. J., Lewis, J. Y., Heineman, W. R., Roston, D. A., and Kissinger, P. T. Cyclic voltammetry experiment, *Journal of Chemical Education*, **1983**, *60*, 772.

[111] Kissinger, P. T., and Heineman, W. R. Cyclic voltammetry, *Journal of Chemical Education*, **1983**, *60*, 702–706.

[112] Hickling, A. Studies in electrode polarisation, *Transactions of the Faraday Society*, **1941**, 27–33.

[113] Hoffmann, R., Kabanov, A. A., Golov, A. A., and Proserpio, D. M. Homo Citans and Carbon Allotropes: For an Ethics of Citation, *Angewandte Chemie International Edition*, **2016**, *55*, 10962–10976.

[114] Kharisov, B. I., and Kharissova, O. V. *Carbon Allotropes: Metal-Complex Chemistry, Properties and Applications*; Springer International Publishing: Cham, **2019**.

[115] Frondel, C., and Marvin, U. B. Lonsdaleite, a hexagonal polymorph of diamond, *Nature*, **1967**, *214*, 587–589.

[116] Wallace, P. R. The band theory of graphite, *Physical review*, **1947**, *71*, 622.

[117] Boehm, H.-P., Clauss, A., Fischer, G., and Hofmann, U. Das adsorptionsverhalten sehr dünner kohlenstoff-folien, *Zeitschrift für anorganische und allgemeine Chemie*, **1962**, *316*, 119–127.

[118] Boehm, H., Setton, R., and Stumpp, E. Nomenclature and terminology of graphite intercalation compounds, *Carbon*, **1986**, *24*, 241–245.

[119] Hummers Jr, W. S., and Offeman, R. E. Preparation of graphitic oxide, *Journal of the american chemical society*, **1958**, *80*, 1339–1339.

[120] Wen, X.-D., Hand, L., Labet, V., Yang, T., Hoffmann, R., Ashcroft, N., Oganov, A. R., and Lyakhov, A. O. Graphane sheets and crystals under pressure, *Proceedings of the national Academy of Sciences*, **2011**, *108*, 6833–6837.

[121] Hong, X., Cheng, S.-H., Herding, C., and Zhu, J. Colossal negative magnetoresistance in dilute fluorinated graphene, *Physical Review B*, **2011**, *83*, 085410.

[122] Haley, M. M., Brand, S. C., and Pak, J. J. Carbon networks based on dehydrobenzoannulenes: synthesis of graphdiyne substructures, *Angewandte Chemie International Edition in English*, **1997**, *36*, 836–838.

[123] Sharma, C. S., Sharma, A., and Madou, M. Multiscale carbon structures fabricated by direct micropatterning of electrospun mats of SU-8 photoresist nanofibers, *Langmuir*, **2010**, *26*, 2218–2222.

[124] Reich, S., and Thomsen, C. Raman spectroscopy of graphite, *Philosophical Transactions of the Royal Society of London. Series A: Mathematical, Physical and Engineering Sciences*, **2004**, *362*, 2271–2288.

[125] Lazzeri, M., Attaccalite, C., Wirtz, L., and Mauri, F. Impact of the electron-electron correlation on phonon dispersion: Failure of LDA and GGA DFT functionals in graphene and graphite, *Physical Review B*, **2008**, *78*, 081406.

[126] Luiggi, N., and Gómez, M. Rhombohedral graphite: Comparative study of the electronic properties, *Journal of Molecular Structure: THEOCHEM*, **2009**, *897*, 118–128.

[127] Latychevskaia, T., Son, S. K., Yang, Y., Chancellor, D., Brown, M., Ozdemir, S., Madan, I., Berruto, G., Carbone, F., Mishchenko, A., and

Novoselov, K. S. Stacking transition in rhombohedral graphite, *Frontiers of Physics*, **2019**, *14*, 1–7.

[128] Li, Z. Q., Lu, C. J., Xia, Z. P., Zhou, Y., and Luo, Z. X-ray diffraction patterns of graphite and turbostratic carbon, *Carbon*, **2007**, *45*, 1686–1695.

[129] Seehra, M. S., Geddam, U. K., Schwegler-Berry, D., and Stefaniak, A. B. Detection and quantification of 2H and 3R phases in commercial graphene-based materials, *Carbon*, **2015**, *95*, 818–823.

[130] Debye, P., and Scherrer, P. Interferenzen an regellos orientierten Teilchen im Röntgenlicht. I., *Nachrichten von der Gesellschaft der Wissenschaften zu Göttingen, Mathematisch-Physikalische Klasse*, **1916**, *1916*, 1–15.

[131] Bernal, J. D. The structure of graphite, *Proceedings of the Royal Society of London. Series A, Containing Papers of a Mathematical and Physical Character*, **1924**, *106*, 749–773.

[132] Lipson, H. S., and Stokes, A. R. The structure of graphite, *Proceedings of the Royal Society of London. Series A. Mathematical and Physical Sciences*, **1942**, *181*, 101–105.

[133] Malard, L. M., Pimenta, M. A., Dresselhaus, G., and Dresselhaus, M. S. Raman spectroscopy in graphene, *Physics Reports*, **2009**, *473*, 51–87.

[134] Laves, F., and Baskin, Y. On the Formation of the Rhombohedral Graphite Modification, *Zeitschrift fur Kristallographie - New Crystal Structures*, **1956**, *107*, 337–356.

[135] Haering, R. R. BAND STRUCTURE OF RHOMBOHEDRAL GRAPHITE, *Canadian Journal of Physics*, **1958**, *36*, 352–362.

[136] Biscoe, J., and Warren, B. E. An X-Ray Study of Carbon Black, *Journal of Applied Physics*, **1942**, *13*, 364–371.

[137] Howe, J. Y., Rawn, C. J., Jones, L. E., and Ow, H. Improved crystallographic data for graphite, *Powder Diffraction*, **2003**, *18*, 150–154.

[138] Manoj, B., and Kunjomana, A. Study of stacking structure of amorphous carbon by X-ray diffraction technique, *Int. J. Electrochem. Sci*, **2012**, *7*, 3127–3134.

[139] Shi, H., Barker, J., Saidi, M., Koksbang, R., and Morris, L. Graphite structure and lithium intercalation, *Journal of power sources*, **1997**, *68*, 291–295.

[140] Arrebola, J. C., Caballero, A., Hernáǹ, L., and Morales, J. Graphitized Carbons of Variable Morphology and Crystallinity: A Comparative Study of Their Performance in Lithium Cells, *Journal of The Electrochemical Society*, **2009**, *156*, A986.

[141] Ferrari, A. C. Raman spectroscopy of graphene and graphite: Disorder, electron-phonon coupling, doping and nonadiabatic effects, *Solid State Communications*, **2007**, *143*, 47–57.

[142] Dresselhaus, M. S., Jorio, A., Hofmann, M., Dresselhaus, G., and Saito, R. Perspectives on Carbon Nanotubes and Graphene Raman Spectroscopy, *Nano Letters*, **2010**, *10*, 751–758.

[143] Henni, Y., Ojeda Collado, H. P., Nogajewski, K., Molas, M. R., Usaj, G., Balseiro, C. A., Orlita, M., Potemski, M., and Faugeras, C. Rhombohedral multilayer graphene: A magneto-Raman scattering study, *Nano Letters*, **2016**, *16*, 3710–3716.

[144] Ferrari, A. C., and Robertson, J. Interpretation of Raman spectra of disordered and amorphous carbon, *Physical Review B*, **2000**, *61*, 14095–14107.

[145] Ferrari, A. C., and Basko, D. M. Raman spectroscopy as a versatile tool for studying the properties of graphene, *Nature nanotechnology*, **2013**, *8*, 235.

[146] Ferrari, A. C., Meyer, J. C., Scardaci, V., Casiraghi, C., Lazzeri, M., Mauri, F., Piscanec, S., Jiang, D., Novoselov, K. S., Roth, S., and Geim, A. K. Raman Spectrum of Graphene and Graphene Layers, *Physical Review Letters*, **2006**, *97*, 187401.

[147] Tuinstra, F., and Koenig, J. L. Raman spectrum of graphite, *The Journal of Chemical Physics*, **1970**, *53*, 1126–1130.

[148] Cançado, L. G., Takai, K., Enoki, T., Endo, M., Kim, Y. A., Mizusaki, H., Jorio, A., Coelho, L. N., Magalhães-Paniago, R., and Pimenta, M. A. General equation for the determination of the crystallite size La of nanographite by Raman spectroscopy, *Applied Physics Letters*, **2006**, *88*, 163106.

[149] Ni, Z., Wang, Y., Yu, T., You, Y., and Shen, Z. Reduction of Fermi velocity in folded graphene observed by resonance Raman spectroscopy, *Physical Review B*, **2008**, *77*, 235403.

[150] Siokou, A., Ravani, F., Karakalos, S., Frank, O., Kalbac, M., and Galiotis, C. Surface refinement and electronic properties of graphene layers grown on copper substrate: An XPS, UPS and EELS study, *Applied Surface Science*, **2011**, *257*, 9785–9790.

[151] Blyth, R., Buqa, H., Netzer, F., Ramsey, M., Besenhard, J., Golob, P., and Winter, M. XPS studies of graphite electrode materials for lithium ion batteries, *Applied Surface Science*, **2000**, *167*, 99–106.

[152] Datsyuk, V., Kalyva, M., Papagelis, K., Parthenios, J., Tasis, D., Siokou, A., Kallitsis, I., and Galiotis, C. Chemical oxidation of multiwalled carbon nanotubes, *carbon*, **2008**, *46*, 833–840.

[153] Estrade-Szwarckopf, H. XPS photoemission in carbonaceous materials: A "defect" peak beside the graphitic asymmetric peak, *Carbon*, **2004**, *42*, 1713–1721.

[154] Harris, P. J. F. Fullerene-related structure of commercial glassy carbons, *Philosophical Magazine*, **2004**, *84*, 3159–3167.

[155] Uden, P. C. Nomenclature and terminology for analytical pyrolysis (IUPAC Recommendations 1993), *Pure and applied chemistry*, **1993**, *65*, 2405–2409.

[156] McDonald-Wharry, J. S., Manley-Harris, M., and Pickering, K. L. Reviewing, Combining, and Updating the Models for the Nanostructure of Non-Graphitizing Carbons Produced from Oxygen-Containing Precursors, *Energy & Fuels*, **2016**, *30*, 7811–7826.

[157] Srinivasan, R., and Braren, B. Ablative photodecomposition of polymer films by pulsed far-ultraviolet (193 nm) laser radiation: Dependence of etch depth on experimental conditions, *Journal of Polymer Science: Polymer Chemistry Edition*, **1984**, *22*, 2601–2609.

[158] Singh, S. P., Li, Y., Zhang, J., Tour, J. M., and Arnusch, C. J. Sulfur-Doped Laser-Induced Porous Graphene Derived from Polysulfone-Class Polymers and Membranes, *ACS Nano*, **2018**, *12*, 289–297.

[159] Kochi, M., Shimada, H., and Kambe, H. Molecular aggregation and mechanical properties of Kapton H, *Journal of Polymer Science: Polymer Physics Edition*, **1984**, *22*, 1979–1985.

[160] Inagaki, M., Ohta, N., and Hishiyama, Y. Aromatic polyimides as carbon precursors, *Carbon*, **2013**, *61*, 1–21.

[161] Hatori, H., Yamada, Y., Shiraishi, M., Yoshihara, M., and Kimura, T. The mechanism of polyimide pyrolysis in the early stage, *Carbon*, **1996**, *34*, 201–208.

[162] Sazanov, Y. N., Antonova, T. A., Stepanov, N. G., Blazo, M., Toth, A., and Szekei, T. Mechanism of polycondensation of polyimides, *Acta Polymerica*, **1991**, *42*, 119–125.

[163] Ortelli, E. E., Geiger, F., Lippert, T., and Wokaun, A. Pyrolysis of Kapton® in Air: An in situ DRIFT Study, *Applied Spectroscopy*, **2001**, *55*, 412–419.

[164] Sharma, S., Sharma, A., Cho, Y. K., and Madou, M. Increased graphitization in electrospun single suspended carbon nanowires integrated with carbon-MEMS and carbon-NEMS platforms, *ACS Applied Materials and Interfaces*, **2012**, *4*, 34–39.

[165] Yamada, Y., Kim, J., Matsuo, S., and Sato, S. Nitrogen-containing graphene analyzed by X-ray photoelectron spectroscopy, *Carbon*, **2014**, *70*, 59–74.

[166] Stobinski, L., Lesiak, B., Malolepszy, A., Mazurkiewicz, M., Mierzwa, B., Zemek, J., Jiricek, P., and Bieloshapka, I. Graphene oxide and reduced graphene oxide studied by the XRD, TEM and electron spectroscopy methods, *Journal of Electron Spectroscopy and Related Phenomena*, **2014**, *195*, 145–154.

[167] Melke, Julia and Peter, Benedikt and Habereder, Anja and Ziegler, Juergen and Fasel, Claudia and Nefedov, Alexei and Sezen, Hikmet and Wöll, Christof and Ehrenberg, Helmut and Roth, Christina, Metal-Support Interactions of Platinum Nanoparticles Decorated N-Doped Carbon Nanofibers for the Oxygen Reduction Reaction, *ACS Applied Materials & Interfaces*, **2016**, *8*, 82–90.

[168] Zeng, D., Yung, K., and Xie, C. XPS investigation of the chemical characteristics of Kapton films ablated by a pulsed TEA CO2 laser, *Surface and Coatings Technology*, **2002**, *153*, 210–216.

[169] Diller, K., Klappenberger, F., Marschall, M., Hermann, K., Nefedov, a., Wöll, C., and Barth, J. V. Self-metalation of 2H-tetraphenylporphyrin on Cu(111): An x-ray spectroscopy study, *Journal of Chemical Physics*, **2012**, *136*.

[170] Chen, Y., Xie, B., Ren, Y., Yu, M., Qu, Y., Xie, T., Zhang, Y., and Wu, Y. Designed nitrogen doping of few-layer graphene functionalized by selective oxygenic groups, *Nanoscale Research Letters*, **2014**, *9*, 646.

[171] Mattevi, C., Eda, G., Agnoli, S., Miller, S., Mkhoyan, K. A., Celik, O., Mastrogiovanni, D., Granozzi, G., Carfunkel, E., and Chhowalla, M. Evolution of electrical, chemical, and structural properties of transparent and conducting chemically derived graphene thin films, *Advanced Functional Materials*, **2009**, *19*, 2577–2583.

[172] Krishnamoorthy, K., Veerapandian, M., Yun, K., and Kim, S. J. The chemical and structural analysis of graphene oxide with different degrees of oxidation, *Carbon*, **2013**, *53*, 38–49.

[173] López, G. P., Castner, D. G., and Ratner, B. D. XPS O 1s binding energies for polymers containing hydroxyl, ether, ketone and ester groups, *Surface and Interface Analysis*, **1991**, *17*, 267–272.

[174] Srinivasan, R., and Mayne-Banton, V. Self-developing photoetching of poly (ethylene terephthalate) films by far-ultraviolet excimer laser radiation, *Applied Physics Letters*, **1982**, *41*, 576–578.

[175] Andrew, J. E., Dyer, P. E., Forster, D., and Key, P. H. Direct etching of polymeric materials using a XeCl laser, *Applied Physics Letters*, **1983**, *43*, 717–719.

[176] Brannon, J. H., Lankard, J. R., Baise, A. I., Burns, F., and Kaufman, J. Excimer laser etching of polyimide, *Journal of Applied Physics*, **1985**, *58*, 2036–2043.

[177] Urech, L., and Lippert, T. Photoablation of polymer materials, *Photochemistry and photophysics of polymer materials*, **2010**, 541–568.

[178] Srinivasan, R. Ablation of polyimide (Kapton™) films by pulsed (ns) ultraviolet and infrared (9.17 μm) lasers, *Applied Physics A Solids and Surfaces*, **1993**, *56*, 417–423.

[179] Lu, X., Wang, X., Li, Q., Huang, X., Han, S., and Wang, G. A ReaxFF-based molecular dynamics study of the pyrolysis mechanism of polyimide, *Polymer Degradation and Stability*, **2015**, *114*, 72–80.

[180] Dong, Y., Rismiller, S. C., and Lin, J. Molecular dynamic simulation of layered graphene clusters formation from polyimides under extreme conditions, *Carbon*, **2016**, *104*, 47–55.

[181] Koren, G., and Yeh, J. Emission spectra and etching of polymers and graphite irradiated by excimer lasers, *Journal of applied physics*, **1984**, *56*, 2120–2126.

[182] Ortelli, E. E., Geiger, F., Lippert, T., Wei, J., and Wokaun, A. UV-Laser-Induced Decomposition of Kapton Studied by Infrared Spectroscopy, *Macromolecules*, **2000**, *33*, 5090–5097.

[183] Dreyfus, R. W. CN temperatures above laser ablated polyimide, *Applied Physics A Solids and Surfaces*, **1992**, *55*, 335–339.

[184] Lazare, S., and Granier, V. Ultraviolet laser photoablation of polymers: a review and recent results, *Laser Chemistry*, **1989**, *10*, 25–40.

[185] Bityurin, N. UV etching accompanied by modifications. Surface etching, *Applied surface science*, **1999**, *138*, 354–358.

[186] Arnold, N., and Bityurin, N. Model for laser-induced thermal degradation and ablation of polymers, *Applied Physics A: Materials Science & Processing*, **1999**, *68*, 615–625.

[187] Dyer, P. E., Pervolaraki, M., and Lippert, T. Experimental studies and thermal modelling of 1064- And 532-nm Nd:YVO 4 micro-laser ablation

of polyimide, *Applied Physics A: Materials Science and Processing*, **2005**, *80*, 529–536.

[188] Yang, H., Yan, R., Chen, H., Lee, D. H., and Zheng, C. Characteristics of hemicellulose, cellulose and lignin pyrolysis, *Fuel*, **2007**, *86*, 1781–1788.

[189] Wanjun, T., Cunxin, W., and Donghua, C. Kinetic studies on the pyrolysis of chitin and chitosan, *Polymer Degradation and Stability*, **2005**, *87*, 389–394.

[190] Küper, S., and Stuke, M. Femtosecond uv excimer laser ablation, *Applied Physics B Photophysics and Laser Chemistry*, **1987**, *44*, 199–204.

[191] Carslaw, H. S., and Jaeger, J. C. *Conduction of heat in solids*; Clarendon press, **1992**.

[192] Ye, R., James, D. K., and Tour, J. M. Laser-Induced Graphene, *Accounts of Chemical Research*, **2018**, *51*, 1609–1620.

[193] Zhang, Z. M., Lefever-Button, G., and Powell, F. R. Infrared refractive index and extinction coefficient of polyimide films, *International Journal of Thermophysics*, **1998**, *19*, 905–916.

[194] Yang Yang,, Di Yin,, Rui Xiong,, Jing Shi,, Fuqiang Tian,, Xuan Wang,, and Qingquan Lei, Ftir and dielectric studies of electrical aging in polyimide under AC voltage, *IEEE Transactions on Dielectrics and Electrical Insulation*, **2012**, *19*, 574–581.

[195] Wan, Z., Nguyen, N.-T., Gao, Y., and Li, Q. Laser induced graphene for biosensors, *Sustainable Materials and Technologies*, **2020**, e00205.

[196] Kaidarova, A., Liu, W., Swanepoel, L., Almansouri, A., Geraldi, N. R., Duarte, C. M., and Kosel, J. Flexible Hall sensor made of laser-scribed graphene, *npj Flexible Electronics*, **2021**, *5*, 1–7.

[197] Vivaldi, F. M., Dallinger, A., Bonini, A., Poma, N., Sembranti, L., Biagini, D., Salvo, P., Greco, F., and Di Francesco, F. Three-dimensional

(3D) laser-induced graphene: structure, properties, and application to chemical sensing, *ACS Applied Materials & Interfaces*, **2021**, *13*, 30245–30260.

[198] Socrates, G. *Infrared and Raman characteristic group frequencies*; John Wiley & Sons, **2004**; p 366.

[199] Garg, M., and Quamara, J. K. FTIR analysis of high energy heavy ion irradiated kapton-H polyimide, *Indian Journal of Pure and Applied Physics*, **2007**, *45*, 563–568.

[200] Speight, J. G. *Lange's handbook of chemistry*; McGraw-Hill Education, **2017**.

[201] Ortelli, E. E., Geiger, F., Lippert, T., Wei, J., and Wokaun, A. UV-Laser-Induced Decomposition of Kapton Studied by Infrared Spectroscopy, *Macromolecules*, **2000**, *33*, 5090–5097.

[202] Ishida, H., Wellinghoff, S. T., Baer, E., and Koenig, J. L. Spectroscopic Studies of Poly[N,N'-bis(phenoxyphenyl)pyromellitimide]. 1. Structures of the Polyimide and Three Model Compounds, *Macromolecules*, **1980**, *13*, 826–834.

[203] Jellinek, H. H. G., and Srinivasan, R. Theory of etching of polymers by far-ultraviolet high-intensity pulsed laser- and long-term irradiation, *The Journal of Physical Chemistry*, **1984**, *88*, 3048–3051.

[204] Ferrari, A. C., Rodil, S. E., and Robertson, J. Interpretation of infrared and Raman spectra of amorphous carbon nitrides, *Physical Review B*, **2003**, *67*, 155306.

[205] Nemethy, G. Hydrophobic interactions, *Angewandte Chemie International Edition in English*, **1967**, *6*, 195–206.

[206] Paulaitis, M. E., Garde, S., and Ashbaugh, H. S. The hydrophobic effect, *Current Opinion in Colloid & Interface Science*, **1996**, *1*, 376–383.

[207] Kaidarova, A., Marengo, M., Marinaro, G., Geraldi, N., Duarte, C. M., and Kosel, J. Flexible and Biofouling Independent Salinity Sensor, *Advanced Materials Interfaces*, **2018**, *5*, 1–6.

[208] Cardoso, A. R., Marques, A. C., Santos, L., Carvalho, A. F., Costa, F. M., Martins, R., Sales, M. G. F., and Fortunato, E. Molecularly-imprinted chloramphenicol sensor with laser-induced graphene electrodes, *Biosensors and Bioelectronics*, **2019**, *124-125*, 167–175.

[209] Nayak, P., Kurra, N., Xia, C., and Alshareef, H. N. Highly Efficient Laser Scribed Graphene Electrodes for On-Chip Electrochemical Sensing Applications, *Advanced Electronic Materials*, **2016**, *2*, 1600185.

[210] Vanholder, R., Baurmeister, U., Brunet, P., Cohen, G., Glorieux, G., and Jankowski, J. A Bench to Bedside View of Uremic Toxins, *Journal of the American Society of Nephrology*, **2008**, *19*, 863–870.

[211] Giardino, I., D'apolito, M., Brownlee, M., Maffione, A. B., Colia, A. L., Sacco, M., Ferrara, P., and Pettoello-Mantovani, M. Vascular toxicity of urea, a new "old player" in the pathogenesis of chronic renal failure induced cardiovascular diseases, *Turkish Archives of Pediatrics/Türk Pediatri Arşivi*, **2017**, *52*, 187.

[212] Yamano, E., Sugimoto, M., Hirayama, A., Kume, S., Yamato, M., Jin, G., Tajima, S., Goda, N., Iwai, K., Fukuda, S., Yamaguti, K., Kuratsune, H., Soga, T., Watanabe, Y., and Kataoka, Y. Index markers of chronic fatigue syndrome with dysfunction of TCA and urea cycles, *Scientific Reports*, **2016**, *6*.

[213] Gropman, A. L., and Batshaw, M. L. Cognitive outcome in urea cycle disorders, *Molecular genetics and metabolism*, **2004**, *81*, 58–62.

[214] Azeem, B., KuShaari, K., Man, Z. B., Basit, A., and Thanh, T. H. Review on materials & methods to produce controlled release coated urea fertilizer, *Journal of controlled release*, **2014**, *181*, 11–21.

[215] Udert, K. M., Larsen, T. A., Biebow, M., and Gujer, W. Urea hydrolysis and precipitation dynamics in a urine-collecting system, *Water research*, **2003**, *37*, 2571–2582.

[216] Wang, Y., Alsmeyer, D. C., and McCreery, R. L. Raman spectroscopy of carbon materials: structural basis of observed spectra, *Chemistry of Materials*, **1990**, *2*, 557–563.

[217] Patake, V. D., Ghogare, T. T., Gulbake, A. D., and Lokhande, C. D. The electrochemical performance of electrodeposited chitosan bio-nanopolymer in non-aqueous electrolyte: a new anodic material for supercapacitor, *SN Applied Sciences*, **2019**, *1*.

[218] Guo, X., Dai, Y., Gong, M., Qu, Y., and Helseth, L. Changes in wetting and contact charge transfer by femtosecond laser-ablation of polyimide, *Applied Surface Science*, **2015**, *349*, 952–956.

[219] Pawlak, A., and Mucha, M. Thermogravimetric and FTIR studies of chitosan blends, *Thermochimica Acta*, **2003**, *396*, 153–166.

[220] Singh, A., Sinsinbar, G., Choudhary, M., Kumar, V., Pasricha, R., Verma, H. N., Singh, S. P., and Arora, K. Graphene oxide-chitosan nanocomposite based electrochemical DNA biosensor for detection of typhoid, *Sensors and Actuators B: Chemical*, **2013**, *185*, 675–684.

[221] Aronson, D., Mittleman, M. A., and Burger, A. J. Elevated blood urea nitrogen level as a predictor of mortality in patients admitted for decompensated heart failure, *The American journal of medicine*, **2004**, *116*, 466–473.

[222] Krajewska, B., Leszko, M., and Zaborska, W. Urease immobilized on chitosan membrane: preparation and properties, *Journal of Chemical Technology & Biotechnology*, **1990**, *48*, 337–350.

[223] Young, R., Lu, D., Day, R., Knoff, W., and Davis, H. Relationship between structure and mechanical properties for aramid fibres, *Journal of materials science*, **1992**, *27*, 5431–5440.

[224] Villar-Rodil, S. and Martínez-Alonso, A. and Tascón, J. M. D., Studies on pyrolysis of Nomex polyaramid fibers, *Journal of Analytical and Applied Pyrolysis*, **2001**, *58-59*, 105–115.

[225] Al-Sulaiman, F. and Yilbas, B. S. and Karakas, F. C. and Ahsan, M. and Mokheimer, E. M. A., Laser hole cutting in Kevlar: Modeling and quality assessment, *International Journal of Advanced Manufacturing Technology*, **2008**, *38*, 1125–1136.

[226] Doyle, D. J., and Kokosa, J. M. The laser cutting of kevlar: A study of the chemical by-products, *Materials and Manufacturing Processes*, **1990**, *5*, 609–615.

[227] Ruan, X., Wang, R., Luo, J., Yao, Y., and Liu, T. Experimental and modeling study of CO2 laser writing induced polyimide carbonization process, *Materials & Design*, **2018**, *160*, 1168–1177.

[228] Lee, H. S., Hong, S. H., Lee, J. R., and Kim, Y. K. Mechanical behavior and failure process during compressive and shear deformation of honeycomb composite at elevated temperatures, *Journal of Materials Science*, **2002**, *37*, 1265–1272.

[229] Smith, M. K. and Luong, D. X. and Bougher, T. L. and Kalaitzidou, K. and Tour, J. M. and Cola, B. A., Thermal conductivity enhancement of laser induced graphene foam upon P3HT infiltration, *Applied Physics Letters*, **2016**, *109*.

[230] Aurbach, D., Teller, H., and Levi, E. Morphology/Behavior Relationship in Reversible Electrochemical Lithium Insertion into Graphitic Materials, *Journal of The Electrochemical Society*, **2002**, *149*, A1255.

[231] Cui, C., Gao, Y., Li, J., Yang, C., Liu, M., Jin, H., Xia, Z., Dai, L., Lei, Y., Wang, J., and Wang, S. Origins of Boosted Charge Storage on Heteroatom-Doped Carbons, *Angewandte Chemie*, **2020**, *132*, 8002–8007.

[232] Gyenge, E., Jung, J., and Mahato, B. Electroplated reticulated vitreous carbon current collectors for lead-acid batteries: Opportunities and challenges, *Journal of Power Sources*, **2003**, *113*, 388–395.

[233] Biesinger, M. C., Payne, B. P., Grosvenor, A. P., Lau, L. W., Gerson, A. R., and Smart, R. S. Resolving surface chemical states in XPS analysis of first row transition metals, oxides and hydroxides: Cr, Mn, Fe, Co and Ni, *Applied Surface Science*, **2011**, *257*, 2717–2730.

[234] Biesinger, M. C. Advanced analysis of copper X-ray photoelectron spectra, *Surface and Interface Analysis*, **2017**, *49*, 1325–1334.

[235] He, G., and Wang, L. One-step preparation of ultra-thin copper oxide nanowire arrays/copper wire electrode for non-enzymatic glucose sensor, *Ionics*, **2018**, *24*, 3167–3175.

[236] Czochralski, J. Ein neues Verfahren zur Messung der Kristallisationsgeschwindigkeit der Metalle, *Zeitschrift für Physikalische Chemie*, **1918**, *92U*, 219–221.

[237] Mills, E. L. Viral infections predisposing to bacterial infections, *Annual review of medicine*, **1984**, *35*, 469–479.

[238] Sieswerda, Elske and De Boer, Mark GJ and Bonten, Marc MJ and Boersma, Wim G and Jonkers, René E and Aleva, Roel M and Kullberg, Bart-Jan and Schouten, Jeroen A and van de Garde, Ewoudt MW and Verheij, Theo J and others, j. Recommendations for antibacterial therapy in adults with COVID-19–an evidence based guideline, **2021**, *27*, 61–66.

[239] Montero, D. A., Arellano, C., Pardo, M., Vera, R., Gálvez, R., Cifuentes, M., Berasain, M. A., Gómez, M., Ramírez, C., and Vidal, R. M. Antimicrobial

properties of a novel copper-based composite coating with potential for use in healthcare facilities, *Antimicrobial Resistance & Infection Control*, **2019**, *8*, 1–10.

[240] Carey, D. E., and McNamara, P. J. The impact of triclosan on the spread of antibiotic resistance in the environment, *Frontiers in microbiology*, **2015**, *5*, 780.

[241] Lerminiaux, N. A., and Cameron, A. D. Horizontal transfer of antibiotic resistance genes in clinical environments, *Canadian journal of microbiology*, **2019**, *65*, 34–44.

[242] Raffi, M., Mehrwan, S., Bhatti, T. M., Akhter, J. I., Hameed, A., Yawar, W., and Ul Hasan, M. M. Investigations into the antibacterial behavior of copper nanoparticles against Escherichia coli, *Annals of Microbiology*, **2010**, *60*, 75–80.

[243] Dupont, C. L., Grass, G., and Rensing, C. Copper toxicity and the origin of bacterial resistance-new insights and applications, *Metallomics*, **2011**, *3*, 1109–1118.

[244] Santo, C. E., Morais, P. V., and Grass, G. Isolation and characterization of bacteria resistant to metallic copper surfaces, *Applied and environmental microbiology*, **2010**, *76*, 1341–1348.

[245] Doll, P., Al-Ahmad, A., Bacher, A., Muslija, A., Thelen, R., Hahn, L., Ahrens, R., Spindler, B., and Guber, A. Fabrication of silicon nanopillar arrays by electron beam lithography and reactive ion etching for advanced bacterial adhesion studies, *Materials Research Express*, **2019**, *6*, 065402.

[246] Tripathy, A., Sen, P., Su, B., and Briscoe, W. H. Natural and bioinspired nanostructured bactericidal surfaces, *Advances in colloid and interface science*, **2017**, *248*, 85–104.

[247] Marr, A. G. Growth rate of Escherichia coli., *Microbiology and Molecular Biology Reviews*, **1991**, *55*, 316–333.

[248] Beloin, C., Roux, A., and Ghigo, J.-M. *Bacterial biofilms*; Springer, **2008**; pp. 249–289.

[249] Burdett, I., Kirkwood, T., and Whalley, J. Growth kinetics of individual Bacillus subtilis cells and correlation with nucleoid extension., *Journal of bacteriology*, **1986**, *167*, 219–230.

[250] Vlamakis, H., Chai, Y., Beauregard, P., Losick, R., and Kolter, R. Sticking together: building a biofilm the Bacillus subtilis way, *Nature Reviews Microbiology*, **2013**, *11*, 157–168.

[251] Grass, G., Rensing, C., and Solioz, M. Metallic copper as an antimicrobial surface, *Applied and environmental microbiology*, **2011**, *77*, 1541–1547.

[252] Tehrani, F., and Bavarian, B. Facile and scalable disposable sensor based on laser engraved graphene for electrochemical detection of glucose, *Scientific Reports*, **2016**, *6*, 27975.

[253] Yoon, H., Nah, J., Kim, H., Ko, S., Sharifuzzaman, M., Barman, S. C., Xuan, X., Kim, J., and Park, J. Y. A chemically modified laser-induced porous graphene based flexible and ultrasensitive electrochemical biosensor for sweat glucose detection, *Sensors and Actuators B: Chemical*, **2020**, *311*, 127866.

[254] Siscovick, D. S., Sotoodehnia, N., Rea, T. D., Raghunathan, T. E., Jouven, X., and Lemaitre, R. N. Type 2 diabetes mellitus and the risk of sudden cardiac arrest in the community, *Reviews in endocrine and metabolic disorders*, **2010**, *11*, 53–59.

[255] Parfrey, P. S., Griffiths, S. M., Barrett, B. J., Paul, M. D., Genge, M., Withers, J., Farid, N., and McManamon, P. J. Contrast material-induced

renal failure in patients with diabetes mellitus, renal insufficiency, or both, *New England Journal of Medicine*, **1989**, *320*, 143–149.

[256] Stefánsson, E., Bek, T., Porta, M., Larsen, N., Kristinsson, J. K., and Agardh, E. Screening and prevention of diabetic blindness, *Acta Ophthalmologica Scandinavica*, **2000**, *78*, 374–385.

[257] Kameyamai, M., Fushmi, H., and Udaka, F. Diabetes mellitus and cerebral vascular disease, *Diabetes research and clinical practice*, **1994**, *24*, S205–S208.

[258] Saeedi, P., Petersohn, I., Salpea, P., Malanda, B., Karuranga, S., Unwin, N., Colagiuri, S., Guariguata, L., Motala, A. A., Ogurtsova, K., Shaw, J. E., Bright, D., and Williams, R. Global and regional diabetes prevalence estimates for 2019 and projections for 2030 and 2045: Results from the International Diabetes Federation Diabetes Atlas, 9th edition, *Diabetes Research and Clinical Practice*, **2019**, *157*, 107843.

[259] Malanda, U. L., Welschen, L. M., Riphagen, I. I., Dekker, J. M., Nijpels, G., and Bot, S. D. Self-monitoring of blood glucose in patients with type 2 diabetes mellitus who are not using insulin, *Cochrane Database of Systematic Reviews*, **2012**,

[260] Clark Jr, L. C., and Lyons, C. Electrode systems for continuous monitoring in cardiovascular surgery, *Annals of the New York Academy of sciences*, **1962**, *102*, 29–45.

[261] Zhang, Y., Su, L., Manuzzi, D., de los Monteros, H. V. E., Jia, W., Huo, D., Hou, C., and Lei, Y. Ultrasensitive and selective non-enzymatic glucose detection using copper nanowires, *Biosensors and Bioelectronics*, **2012**, *31*, 426–432.

[262] Wong, C. M., Wong, K. H., and Chen, X. D. Glucose oxidase: natural occurrence, function, properties and industrial applications, *Applied Microbiology and Biotechnology*, **2008**, *78*, 927–938.

[263] Park, S., Chung, T. D., and Kim, H. C. Nonenzymatic glucose detection using mesoporous platinum, *Analytical chemistry*, **2003**, *75*, 3046–3049.

[264] Jena, B. K., and Raj, C. R. Enzyme-free amperometric sensing of glucose by using gold nanoparticles, *Chemistry–A European Journal*, **2006**, *12*, 2702–2708.

[265] Meng, L., Jin, J., Yang, G., Lu, T., Zhang, H., and Cai, C. Nonenzymatic electrochemical detection of glucose based on palladium- single-walled carbon nanotube hybrid nanostructures, *Analytical chemistry*, **2009**, *81*, 7271–7280.

[266] Toghill, K. E., Xiao, L., Phillips, M. A., and Compton, R. G. The non-enzymatic determination of glucose using an electrolytically fabricated nickel microparticle modified boron-doped diamond electrode or nickel foil electrode, *Sensors and actuators B: Chemical*, **2010**, *147*, 642–652.

[267] Bai, X., Chen, W., Song, Y., Zhang, J., Ge, R., Wei, W., Jiao, Z., and Sun, Y. Nickel-copper oxide nanowires for highly sensitive sensing of glucose, *Applied Surface Science*, **2017**, *420*, 927–934.

[268] Zhang, Y., Li, N., Xiang, Y., Wang, D., Zhang, P., Wang, Y., Lu, S., Xu, R., and Zhao, J. A flexible non-enzymatic glucose sensor based on copper nanoparticles anchored on laser-induced graphene, *Carbon*, **2020**, *156*, 506–513.

[269] Guo, C., Wang, Y., Zhao, Y., and Xu, C. Non-enzymatic glucose sensor based on three dimensional nickel oxide for enhanced sensitivity, *Analytical Methods*, **2013**, *5*, 1644–1647.

[270] Luo, L., Zhu, L., and Wang, Z. Nonenzymatic amperometric determination of glucose by CuO nanocubes-graphene nanocomposite modified electrode, *Bioelectrochemistry*, **2012**, *88*, 156–163.

[271] Fan, Z., Liu, B., Liu, X., Li, Z., Wang, H., Yang, S., and Wang, J. A flexible and disposable hybrid electrode based on Cu nanowires modified graphene transparent electrode for non-enzymatic glucose sensor, *Electrochimica Acta*, **2013**, *109*, 602–608.

[272] Yang, J., Jiang, L. C., Zhang, W. D., and Gunasekaran, S. A highly sensitive non-enzymatic glucose sensor based on a simple two-step electrodeposition of cupric oxide (CuO) nanoparticles onto multi-walled carbon nanotube arrays, *Talanta*, **2010**, *82*, 25–33.

[273] Bao, J., Hou, C., Zhang, Y., Li, Q., Huo, D., Yang, M., and Luo, X. A Non-Enzymatic Glucose Sensor based on Copper Oxide Nanowires-Single Wall Carbon Nanotubes, *Journal of The Electrochemical Society*, **2015**, *162*, B47–B51.

[274] Reitz, E., Jia, W., Gentile, M., Wang, Y., and Lei, Y. CuO Nanospheres Based Nonenzymatic Glucose Sensor, *Electroanalysis*, **2008**, *20*, 2482–2486.

[275] Meng, Z., Sheng, Q., and Zheng, J. A sensitive non-enzymatic glucose sensor in alkaline media based on Cu/MnO2-modified glassy carbon electrode, *Journal of the Iranian Chemical Society*, **2012**, *9*, 1007–1014.

[276] Wang, L., Lu, X., Wen, C., Xie, Y., Miao, L., Chen, S., Li, H., Li, P., and Song, Y. One-step synthesis of Pt-NiO nanoplate array/reduced graphene oxide nanocomposites for nonenzymatic glucose sensing, *Journal of Materials Chemistry A*, **2015**, *3*, 608–616.

[277] Liu, Y., Wang, M., Zhao, F., Xu, Z., and Dong, S. The direct electron transfer of glucose oxidase and glucose biosensor based on carbon nanotubes/chitosan matrix, *Biosensors and Bioelectronics*, **2005**, *21*, 984–988.

[278] Lu, W., Sun, Y., Dai, H., Ni, P., Jiang, S., Wang, Y., Li, Z., and Li, Z. CuO nanothorn arrays on three-dimensional copper foam as an ultra-highly

sensitive and efficient nonenzymatic glucose sensor, *RSC Advances*, **2016**, *6*, 16474–16480.

[279] Sun, S., Zhang, X., Sun, Y., Yang, S., Song, X., and Yang, Z. Facile water-assisted synthesis of cupric oxide nanourchins and their application as nonenzymatic glucose biosensor, *ACS applied materials & interfaces*, **2013**, *5*, 4429–4437.

[280] Li, J.-Y., Xiong, S., Pan, J., and Qian, Y. Hydrothermal Synthesis and Electrochemical Properties of Urchin-Like Core-Shell Copper Oxide Nanostructures, *The Journal of Physical Chemistry C*, **2010**, *114*, 9645–9650.

[281] Wang, Z., Xiao, Y., Cui, X., Cheng, P., Wang, B., Gao, Y., Li, X., Yang, T., Zhang, T., and Lu, G. Humidity-Sensing Properties of Urchinlike CuO Nanostructures Modified by Reduced Graphene Oxide, *ACS Applied Materials & Interfaces*, **2014**, *6*, 3888–3895.

[282] Sedighi, A., Montazer, M., and Mazinani, S. Synthesis of wearable and flexible NiP0.1-SnOx/PANI/CuO/cotton towards a non-enzymatic glucose sensor, *Biosensors and Bioelectronics*, **2019**, *135*, 192–199.

[283] Zhang, Z., Song, M., Hao, J., Wu, K., Li, C., and Hu, C. Visible light laser-induced graphene from phenolic resin: A new approach for directly writing graphene-based electrochemical devices on various substrates, *Carbon*, **2018**, *127*, 287–296.

[284] Zhang, K., Rossi, C., Tenailleau, C., Alphonse, P., and Chane-Ching, J.-Y. Synthesis of large-area and aligned copper oxide nanowires from copper thin film on silicon substrate, *Nanotechnology*, **2007**, *18*, 275607.

[285] Park, Y.-W., Seong, N.-J., Jung, H.-J., Chanda, A., and Yoon, S.-G. Growth Mechanism of the Copper Oxide Nanowires from Copper Thin Films Deposited on CuO-Buffered Silicon Substrate, *Journal of The Electrochemical Society*, **2010**, *157*, K119.

[286] Mattevi, C., Kim, H., and Chhowalla, M. A review of chemical vapour deposition of graphene on copper, *Journal of Materials Chemistry*, **2011**, *21*, 3324–3334.

[287] Gromov, D. G., Gavrilov, S. A., Redichev, E. N., and Ammosov, R. M. Kinetics of the melting-dispersion process in copper thin films, *Physics of the Solid State*, **2007**, *49*, 178–184.

[288] Gromov, D. G., and Gavrilov, S. A. *Thermodynamics - Physical Chemistry of Aqueous Systems*; InTech, **2011**.

[289] Han, Y., Lai, K. C., Lii-Rosales, A., Tringides, M. C., Evans, J. W., and Thiel, P. A. Surface energies, adhesion energies, and exfoliation energies relevant to copper-graphene and copper-graphite systems, *Surface Science*, **2019**, *685*, 48–58.

[290] de Gennes, P. G. Wetting: statics and dynamics, *Reviews of Modern Physics*, **1985**, *57*, 827–863.

[291] Jiang, X., Herricks, T., and Xia, Y. CuO Nanowires Can Be Synthesized by Heating Copper Substrates in Air, *Nano Letters*, **2002**, *2*, 1333–1338.

[292] Pfefferkorn, G. Elektronenmikroskopische Untersuchungen über den Oxydationsvorgang von Metallen, *Naturwissenschaften*, **1953**, *40*, 551–552.

[293] Kolta, G., and Askar, M. Thermal decomposition of some metal sulphates, *Thermochimica Acta*, **1975**, *11*, 65–72.

[294] Meghana, S., Kabra, P., Chakraborty, S., and Padmavathy, N. Understanding the pathway of antibacterial activity of copper oxide nanoparticles, *RSC Advances*, **2015**, *5*, 12293–12299.

[295] Rietveld, H. M. A profile refinement method for nuclear and magnetic structures, *Journal of applied Crystallography*, **1969**, *2*, 65–71.

[296] Xu, J. F., Ji, W., Shen, Z. X., Li, W. S., Tang, S. H., Ye, X. R., Jia, D. Z., and Xin, X. Q. Raman spectra of CuO nanocrystals, *Journal of Raman Spectroscopy*, **1999**, *30*, 413–415.

[297] Akgul, F. A., Akgul, G., Yildirim, N., Unalan, H. E., and Turan, R. Influence of thermal annealing on microstructural, morphological, optical properties and surface electronic structure of copper oxide thin films, *Materials Chemistry and Physics*, **2014**, *147*, 987–995.

[298] Marioli, J. M., and Kuwana, T. Electrochemical characterization of carbohydrate oxidation at copper electrodes, *Electrochimica Acta*, **1992**, *37*, 1187–1197.

[299] Guo, M. M., Xia, Y., Huang, W., and Li, Z. Electrochemical fabrication of stalactite-like copper micropillar arrays via surface rebuilding for ultrasensitive nonenzymatic sensing of glucose, *Electrochimica Acta*, **2015**, *151*, 340–346.

[300] Hou, L., Zhao, H., Bi, S., Zhu, L., Xu, Y., and Lu, Y. Ultrasensitive and highly flexible nonenzymatic glucose biosensor based on laser-scribed carbon paper substrate, *Applied Surface Science*, **2019**, *465*, 320–331.

[301] Johnson, K. A., and Goody, R. S. The original Michaelis constant: translation of the 1913 Michaelis–Menten paper, *Biochemistry*, **2011**, *50*, 8264–8269.

[302] Feng, H., Huang, Z., Lou, X., Li, J., and Hui, G. Study of a Sucrose Sensor by Functional Cu Foam Material and Its Applications in Commercial Beverages, *Food Analytical Methods*, **2017**, *10*, 407–418.

[303] Jin, J., Zheng, G., Ge, Y., Deng, S., Liu, W., and Hui, G. A non-enzyme electrochemical qualitative and quantitative analyzing method for glucose, D-fructose, and sucrose utilizing Cu foam material, *Electrochimica Acta*, **2015**, *153*, 594–601.

Acronyms

Acronym	Definition
BE	Binding energy
BSE	Backscattered electrons
C-MEMS	Carbon micro-electromechanical systems
CV	Cyclic voltammetry
CVD	Chimical vapor deposition
DNA	Deoxyribonucleic acid
EDX	Electro dispersive x-ray spectroscopy
FTIR	Fourier transform infrared spectroscopy
FWHM	Full width at half maximum
HOPG	Highly oriented pyrolytic graphite
IoT	Internet of Things
IR	Infrared
LASER	light amplification by stimulated emission of radiation
LC	Laser carbon
LIC	laser-induced carbonisation
MEMS	Micro-electromechanical systems
PA	Polyaramid

Acronym	Definition
PC	Polycarbonate
PDMS	Polydimethylsiloxane
PET	Polyethylene terephthalate
PI	Polyimide
RFID	Radio-frequency identification
SAED	Selected area electron diffraction
SEM	Scanning electron microscopy
STEM	Scanning transmission electron microscopy
TEM	Transmission electron microscopy
UV	Ultraviolet
XPS	X-ray photoelectron spectroscopy
XRD	X-ray diffractometry

Acknowledgement

I would like to acknowledge funding provided by the Ministry of Science, Research and Arts, Baden-Württemberg, Germany (Az: 33-7533-30-20/3/3) within HEiKA Center FunTECH-3D initiative and Deutsche Forschungsgemeinschaft under Germany's Excellence Strategy via the Excellence Cluster 3D Matter Made to Order (EXC-2082/1-390761711).

I would like to thank my supervisors Prof. Jan G. Korvink, Prof. Uli Lemmer and Dr. Swati Sharma for their expertise and guidance, which were invaluable in stating the research goals and the required methodology. Their insightful feedback allowed me to sharpen my thinking and brought my work to a higher level.

I would like to heartily acknowledge Prof. Svetlana P. Gulyayeva, Dr. Ruslan S. Mamleyev, Yekaterina G. Gulyayeva and Dr. Irina P. Marunova for their thorough wise counsel during the whole course of doctorate, their sacrifice, parental support, immense understanding and sympathetic ear.

Dr. Dario Mager and all members of low-cost MEMS group, in particular Dr. Omar Nassar, Anna Zakhurdeyeva, Sagar Wadhwa, Ahsana Sadaf and Nan Wang.

I would like to thank my collaborators and research colleagues for the assistance in fundamental understanding of involved processes and great guidance in performed experiments Dr. Alexei Nefedov, Dr. Vladislav V. Kudryashov, Dr. Kirill Poletkin, Dr. Nurdiana Nordin, Dr. Neil MacKinnon, Fabian Falk, Stefan Heissler, Dr. Peter Weidler, Dr. Vitor Vlnieska, Andrey Mikhailov, Dr. Hossein Davoodi, Albina Julius, Prof. Christian Kübel, Dr. C.N. Shyam Kumar, Prof. Christof Wöll, Dr. Asa Asadollahbaik, Dr. Margarita Zakharova, Dr. Otto Markus, Konradin Kaiser, Dr. Joachim Schultz, Dr. Ali Moazenzadeh, Dr. Ronald Kampmann and Dr. Talgat Mamyrbayev.

Additionally I would like to acknowledge my office colleagues Dr. Erwin Fuhrer, Dr. Pedro Silva and Mehrdad Alinaghian for fruitful discussions and setting great working environment.
I would like to heartily acknowledge the dearest Julia Schulte-Hermann for understanding and support in difficult moments. Pim. I would like to thank my dear friends and colleagues Andrea Hurtado Rivera, Natalia Kiseleva, Dr. Michael Oldenburg, Roman Lyubimenko, Moritz Becker, Leon Geiger and Markus Meisner.
Additionally I would like to acknowledge the clean room staff Dr. Uwe Köhler, Heike Fornasier, Dr. Alban Muslija, Richard Theilen and the staff of Institute of Microstructure Technology, specifically Nina Giraud, Manuel Frisman Terrero, Jürgen Benz and Guiseppe Papagno for their wonderful support and assistance with all conducted research.
Separately, I would like to thank David Gilmour, Nick Masson, for their immortal contribution to culture moving heart in difficult moments in course of my Ph.D. with *Dark Side of the Moon* and *Echoes*.

A Thermal Simulation of Laser Pulse

A-1 Precursors Exhibiting Laser-Induced Carbonisation

Table A1: List of Precursors for Laser-Induced Carbonisation.

Commercial Name	Chemical Class	Thermal Conductivity, $W\,m^{-1}\,K^{-1}$	Specific Heat, $J\,g^{-1}\,K^{-1}$
	Chlorinated polyvinyl chloride	0.16	0.9
Kapton	Polyimide	0.12	1.09
Kevlar	Para-aramid	0.04	1.42
Nomex	Meta-aramid	0.12	1.26
	Polybenzimidazole	0.36	1.13
	Polyether ether ketone	0.25	1.34
	(Chloromethyl)polystyrene	0.1	1.2
	Polyphenylene sulfide	0.27	1.25
Torlon	Polyamide-imide	0.36	1
Ultem	Polyetherimide	0.22	2
Ultrason	Polysulfone	0.18	1

A-2 MATLAB Codes for the Thermal Simulation

Listing A.1: Standard thermal simulation.

```
function DM = DyerModel(P0, v0, r, t)
% The interpretation of the model desribed by [Dyer2005].
% r - the depth of the measurement in the simulation, [m];
% t - time duration of the simulation, [s];
% P_0 - input power, [%];
% v_0 - speed of the raster scan, [%]

%% Definition of the parameters and constants
LaserRad = 60e-6; % Laser spot radius, [m]
nu = v0*1.27*1000/2.54; % Frequency of the pulse, [s-1]
```

```
tp = P0/100/(v0*1.27/100*1000/2.54*100); % Pulse duration, [s]
Fl_peak = 40 * tp /(pi*LaserRad^2)/exp(1); %Peak laser fluence, [J/m2]

R = 0.05; % Reflection coefficient
% Absorption coefficient at 10.6 um radiation for Kapton, [cm-1]
AbsCoef = 149;
rho = 1420; % Density of Kapton, [kg m-3]
specificHeat = 1090; % Specific heat of Kapton, [J kg-1 K-1]
thermCond = 0.12; % Thermal conductivity of Kapton, [W m-1 K-1]
kappa = thermCond/rho/specificHeat; % Thermal diffusivity, [m2 s-1]

%% Start of the function

    % The pulse overlap, [%]
    chI = [1.0000    0.7325    0.4776  0.2497    0.0704];
    T = 0; % Initial temperature, [K]

    %% Iterations on the number of pulses
    for i_n = 0 : (5-1)

        tm = i_n/nu : (t/5/1e3) : t;
        T0 = Fl_peak*chI(i_n+1)*(1-R)*AbsCoef ...
        *100/(specificHeat*rho);

        T1 = T0* (exp(-r^2 ./(4*kappa.*(tm - i_n/nu) ...
        + LaserRad^2))./(4*kappa.*(tm - i_n/nu)./LaserRad^2 + 1);
        if T == 0
            T = 0; tf = tm;
        else T1 = [zeros(1,(numel(T) - length(T1))) T1];
        end
        T = T + T1;

    end

%% Storing the values

DM = [ones(length(T),1)*Fl_peak tf' T'];
plot(DM(:,2),DM(:,3))
xlabel 'Time, s'
ylabel 'Temperature, K'

filename2 = [ 'DK_P0_' num2str(floor(P0)) '_v0_' num2str(floor(v0)) ...
'_r_' num2str(floor(r)) 'um' '_t_' num2str(floor(t*1e3)) 'ms'];
print(filename2,'-dpng');
end
```

Listing A.2: Updated thermal simulation with the physico-chemical properties switch.

```
function DM = DyerModelGRF_FP(Fl_I, P0, r, t)
% The updated simulation model described by [Dyer2005].
% During the procedure after reaching threshold temperature,
% implemented switch to the glassy carbon properties with
% temperature over 823 [K] (550 [C]) and to graphite with
% temperature over 1773 [K] (1500 [C])
    % Fl_I - the input fluence, [J/cm2];
    % r - the depth of the measurement in the simulation, [m];
    % t - the time duration of simulation, [s];
    % P_0 - input power, [%]; v_0 - speed of the raster scan, [%]

    %% Definition of the parameters and constants
    LaserRad = 60e-6; %Laser spot radius, [m]

    % Redifining speed from set Fluence
    Fl0 = Fl_I*1e4; % transfer of fluence to SI, [J/m2]
    tp = Fl0 /(40 /(pi*LaserRad^2)/exp(1)); % Pulse duration, [s]
    v0 = (P0/100/(tp*1.27/100*1000/2.54*100)); % speed of the head, [%]

    R = 0.05; %reflection coefficient
    % Kapton properties
    % Absorption coefficient at 10.6 um radiation for Kapton, [cm-1]
    AbsCoef = 149;
    rho = 1420; % density of Kapton, [kg/m^3]
    specificHeat = 1090; % specific heat of Kapton, [J kg-1 K-1]
    thermCond = 0.12; % Thermal conductivity of Kapton, [W m-1 K-1]
    kappa = thermCond/rho/specificHeat; % Thermal diffusivity, [m2 s-1]

    % Glassy carbon properties
    % Absorption coefficient at 10.6 um radiation for graphite, [cm-1]
    AbsCoefGC = 15412;
    rhoGC = 1485; % density of GC, [kg/m^3]
    specificHeatGC = 715; % specific heat of GC, [J kg-1 K-1]
    thermCondGC = 6.6; % Thermal conductivity of GC, [W m-1 K-1]
    % Thermal diffusivity of GC, [m2 s-1]
    kappaGC = thermCondGC/rhoGC/specificHeatGC;

    % Graphite properties
    % Absorption coefficient at 10.6 um radiation for graphite, [cm-1]
    AbsCoefG = 15412;
    rhoG = 1888.5; % density of graphite, [kg/m^3]
    specificHeatG = 726.19; % specific heat of graphite, [J kg-1 K-1]
    thermCondG = 133.02; % Thermal conductivity of graphite, [W m-1 K-1]
    % Thermal diffusivity of graphite, [m2 s-1]
```

```
45      kappaG = thermCondG/rhoG/specificHeatG;

        %% Start of the function

        chI = [1.0000    0.7325    0.4776    0.2497    0.0704];
50      % The pulse overlap, [%]
        T = 0;

        %% Iterations on the number of pulses
        for i_n = 0 : (5-1)
55      %Initital temperatire at r =0 with changing fluence after each
        %pulse

        tm = i_n/nu : (t/5/1e3) : t;
        T0 = Fl0*chI(i_n+1)*(1-R)*AbsCoef*100/(specificHeat*rho);
60      T1 = T0* (exp(-r^2 ./(4*kappa.*(tm - i_n/nu) + LaserRad^2)))./ ...
        (4*kappa.*(tm - i_n/nu)./LaserRad^2 + 1);
        if T == 0
        T = 0; tf = tm;
        else T1 = [zeros(1,(numel(T) - length(T1))) T1];
65      end
        T = T + T1;
        %   Switches to GC and Graphite
                if max(T) >= 823
                    AbsCoef = AbsCoefGC;
70                  rho = rhoGC;
                    specificHeat = specificHeatGC;
                    thermCond = thermCondGC;
                    kappa = kappaGC;
                end
75
                if max(T) >= 1773
                    AbsCoef = AbsCoefG;
                    rho = rhoG;
                    specificHeat = specificHeatG;
80                  thermCond = thermCondG;
                    kappa = kappaG;
                end


85      end

        %% Storing the values
        DM = [ones(length(T),1)*Fl0 tf' T'];
        plot(DM(:,2),DM(:,3))
90      xlabel 'Time, s'
```

```
    ylabel 'Temperature, K'

    end
```

Listing A.3: The script of input parameters variation.

```
function SPFiKGC = scriptGC_P0Fl0r0
    %Script to run multiple iterations for variation of the power, ...
    % fluence and thickness

    %% Input constant parameters
    t = 0.75e-1; % time duration of the simulation, [s];
    % 0.75e-1 optimised for cooling to the room temperature

    % r - the depth increment of the measurement in the simulation, [m]
    r_inc = 1e-6;
    P0_max = 20; %maximal power, [%]
    P0_inc = 0.05; %increment in power, [%]
    Fl_max = 10; %maximal fleunce, [J/cm2]
    Fl_inc = 0.05; %increment fleunce, [J/cm2]

    SPFiKGC = zeros(((Fl_max/Fl_inc)-1)*((Fl_max/Fl_inc)-1), ...
    4*floor(125e-6/r_inc)); % Zero array to store the output values

    r_ind = 0; % indexing for width by the array
    PFl_ind = 0; %indexing for length of the array

    %% Loops for iteration of the power [%], the fluence [J cm-2],
    % and the thickness of the measurement, [um]
    for r = 0 : r_inc : 125e-6

    for P0 = 1 : Fl_inc : P0_max
    for Fl0 = 1 : P0_inc : Fl_max

    PFl_ind = PFl_ind +1; %counter

    DM = DyerModelGCRF_FP(Fl0, P0, r, t);
    Fl = max(DM(:,1))*1e-4; % Fluence at selected parameters, [J/cm2]
    TMax = max(DM(:,3)); % maximal temperature, [K].

    SPFiKGC(PFl_ind, r_ind+1) = Fl;
    SPFiKGC(PFl_ind, r_ind+2) = P0;
    SPFiKGC(PFl_ind, r_ind+3) = r;
    SPFiKGC(PFl_ind, r_ind+4) = TMax;
```

```
    end
    end
    r_ind = r_ind +4; %counter
    PFl_ind = 0; %indexing for length of the array
    end

    end
```

Listing A.4: The extraction and export of computed values.

```
nSPFiK = [];

cSPFiK=size(SPFiK,2)/4 - 1;

for i = 0:cSPFiK
    nM = [SPFiK(:,i*4+1) SPFiK(:,i*4+2) SPFiK(:,i*4+3) SPFiK(:,i*4+4)];
    nSPFiK = [nSPFiK; nM];
end
writematrix(SPFiK,'01_ResultK.csv')
```

A-3 FTIR Analysis of Kapton Films

Table A2: The characteristic vibrations in the polyimide. [194, 199, 202]

Group		Chemical bond	Wavenumber (cm^{-1})			
			Initial film	$2.4\,J/cm^2$	$2.6\,J/cm^2$	$3.3\,J/cm^2$
Imide rings		C–N–C in-plane bending	568	568	568	568
		C–N–C out-of-plane bending	721	722	722	722
		Imide C–N–C transverse stretching	1112	1112	1112	1112
		C–N–C axial stretching	1374	1372	1374	1374
		C=O out-of-phase stretching	1711	1711	1711	1711
		C=O in-phase stretching	1775	1775	1775	1775
Aromatic rings	Tangential	C_6H_4	1014	1014	1012	1012
		C_6H_4	1087	1087	1089	1087
		C_6H_3	1166	1166	1166	1166
		C_6H_3	1288	1288	1288	1288
		C_6H_4	1305	1305	1305	1307
		C_6H_5	1497	1497	1497	1497
		C_6H_4	1599	1599	1599	1599
	Out-of-plane bending	C_6H_3	604	604	604	604
		C_6H_4	704	704	704	704
		C_6H_4	774	775	774	775
		C_6H_4	799	799	799	799
		C_6H_4	815	816	816	816
		C_6H_3	881	881	881	881
		C_6H_3	918	916	916	918
		C_6H_4	937	939	939	939
Other		C–O–C out-of-phase stretching	1239	1238	1238	1238
		CH_2 in-plane bending	1455	1455	1455	1455

A-4 Thermal Model on Glassy Carbon, Graphite and Kapton

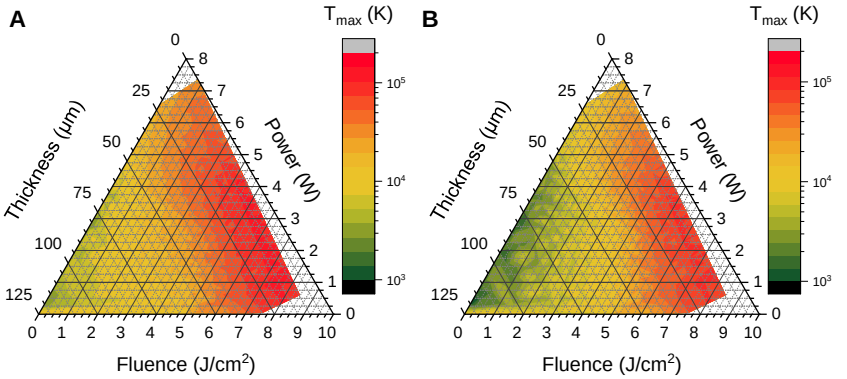

Figure A1: The ternary diagram of simulated maximal temperature on the fluence, the applied power and the distance from the beam centre for (A) glassy carbon and (B) graphite.

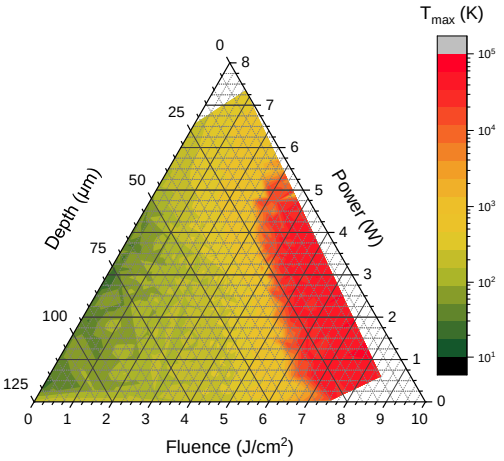

Figure A2: The ternary diagram of simulated maximal temperature on the fluence, the applied power and the distance from the beam centre for modified Kapton after consecutive phase transformations to glassy carbon and graphite.

B Kapton Laser-induced Carbonisation

B-1 Laser Carbon Surface Morphology

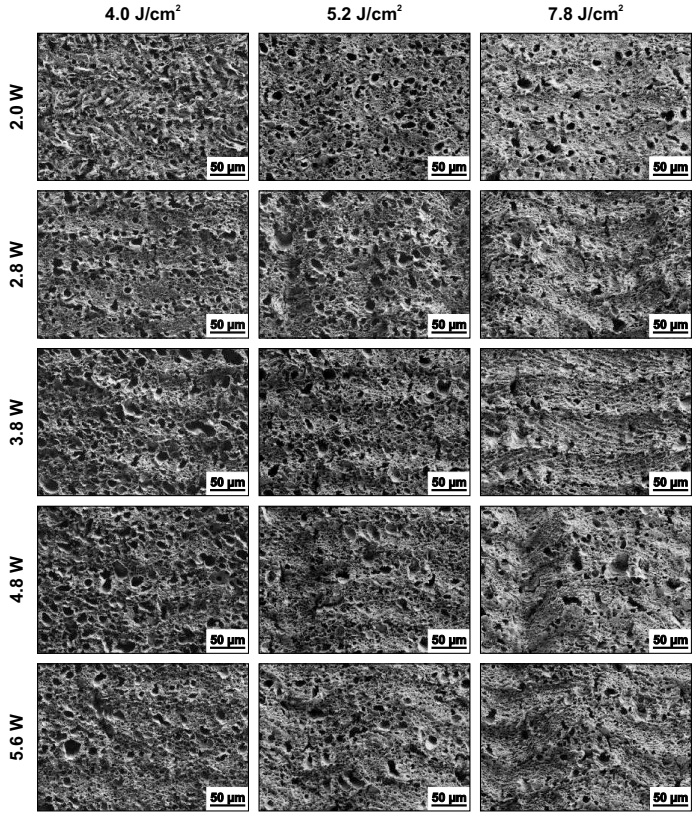

Figure B1: The surface morphology of the laser carbon fabricated in air correlated to used fluence and power.

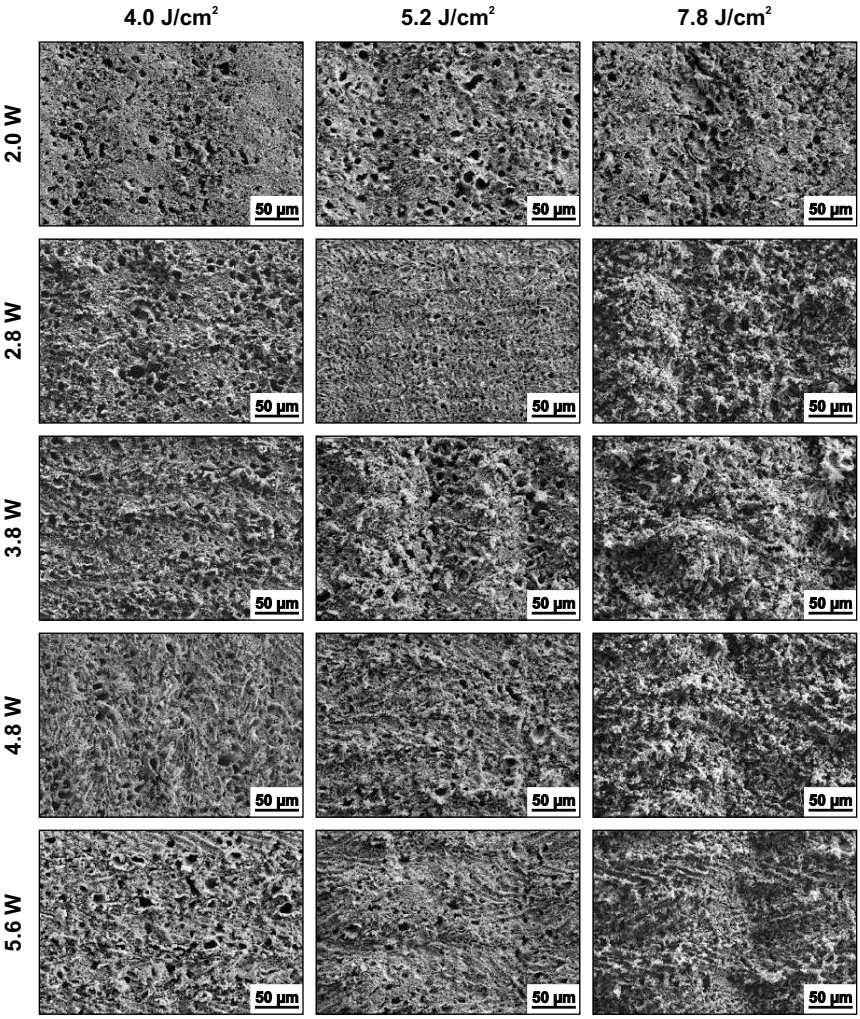

Figure B2: The surface morphology of the laser carbon fabricated under nitrogen flow correlated to used fluence and power.

B-2 XPS Deconvolution

Table B1: Deconvolution of XPS peaks *C 1s, N 1s* and *O 1s* for five selected samples prepared in air and under nitrogen.

	1			2			3			4			5		
	BE (eV)	FWHM (eV)	Area, %	BE (eV)	FWHM (eV)	Area, %	BE (eV)	FWHM (eV)	Area, %	BE (eV)	FWHM (eV)	Area, %	BE (eV)	FWHM (eV)	Area, %
Fabricated in air															
C 1s															
C=C	284.0	1.5	25.1	284.2	1.7	23.0	284.5	1.1	53.3	284.4	1.2	34.5	284.5	1.3	24.3
C-C/C-H	285.0	1.3	39.6	284.7	1.7	52.7	285.0	1.9	27.8	285.0	1.8	31.0	285.0	1.8	53.4
C-N	285.5	1.3	0.9	285.5	1.3	1.2	285.7	1.3	0.6	285.7	1.3	3.8	285.7	1.5	2.4
C-O, C-O-C	286.0	1.5	12.4	286	1.7	12.4	286.4	1.3	5.3	286.3	1.4	12.5	286.3	1.3	13.2
C=O	287.2	1.6	4.8	287.5	1.8	6.6	287.4	1.5	5.8	287.6	1.7	9.3	287.2	1.7	2.0
O-C=O	288.7	1.5	3.4	289	1.8	4.1	288.7	1.6	2.9	288.8	1.3	2.1	288.7	1.3	4.5
Shake-up	-	-	-	-	-	-	290.6	2.5	4.3	290	2.5	3.9	292	2.3	0.2
N 1s															
N6	398.2	1.7	8.9	398.2	1.7	7.3	398.2	1.8	15.89	398.5	1.7	5.3	398.3	1.7	10.7
Amide	-	-	-	-	-	-	-	-	-	399.4	1.4	12.9	-	-	-
N5	399.9	1.7	34.7	400.1	1.7	44.5	399.8	1.6	26.5	400.2	1.6	56.2	400.2	1.5	80.7
NQ	401.2	1.4	56.4	401.7	1.7	48.2	401.8	2.0	57.6	401.5	1.7	20.3	401.2	1.5	8.7
O 1s															
C=O (aromatic)	530.7	1.7	15.7	530.7	1.7	18.7	530.7	1.9	26.8	530.9	1.5	5.4	530.8	1.4	2.8
C=O (aliphatic)	532.0	1.6	18.6	532.0	1.4	20.7	531.9	1.7	35.0	532.2	1.7	37.6	532.2	1.5	32.5
C-O-C (aromatic)	533.0	1.5	21.5	533.0	1.3	19.7	533.0	1.3	8.0	533.0	1.3	11.4	533.0	1.5	25.6
C-O	534.0	1.7	22.6	534.0	1.7	19.3	534	2.3	30.3	533.6	2.0	44.5	533.5	1.9	39.1

Table B2: Deconvolution of XPS peaks *C 1s*, *N 1s* and *O 1s* for five selected samples prepared under nitrogen flow.

	1			2			3			4			5		
	BE (eV)	FWHM (eV)	Area, %	BE (eV)	FWHM (eV)	Area, %	BE (eV)	FWHM (eV)	Area, %	BE (eV)	FWHM (eV)	Area, %	BE (eV)	FWHM (eV)	Area, %
Fabricated in nitrogen															
C 1s															
C=C	284.1	1.3	40.3	284.2	1.7	23.0	284.0	1.3	41.8	284.0	1.3	27.1	284.0	1.3	22.3
C-C/C-H	285.0	1.9	43.5	284.9	2.0	35.6	285.0	2.0	41.1	285.0	2.3	54.1	285.8	2.3	59.0
C-N	285.7	1.7	3.0	285.5	1.3	3.5	285.7	1.3	3.5	285.7	2	4.5	285.7	1.7	3.5
C-O, C-O-C	286.4	1.3	5.0	286.0	1.5	4.3	286.4	1.3	4.3	286.4	1.6	5.9	286.4	1.5	5.5
C=O	287.5	1.3	4.0	287.2	1.6	4.3	287.5	1.5	4.3	287.5	1.4	4.0	287.5	1.3	3.64
O-C=O	288.7	1.6	2.0	288.7	1.5	3.3	288.7	1.9	3.3	288.7	1.7	2.7	288.7	1.5	2.7
Shake-up	290.0	2.5	1.0	291.5	1.3	1.7	290.6	2.0	1.7	290.0	2.5	1.7	290.2	2.5	2.4
N 1s															
N6	398.2	1.7	3.0	398.8	1.7	14.8	398.8	1.4	9.4	398.8	1.6	30.2	398.8	1.5	9.1
Amide	-	-	-	399.4	1.3	2.5	399.4	1.3	7.5	399.4	1.3	9.6	399.4	1.3	12.1
N5	400.2	1.7	61.2	400.2	1.9	49.5	400.2	1.7	54.7	400.2	1.7	45.7	400.2	1.7	54.7
NQ	401.6	1.7	32.0	401.8	1.8	31.7	401.5	1.7	27.5	401.8	1.7	14.1	401.4	1.7	23.4
NX	404.1	1.7	4.0	404.1	1.8	1.5	404.1	1.7	1.0	404.1	1.3	0.3	404.1	1.7	0.7
O 1s															
C=O (aromatic)	530.8	1.7	4.1	530.9	1.3	7.0	530.7	1.7	14.8	530.7	1.7	8.5	530.7	1.7	13.7
Amide	-	-	-	531.3	1.3	1.6	531.4	1.4	3.9	531.4	1.3	4.4	531.4	1.3	5.3
C=O (aliphatic)	532.0	1.7	29.11	532.0	1.7	42.8	532.2	1.7	38.9	532.2	1.7	36.7	532.1	1.7	42.0
C-O-C (aromatic)	533.0	1.5	21.5	533.0	1.3	15.0	533.1	1.6	24.0	533.1	1.3	14.1	533.1	1.5	23.1
C-O	534.0	2.0	45.3	534.0	2.0	33.6	534.0	2.0	18.3	534.0	2.0	36.3	534.0	1.8	15.88

C Nomex Laser-Induced Carbonisation

C-1 XPS Deconvolution

Table C1: Deconvolution of the detailed XPS spectra from Nomex derived laser carbon.

	Specie	LC	LC in N_2	Specie	LC	LC in N_2
C 1s						
Position, eV		284.6	284.6		285.6	–
FWHM, eV	C=C,C–C/C–H	1.4	1.4	C–N	1.4	–
Area, %		65.0	68.4		5.4	–
Position, eV		286.1	286.1		287.6	287.2
FWHM, eV	C–O	1.7	1.4	C=O	1.6	1.5
Area, %		15.2	13.7		5.4	8.5
Position, eV		288.9	288.7		291.0	291.0
FWHM, eV	O–C=O	1.9	1.9	Shake up	2.3	2.4
Area, %		5.2	4.8		3.7	4.6
O 1s						
Position, eV		531.0	530.7		531.0	–
FWHM, eV	C=O (ar)	1.6	1.9	Amide	2.0	–
Area, %		28.3	15.6		22.7	–
Position, eV		532.8	532.3		534.2	534.1
FWHM, eV	C=O (al)	1.8	2.0	C–OH	1.7	2.0
Area, %		16.7	48.6		16.8	35.8
N 1s						
Position, eV		398.8	398.5		399.8	400.2
FWHM, eV	N-6	1.6	1.5	N-5	1.7	1.6
Area, %		37.5	20.3		44.6	25.5
Position, eV		401.8	401.6		404.2	404.1
FWHM, eV	N-Q	1.9	2.0	N-O_x	1.9	1.7
Area, %		13.9	36.0		4.1	17.2

C-2 Size Distribution after Copper Electroplating and Annealing

Table C2: The microspheroids size in Cu-MS films with the variation in copper electroplating time of the precursor film at 1100 °C.

Electroplating time,min	Microspheroid diameter, μm
2.5	7.1 ± 1.8
5.0	5.6 ± 1.3
10	6.6 ± 1.3
20	0.8 ± 0.3 10.2 ± 2.6 36.0 ± 14.3

Table C3: Size of microspheroids in Cu-MS films after 10 min electroplating annealed at different temperatures.

Annealing temperature,°C	Microspheroid diameter, μm
800	–
900	–
1000	0.35 ± 0.12 7.35 ± 1.47 16.79 ± 7.46
1100	0.8 ± 0.3 10.2 ± 2.6 36.0 ± 14.3

Table C4: Size of micro-urchins in CuO-U films after 10 min electroplating annealed at different temperatures.

Annealing temperature,°C	Microspheroid diameter, μm
800	–
900	–
1000	8.82 ± 2.64 17.87 ± 5.96
1100	1.12 ± 0.44 16.82 ± 7.54

C-3 XPS Deconvolution after Copper Electroplating and Annealing

Table C5: Deconvolution of detailed XPS spectra in each spectral line.

Specie		Electroplated Cu	Cu spheroids	CuO urchins
C 1s				
C=C,C–C/C–H	Position, eV	284.6	284.6	284.6
	FWHM, eV	1.5	1.4	1.5
	Area, %	71.3	77.4	73.2
C–N	Position, eV	285.7	–	–
	FWHM, eV	1.5	–	–
	Area, %	1.6	–	–
C–O	Position, eV	286.3	286.1	286.0
	FWHM, eV	1.4	1.5	1.6
	Area, %	11.7	13.6	13.7
C=O	Position, eV	287.5	287.2	287.5
	FWHM, eV	1.8	1.3	1.7
	Area, %	4.8	3.9	6.9
O–C=O	Position, eV	288.7	288.7	288.7
	FWHM, eV	1.9	1.6	1.9
	Area, %	4.8	2.3	3.3
Shake up	Position, eV	291.5	290.5	291.0
	FWHM, eV	1.7	2.4	2.5
	Area, %	5.9	2.7	2.9
O 1s				
CuO	Position, eV	529.5	529.8	529.8
	FWHM, eV	1.4	2.0	1.3
	Area, %	12.6	4.6	38.1
Cu_2O	Position, eV	530.4	530.4	530.2
	FWHM, eV	2.0	2.0	1.3
	Area, %	33.0	4.6	4.9
C=O (ar)	Position, eV	530.9	530.9	530.9
	FWHM, eV	1.4	1.3	2.0
	Area, %	31.9	7.5	23.0
C=O (al)	Position, eV	532.1	532.2	532.1
	FWHM, eV	1.8	1.6	1.9
	Area, %	20.0	69.4	29.2
C–OH	Position, eV	534.3	533.7	534.2
	FWHM, eV	1.7	1.8	2.0
	Area, %	2.5	13.9	5.0
Cu 2p				
Cu	Position, eV	932.4	932.4	932.7
	FWHM, eV	1.8	1.8	1.8
	Area, %	30.5	27.7	6.8
Cu_2O	Position, eV	932.2	932.2	932.9
	FWHM, eV	1.3	1.3	1.8
	Area, %	19.9	16.4	16.8
CuO	Position, eV	933.2	934.0	934.1
	FWHM, eV	3.0	2.9	2.3
	Area, %	17.7	27.3	42.4
$Cu(OH)_2$	Position, eV	935.4	935.4	935.7
	FWHM, eV	4.0	3.7	4.0
	Area, %	23.2	16,0	21.5
$CuSO_4$	Position, eV	935.2	–	–
	FWHM, eV	2.0	–	–
	Area, %	7.6	–	–

C-4 Saccharose Sensing with Amperometric Biosensor

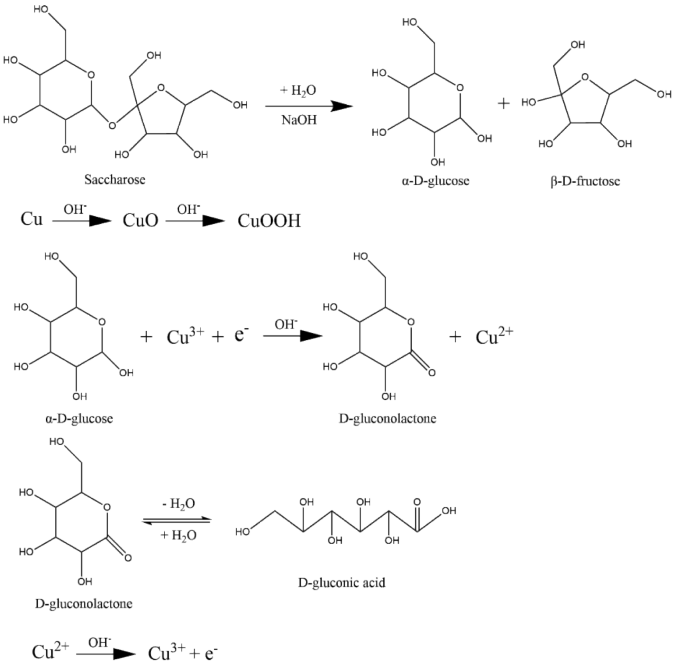

Figure C1: Saccharose hydrolysis and a catalytic oxidation of produced glucose by Cu micro and nanostuctures (adopted from Ref.[303]).

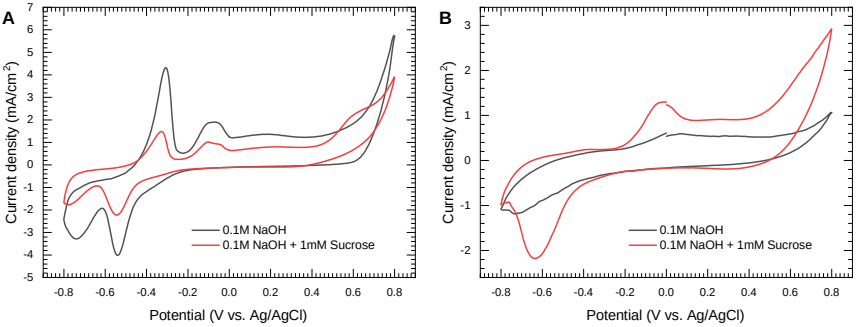

Figure C2: Cyclic voltammetry performed in various solutions on (A) Cu-MS and (B) CuO-U films.

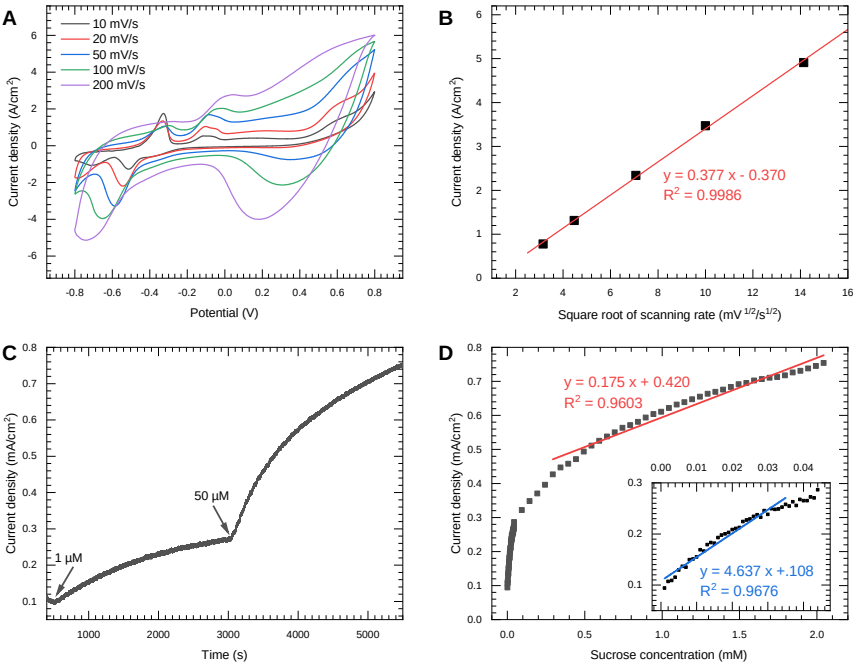

Figure C3: (A) Cyclic volatemetry in 0.1 M NaOH and 1 mM sucrose with variation of the scannining rate on Cu spheroid film. (B) Dependence of the oxidation current density at 0.5 V on the scanning rate. (C) Amperometric response of the copper spheroids by delivery of sucrose. (D) Amperometric responce on the sucrose concentration with the fitted curves.

List of Figures

List of Tables